UNIVERSITY OF CALIFORNIA
RIVERSIDE

ϕ Meson Production in Au-Au Collisions at 200 GeV Measured by the PHENIX Experiment at the Relativistic Heavy Ion Collider

A Dissertation submitted in partial satisfaction
of the requirements for the degree of

Doctor of Philosophy

in

Physics

by

Mohammed Muniruzzaman

June 2003

Dissertation Committee:

Professor Richard Seto, Chairperson

Professor Kenneth Barish

Professor Jose Wudka

The Dissertation of Mohammed Muniruzzaman is approved:

Committee Chairperson

University of California Riverside

ACKNOWLEDGMENTS

I would like to thank a long list of people who helped make this dissertation possible. On the top of the list is my thesis advisor, Professor Richard Seto. I gratefully acknowledge his encouragement, support and guidance. His enthusiasm for heavy-ion physics was really infectious. I consider myself fortunate that I was able to work under his guidance.

When I started my research work, PHENIX was in the hardware stage. I was encouraged to get involved in the hardware, electronics and software. This was a valuable experience for me. In fact this part of my work helped me to be better equipped for the challenges in my future career endeavors. I thank the UCR Heavy-Ion Research group for giving me the opportunity to work at the great PHENIX experiment at the Brookhaven national Laboratory.

I thank Professor Kenneth Barish for his encouragement and valuable suggestions. I also thank Dr. Basanta Nandi for many invaluable brainstorming hours. I thank Dr. Xin-Hua Li, Dr. Hai-Qiao Wang and Dr. Wen-Chen Chang, whom I worked with for detector hardware. I also thank Dr. Xie Wei for his suggestions time to time. I appreciate Dmitri Kotchetkov, my fellow graduate student, for many lively discussions we had not only on physics, but also on the bigger picture of life.

I am indebted to the PHENIX Collaboration. My thanks to the Light Vector Mesons and Heavy Flavor Physics working group for their comments and suggestions on my presentations. I specially thank Professor Jamie Nagle, Dr. Yasuyuki Akiba, Dr. Ralf Averbeck and Dr. Vince Cianciolo for their interest, comments and encouragement on the work.

My thanks to the members of the Paper Preparation Group on Phi Mesons (PPG016), specially Professor Charles Maguire, Dr. Debsankar Mukhopadhyay and Dr. Dipali Pal. Much of the analysis were accomplished in connection to the preparation for the publication. Professor Maguire was a great source of knowledge, especially when it comes to simulation. He was always helpful with his comments and suggestions. Discussion with Dr. Mukhopadhyay was always productive.

I would like to thank my parents, although I know that words are not enough to acknowledge of what they have done for me. They brought me to this world and taught me how beautiful the life is. Their only expectation from me is that I grow up to be a good person. They are thousands of miles away from in a small country named Bangladesh, but their love always reminded me that they are with me at all the time.

Finally, I would like to thank my loving wife Tahsina Ferdousi for her love and support during my graduate studies. She has been my strength throughout these years. She, also being a member of the PHENIX collaboration, could understand what it takes to get the job done. I remember we spent many evenings discussing about PHENIX and physics. She sacrificed a lot for me to complete the thesis. Thank you Tahsina!

Dedication

To my parents

ABSTRACT OF THE DISSERTATION

ϕ Meson Production in Au-Au Collisions at 200 GeV Measured by the PHENIX Experiment at the Relativistic Heavy Ion Collider

by

Mohammed Muniruzzaman

Doctor of Philosophy, Graduate Program in Physics
University of California Riverside, June, 2003
Professor Richard Seto, Chairperson

The production and decay of the ϕ meson in relativistic heavy ion collisions is of considerable interest. An enhanced ϕ meson yield has been suggested as a signature for the formation of a deconfined phase. Furthermore, medium modifications of ϕ meson properties might be related to the expected chiral phase transition.

In the year of 2001, the PHENIX experiment at RHIC has measured Au-Au collisions at $\sqrt{s_{NN}} = 200$ GeV. The trajectories and momenta of charged particles are measured with the PHENIX central arm tracking detectors. The additional velocity measurements from the high resolution Time-of-Flight detector as well as the broader acceptance Electromagnetic Calorimeter give PHENIX excellent capabilities to identify charged kaons. An excellent pair mass resolution of approximately 1.3 MeV was achieved for the combined systems. Results on the transverse mass distribution, the centrality dependence of the yield, inverse slope parameter, and the resonance and width of ϕ are presented.

Contents

List of Figures

List of Tables

Chapter 1

Introduction

The relativistic heavy ion physics is the study of nuclear matter in extreme conditions of density and temperature. Nuclear matter is build up of quarks, but no free quarks are observed yet. In the extreme conditions a phase transition is expected where the quarks and gluons will be *free* over a short period of time.

The quarks interact among themselves via the exchange of gluons. The state of the nuclear matter is described by the Quantum Chromodynamics (QCD). The QCD exhibits a property called the *asymptotic freedom* [1, 2]. The running coupling constant α_s, which depends on the momentum transfer among the quarks and gluons, is large at small momentum transfer. Small momentum transfer is equivalent to large distance. This means that if one wants to pull quarks apart, the force of interaction grows so large that quarks cannot be isolated. On the other hand, the for large momentum transfer, which is equivalent to small distance, the force of interaction becomes small. Here lies the clue that although quarks can not be isolated, but a situation can be created where a soup of quarks and gluons can be created in a small space-time region. This can be achieved with heating up the system (high momentum transfer) and/or compressing the nuclear matter (small distance). This state of matter is commonly called as the Quark-Gluon Plasma (QGP).

It is believed that the Quark-Gluon Plasma existed in the early universe a few microseconds after the Big Bang. The QGP can be created in the laboratory by heating up and/or compressing the nuclear matter. We can make a rough estimate of the critical temperature T_c and the baryon density ρ_c needed for the QGP creation. It is estimated that if the distance is of the order of 1 fm, the QCD interactions become *weak*. From there we can estimate that $T_c \approx \hbar/1$ fm $\approx$ 200 MeV. On the other extreme, the individual nucleons will lose their identity if they are compressed beyond the nucleon radius, which is $\sim$ 0.8 fm. The density of normal nuclear matter is about 0.16 fm^{-3}. Thus about ten times the density of the normal nuclear matter, the QGP may be created. Lattice calculations also give similar estimations. With these estimations in mind a QCD phase diagram is drawn in Fig. 1.1. The location of the phase boundary is not well known. The magenta band represents the uncertainty of the phase boundary estimation.

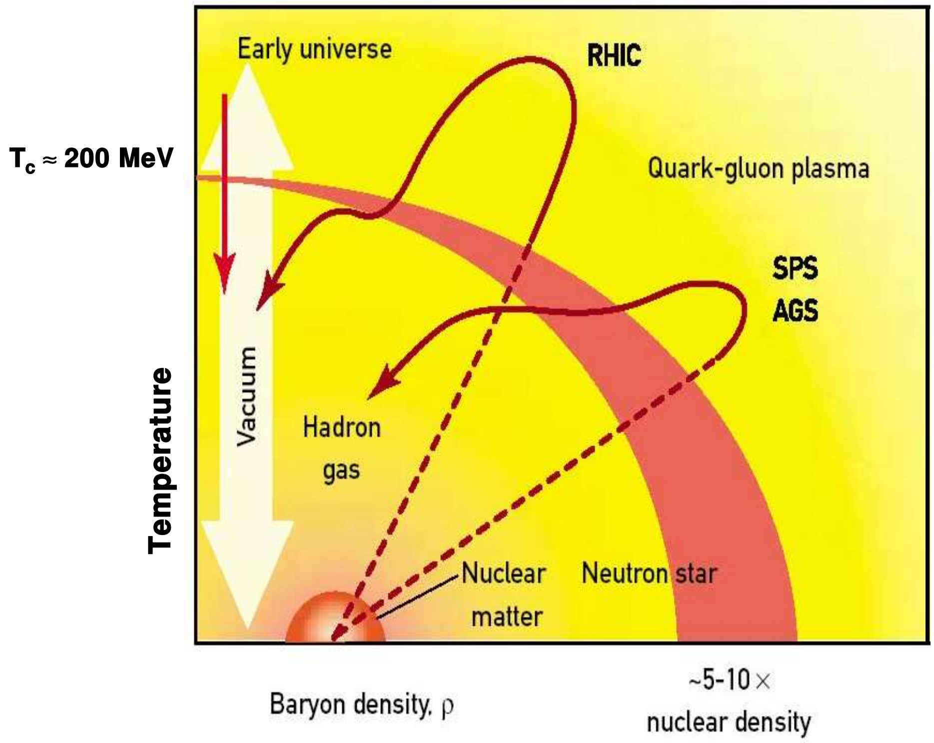

Figure 1.1: QCD phase diagram

Early experiments in heavy ion collisions were conducted at the Bevatron/Bevalac at Berkley in early 70's. More concerted effort to study the hot dense nuclear matter began in mid 80's at the Alternating Gradient Synchrotron (AGS) at the Brookhaven National Laboratory in New York, The Super Proton Synchrotron (SPS) at CERN in Geneva, Switzerland and GSI at Darmstadt, Germany. These facilities provided valuable and important information for the hot dense matter. But there were no definitive answer for observation of the expected phase transition. This eluded to build the Relativistic Heavy Ion Collider (RHIC) at the Brookhaven National Laboratory. Already in its third year in operation RHIC produced a wealth of valuable data from the Au-Au, p-p and d-Au collisions. The data are being analyzed to sought the answer for the existence of the deconfined phase. An even more powerful collider, named the Large Hadron Collider (LHC) is being constructed at CERN and expected operate from 2007.

1.1 Probing the Deconfined Phase with ϕ Meson

If a phase transition occurs in a heavy ion collision, it will manifest itself through a variety of signatures. ϕ meson is considered as a probe for the deconfined phase. The properties of ϕ meson are expected to be modifies as a consequence of the medium modification and chiral symmetry restoration. The study of ϕ meson in heavy ion collisions are important in view of the following aspects:

- An enhancement of ϕ meson production is expected if a phase transition occurs.
- The mass and width of ϕ may change due to medium effect and possible chiral symmetry restoration.
- Due to the medium modification, the ratio of ϕ decaying in the hadronic and leptonic channels may change.

We will elaborate the reasons why such effects are expected if a phase transition happens in a heavy ion collision. They are the consequences of the strangeness production and expected chiral symmetry restoration in a heavy ion collision.

1.2 Strangeness Enhancement in Heavy Ion Collisions

It has been proposed that the strangeness content may change if a phase transition occurs in a heavy ion collision [10]-[19]. It is suggested that there will be an enhancement of strangeness. In nuclear matter the valence quarks consists of up and down quarks. the s and $\overline{s}$ content is small. In nucleon-nucleon collisions $u\overline{u}$, $d\overline{d}$ and $s\overline{s}$ pairs are produced. The strangeness production mechanism can be described through the cartoon in Fig. 1.2. Let us consider a quark soup at zero temperature. The quark content of this soup is primarily u and d. Since the mass of u and d are almost zero, the Fermi energy of the soup is almost equal to the Fermi momentum. Now let us consider that the Fermi energy increases as a consequence of a heavy ion collision. The available states will first be filled by the u and d quarks. But when the Energy exceeds the rest mass of $s\overline{s}$ pairs, $E_{threshold} \simeq 2m_s \simeq 300 - 400$ MeV, the strange quarks have the equal probability to fill the available states. Therefore $s\overline{s}$ pairs will be created almost equally as $u\overline{u}$ and $d\overline{d}$ pairs. Thus there will be an enhancement of strangeness production.

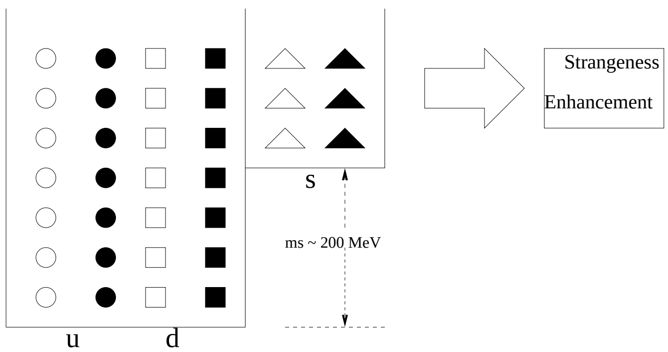

Figure 1.2: Mechanism of strangeness enhancement

In the plasma s and $\overline{s}$ are produced by collisions among the constituents of the plasma. The plasma mainly consists u, $\overline{u}$, d, $\overline{d}$ and g. Strange quarks and anti-quarks can be produced by light quark and anti-quark collisions through the reactions

$$u + \overline{u} \rightarrow s + \overline{s} \tag{1.1}$$

$$d + \overline{d} \rightarrow s + \overline{s} \tag{1.2}$$

The reactions (1.1) and (1.2) proceeds by the conversion of the $u\overline{u}$ (or $d\overline{d}$) pairs into a gluon, with the subsequent emission of $s\overline{s}$ pairs. This is represented by the Feynman Diagram in Fig. 1.3 The reactions (1.1) and (1.2) are not the only processes that

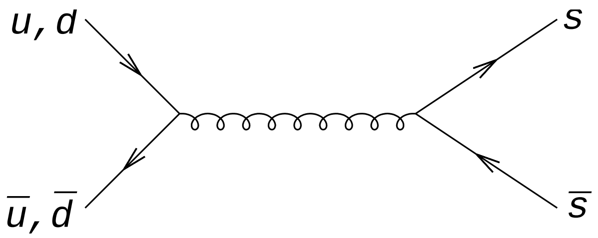

Figure 1.3: Feynman Diagram for $u + \overline{u} \rightarrow s + \overline{s}$ and $d + \overline{d} \rightarrow s + \overline{s}$ production

produces strangeness. Strangeness can also be produced through gluon fusion:

$$g + g \rightarrow s + \overline{s} \tag{1.3}$$

This processes are represented by the Feynman diagrams in Fig. 1.4.

Measurements made by CERN WA97[20] and NA49 [21] collaborations demonstrate a relative enhancement of the mutistrange particles yields (Λ, $\Xi\,\Omega$) in nucleus-nucleus collisions compared to proton-nucleus collisions. But one ought to be careful to claim an strangeness enhancement in A-A collision due to the fact of the complexity of hadronic interactions in such a collision. At RHIC where the QGP is expected to be formed for a longer time, provides better conditions for measurement of strangeness contents.

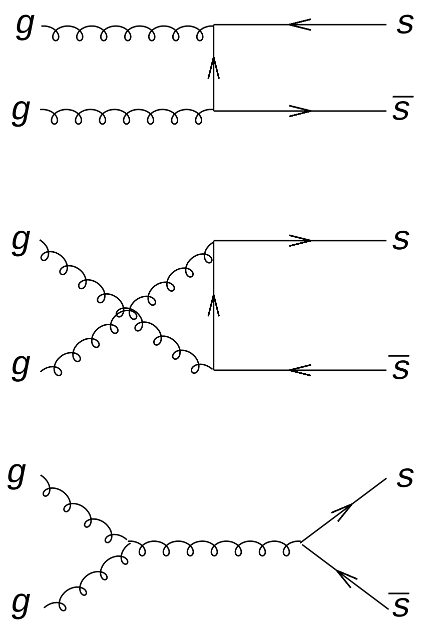

Figure 1.4: Feynman Diagram for $g + g \rightarrow s + \overline{s}$ production

1.3 Chiral Symmetry Restoration

The chiral symmetry is associated with the limit of vanishing quark masses. It the symmetry of QCD where quark masses approach zero. Although the quark have finite masses, the masses of quarks, specially the up and down quarks, are negligible compared to the hadron masses. Therefore we can consider the chiral symmetry as an approximate symmetry in strong interactions.

The chiral symmetries are symmetries which mix fields of the same handedness among themselves, such that the amount of mixing of the right-handed fields among themselves is independent of the amount of mixing of the left-handed fields among themselves. The $SU(3)$ QCD Lagrangian contains a mass term of the form $\overline{\psi}M\psi$. The chirality $\psi_{L,R} = \frac{1}{2}(1 \pm \gamma_5)\psi$ would conserve symmetry if the mass diagonal matrix M is zero, meaning quarks are mass less. In that situation, the $SU(3)$ QCD Lagrangian would be an unbroken symmetry.

The vacuum expectation value $< \overline{\psi}\psi >$ is not zero. This means that the chiral symmetry is spontaneously broken. In this situation the Hamiltonian possesses the symmetry, but not the ground state. An important consequence of the spontaneous breakdown of symmetry is the existence of the mass less Goldstone boson. In our case the Goldstone boson is pion. Thus if the chiral symmetry is a perfect symmetry, pions would be mass less. Since the chiral symmetry is only approximate, the pions are expected to have a finite, but small mass.

In the limit of sufficiently high temperature or density, the chiral symmetry is expected to be restored. What this means that states at high temperatures and densities will have same symmetry as the Hamiltonian. If the chiral symmetry is restored, there will be an absence of Goldstone bosons and pions are expected to become massive, with comparable mass as the hadrons.

The chiral symmetry restoration and the deconfinement walk hand to hand. The current lattice calculation suggests that the chiral symmetry restoration and the deconfinement take place at the same temperature. When the chiral symmetry is restored, the vacuum expectation value $< \overline{\psi}\psi > = 0$. On the other hand when the deconfinement takes place the quarks are asymptotically free within the small volume of space and $< \overline{\psi}\psi > = 0$ as well. Therefore it is suggested that the chiral symmetry restoration and the deconfinement might be two aspects of the QCD phase transition [22].

There are some very important aspects of the chiral symmetry restoration on the hadronic masses. The mass less Goldstone bosons will acquire masses. That means pions will become massive. This may be true to some extent to kaon masses. But one should be careful about the effect of the pion-nucleon and kaon-nucleon potential. Various approaches and models have been used to study theoretically the meson masses in nuclear matter. These include the scaling ansatz of Brown and Rho [23], the QCD sum-rule approach [24, 25, 26, 27, 28], the quark coupling model [29] and quantum hydrodynamics (QHD) [30, 31, 32]. All these seem to suggest that decrease

Quantum Number	$I^G\ (J^{PC})\ =\ 0^-\ (1^{--})$
Mass	1019.456 ± 0.020 MeV/c^2
Full Width, Γ	4.26 ± 0.05 MeV/c^2
Decay Mode	**Branching ratio**
$\phi \to K^+K^-$	$\left(49.2^{+0.6}_{-0.7}\right)$ %
$\phi \to K_L^0 K_S^0$	$(33.7\ \pm\ 0.5)$ %
$\phi \to \rho\pi\ +\ 3\pi$	$(15.5\ \pm\ 0.05)$ %
$\phi \to e^+e^-$	$(2.96\ \pm\ 0.04)\ \times\ 10^{-3}$%
$\phi \to \mu^+\mu^-$	$\left(2.87^{+0.18}_{-0.22}\right)\ \times\ 10^{-4}$%

Table 1.1: ϕ Meson properties [3]

in the vector meson masses is a consequence of the chiral symmetry restoration at high temperature and/or high densities.

1.4 The ϕ Meson

The ϕ meson is a vector meson in the pure $s\bar{s}$ state. The mass, width and principal decay modes in hadronic and leptonic channels are given in Table 1.1.

The K^+K^- decay channel is dominant among the hadronic decay channels. Naively one would expect the preferred hadronic decay channel ϕ to be into pions over kaons, since decay in pions have much more phase space available:

$$\Delta m\ (\phi\ \to\ \pi^+\pi^-\pi^0)\ \approx\ 601\ \mathrm{MeV/c}^2$$

$$\Delta m\ (\phi\ \to\ K^+K^-)\ \approx\ 32\ \mathrm{MeV/c}^2$$

It is to mention here that the $\phi\ \to\ \pi^+\pi^-$ is forbidden by G-parity conservation. Now, although the phase space available in decays in pions are more than the phase space in kaon decays, the suppression in the pion decay channels is explained by the OZI rule [4, 5]. According to the OZI rule, strong interaction processes where the final state can only be reached through quark anti-quark annihilation is suppresses. The

OZI rule can be explained in the diagram in Fig. 1.5. The figure at the left describes the $\phi \rightarrow \pi^+\pi^-\pi^0$ process. This involves the annihilation of the $s\overline{s}$. Such a process is suppressed in strong interactions. On the other hand, the $\phi \rightarrow K^+K^-$ process is described on the right. This process does not involve the annihilation of $s\overline{s}$, and therefore is not suppressed.

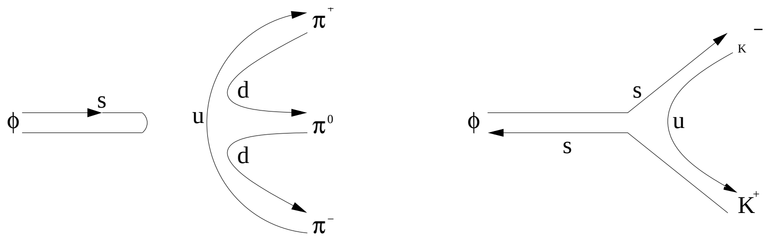

Figure 1.5: ϕ decay in 3π and $2K$ channels. The Decay in 3π is OZI suppressed.

1.4.1 ϕ Production

There are several mechanism proposed for the ϕ meson production in heavy ion collisions. ϕ mesons are produced in the baryon-baryon interaction channels and the meson-baryon channels:

$$B\,B \;\rightarrow\; \phi\,N\,N \tag{1.4}$$

$$(\pi,\rho)\,B \;\rightarrow\; \phi\,B \tag{1.5}$$

where $B \equiv N$, Δ, N^*. These types of processes were dominant ϕ production channel at SIS energies (1-2 A GeV) [6]. At AGS energies ($\sim$11 A GeV)[7], the same processes with one or more pions in final state may contribute to ϕ production as well. These processes are OZI suppressed. In both types of processes given in Eqn.(1.4) and (1.5), the ϕ is created at a $\rho\pi\phi$ vertex. The Feynman diagram for such processes are shown in Fig. 1.6. There are other non-OZI suppressed processes for ϕ production which involve the production of additional kaons:

$$\pi\,N \;\rightarrow\; N\,K\,\overline{K}\,\phi \tag{1.6}$$

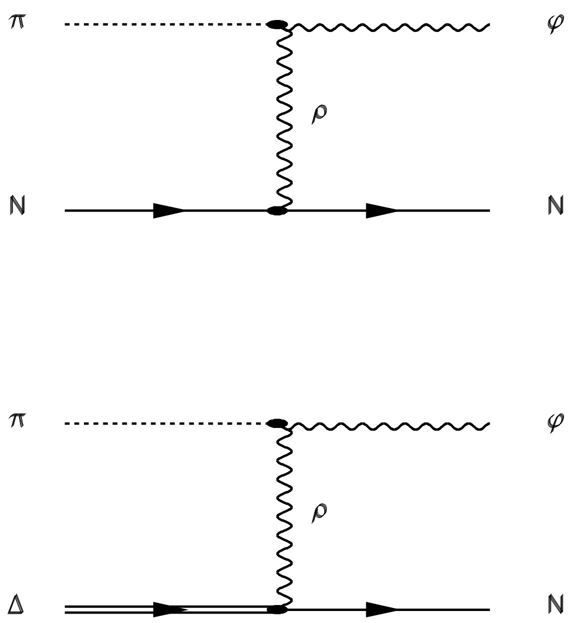

Figure 1.6: Feynman Diagram for $\pi B \rightarrow \phi B$ production

$$N\,N \quad \rightarrow \quad N\,N\,K\,\overline{K}\,\phi \tag{1.7}$$

But these processes are suppressed by other kinematic and dynamic factors [8]. ϕ can also be produced in kaon exchange reactions such as:

$$K\,\overline{K} \quad \rightarrow \quad \rho\,\phi \tag{1.8}$$

$$K\,\Lambda \quad \rightarrow \quad N\,\phi \tag{1.9}$$

The other important mechanism for ϕ production kaon coalescence. It was proposed [9] on the argument that the phase space density of K and $\overline{K}$ are much higher in a heavy ion collision than a simple $p-p$ collision. In such a situation a coalescence of hadronic state kaon may result in a $s\overline{s}$ bound state to produce ϕ.

1.4.2 Enhancement of ϕ Meson Production

The production of ϕ meson in hadronic interactions such as Eqs. (1.4) or (1.5) are OZI suppressed. But what happens if a phase transition occurs in a heavy ion collision? There will be an abundance of the strange quark content in the fireball. This strangeness production in heavy ion collision may lead to an increased ϕ meson production. The $s\bar{s}$ coalescence is not OZI suppressed. Therefore ϕ meson production is expected to increase as a consequence of the strangeness production. The enhancement of ϕ meson production is proposed as a signature of the deconfined phase.

1.4.3 Medium Modification of ϕ Mass and Width

As a consequence of the chiral symmetry restoration and medium effect the ϕ mass in expected to decrease. Also the width of ϕ may change. The dominant hadronic decay channel $\phi \rightarrow K^+K^-$ may show a change in the width as consequence of the decrease in both ϕ mass and kaon masses in nuclear medium. If the decrease of $m^*_{K^+} + m^*_{K^-}$ is larger than m^*_ϕ in the medium, there will be broadening in the ϕ width. A theoretical calculation by Rapp [33] is shown in Fig. 1.7 demonstrating the expected broadening of the width.

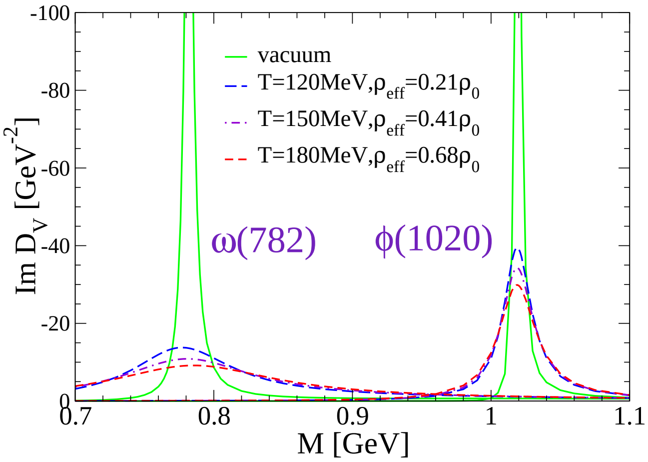

Figure 1.7: Expected broadening of widths of vector mesons

1.4.4 Ratio of ϕ Yields in Hadronic and Leptonic Channels

ϕ decays can be detected experimentally both in hadronic and leptonic channels. The reconstruction in the K^+K^- decay channel will be affected by the kaon and anti-kaon final state interaction. The detection in this channel will only include ϕ those decay at and after the freeze-out. But the leptons do not suffer such an interaction. Therefore the dilepton channel will also detect ϕ that decays inside fireball. The situation can be described in the cartoon in Fig. 1.8 The ratio of the ϕ yields in the hadronic and

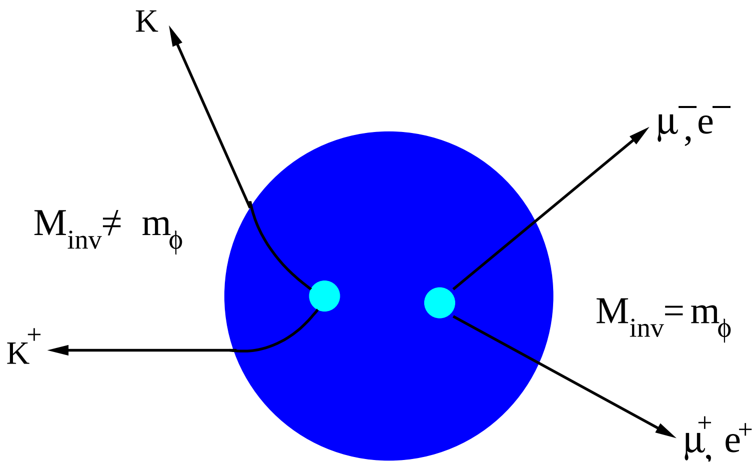

Figure 1.8: ϕ reconstruction in the hadronic and leptonic channels. The hadronic channel suffer strong final state interaction

leptonic channels will this be different in a heavy ion collision compared to that in vacuum. The combined measurements of the ϕ in both the hadronic and the leptonic channels may be a very powerful diagnostic tool for the QCD phase transition.

1.5 Organization of the Thesis

The measurement of the ϕ mesons in Au-Au collisions at $\sqrt{s_{NN}} = 200$ GeV will be presented. The results will include the ϕ Yields and lineshape analysis.

In Chapter 1, an introduction to heavy ion physics is given. The importance of the ϕ meson measurements in the heavy ion collisions and the connection of ϕ meson measurements to the expected phase transition is discussed.

In Chapter 2, An overview is given for the kinematic variables used in the thesis. This chapter is intended to the establish the language for relativistic heavy ion collisions.

In Chapter 3, The Machine and detector setup is discussed. A brief discussion on the Relativistic Heavy Ion Collider (RHIC) is given. The PHENIX detector subsystem is discussed. Emphasis is given for the detector components used for the present analysis.

In Chapters 4, 5, 6 and 7 we discuss furnish the details of the analysis procedure. The analysis uses a set of conditions for the data selection. In Chapter 4, we discuss the data selection criterion for the analysis. The inclusive kaon analysis is given in Chapter 5. The ϕ signal generation is discussed in Chapter 6. There we discuss the invariant mass reconstruction, event mixing and background normalization procedures. In Chapter 7, we give the necessary corrections applied to the analysis.

In Chapters 8 and 9 we give our results. We present the results for the ϕ mass and width in Chapter 8. In Chapter 9, we present the results on the ϕ Yields in Au-Au collision. In Chapter 9, we describe the systematic error measurements.

In Chapter 10, discussions on the results are presented.

Chapter 2

Kinematics

In relativistic heavy-ion experiments there are some kinematic variables that are widely used in the field. In this chapter we intend to provide an introduction of the variables in order for a general reader to understand. Also we introduce notations and conventions used in this thesis. The discussion of kinematic variables, collision centrality and resonance will then establish proper language for relativistic heavy-ion collisions.

2.1 Conventions & Notations

We use the natural units $c = \hbar = 1$. The space-time coordinate is written as x=(t,$\mathbf{x}$) and the momentum 4-vector is written as p=(E,$\mathbf{p}$). The 4-vectors will be written in italic typeface(p), while ordinary 3-vectors will be written in boldfaces($\mathbf{p}$). The space-time metric tensor $g_{\mu\nu}$ will be written in the following convention:

$$g_{\mu\nu} = \mathrm{diag}(1, -1, -1, -1) \tag{2.1}$$

The scalar product of two vectors a=(a^0,$\mathbf{a}$) and b=(b^0,$\mathbf{b}$) is defined as

$$a.b = a^{\mu} b_{\mu} = g_{\mu\nu} a^{\mu} b^{\nu} = a^0 b^0 - \mathbf{a}.\mathbf{b} \tag{2.2}$$

The coordinate system for the experiment is shown in Fig.(2.1). The axis of col-

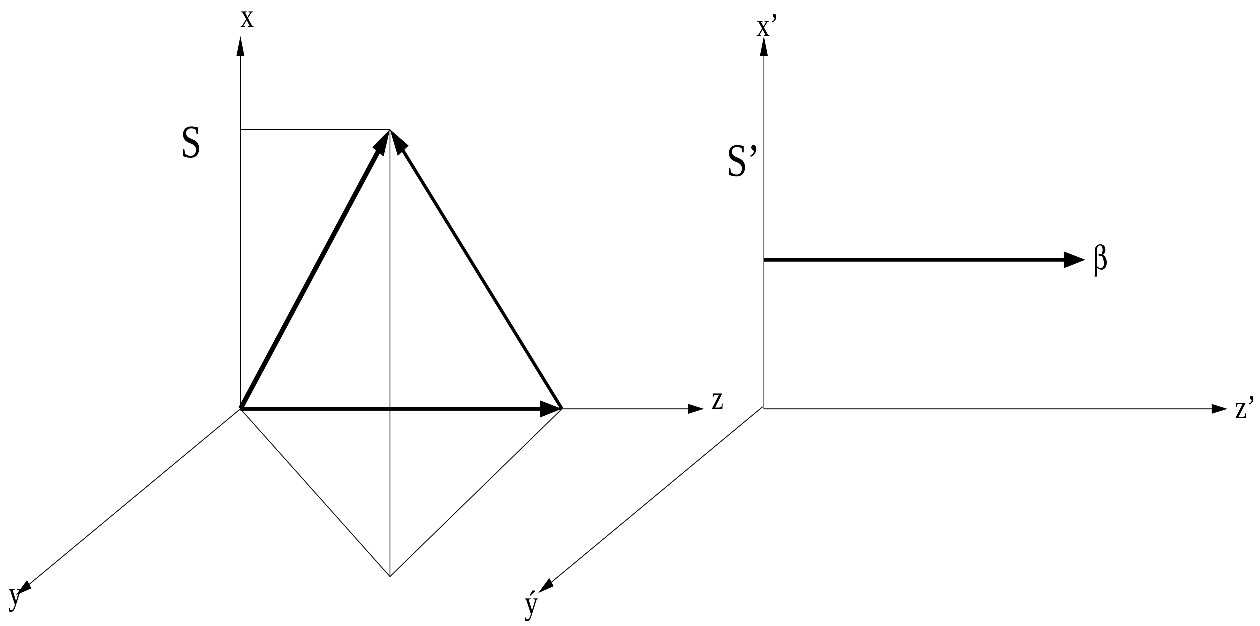

Figure 2.1: Coordinate System

lision (beam axis) is defined as the z-axis. It is convenient to use kinematic variables that have simple properties under a change of frame of reference, *i.e.*, either Lorentz invariant or which transfer trivially under Lorentz boost along this axis. Components along the beam axis are called the *longitudinal* components. Components lying in the $x-y$-plane are called the *transverse* components. θ is the polar angle measured from the z-axis. ϕ is the azimuthal angle, measured clockwise from the x-axis.

2.2 Momentum & Energy

Let a particle be characterize by its rest mass m and momentum $\mathbf{p}$. The momentum component along the along the beam-axis, the longitudinal momentum is defined as:

$$p_z = p\cos\theta \tag{2.3}$$

here p is the magnitude of 3-momentum $\mathbf{p}$. and the transverse momentum, which is a Lorentz invariant, is given by

$$p_T = \sqrt{p_x^2 + p_y^2} = p \sin\theta \tag{2.4}$$

The energy of the particle is

$$E = \sqrt{\mathbf{p}^2 + \mathrm{m}^2} = m\gamma \tag{2.5}$$

There are some handy relationships between β, γ, E and $\mathbf{p}$:

$$\gamma = (1-\beta^2)^{-1/2} \tag{2.6}$$

$$\gamma = \frac{E}{m} \tag{2.7}$$

$$\beta = \frac{p}{E} \tag{2.8}$$

again p being the magnitude of 3-momentum $\mathbf{p}$.

Another quantity we need to introduce is the transverse mass:

$$m_T = \sqrt{p_T^2 + m^2} \tag{2.9}$$

2.3 Rapidity & Pseudorapidity

One of the most commonly used longitudinal variable is the rapidity y. The rapidity of a particle is defined in by

$$y = \frac{1}{2}\ln\left(\frac{E+p_z}{E-p_z}\right) = \frac{1}{2}\ln\left(\frac{1+\beta\cos\theta}{1-\beta\cos\theta}\right) \tag{2.10}$$

Rapidity is a dimensionless quantity. It is not Lorentz invariant, but it has the advantage of being additive under Lorentz transformation along z. This has very important consequence. The differences in the rapidity dy are invariant and the rapidity spectra dN/dy translate in y while their shapes are preserved.

From the definition Eq.(2.10) we have

$$e^y = \sqrt{\frac{E+p_z}{E-p_z}} \tag{2.11}$$

therefore;

$$\begin{aligned} E &= m_T \cosh y && (2.12) \\ p_z &= m_T \sinh y && (2.13) \end{aligned}$$

To characterize the rapidity of a particle, it is necessary to measure two quantities of the particle such as its energy and its longitudinal momentum. In many experiments, it is only possible to measure the angle of the particle relative to the beam axis. In that case it is convenient to utilize this information by using the *pseudorapidity* variable η to characterize the detected particle. The pseudorapidity variable of a particle is defined as

$$\eta = -\ln \tan \theta/2, \tag{2.14}$$

where θ is the angle of between the particle momentum p and the beam axis.

Thus we see that

$$\begin{aligned} p &= p_T \cosh \eta && (2.15) \\ p_z &= p_T \sinh \eta && (2.16) \end{aligned}$$

We can write the components of the 4-momenta in terms of the transverse momenta, angle ϕ and rapidity y as

$$(E,\ p_x,\ p_y,\ p_z) = (m_T \cosh y,\ p_T \cos \phi,\ p_T \sin \phi,\ m_T \sinh y) \tag{2.17}$$

2.4 Kinematics of Two-Body Decay

If a particle decays into two particle of 4-momenta

$$\begin{aligned} p_{1\mu} &\equiv (E_1, \mathbf{p_1}) \\ p_{2\mu} &\equiv (E_2, \mathbf{p_2}) \end{aligned} \tag{2.18}$$

then the invariant mass of the daughters are related to the rest mass of the parent by

$$\begin{aligned} M^2 &= (p_1 + p_2)^2 \\ &= (E_1 + E_2, \mathbf{p_1} + \mathbf{p_2})^2 \\ &= (E_1 + E_2)^2 - (\mathbf{p_1} + \mathbf{p_2})^2 \end{aligned} \tag{2.19}$$

Another important invariant quantity is the difference of the 4-momentum of the particles:

$$k = \sqrt{-Q^2} \tag{2.20}$$

where,

$$\begin{aligned} Q^2 &= (p_1 - p_2)^2 \\ &= (E_1 - E_2, \mathbf{p_1} - \mathbf{p_2})^2 \\ &= (E_1 - E_2)^2 - (\mathbf{p_1} - \mathbf{p_2})^2 \\ &= (E_1 - \mathbf{p_1})^2 + (E_2)^2 - \mathbf{p_2})^2 - 2E_1E_2 + 2\mathbf{p_1}.\mathbf{p_2} \\ &= m_1^2 + m_2^2 - 2E_1E_2 + 2\mathbf{p_1}.\mathbf{p_2} \end{aligned}$$

If both the daughters are of same kind, *e.g.* $\phi \to K^+K^-$ then $m_1^2 = m_2^2$. Then

$$k = \sqrt{-2(m^2 - E_1E_2 + \mathbf{p_1}.\mathbf{p_2})} \tag{2.21}$$

2.5 Centrality

During a collision not all the nucleon take part in the collision. Depending on the geometry of the collision, some of them may participate in the collision and some may not. In Fig.2.2 illustrates of what happens to the nucleons during a collision. Nucleons that take part in the collision are called *Participants* and those that do not take part in the collision are called *Spectators*.

We characterize a collision or an event by the way the two beams collide. If the two means overlaps with which other during the collisions, we call them a central

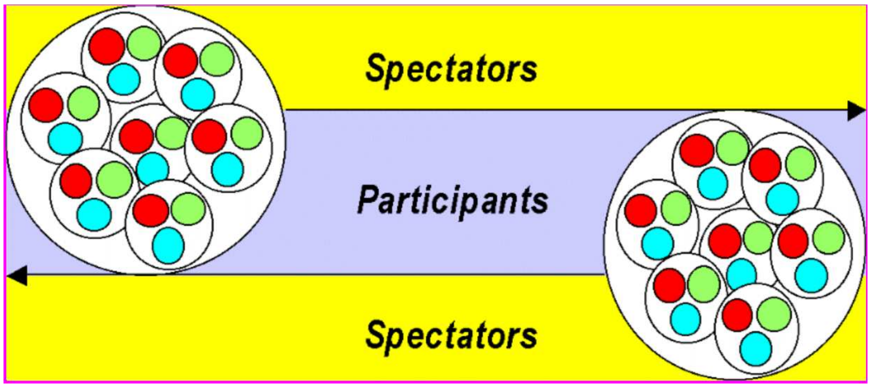

Figure 2.2: The *Participants* and *Spectators* nucleons in a collision

event, whereas if they barely touches each other, we call the collision as peripheral. We illustrate this in Fig.2.3. The distance between the centers of the two nuclei is

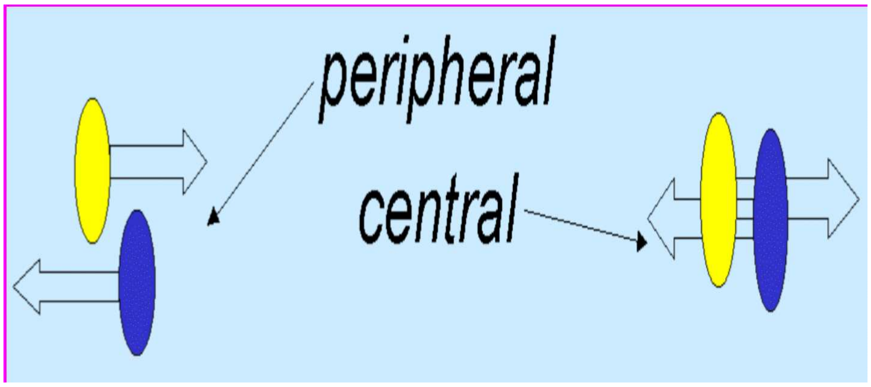

Figure 2.3: Collisions between two beams.

called the impact parameter. So the larger the impact parameters the more peripheral the collision and the smaller the impact parameters the more central the events are. A minimum bias sample is a collection of all possible impact parameter collisions.

How do we measure the centrality experimentally? The idea is very simple. We need to measure the number of participants and the number of spectators in each collision. For a central event there will be more participants than the spectators. While in a peripheral collision the spectators will outnumber the participants. A correlation of the two measurements will give the centrality of the event. We will discuss later that in PHENIX we have two independent detectors dedicated for this purpose. There are two Zero Degree Calorimeters on either side of the interaction region, away from the collision vertex, but along the beam pipe where the spectator nucleons are deposited. There are two sets of Beam-Beam counters within the interaction region along the beam pipe that measure the tracks originating from the participants. The two measurements enable us to measure the centrality of the collision.

2.6 Yield and Cross Section

The particle production in a heavy-ion or high-energy collision is expressed in terms of the cross sections. The cross section for the production of a particular final state is defined as

$$\sigma \equiv \frac{\text{transition rate to the final state per scatterer}}{\text{incident beam flux}} \tag{2.22}$$

But in heavy-ion reactions the cross section is not commonly used. Instead the particle production is quoted in terms of *yields*:

$$\text{Yield} \equiv \frac{\text{number of particles produced in event type X}}{\text{number of events of type X}} \tag{2.23}$$

Experimentally we define a number of phase-space bins and count the number of particles in each bin. In this way we do measure the differential yields of particles. The total particle yields then obtained by integrating the differential yields over the phase-space. For example, in the present analysis, we make a number of bins in the $(y,\ m_T)$ space. We count how many ϕ are produced in each bin over the number of trigger events. This gives us the differential yield. The differential yield is then integrated over the complete y and m_T range that the experiment covers in order to extract the total ϕ yield.

Let us derive the mathematical form of the differential cross section and yields. If we are considering the momentum space, then the differential yield is the number of particles produced in a unit volume of momentum space per interaction. we would naively think that if the total N number of particles are produced, it would be something like d^3N/dp^3. Thus

$$N = \int \frac{d^3N}{dp^3} dp^3 \tag{2.24}$$

which is a Lorentz-invariant. But dp^3 is not a Lorentz invariant quantity and thus neither is d^3N/dp^3. Therefore the task now is to find true Lorentz invariant form of the differential cross-section. The momentum-space volume element dp^4 is Lorentz invariant. But the volume element dp^4 includes particles those are both real and imaginary. In order for the volume element hold for the real particles only we can incorporate a delta function to the volume element. Therefore we can write

$$\int \delta(p.p - m^2) dp^4 = \delta(E^2 - \mathrm{p}^2 - m^2) dE dp^3 = \frac{dp^3}{2E} \tag{2.25}$$

Thus Eq. (2.24) can be re-written as:

$$N = \int E \frac{d^3N}{dp^3} \frac{dp^3}{E} \tag{2.26}$$

Thus we see from Eq. (2.26) that the Lorentz invariant differential cross section is Ed^3Ndp^3. Experimentally we do not usually measure $(p_x,\ p_y,\ p_z)$. But using Eq. (2.17), we can express the differential cross section in terms of the experimentally measurable quantities $(p_T,\ \phi,\ y)$.

$$\frac{dp_x dp_y dp_z}{E} = p_T dp_T d\phi dy \tag{2.27}$$

Then Eq. (2.26) can be written as,

$$N = \int \frac{d^3N}{p_T dp_T d\phi dy} p_T dp_T d\phi dy \tag{2.28}$$

Therefore, the Lorentz invariant differential cross section is expressed as:

$$\frac{d^3N}{p_T dp_T d\phi dy} \tag{2.29}$$

Now in heavy ion experiments, the measurement of the reaction plane is not usually made. Also the particles are produced random in azimuth. Thus the ϕ dependence can be averaged. The Eq.(2.28) can then be written as,

$$N = \int \frac{d^2N}{2\pi p_T dp_T dy} \, 2\pi p_T dp_T dy \tag{2.30}$$

and the differential cross section is expressed as:

$$\frac{1}{2\pi p_T} \frac{d^2N}{dp_T dy} \tag{2.31}$$

Since $p_T dp_T = m_T dm_T$, Eq.(2.31) can also be expressed as

$$\frac{1}{2\pi m_T} \frac{d^2N}{dm_T dy} \tag{2.32}$$

Chapter 3

Experiment Overview

The Relativistic Heavy Ion Collider is capable of colliding nuclear beam as light as protons to as heavy as gold. The collisions at RHIC energies are expected to produce a new state of matter. There are four experiments currently to analyze the data from the RHIC beam collisions. PHENIX is one of the large detectors. The other detectors are STAR, BRAHMS and PHOBOS.

There is no singe measurement that can confirm the existence of the new phase of matter in the RHIC beam collisions. Rather there are a large set of observables that to be looked at simultaneously in order to search for the new state of matter. PHENIX is designed with this scenario in mind. That is why PHENIX searches for the possible signatures through measurements of hadrons, photons, electrons and muons. In short, PHENIX is capable of measuring all types of particles originating from the collision.

3.1 The Relativistic Heavy Ion Collider

The process of accelerating a gold ion involves several accelerators that make up the RHIC complex. Fig. 3.1 shows the RHIC complex.

The ion beam starts its journey in the Tandem Van de Graaff. It consists of two electrostatic accelerators, each 24 meters of length and capable of producing voltages

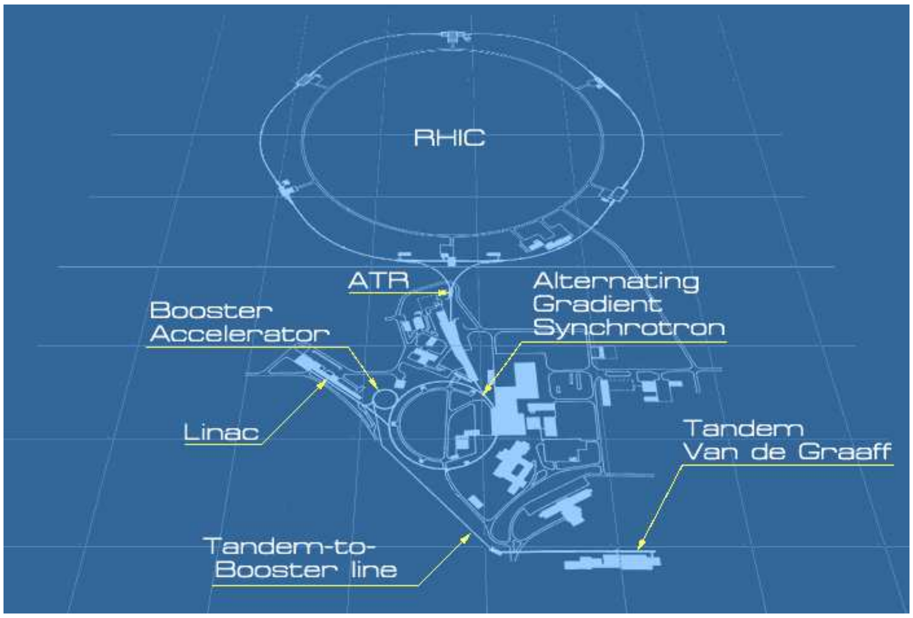

Figure 3.1: The RHIC Complex

up to 15 million volts. These electrostatic accelerators can provide up to 40 different kinds of ions, including gold.

The ion beams begin their journey here at the accelerators and go to the Heavy Ion Transfer Line (HITL). Once the ions reach the HITL, they are carried through a vacuum using a magnetic field, traveling at 5% of the speed of light. Then the ions are provided with more energy at the Booster accelerator with electromagnetic waves. In the Booster accelerator they reach a speed of 37% that of light. From there, the ions make their way to the AGS where they reach 99.7% of the speed of light. The AGS consists of 240 magnets. The field gradient of these magnets is alternated, hence the name. Once they are traveling at this ultra-relativistic speed, they are transfer to RHIC via the AGS-To-RHIC (ATR) transfer line. Once they reach the end of the ATR transfer line, the ions are divided into 2 bunches, traveling either clockwise or counterclockwise in the so-called *blue* and *yellow* lines.

RHIC ring has a circumference of 3.8 kilometers in circumference. The design

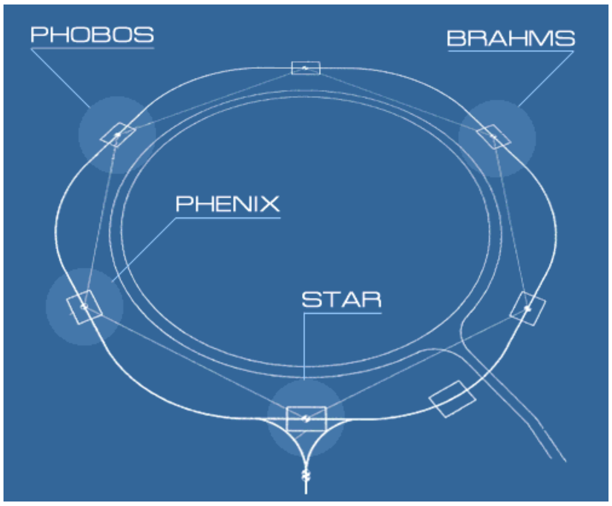

Figure 3.2: RHIC Beam Interaction Points. The Locations of the four experiments are shown.

luminosity of RHIC is $2\text{x}10^{26}\text{cm}^{-2}\text{s}^{-1}$. However in the run of 2000, only about 10% of the design luminosity could be achieved. The luminosity, which is the number of ions passing per unit area per unit time, can be calculated for the two colliding beams containing n_1 and n_2 ions per bunches as:

$$L = f\frac{n_1 n_2}{4\pi\sigma_x\sigma_y} \tag{3.1}$$

where f is the beam frequency, and σ_x and σ_y are the widths of the beams perpendicular to the beam axis. the number of ions per bunch is about 10^9 for Au-Au and 10^{11} for p-p. The event rate R in a collider is related to the luminosity L and the interaction cross-section by:

$$R = L\sigma_{int} \tag{3.2}$$

There are six interaction points where RHIC can collide beams. If RHIC's ring is thought of as a clock face, the four current experiments are at 6 o'clock (STAR), 8 o'clock (PHENIX), 10 o'clock (PHOBOS) and 2 o'clock (BRAHMS)(Fig. 3.2). There are two additional intersection points at 12 and 4 o'clock where future experiments may be placed.

One of RHIC's two smaller detectors is the Broad Range Hadron Magnetic Spectrometer, or BRAHMS. It measures particles emerging from a specific set of angles during each collision. The momentum, energy and other characteristics of the particles are measured very precisely. It is capability of measuring inclusive momentum spectra of identified charged hadrons over a wide range in rapidity and transverse momentum.

PHOBOS, the other of the two small experiments, looks for rare but interesting events among a large number of collisions. For each collision, PHOBOS gives a global picture of the consequences of the collision and detailed information about a small subset of the nuclear fragments ejected from the fireball.

STAR, or Solenoidal Tracker At RHIC, is one of the two large experiments. It specializes in tracking the thousands of particles produced by each ion collision at RHIC. STAR physics program concentrates on searching for the signatures of quark-gluon plasma. It is also used to investigate the behavior of matter at high energy densities by making measurements over a large area.

PHENIX, the Pioneering High Energy Nuclear Interaction Experiment, is the other large experiment. PHENIX is a multi purpose detector in the sense that it can measure hadrons, electrons muons and photons. It has an excellent particle identification capability. Our analysis is using the PHENIX detector. In the subsequent sections we describe the PHENIX detector and its various detector components in details.

3.2 Physics Goals of PHENIX

As mentioned, the heavy ion collisions at RHIC energies are expected to produce a new phase of matter where quarks and gluons will be free in small volume. The new state would thermalize followed by expansion and cooling leading to hadronization. PHENIX probes each phase by studying the hadronic production and also through rare processes involving photons, electrons and muons. The physics issues related to the new phase of matter being studied by PHENIX are summarized in Table 3.1[34] Let us briefly describe some of the important signatures.

Table 3.1: Physics Issues Related to the new Phase of Matter

Physics Issues	Probes
Debye Screening of QCD Interactions • $r(\Upsilon) = 0.13$ fm $< r(J/\psi) = 0.29$ fm $< r(\psi') = 0.56$ fm $J/\psi \to e^+e^-$ at $y \simeq 0$. $J/\psi \to \mu^+\mu^-$ at $y \simeq 2$. $\psi', \Upsilon \to \mu^+\mu^-$ at $y \simeq 2$.	Electrons Muons
Chiral Symmetry Restoration • Mass, Width, Branching Ratio: $\phi \to e^+e^-$, K^+K^- with $\Delta m \leq 5$ MeV. • Baryon Susceptibility: Production of antinuclei. • Narrow σ-meson?	Electrons Hadrons
Thermal Radiation of Hot Gas • Prompt γ, Prompt $\gamma^* \to e^+e^-$.	Photons, Electrons
Deconfinement: Nature of the Phase Transition • First-order: Entropy Jump $\to$ Second rise in the $< p_T >$ spectra of π, K, p. • Second-order: Fluctuation $\to N(\pi^0)/N(\pi^+ + \pi^-), d^2N/d\eta d\phi$.	Hadrons Hadrons, Photons
Strangeness and Charm Production • Production of K^+, K^-, K^0_L. $\phi \to e^+e^-$, K^+K^- at $y \simeq 0$, $\phi \to \mu^+\mu^-$ at $y \simeq 2$. D-meson: $e\mu$ coincidence.	Hadrons Electrons Muons
Jet Quenching • High p_T jets via leading particle spectra.	Hadrons
Space-Time Evolution • HBT correlations for $\pi\pi$ and KK.	Hadrons

- **Jets**: Jets are produced in the initial state due to hard scattering. Jets are sensitive to the medium properties. So a phase transition and QGP formation can change the jet properties significantly.

- **Direct Photons**: Direct photons and lepton pairs which emerge from the collision with a minimum of final state interaction are sensitive to the full time evolution from the initial state through thermalization. The capability to measure direct photons over a wide range of p_T is unique to PHENIX and is important for relating their momentum to the temperature of the emitting source.

- **Deconfinement**: PHENIX studies the deconfined state and Debye screening by observing the yields of the J/Ψ and Ψ' relative to that of the Υ. Deconfinement is closely related to the Debye screening of the QCD potential. The basic mechanism of J/ψ suppression is that, if the J/ψ radius is longer than the screening length, then a c$\bar{\text{c}}$ pair would not be able to form a bound state due to a Debye suppression of the long-range term of the c$\bar{\text{c}}$ potential and, thus, J/ψ production is suppressed The degree of suppression depends strongly on the relative size difference between the meson radius and the screening length. Because $r(\psi') = 0.51$ fm $> r(\text{J}/\psi) = 0.25$ fm $> r(\Upsilon) = 0.13$ fm, we expect that the ψ' must melt first, then the J/ψ, and finally the Υ.

- **Chiral Symmetry Restoration**: The medium modification of light vector mesons, especially ϕ and possible ρ and ω might be related to the expected chiral phase transition. The Mass and width of light vector mesons may change. Also nn enhanced ϕ meson yield has been suggested as a signature for the formation of a deconfined phase.

- **HBT**: After hadronization the expansion of the fireball is studied by measurement of Hanbury-Brown-Twiss correlations and the coalescence probabilities of various nuclei and anti-nuclei give insights into the space-time evolution of the collision. Precision time of flight (ToF) allows measurement of the identified charged hadron spectrum over a wide p_T range. Many of the above signals can also be produced from interactions between particles in hot hadronic matter. It is thus necessary to understand the purely hadronic effects. For this reason PHENIX studies the above signals using p-p and p-A collisions to gain a better understanding of effects distorting signals from the QGP.

- **Spin Program**: A second major goal of the PHENIX experiment is to measure the spin structure of the nucleon. RHIC accelerates beams of polarized protons up to 250 GeV with polarizations up to 50%. Work of the EMC collaboration and others indicated that the fraction of the proton spin carried by the quarks was only about half of the expected value. PHENIX studies the gluon polarization by measuring high p_T prompt photon production using the highly segmented EM Calorimeter to minimize interference from photons from π^0 decays. The anti-quark polarization is measured by observing the parity violating asymmetry for W production. The W particles are identified by the detection of muons or electrons with $p_T \geq 20GeV/c$ using the PHENIX north and south muon arms or the central spectrometer, respectively.

3.3 A Brief Description of the Detector Components

PHENIX detector consists of a large acceptance charged particle detector and four spectrometer arms - a pair of spectrometers measuring electrons, photons and hadrons at mid rapidity and a pair of muon spectrometers at forward rapidities. PHENIX consists of eleven different detector subsystems. Fig. 3.3 shows the schematic drawing of PHENIX detector. Two gold beams coming from the left and right will be made to collide at the center of the detector. At the center there is the central charged

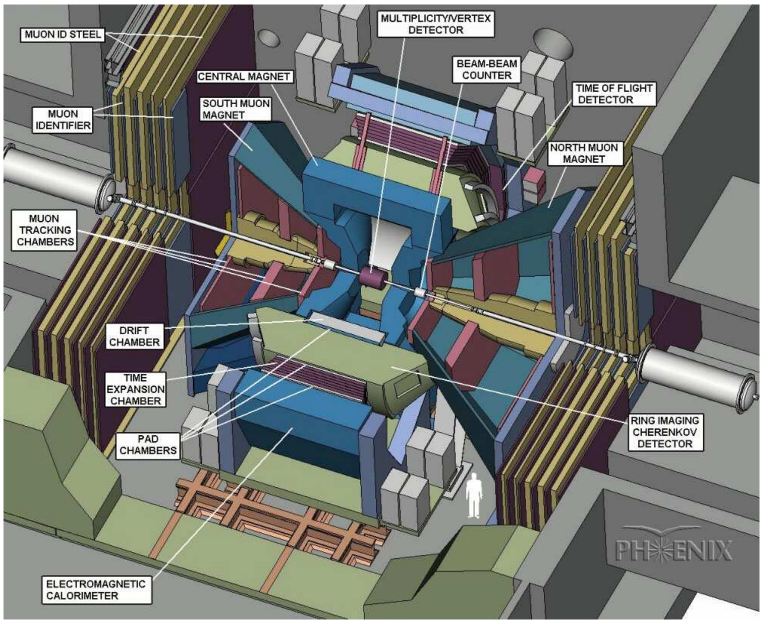

Figure 3.3: Schematic of the PHENIX Experiment at RHIC

particle detector. At the top and the bottom of the figure there are the two *central arms*, called east arm and west arm, a spectrometers systems for electrons, photons and hadrons. There are two *muon arms* at the north and south side. Fig. 3.4 shows the PHENIX from beam line.

The design philosophy of PHENIX is to identify and trigger on exclusive leptons, photons and high p_T hadrons with excellent momentum and energy resolution. The detector system can be classified into three categories:

- **Global Detectors**
  - Silicon **Multiplicity and Vertex Detector (MVD)** of strip and pad arranged around the interaction region
  - **Beam Beam Counter (BBC)** on the either side of vertex
  - **Zero Degree Calorimeter (ZDC)** along the beam pipe, but away from the interaction region.

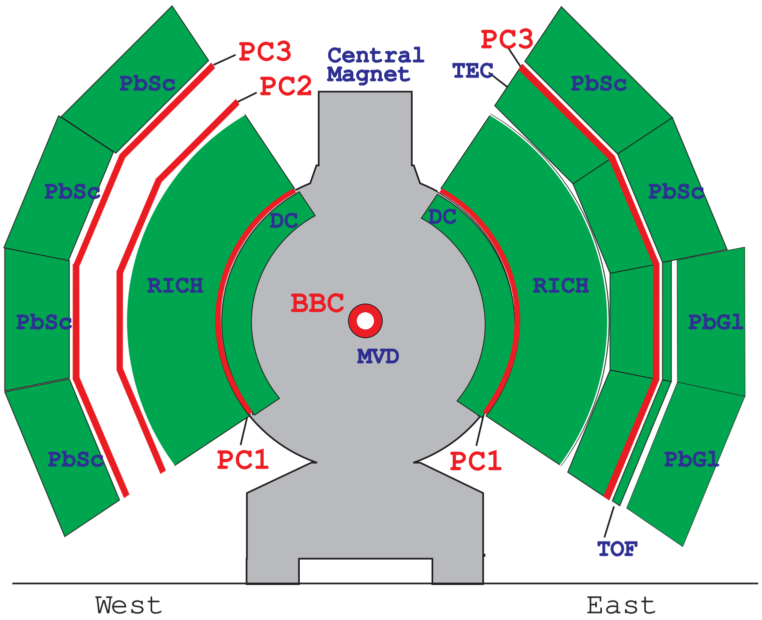

Figure 3.4: PHENIX View from Beam line.

- **Central Arm Detectors**
  - **Central Magnet**. The North and South poles of the Central Magnet are positioned on the collision axis at 0.45m and -0.45m respectively.
  - An intermediate tracker made of **Drift Chamber DCH)** and **Pad Chambers (PC1)**
  - A ring imaging **Cerenkov Detector(RICH)**
  - Outer Tracker composed of a pad chambers **PC3** and **Time Expansion Chamber (TEC)** in the east arm and two pad chambers **PC2** and **PC3** in the west arm.
  - A **Time of Flight (TOF)** scintillators in the east arm.
  - An **Electromagnetic Calorimeter (EMCal)** . One half of the east arm is equipped with Lead Glass type (**PbGl**) and the rest half of east arm and west arm is equipped with lead scintillators (**PbSc**)

Element	θ (deg.)	η	ϕ (deg.)	$\Delta\Omega$ (sr)
Inner Detectors	2–178	-4.0–4.0	0–360	$\sim 4\pi$
Central Arms	70–110	-0.35–0.35	$\pm$(22.5–112.5)	1.07
Muon Arm	10–35	1.15–2.44	0–360	1.17

Table 3.2: Angular and Pseudorapidity Coverage of PHENIX

- **Muon Arms**
  - Three tracking stations (**muTr**)
  - A muon Identifier (**muID**)

The geometrical coverage of the detectors can be summarized in the Table 3.2: The detectors are thus also classified, according to their usage, as:

- Vertex Finding : BBC, MVD, and ZDC
- Level-1 Trigger : BBC, ZDC
- Centrality Selection : BBC, ZDC
- Tracking : DCH, PC1, PC2, PC2, TEC, μTr
- Particle Identification : TOF, RICH, EMCal, μID

We will furnish a brief description on the detectors. Emphasis will be given on the detectors used for this analysis. More detailed information of the detectors can be obtained from the PHENIX NIM articles [35].

3.4 Global Detectors

The PHENIX global detectors are employer in order to characterize the nature of the event. They determine whether the events occurred in the PHENIX fiducial region and whether the event satisfy the minimum bias trigger condition. Also the global detectors characterize the centrality of the collision.

3.4.1 Beam Beam Counter (BBC)

The beam beam counters perform three major tasks. They determine the zero time when the beams collide. This information is used for particles time of flight measurements. The other task is to measure the collision vertex point. The BBC serves as the level1 trigger in conjunction of the Zero Degree Calorimeter. BBC measures the charge deposited by the tracks which can be correlated to the ZDC measurements to find the event centrality.

The BBC consists of two identical sets of counters installed on both sides of the collision point along the beam axis, one on the North side and the other on the South side of the PHENIX coordinate system where each counter Are named BBCN and BBCS, respectively. The BBC's are placed 144 cm from the center of the interaction diamond and surround the beam pipe. This corresponds to a pseudorapidity range from 3.0 to 3.9 over the full azimuth.

The BBC needs to satisfy the following requirements:

1. The number of charged particles generated by Au-Au collisions at $\sqrt{s_{NN}} =$ 200 GeV within the BBC acceptance is as much as a few thousands for central collisions. Moreover the BBC also needs to operate with p-p collisions up to $\sqrt{s}$=500 GeV. The BBC must thus have a capability to function over a large dynamic range from 1 MIP to 30 MIP's.

2. Since the BBC is placed in a very high-level radiation area around the beam pipe near the interaction point, it is required to be radiation hard.

3. The BBC is installed just behind the PHENIX central spectrometer magnet. The expected magnetic field along the beam axis around this location is 3 kG.

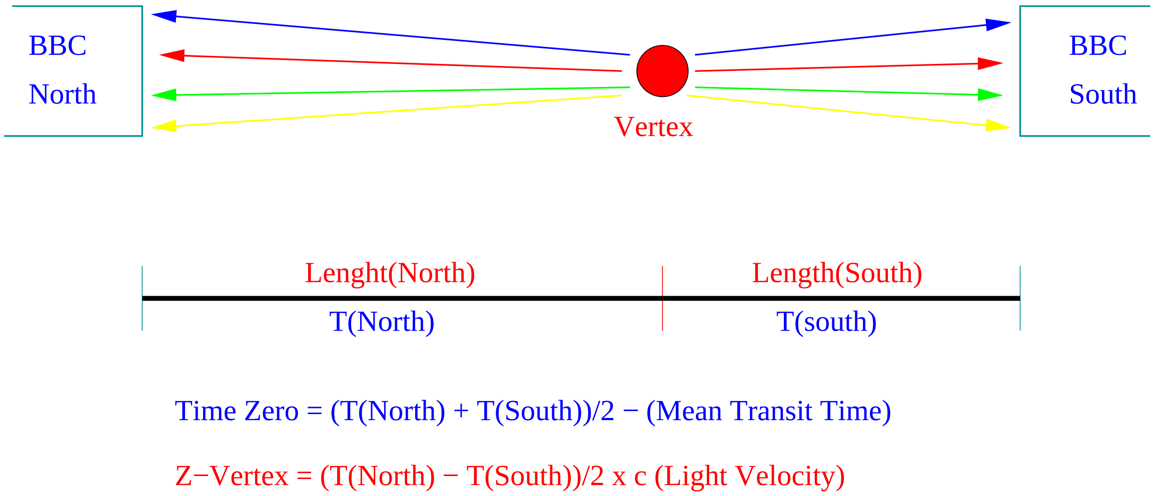

Figure 3.5: BBC Zero Time and Z-vertex Measurement

Therefore the BBC needs to work in a high magnetic field environment.

Each counter is composed of 64 one-inch diameter mesh-dynode photomultiplier tubes (Hamamatsu R6178) equipped with 3 cm quartz on the head of the PMT as a Cerenkov radiator. The outer diameter of the BBC is 30 cm and the inner diameter is 10 cm with clearance between the beam pipe and the BBC of 1 cm. For this configuration the expected number of charged particles for a central Au-Au collision at 200 GeV is expected to be 15 particles per BBC element. The Beam-Beam Counter provides the z-vertex position and Time zero. The cartoon in Fig. 3.5 describes roughly how the collision start time and vertex measurement is done with BBC. The interaction position along the beam axis is calculated from individual time measurements of fast leading particles hitting BBC on the both sides of the interaction point. With an intrinsic timing resolution of 70 ps, BBC determines the interaction position with a precision of approximately 2 cm.

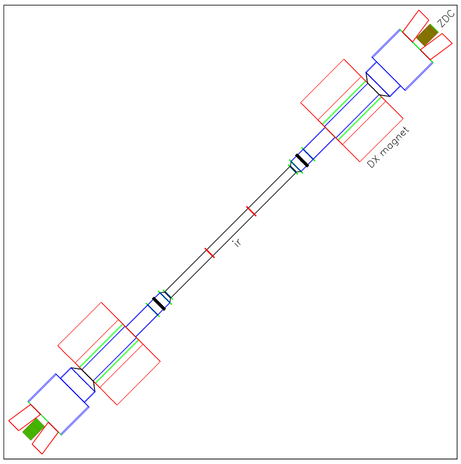

Figure 3.6: Beam line geometry around the interaction regions showing the beam splitting dipoles and the zdc detector placement.

3.4.2 Zero Degree Calorimeter (ZDC)

The Zero Degree Calorimeter (ZDC) is a detector standard to all four experiments at RHIC. The ZDC measures the beam energy neutrons emitted in the breakup of the nuclear remnant that misses the interaction zone. The calorimeters are also the principle device to monitor the beam luminosity during the run and serves as an event trigger for all four RHIC experiments.

In Heavy Ion collisions, the collision impact parameter is, in principle, a measurable and useful quantity. In the search for new states of matter under conditions of extreme density and temperature it will be useful to characterize collisions using global measurements that don't bias the signal of interest. In order to compare results from different experiments measurements of global event properties are made using common instrumentation. And this common instrument is the ZDC.

In PHENIX, the two ZDCs are located at 8 m up and downstream from the collision vertex. Each of them covers a polar angle of $\theta < 4$ mrad. Fig. 3.6 shows the beam geometry and the detector location. The vertex position measurement procedure is similar to that described for BBC (see Fig. 3.5).

3.4.3 Multiplicity and Vertex Detector (MVD)

The multiplicity and vertex detector (MVD), which is placed just outside the beam pipe, provides centrality trigger and more accurate vertex information. The MVD is comprised of two parts: two end caps and two concentric central barrel covered with silicon pads and strips. Vertex finding can be done with good efficiency using the hits from the central barrels for z-position up to ± 40 cm with a position resolution < 2 mm. The disk shaped end caps, located at z-positions of ± 35 cm and are composed of silicon pads. Analog sums of the signal from the end caps and also from the central barrel, allow formation of multiplicity triggers from different ranges of pseudorapidity.

3.5 Central Spectrometer

The central arm is equipped with detectors for electron, hadron and photon measurements. The separation of negative and positive tracks are done by applying a magnetic field. The drift chambers provide excellent momentum measurement and it is a part of the tracking system which also include the Pad Chambers and the Time Expansion Chambers. Hadron identification is achieved through the Time of Flight Detectors and the Electromagnetic Calorimeter. Electron identification is done through the Ring Imaging Cerenkov Detector and the Electromagnetic Calorimeter. The Electromagnetic Calorimeter provides the energy measurement for photons.

3.5.1 Central Magnet

In the central arm of PHENIX a magnet is employed to focus the tracks into the PHENIX central arm acceptance. This Central Magnet is an axial field magnet energized by two pairs of concentric coils, which can be run separately, together, or in opposition. In Fig. 3.7 is shown the field lines when both coils are turned on. The magnet is 9 meters tall and has a rapidity coverage of ± 0.35 units. The magnet provides a field integral ($\int \vec{B}.d\vec{l}$) of 0.78 Tesla-meters at 90 degrees in polar angle from

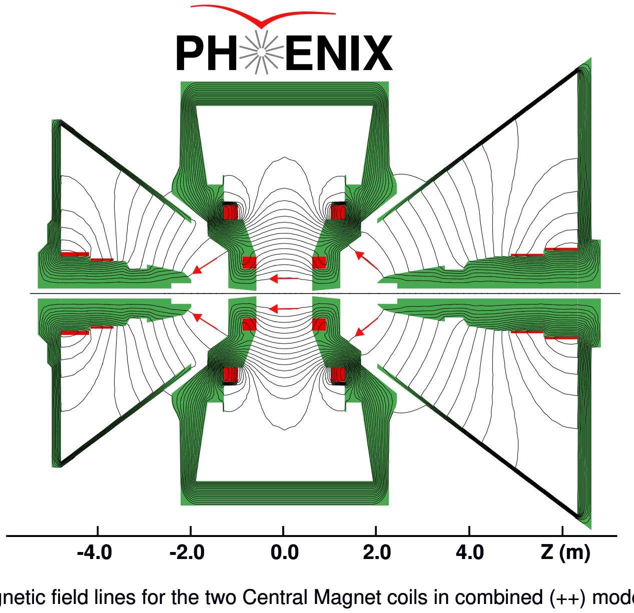

Figure 3.7: PHENIX Central Magnet Field Lines

the beam axis. Due to this, PHENIX could achieve an excellent particle resolution. The measured single particle momentum resolution at the Drift Chambers is 0.5% between 200 MeV/c and 1 GeV/c. In order to minimize the distortion of the particle tracks, the magnet is designed to achieved an integral field of 100 gauss-meters from a radius of 2.4 meters to 4.0 meters. The fields near the EMCal phototubes, which sit farthest from the beam pipe, the field is less than 10 gauss. The pole faces of the Central Magnet serves as the primary absorber of hadrons for the Muon arm spectrometers.

3.5.2 Drift Chambers (DC)

The principal objective of the multi-wire low mass Drift Chambers is to measure the momentum of the tracks generated in the RHIC beam collisions. The Drift Chambers also provide the position information which, together with the other tracking devices, give excellent pattern recognition.

The Drift Chambers are located in both arms of PHENIX. The east and west DCs are identical in design. The location of the Drift Chamber in the PHENIX detector system can be seen in Fig. 3.4. The Drift Chambers are cylindrical in shape. They are located between 2 meters and 2.4 meters from the beam direction. They span 2 meters in the beam direction covering $\sim \pm 0.35$ units of rapidity. The drift chambers are made of independent and identical ϕ sections called *supermodules* which in turn are composed of drift cells The chambers are arranged into 160 drift cells . A drift cell contains 6 types of wires namely: X1,U1,V1,X2,U2,V2 and covers $1°$ in azimuth, which translates into a 2 - 2.5 cm drift space, and 6 mm in radial. The X1 and X2 wire cells run in parallel to the beam to perform precise track measurements in r-ϕ. These wire cells are followed by two sets of small angle U,V wire planes used in the pattern recognition. U1, V1, U2, and V2 wires have stereo angles of about $6°$ relative to the X wires and measure the z coordinate of the track. The stereo angle was selected to minimize track ambiguities by matching the z resolution of the pad chambers.

For the track reconstruction in the Drift Chambers, the combinatorial Hough Transformation method technique is used. A simple description of the Hough transformation is sketched in Fig. 3.8. The $r - \phi$ information of the tracks measured by the chambers are combined with the deviation α of the track from a straight line. For a n-point hit in the DC, a 3-D plot of the amplitude of the signal in Hough space and the $\phi - \alpha$ pairs are made. A track is represented as a local maximum in the Hough space. The position of the maximum in the $\phi - \alpha$ space is the direction of the track.

The momentum (in GeV) determined by drift chamber is related to the angle α (in mrad) by:

$$p = \frac{87}{\alpha}$$

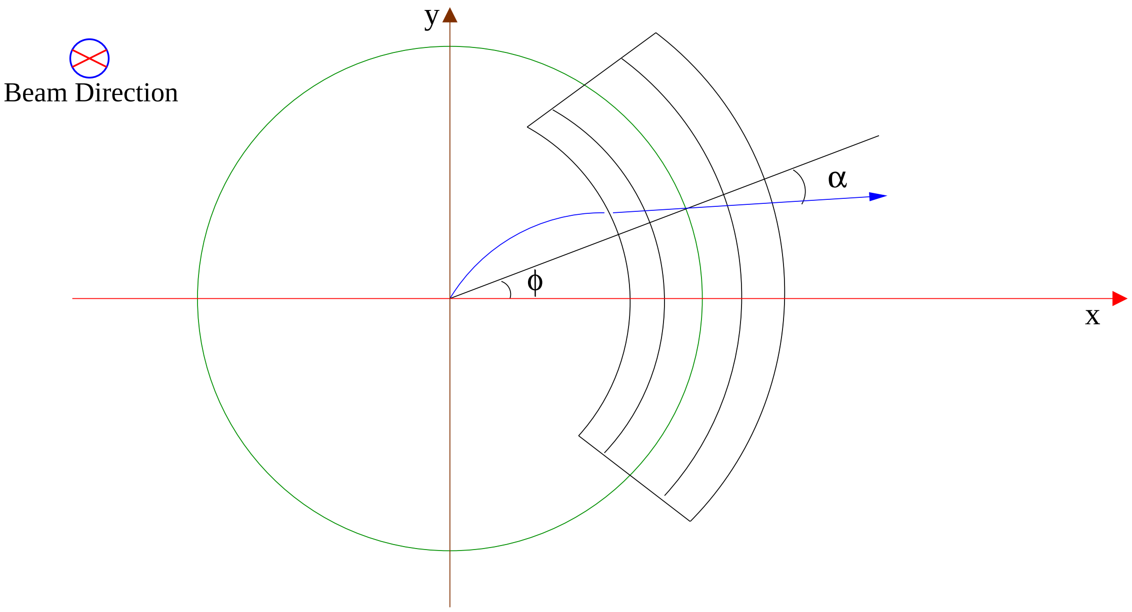

Figure 3.8: Hough transformation technique for track reconstruction in the Drift Chambers

Where, 87 mrad GeV is simply the field integral:

$$K_1 = \int_{0.3/R_{DC}} lBdl$$

The momentum resolution depends upon a combination of the intrinsic angular resolution of the drift chamber and the multiple scattering of a charged particle as it travels upto the drift chamber due to the intervening matter such as the MVD cladding, air, DC Mylar window, He-bag Mylar window etc. The momentum resolution is given by:

$$\left(\frac{\delta p}{p}\right)^2 = \left(\frac{\sigma_\alpha}{K_1}p\right)^2 + \left(\frac{\sigma_{ms}}{K_1\beta}\right)^2$$

where σ_α is the angular resolution and σ_{ms} is the multiple scattering term. The momentum resolution for the Au-Au runs at 200 GeV is obtained as $\delta\, p/p \approx 1.0 \pm 0.1\,\%$ [36]. For more information on momentum resolution, please see Sections 4.5 and 6.3.2

3.5.3 Pad Chambers (PC)

Pad Chambers are multi-wire proportional chambers. The Pad Chambers contain a single plane of wires in a gas volume surrounded by two cathode planes. The primary functions of the Pad Chambers are to perform measurements of non-projective three dimensional spatial points to be used for both momentum determination and pattern recognition. There are three sets of Pad Chambers instrumented in PHENIX, called PC1, PC2 and PC3. The PC1 is located immediately behind the Drift Chambers. The PC2 in the west arm is behind the RICH and the PC3 in both arms are in front of the Electromagnetic Calorimeter. The location of the Pad Chambers can be seen in Fig. 3.4.

Pad Chambers are composed of three layers of pixel detectors. A single "PIXEL" is small copper rectangle that is connected to 8 other small copper rectangles. All 9 pixels are read out by a single discriminator. The object that is composed of 9 connected Pixels is called a "PAD". Whenever a charged track passes through the pad chamber, there should be three neighboring PADs which all receive an induced signal large enough to trigger their three separate discriminators. The 9-fold ambiguity of which PIXEL is hit is resolved (usually) by looking at which set of three PADs have hits. The structure of three neighboring PIXELS that gets uniquely identified as the location of the track is called a "CELL".

The Pad Chambers provide the track information to reduce the track matching ambiguities. The PC1 is the principal source of z-information for the PHENIX tracking reconstruction software. They help separate the neutral EMCal showers from charged tracks. PC information is also essential for particle identification, particularly for critical electron identification. The combination of the pattern recognition through DC+PC1+TEC+PC3 or DC+PC1+PC2+PC3, with the responses from the particle identifying detectors help identify the tracks in the most efficient way.

3.5.4 Time Expansion Chamber (TEC)

The time expansion chamber (TEC) is mounted on the east arm in PHENIX. It performs both particle identification and tracking functions. It measures charged particle ionization energy losses (dE/dx). This allows separating of electrons from pion over a momentum range 0.25 -3 GeV. The TEC is planning to upgrade to a Transition Radiation Detector (TRD). Once upgraded, it can separate e/π over a momentum range 0.25- 50 GeV via transition X- radiation detection. TEC tracks all charged particles and produces direction vectors that match tracking information from the Drift and Pad Chambers to complete track determination in the PHENIX. It has a single point track resolution of 250 μm and two track separation of 2 mm. It also Measuring the transverse momentum of charged tracks.

The wires in the time expansion chambers are arranged in 6 planes and 4 sectors. In the year-1 only 4 planes were instrumented electronically. It covers 90° of the PHENIX azimuthal angle ϕ and 0.35 units of pseudorapidity η (approximately 40° of the polar angle θ). the detectors location from the collision vertex is approximately R = 410- 457 cm. It consists of 64,080 wires and 20,480 readout channels.

The tracking is done using the same principle as in the drift chambers using the Hough transformations (Fig. 3.8). The transverse momentum is related to the inclination angle α by the relation [37]

$$p_T = \frac{1}{21.5\alpha} \tag{3.3}$$

3.5.5 Time-of-Flight Counters (TOF)

The Time-of-Flight (TOF) counters are used for the hadron identification. They are also used in conjunction to the Ring Imaging Cerenkov detector for electron identification. For the purpose particle identification, the time of flight of the particles are compared to the measured momentum of the particle.

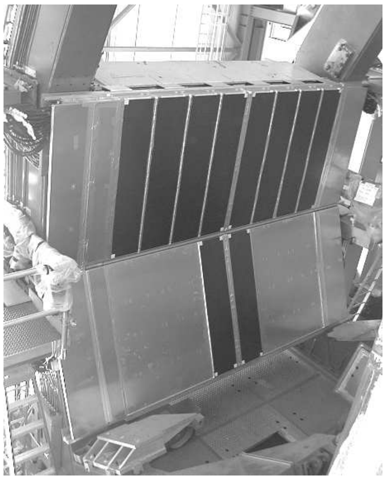

Figure 3.9: The TOF hardware mounted in the PHENIX

The location of the TOF in the PHENIX detector system is shown in Fig. 3.4. TOF is instrumented only in the east arm. They are located 510 cm away from the collision vertex, behind the Pad Chambers3 and in front of the Electromagnetic Calorimeter. A total 10 TOF panels were instrumented. Fig. 3.9 shows a photo of the TOF detector. This looks like a "T", with 8 panels on the upper part of the T and 2 panels in the lower. They are designed like that in order to optimize the high-p_T hadron measurement. The number of segments in the ToF system is determined by minimizing the probability of two or more particles hitting a single segment. For the ToF system design the double hit probability is kept as low as possible. Assuming the charged particle rapidity density to be $dN_{ch}/dy = 1500$, the charged particle multiplicity on the ToF wall is expected to be 9. In order to keep the occupancy below 10%, the segmentation is about 1000 and the required area of each segment at a distance of 5.1 m away from the vertex is 100 cm^2. That is why each of the TOF panels, which are 200 cm long and 48 cm wide, consist 96 scintillators slats. There are 2 photomultiplier tubes corresponding to each slat. The slat is oriented along the r-ϕ direction and provides time and longitudinal position information of particles that hit the slat.

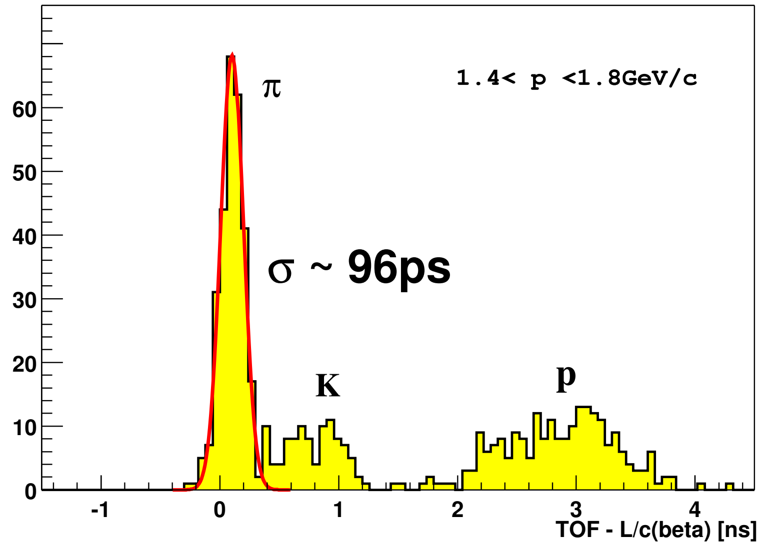

Figure 3.10: The Timing resolution in TOF for

The timing resolution of the TOF is about 100 ps. The TOF timing resolution can be demonstrated by looking at the difference of the measured time of flight of tracks and the expected time of pions. In Fig. 3.10 we show such a plot. A 96 ps timing resolution is achieved. This allows a 4σ π / K separation upto 2.4 GeV/c and a K / p separation upto 4.0 GeV/c. For more information on the particle identification, please see Section 4.5.

3.5.6 Ring Imaging Cerenkov Counters (RICH)

The Ring Imaging Cerenkov (RICH) detector is used for the identification of electrons. The detector is located outside of the PHENIX central magnet, having inner and outer radii of r = 2.6 m and r = 4.0 m as measured from the collision point. The entire region is filled with a Cerenkov radiator gas of index of refraction n (C_2H_6, $n \sim 1.0008$ or CH_4, $n \sim 1.00044$). RICH measure the Cerenkov radiation emitted by charged particles move through gas at a speed larger than c/n, where c is the speed of light. The radiation is emitted along a cone, where the opening angle of the cone with respect to the apex is $\theta_c = cos^{11}(1/n\beta)$, where $\beta = v/c$. The momentum beyond which a charged pion will radiate is about 3.5 GeV/c in ethane, and about 4.7 GeV/c in methane. The Cerenkov photons generated by electrons, positrons, and high momentum hadrons are reflected by spherical mirrors placed within the radiator volume, and the photons are focused onto photon detectors placed just behind the PHENIX central magnet.

3.5.7 Electromagnetic Calorimeter (EMCal)

The Electromagnetic Calorimeter (EMCal) in PHENIX is used primarily to electron and photon identification and to measure their position and energy. Comparison of the momentum of charged particles, measured in the drift chambers or in the time expansion chambers, with the energy response of the calorimeter provides a tool for electron identification. The timing resolution is about 600 ps. This precision of measurement of arrival time of a track on the EMCal enables additional particle identification for both neutral and charged particles by combining calorimeter time with amplitude information.

There are two types of Electromagnetic Calorimeters in the east arm covering all four sectors, lead-scintillators (PbSc) sampling calorimeter and lead-glass (PbGl) Cerenkov Calorimeter. The PbGl part of the Electromagnetic Calorimeters are located behind the Time-of-Flight detector. In the west arm, all four sectors of the Electromagnetic Calorimeters are PbSc, located behind the Pad Chambers3. The PbGl has better granularity and energy resolution. The PbSc, on the other hand, has better linearity and timing resolution. The hadronic responses are better understood in the PbSc.

The Pb-scintillators electromagnetic calorimeter is a shashlik type sampling calorimeter made of alternating tiles of Pb and scintillators consisting of 15552 individual towers and covering an area of approximately 48 m^2. Each tower contains 66 sampling cells. Each cell is a 1.5 mm Pb and 4 mm Sc ganged together by penetrating wavelength shifting fibers for light collection. The timing resolution is ∼100 ps for electronic shower and ∼480 ps for hadronic showers, which allows good kaon separation between 300 MeV/c and 1.2 GeV/c. The energy resolution is

$$\frac{\sigma_E}{E} = \frac{8.2\%}{\sqrt{E}} \oplus 1.9\%$$

The PbGl is located behind the TOF in bottom two sectors in the PHENIX east arm. Each sectors comprises of 192 supermodules. Each PbGl supermodule comprises 24 PbGl modules in a array of 6 PbGl modules wide by 4 modules high. Each PbGl module is 40 mm × 40 mm × 400 mm in size. The timing resolution for hadronic showers are ∼600 ps. Since high resolution TOF is located in front of the PbGl, they are not used in analysis involving hadrons. The energy resolution is

$$\frac{\sigma_E}{E} = \frac{5.5\%}{\sqrt{E}} \oplus 3.0\%$$

3.6 Muon Spectrometers

The two forward muon spectrometers give PHENIX acceptance for J/Ψ decaying into dimuons at rapidities of $-2.25 \leq y \leq -1.15$ for the south arm and $1.15 \leq y \leq 2.44$ for the north arm. Each spectrometer is based on a muon tracker inside a radial magnetic field followed by a muon identifier, both with full azimuthal acceptance. The muon trackers consist of three stations of multi-plane drift chambers that provide precision tracking. The muon identifiers consist of alternating layers of steel absorbers and low resolution tracking layers of streamer tubes of the Iarocci type. With this combination the pion contamination of identified muons is typically 3×10^{-3}. The complete north arm will be installed prior to the year-3 PHENIX runs.

3.7 Computing

RHIC deliverers beam at PHENIX. These data need to be selected and archived in order to optimize the physics interest of PHENIX and also a cost effective way. The interaction rate at the design RHIC luminosity varies from a few kHz for Au-Au central collisions to 500 KHz in p-p collisions. PHENIX has large channel counts. The total number of detector channels in PHENIX is 282,922 [38]. It is very important to coordinate between the electronics and computing in order to optimize the data collection efficiency.

The overall data management in PHENIX is carried out in two stages. The On-Line Computing System (ONCS) provides the control and monitoring of the electronics, trigger and data acquisition system. The Off-Line Computing provides all other aspects of the data handling, such as reconstruction, simulation, and data analysis among others.

The data collection and storage can be described in Fig. 3.11. The data collection rate is ∼150 events per second in a Au-Au collision and ∼1000 events per second in a p-p collision. The typical event size in a Au-Au collision is 200 kbytes and 60 kbytes in p-p. PHENIX employs custom made Front-End Electronics (FEM) for digitization. At this stage the level-1 trigger makes a decision of accepting or rejecting the event based on the information from a number of subsystems. The digitized data are then transferred to the Data Collection Module (DCM) through optical fibers. The data are then zero-suppressed, packaged, and shipped to the Event Builder (EvB). The EvB assembles a full event from the individual fragments of data from the DCM's. When the event is fully assembled and passes the level-2 trigger, it is temporarily stored on a local disk. A fraction of the events are made available to processes on a farm of PC's running Linux for on-line monitoring purposes. Long-term storage is provided by a HPSS-based tape robot system operated by the RHIC Computing Facility (RCF). The average rate of transfer of data to HPSS is 20 Mbytes/s but for

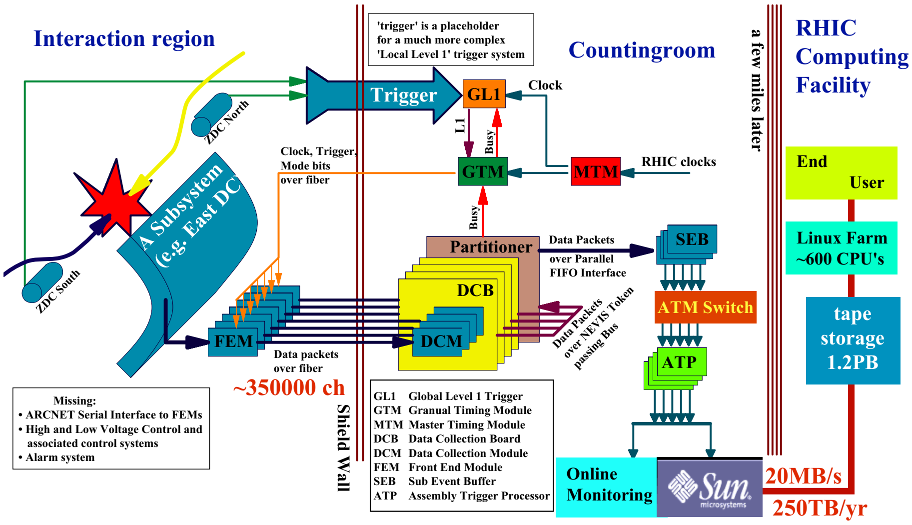

Figure 3.11: The TOF hardware mounted in the PHENIX

short time intervals rates as high as 60 Mbytes/s have been obtained.

Once the data is transferred to the HPSS, the responsibility of the data handling is on the PHENIX off-line computing. The volume of the data collected over a typical RHIC run period is ∼200 Tbytes of raw data, ∼100 Tbytes of reconstructed data, ∼100 Tbytes of physics analysis data and tens of Tbytes of detector simulation data. Both for reconstruction of this large amount of data and analyses of the reconstructed data by 400+ collaborators require a substantial computing power. The resources are shared using the Load Sharing Facility (LSF).

Another challenge is the quality of the software. PHENIX reconstruction, analysis and simulation code consists of about 500,000 lines of codes. PHENIX maintains a very high quality of software contributed by many people in the collaboration. The codes are written in the C++ language. We use ROOT, an object-oriented analysis framework developed at CERN, to provide the I/O interface to our reconstruction and analysis framework. ROOT is also used as a late-stage physics analysis tool for filling and visualizing histograms.

3.8 Subsystems Used For This Analysis

The $\phi \rightarrow K^+K^-$ analysis involves event selection, centrality determination, momentum measurement, tracking and PID. The present analysis uses the following detectors in the PHENIX east arm:

- Vertex and trigger selection: BBC, ZDC
- Centrality selection: BBC, ZDC
- Momentum measurement: DC, Central magnet
- Tracking: DC, PC1, and PC3
- Initial time of collision: BBC
- Particle Identification: TOF, PbSc.

Chapter 4

Data Selection

4.1 Run Selection

In the year of 2001, RHIC collided gold beams at $\sqrt{s}$=200GeV per nucleon. The official 200 GeV Au-Au runs for run 2 was from August 17 (00:00 hrs) to November 25 (06:00 hrs). The integrated luminosity delivered at PHENIX by RHIC was 84 μb^{-1}. But only about half of the events were within PHENIX fiducial region of $z = \pm 45$ cm. Therefore the effective luminosity at PHENIX was about 42 μb^{-1}. About 55% of the data were collected during the last two weeks of run. Fig. 4.1 shows the integrated luminosity delivered by RHIC during Run-2, as well as in Run-1.

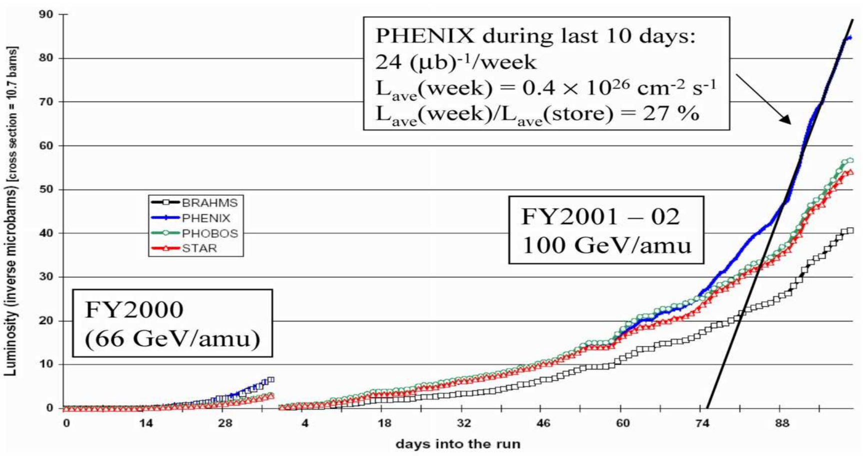

Figure 4.1: The Integrated Luminosity vs Day in run.

The total number of the collected minimum bias data were about 92 millions. They then went under strict quality control. The collected data were checked against the detector performances. A good number of events were discarded based on some the following conditions[39]:

1. Number of DC tracks: Average number of Drift Chamber tracks in each run. A run is considered a good run if the average numbers of DC tracks are in the range of 105 to 128.

2. Mean momentum: Average momenta of Drift Chamber tracks in each run. Range in good runs is between 0.55 and 0.65.

3. PC3 Match mean: Mean value of residual at Pad Chamber 3, in units of calibrated sigma. Range in good runs: -0.10 to +0.10.

4. PC3 Match sigma: Sigma of residual at PC3, from the fit used for item 3. Range in good runs: $<$1.6

5. Is it a proton? A probability is calculated for a track to be a proton. The quantity, denoted as isP, is the difference between the mass-squared for each track matching a TOF hit and the expected mass-squared for a proton. Units are sigma for the mass-squared, expected value is 0. An exponential background and energy loss cut are included. Range in good runs: (-0.6) - (+0.6)

6. Is it a proton - sigma? Sigma of the Gaussian fit to isP. Range in good runs: < 1.6

7. Is it a proton according to EMCAL timing? Centroid of fit to mass-squared distribution using EMCAL timing. The fit is done for all particles with mass-squared > 0.83. Range in good runs: 0.875 - 0.91

8. E/p ratio for electron candidates. Energy to momentum ratio for electron candidates. Range in good runs: 0.90 - 1.1

All of the analysis to be shown here is based on the so-called after-burned CNT nanoDSTs generated in mid-June 2002, and residing on the /phenix/data26 to /phenix/data29 disks. These include only the Au+Au runs at the present time. The complete Au+Au run list was pared down according to the following choices

1. Zero field, photon converter, and reverse field runs were eliminated.
2. Runs with problematic Drift Chamber or Drift Chamber plus Pad Chamber tracking performance were ignored.
3. Runs based on PC HV outages.
4. We examine our Run lists against Run lists used by other analyses in case we still are including some Runs that we should not for some reason.

After applying all of the above conditions, we end up with 180 Runs, which we call the **Golden Runs**. There are 4775 file segments in the selected runs that we use for our analysis. The complete list of runs and files are given in Appendix A.

4.2 Event Selection

The event selection is determined mainly by three factors:

- Whether the event satisfies the PHENIX minimum bias trigger condition (Isminbias).
- Whether the event vertex is in the PHENIX fiducial volume (vertex cut).
- What fraction of the cross section the event corresponds (centrality)

In PHENIX we have two detectors that do the jobs. They are the Beam Beam Counters (BBC) and Zero Degree Calorimeter (ZDC). It is worth mentioning here that PHENIX does not measure the total geometrical cross section. We rely on a model dependent calculation to find the number of participants in a collision. BBC measures the vertex position along the beam axis. In PHENIX coordinate system beam axis is the z-axis. Only events with $|z| < 30$ cm are selected for this analysis.

4.2.1 Minimum Bias Trigger

Zero Degree Calorimeter and Beam Beam Counters were used as the minimum bias triggering device. The BBC and ZDC both detect collision fragments/particles that are emitted at forward pseudorapidities (η). The BBC covers a more central region ($3.0 < \eta < 3.9$) symmetric around z = 0. It also covers the full azimuth and is sensitive to the Cerenkov radiation of charged particles 4. The ZDC is located at a more forward η (6) and is sensitive to the neutral particles that do not get deflected by the Dx sweeping magnets.

The primary interaction trigger is generated by a coincidence between the north and south BBC with at least two photo multipliers fired in each of them. Another trigger is generated by a coincidence between the two ZDC, each one with an energy signal larger than 10 GeV. The minimum bias trigger can be thought of as the logical AND of a coincidence between the north and south ZDC ($ZDCN\&\&ZDCS$) and the north and south Beam Beam Counters (Beam Beam Local Level 1 ($BBLL1$)). For gold-gold collisions, the Boolean $IsMinBias()$ in the $PHTrig$ class return $TRUE$ if the level-1 trigger $BBLL1 \geq 2$ and level-1 trigger $ZDCNS$ both fired. The $ZDCNS$ trigger efficiency for $BBLL1 \geq 2$ is $99^{+1.0}_{-1.5}\%$[40]

4.2.2 Event Centrality

We have discussed in section 2.5 the general idea of centrality of an event. In this section we will discuss the procedures we use in PHENIX do determine the centrality. For illustration we refer to Fig.4.2. As mentioned we need two detectors in order to

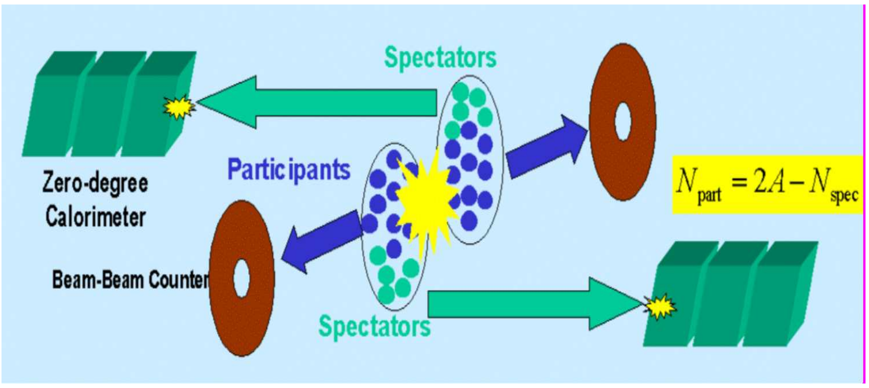

Figure 4.2: Determination of Centrality in PHENIX

record the number of particles produced and the number of spectator nucleons. To record the number of particles produced, the detector should be within the interaction region. To record the spectator nucleons, the detector should be away from the collision vertex, but along the beam line. That is why in PHENIX we use the Beam-beam counter (BBC), which is located along the beam line up and downstream of the beam crossing point and within the interaction region, to record the number of produced particles. The Zero Degree Calorimeter (ZDC), which is also located along the beam line up and downstream of the beam crossing point, but outside of the interaction region (18 m), is used to record the number of the spectator nucleons. The BBC measures charge deposited by the tracks produced in the collisions and the ZDC record the energy of the deposited spectator nucleons.

We adopt the procedure described in the reference[41]. We plot a 2-dimensional plot of BBC charge (Q)vs ZDC energy (E). For a given point on the graph, one can calculate the angle ϕ of a given (Q,E) point with respect to a fixed origin (Q_0,E_0).

This method allows a quick and simple calculation of a centrality based on the BBC Q and ZDC E. The centrality angel ϕ_{cent} is determined from the 2D (Q,E) space.

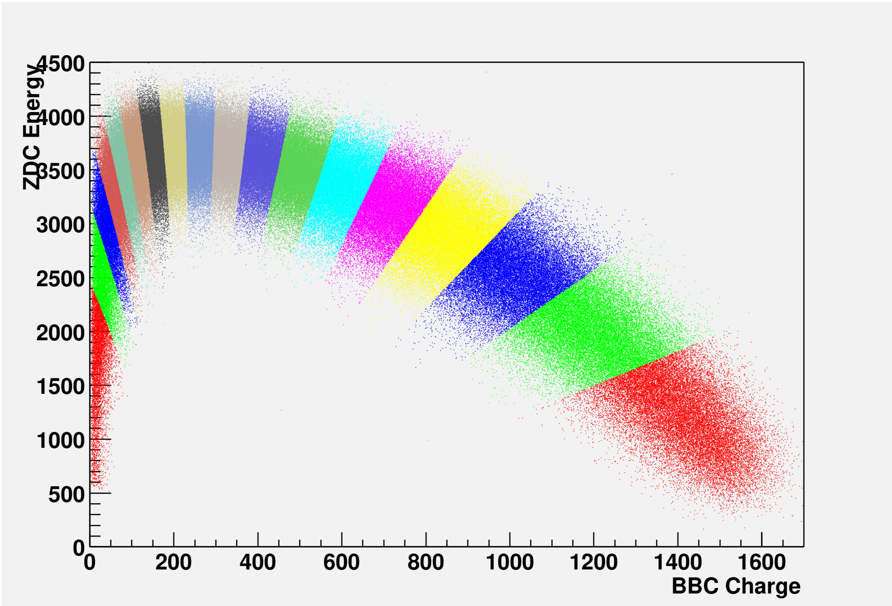

Figure 4.3: Centrality Selection from BBC Analog Sum and ZDC Energy Sum

Fig. 4.3 shows the BBC charge vs ZDC energy plot. The maximum BBC charge Q_{max} is 1700 and the maximum ZDC energy E_{max} is 4500 GeV. Then

$$\phi_{cent} = \tan^{-1}\left(\frac{(Q - Q_0)/Q_{max}}{E/E_{max}}\right) \tag{4.1}$$

where $Q_0 = 0.15 Q_{max}$

with the centrality bins shown in alternate colors. The bin at the bottom right corner corresponds to the top 5% most central events, the next bin is 5%-10% of the most central events, and so on. The centrality classes and the corresponding upper and lower value of the ϕ_{cent} is tabulated in Table 4.1.

For more peripheral events the BBC charge tends to zero and the ZDC energy should be in the higher range. But from Fig. 4.3 we see that for more peripheral events the BBC charge tends to zero and so does the ZDC energy. This is an indication that

Centrality (%)	N_{evt}	ϕ_{min}	ϕ_{max}
min bias (0-92)	20009063	-0.52014	1.99998
20-30	2179573	0.23758	0.45478
30-40	2179038	0.09242	0.23758
40-50	2206354	-0.01034	0.09242
50-60	2185476	-0.08322	-0.01034
60-70	2197392	-0.14102	-0.08322
70-80	2162280	-0.19986	-0.14102
80-92	2485953	-0.52014	-0.19986

Table 4.1: The angular coverage of centrality classes in the (BBCQ,ZDCE) space.

PHENIX does not measure the total geometrical cross section. In order to determine the number of participants we need to use a model dependent calculation.

4.2.3 Number of Participants

In this section we describe the way PHENIX measures the number of participants (N_{part}) and the number of binary collisions (N_{coll}) in a nuclear collision. The discussion is based on Reference[41]-[43]. The calculations are based on the measurements made in the BBC and ZDC. The calculation uses the Glauber Model with a Woods-Saxon density profile distribution for the nucleus.

The Glauber model calculates the thickness of a nuclear matter in the direct path of each incoming nucleon and uses the nucleon-nucleon inelastic cross-section (σ_{nn}^{inel}) to decide whether a nucleon-nucleon collision has occurred. The integration over the total nucleon distribution in each nucleus gives the number of nucleons that took part in the collision. The model uses a few simple assumptions:

1. Nucleons of one nucleus passes straight through the other nucleus.

2. Nucleon-nucleon cross-section remains unchanged in the collisions.

A Monte-Carlo approach is used for the determination of N_{part} and N_{coll}. The

Centrality	$< N_{part} >$
0%-10%	323.6±1.5
10%-20%	235.1±1.1
10%-40%	172.2±1.4
20%-40%	140.7±1.0
40%-50%	73.6±0.6
40%-60%	60.0±0.6
40%-92%	28.4±0.5
50%-60%	46.4±0.5
60%-92%	12.6±0.2

Table 4.2: Number of participants for different centralities.

nucleons of the two gold nuclei are randomly distributed according to a Woods-Saxon distribution :

$$\rho(r) = \frac{1}{1 + \exp\left(\frac{r - r_n}{d}\right)} \tag{4.2}$$

where,

$$\begin{aligned} r_n &= 1.19\ A^{1/3} - 1.61\ A^{-1/3} \\ A &= 197 \\ d &= 0.54 \text{ fm} \end{aligned} \tag{4.3}$$

In the Glauber calculation the nucleons interact like little black disks with an inelastic cross section of $\sigma_{nn} = 40$ mb. For the above parameters inelastic Au+Au cross-section of is 7200 mb. The number of participants and the binary collisions calculated from the model is tabulated in Table 4.2.

4.3 Single Track Selection

Tracks are reconstructed in conjunction of the Beam Beam counter that provides the collision vertex, the Drift Chamber and the hit positions on the Pad Chamber1, which is physically located just behind the Drift Chambers. Tracks are assigned a "quality" depending on the reconstruction. Only the best quality tracks are considered for this analysis. These tracks are then matched to the Tome-of-Flight detector, Pad Chambers3 and the Electromagnetic Calorimeter.

4.3.1 Drift Chamber Track Quality

The Drift Chamber has two sets of XUV wires. The PHENIX tracking algorithm associates hits in X1, or X2 , or both. This provides the x and y position in the PHENIX coordinate system. The UV wires are called stereo wires, and are tilted with respect to the z axis. The UV wires provide the z information of the track. The tracking algorithm works in the following way:

1. The algorithm operates with the PC1 as the principle source of z information. BBC vertex is projected onto PC1.

2. If the PC1 choice is unique, a UV verification is sought. The choice here is either a 1 (UV hit exists) or a 0 (UV hit does not exist).

3. If the PC1 choice is unique and UV verify, then UV hits are unique.

4. If PC1 choice is not unique, UV inspects each possible PC1 choice. In this case one either gets no UV, a best choice, or remaining ambiguity (tied)

The bit patters and the valid patterns are given in Table 4.3.

So the valid patterns can be summarized in Table 4.4

From the Table 4.3 we see that the very best case is 63. Second best is 31. In Fig. 4.4 plotted the Dch tracks quality for run number 31464. The most of the tracks are either of quality 63 or 31.

X1 used	X2 used	UV found	UV unique	PC1 found	PC1 unique	Quality
2^0	2^1	2^2	2^3	2^4	2^5	
1	1	1	1	1	1	63
0	1	1	1	1	1	62
1	0	1	1	1	1	61
1	1	0	0	1	1	51
0	1	0	0	1	1	50
1	0	0	0	1	1	49
1	1	1	1	1	0	31
0	1	1	1	1	0	30
1	0	1	1	1	0	29
1	1	1	0	1	0	23
0	1	1	0	1	0	22
1	0	1	0	1	0	21
1	1	0	0	1	0	19
0	1	0	0	1	0	18
1	0	0	0	1	0	17

Table 4.3: Bit Pattern and Valid Patterns for Dch Track Quality

Quality	2^0	2^1	2^2	2^3	2^4	2^5	Comment
61,62,63	x	x	1	1	1	1	PC1 found/unique UV found/unique
49,50,51	x	x	0	0	1	1	PC1 found/unique no UV
29,30,31	x	x	1	1	1	0	PC1 found/ambiguous, UV found with one best choice
21,22,23	x	x	1	0	1	0	PC1 found/ambiguous, UV found but tied
17,18,19	x	x	0	0	1	0	PC1 found/ambiguous no UVs

Table 4.4: Valid Patterns for Dch Track Quality

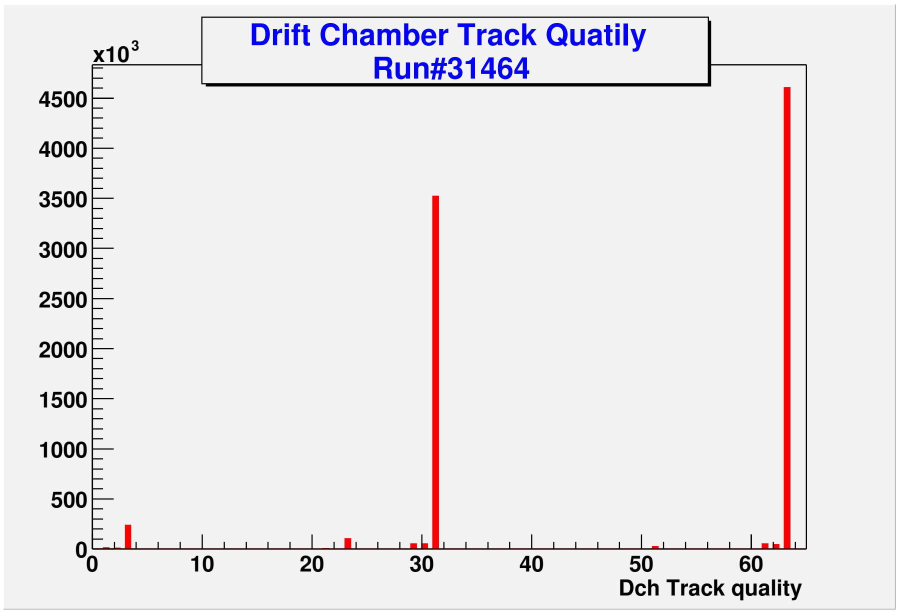

Figure 4.4: Drift Chamber Track Quality for Run 31464

4.4 Track Association

The PHENIX the hit positions at a detector is recorded. Except for the Time Expansion Chambers, the hit position is measured in ϕ and z, whereas TEC measures in ϕ and α. A detector can be hit by a real track, or it can be hit by a decay product from a track or shower particles from the central magnets. These background contributions need to be taken out from the tracks. For this purpose a track association is done between the detectors and the drift chamber tracks.

Since TEC or PbGl are not used for this analysis, we will concentrate on the hit associations at the Time-of-Flight, Pad Chambers3 and east arm PbSc. The ϕ and z resolution of the detector are usually momentum dependent. We will give the momentum dependent description of detector resolution. The track association is performed in the following way:

- The σ of the ϕ and z measurements for the detectors are determined. Usually they are momentum dependent.

- A correction is made for any ϕ or z offset of the detectors.
- The hits (ϕ_{hit}, z_{hit}) at the detector are measured.
- The drift chamber tracks are projected onto the detectors and the projected hit positions (ϕ_{proj}, z_{proj}) at the detector are measured.
- The difference in ϕ of the hits and the projected tracks, $\Delta\phi$ and s of the hits and the projected tracks, Δz are determined is determined.
- from the σ of the detector, offset and $\Delta\phi$ and Δz the number of σ matching in ϕ and z at the detector are determined.

Lets consider that a detector resolutions are $\sigma_\phi(p)$ and $\sigma_z(p)$ for ϕ and z measurement resolution. There are some offset in the measurements which are given by ϕ_0 and z_0. The hit position is measured to be (ϕ_{hit}, z_{hit}) and the Dch track projection onto the detector is (ϕ_{proj}, z_{proj}). Then $\Delta\phi = \phi_{hit} - \phi_{proj}$ and $\Delta z = z_{hit} - z_{proj}$. The number of σ matching in ϕ is given by,

$$n_\phi = (\Delta\phi - \phi_0)/\sigma_\phi(p); \tag{4.4}$$

and the number of σ matching in z is given by,

$$n_z = (\Delta z - z_0)/\sigma_z(p); \tag{4.5}$$

The n-sigma radius is then calculated as:

$$n_\sigma^2 = n_\phi^2 \ + \ n_z^2; \tag{4.6}$$

For the present analysis a 3σ radius cut is applied at TOF, PC3 and PbSc.

$$n_\phi^2 \ + \ n_z^2 < 9.0 \tag{4.7}$$

We will give the momentum dependent resolution of the and the other parameters necessary for the measurements of the track association at TOF, PC3 and PbSc.

4.4.1 Track Association at Time of Flight

ϕ Matching:

$$\sigma_\phi^2 = \frac{A^2}{p^2} + B^2; \tag{4.8}$$

where $A = 2.19 \times 10^{-3}$ rad.GeV/c, $B = 3.69 \times 10^{-3}$ rad.

The ϕ offset are momentum and charge dependent. They are given by,

$$\phi_0 = \frac{C}{|p|} + D \quad \text{(positive tracks)} \tag{4.9}$$

$$\phi_0 = \frac{E}{|p|} + F \quad \text{(negative tracks)} \tag{4.10}$$

where $C = 0.66 \times 10^{-3}$ rad.GeV/c, $D = 1.57 \times 10^{-3}$ rad, $E = -0.73 \times 10^{-3}$ rad.GeV/c and $F = 0.77 \times 10^{-3}$ rad. The number of σ matching in ϕ is then calculated using Eq. 4.4.

z Matching:

$$\sigma_z^2 = \frac{G^2}{p^2} + H^2; \tag{4.11}$$

where $G = 0.91$ cm.GeV/c and $H = 0.95$ cm.

The z offset does not depend on momentum or charge. It is given by,

$$z_0 = -0.445 \text{ cm} \tag{4.12}$$

The number of σ matching in z is then calculated using Eq. 4.5.

4.4.2 Track Association at PC3

ϕ Matching:

$$\sigma_\phi^2 = \frac{A^2}{p^2} + B^2; \tag{4.13}$$

where $A = 2.0 \times 10^{-3}$ rad.GeV/c, $B = 1.80 \times 10^{-3}$ rad.

The ϕ offset are independent of momentum and charge. They are given by,

$$\phi_0 = 0.64 \times 10^{-3} \text{ rad} \quad \text{(positive tracks)} \tag{4.14}$$

$$\phi_0 = 0.37 \times 10^{-3} \text{ rad} \quad \text{(negative tracks)} \tag{4.15}$$

z **Matching:**

$$\sigma_z^2 = \frac{E^2}{p^2} + F^2; \tag{4.16}$$

where $E = 0.81$ cm.GeV/c and $F = 0.83$ cm.

The z offset does not depend on momentum or charge. It is given by,

$$z_0 = -0.16 \text{ cm} \tag{4.17}$$

4.4.3 Track Association at East PbSc

ϕ **Matching:**

$$\sigma_\phi^2 = \frac{A^2}{p^2} + B^2; \tag{4.18}$$

where $A = 2.6 \times 10^{-3}$ rad.GeV/c, $B = 4.6 \times 10^{-3}$ rad.

The ϕ offset are momentum and charge dependent. They are given by,

$$\phi_0 = \frac{C}{|p|} + D \quad \text{(positive tracks)} \tag{4.19}$$

$$\phi_0 = \frac{E}{|p|} + F \quad \text{(negative tracks)} \tag{4.20}$$

where $C = 1.81 \times 10^{-3}$ rad.GeV/c, $D = 2.18 \times 10^{-3}$ rad, $E = -2.12 \times 10^{-3}$ rad.GeV/c and $F = 1.32 \times 10^{-3}$ rad.

z **Matching:**

In the PbSc there is lower bound of 210 MeV/c for the momentum for the z matching.

$$\sigma_z^2 = \frac{G^2}{p^2} + H^2; \tag{4.21}$$

where $G = 1.4$ cm.GeV/c and $H = 2.5$ cm.

The z offset does not depend on charge, but it depends on the momentum of the track and Dch β angle. It is given by,

$$z_0 = K + [M + N.\log(|p| - 0.2)] * \cos\beta \tag{4.22}$$

where $K = -0.35$ cm, $M = 10.9$ cm and $N = 2.03$ cm.c/GeV.

It was observed during the analysis that the PC3 in from of TOF had a large inefficient area. This is evident from Fig. 4.5. This PC3 inefficiency existed throughout all the runs. Since the TOF has an excellent particle identification capability, it was decided not to use the PC3 matching condition for tracks identified in the TOF. Fig. 4.6 shows the status of the tracks when a 3-sigma track projection matching at TOF is imposed without a PC3 matching condition. For tracks identified in the PbSc we impose track projection matching cuts both at PC3 and PbSc as the particle identification through the PbSc is not as good as that of TOF.

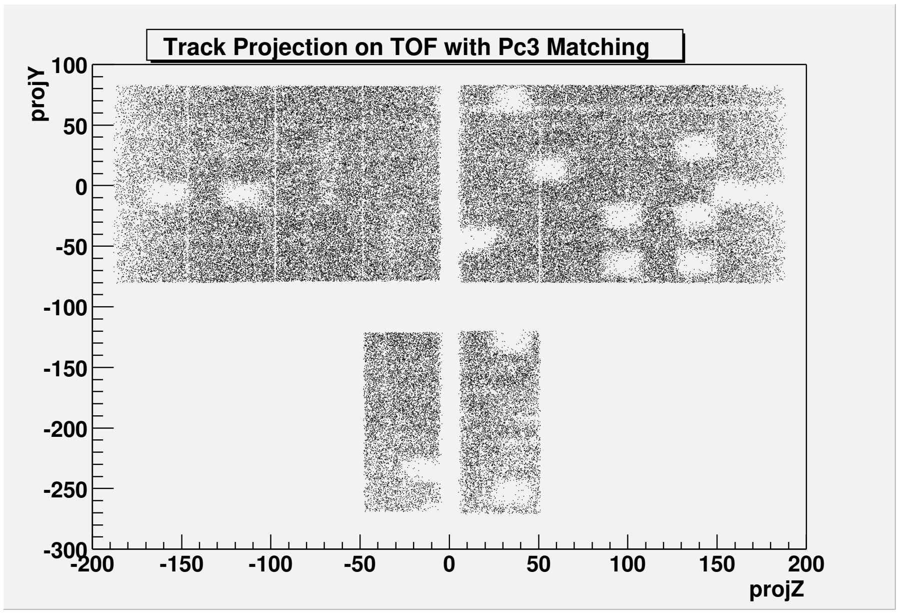

Figure 4.5: X and Y Track Projection at TOF with 3-sigma Matching at TOF and PC3

4.5 Particle Identification

PHENIX has an excellent particle identification capability. The particle identification of hadrons are achieved through the high resolution Time-of-Flight detector that is instrumented in two sectors in the east arm. Additional time of flight information is

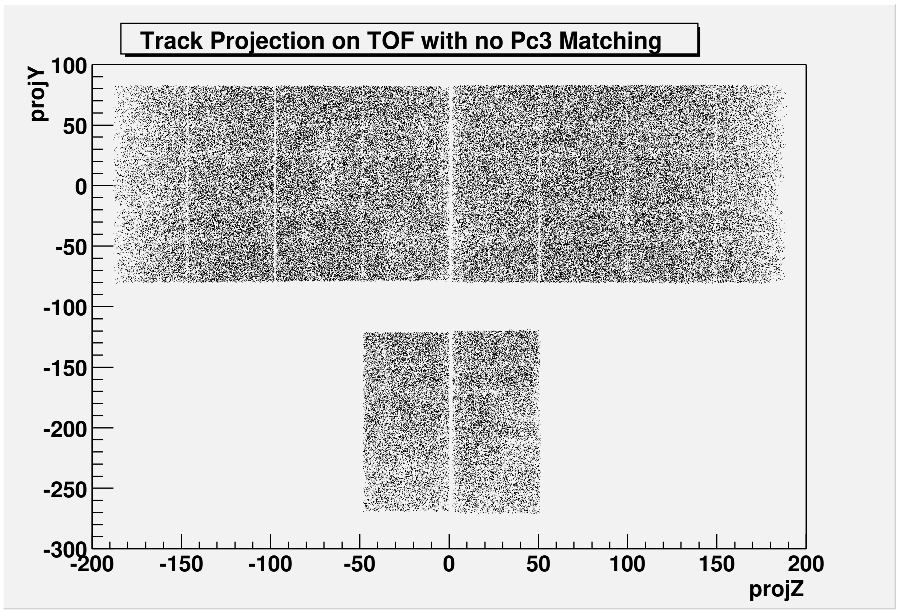

Figure 4.6: X and Y Track Projection at TOF with 3-sigma Matching at TOF only

achieved through the Electromagnetic Calorimeters. There are two types of Electromagnetic Calorimeters in the east arm covering all four sectors, PbSc and PbGl. The PbGl part of the Electromagnetic Calorimeters are located behind the Time-of-Flight detector. The west arms Electromagnetic Calorimeters are all PbSc. This analysis is based on the particle detected in the east arm of PHENIX. the Time-of-Flight detector has a timing resolution of about 80 ps. The PbSc portion of the EMCal has a timing resolution of about 480 ps, whereas the PbGl time resolution is 600 ps. Since high resolution TOF covers almost same region as the PbGl, PbGl is not used for this analysis.

The particle identification is based on the simultaneous measurements of particle momentum, pathlength it covers from the origin to the detection point (a TOF or PbSc hit) and the time of flight. The momentum information of the particle is determined in the Drift Chambers and the pathlength and the time of flight are measured at TOF and PbSc, with the initial time information (time of collision) coming from the Beam Beam counters. The mass of a particle is related to the its energy and momentum by,

$$m^2 = E^2 - p^2 \tag{4.23}$$

The energy and momentum is related to particle's speed by

$$\beta = \frac{p}{E} \tag{4.24}$$

From Eq. (4.23) and (4.24) we can write

$$m^2 = \frac{p^2(1-\beta^2)}{\beta^2} \tag{4.25}$$

But if the particles time of flight is measured as t and the pathlength is L then

$$\beta = \frac{v}{c} = \frac{L}{t.c} \tag{4.26}$$

As p t and L are measured experimentally, the mass of the track can be determined.

The mass squared is momentum dependent. Also it depends on the resolution of the detector. The general form of the width of the mass squared distribution can be written as:

$$\sigma_{m^2}^2 = A(p)\sigma_p^2 + B(p)\sigma_t^2 \tag{4.27}$$

where σ_p^2 is the momentum resolution, which is the momentum resolution of the Drift Chambers, and σ_t^2 is the timing resolution of the PID detector, either the TOF or the EMCal. The analytical form of the width of mass squared can be written as:

$$\sigma_{m^2}^2 = 4\frac{m^4}{p^2}\sigma_p^2 + 4\frac{p^4}{\beta^2}\left[\frac{\sigma_t}{t}\right]^2 \tag{4.28}$$

The Drift Chamber momentum resolution depends on the angular resolution σ_α and the multiple scattering σ_{ms}. The momentum resolution is written as

$$\sigma_p^2 = \frac{\sigma_\alpha^2}{K_1^2}p^4 + \frac{\sigma_{ms}^2}{K_1^2}\frac{p^2}{\beta^2} \tag{4.29}$$

Using Eq. (4.29) together with Eq. (4.24) in q. (4.28) we write

$$\sigma_{m^2}^2 = 4\left[\frac{\sigma_\alpha^2}{K_1^2}m^4p^2 + \frac{\sigma_{ms}^2}{K_1^2}\left[m^4\left(1+\frac{m^2}{p^2}\right)\right] + \frac{\sigma_t^2}{t^2}p^2(p^2+m^2)\right] \tag{4.30}$$

where for the Drift Chamber parameters for year-2 are:$\sigma_{ms} = 0.835$ mrad.GeV/c, $\sigma_\alpha = 0.86$ mrad and $K_1 = 87.0$.

The particles are selected in the following way.

- The mass squared of a particle is calculated.
- The centroid of the mass squared distribution for $\pi^\pm$, $K^\pm$, p, $\overline{p}$ are calibrated. The centroids are corrected for any offset. The momentum dependence of the centroid is taken into account.
- The momentum dependent $\sigma^2_{m^2}$ is calculated
- The difference of the mass squared and the calibrated centroid for the mass squared will give the spread of the track from the centroid of a particular type of species. In other words, this will indicate whether the track is a pion, kaon or a proton.
- The number of sigma of the track is given by

$$n = \frac{|m^2_{\text{meas}} - m^2_{\text{centroid}}|}{\sigma^2_{m^2}} \tag{4.31}$$

So each track will associate with three type of n-sigma, probabilities to be either a pion, or a kaon or a proton. They are called isPi, isK and isP. We can make a choice a particular band by using appropriate numbers of isPi, isK or isP. For example if we want to choose a 2-sigma band of kaon, we simply choose |isK| < 2.

4.5.1 Particle Identification Through the Time-of-Flight Detector

The Time-of-Flight detector has excellent particle identification capability. Fig. 4.7 shows the particle identification through the Time-of-Flight detector. A scatter plot is drawn between the particles time of flight measured at the TOF and the inverse of the particle's momentum times the charge of the track. Clear and very distinct particle bands are observed on the plot. Kaons are well separated between 0.2 GeV/c and 2.2 GeV/c. For this analysis the momentum range for the selected kaons in the Time-of-Flight is 0.3 GeV/c $< p <$ 2.0 GeV/c.

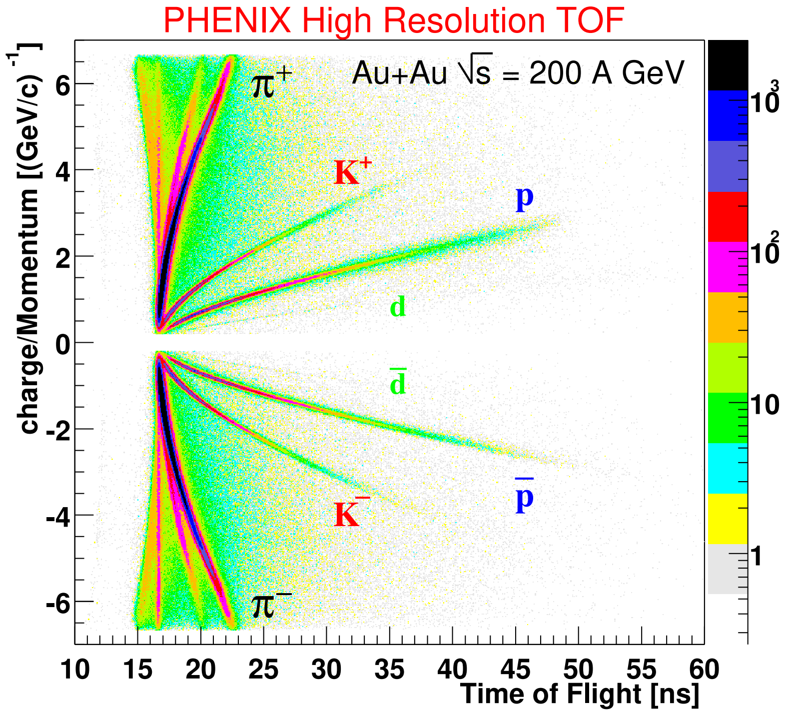

Figure 4.7: Particle Identification Through the High-Resolution Time-of-Flight Detector. The unlabeled bands are muons and electrons.

The mass squared of the tracks are shown Fig. 4.8 and as a function of momentum is shown in Fig. 4.9. It is evident from the plot that the mass squared depends on the momentum of the particle. Also it depends on the resolution of the detector. The calibrated timing resolution for the Time-of-Flight detector for year-2 used to calculate the width of the mass squared was 120 ± 2 ps. We choose 2-sigma band of kaons ($|\mathrm{isK}| < 2$).

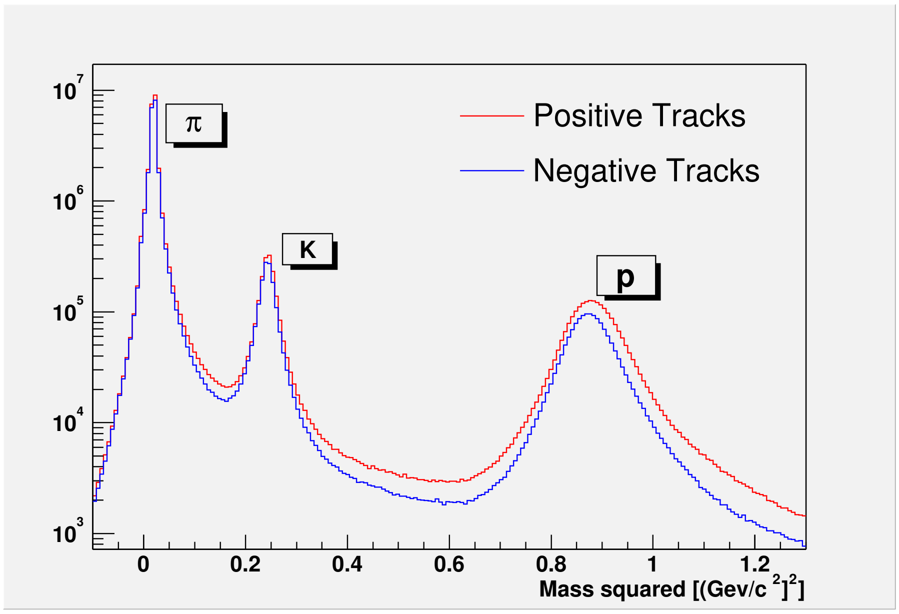

Figure 4.8: Mass Squared of Identified Particles in the Time-of-Flight Detector

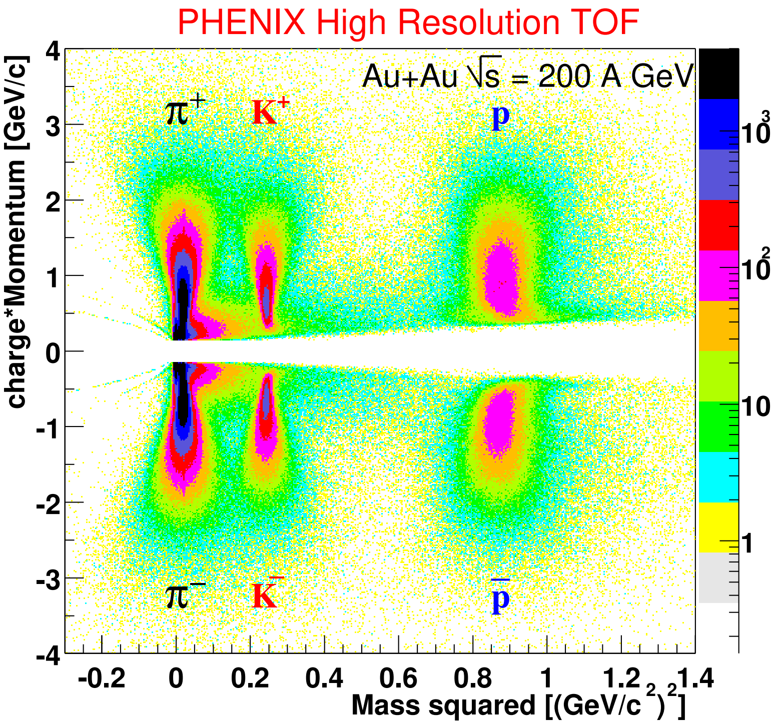

Figure 4.9: Mass Squared of Identified Particles in the Time-of-Flight Detector

To show the momentum dependence of the mass squared in TOF we plot the mass squared of tracks in eight momentum bins in Fig. 4.10. It is evident that the width of the distribution gets wider with the increase in momentum. The behavior of the Kaon mass squared width and the centroid with the variation of momentum is shown in Fig. 4.11, Fig. 4.12 and Fig. 4.13. The sigma of the mass squared is fitted with a function like Eq. (4.30). The variation of mean of the mass squared is very small with momentum.

4.5.2 Particle Identification Through the Electromagnetic Calorimeters

The EMCal are the other detectors used for particle identification. The EMCal timing resolution is about 480 ps. But they have larger coverage. The mass squared in the EMCal are calculated the same way as in the TOF. The particle identification plots in the EMCal are given in Figs. 4.14 and 4.15. The distinct particle bands are observed. The kaons are well separated between 0.2 GeV/c and 1.2 GeV/c. For this analysis the momentum range for the selected kaons in the east arm Electromagnet Calorimeter is 0.3 GeV.c $< p <$ 1.0 GeV/c.

EMCal Mass Renormalization

The CNT nanoDSTs contain the information about the EMCal clusters which are associated to a reconstructed track. These data include the time–of–flight to the cluster and the calculated path length to the cluster. Using these two pieces of EMCal information together with the momentum reconstruction value for the track enables one to derive the mass of the particle. The sectors E2 and E3 should have approximately 400 ps time resolution for hadrons. Hence, one may expect to obtain useful K/π mass resolution up until about 1 GeV/c.

An example of such a mass spectrum for positive particles is shown in Fig. 4.16. One normally plots the square of the mass since the mass value m is derived from the

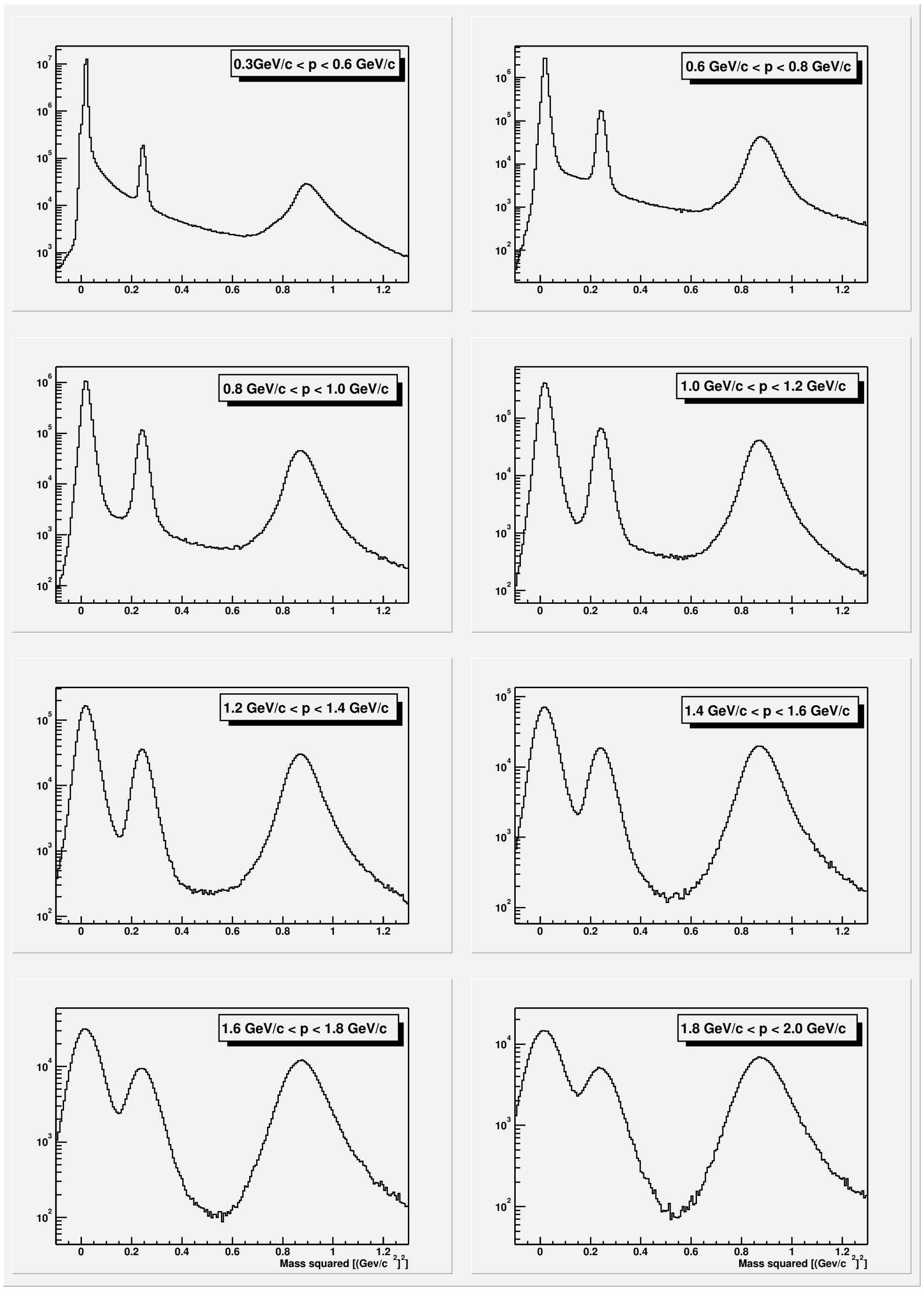

Figure 4.10: Mass Squared of Identified Particles in the Time-of-Flight Detector in 8 momentum bins

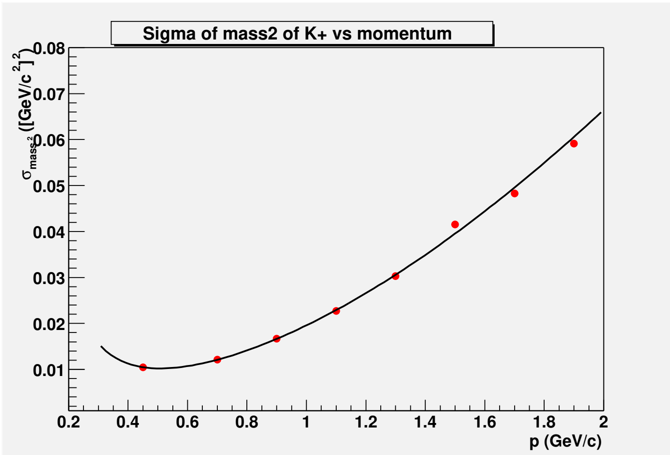

Figure 4.11: Sigma of Mass Squared of Positive Kaons Identified in the Time-of-Flight Detector vs momentum

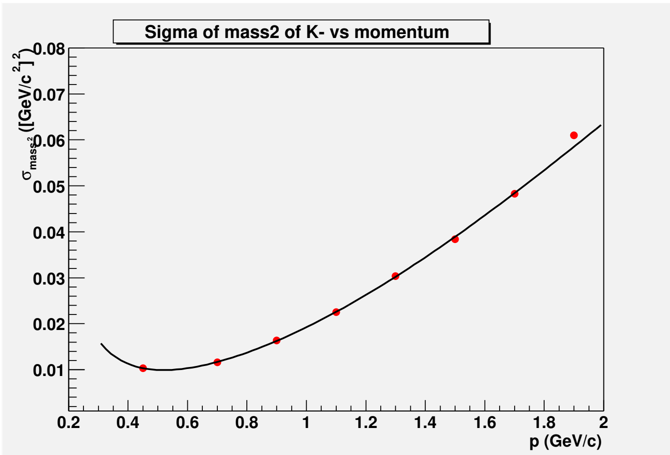

Figure 4.12: Sigma of Mass Squared of Negative Kaons Identified in the Time-of-Flight Detector vs momentum

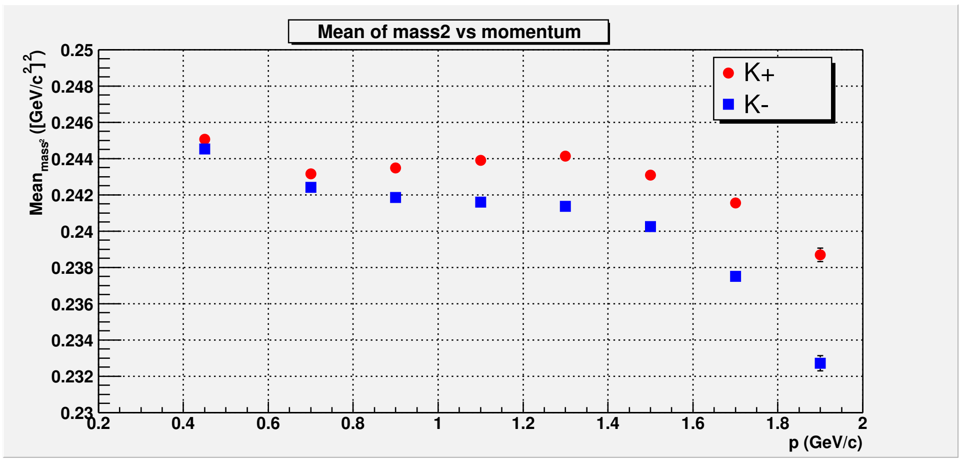

Figure 4.13: Mean of Mass Squared of Kaons Identified in the Time-of-Flight Detector vs momentum

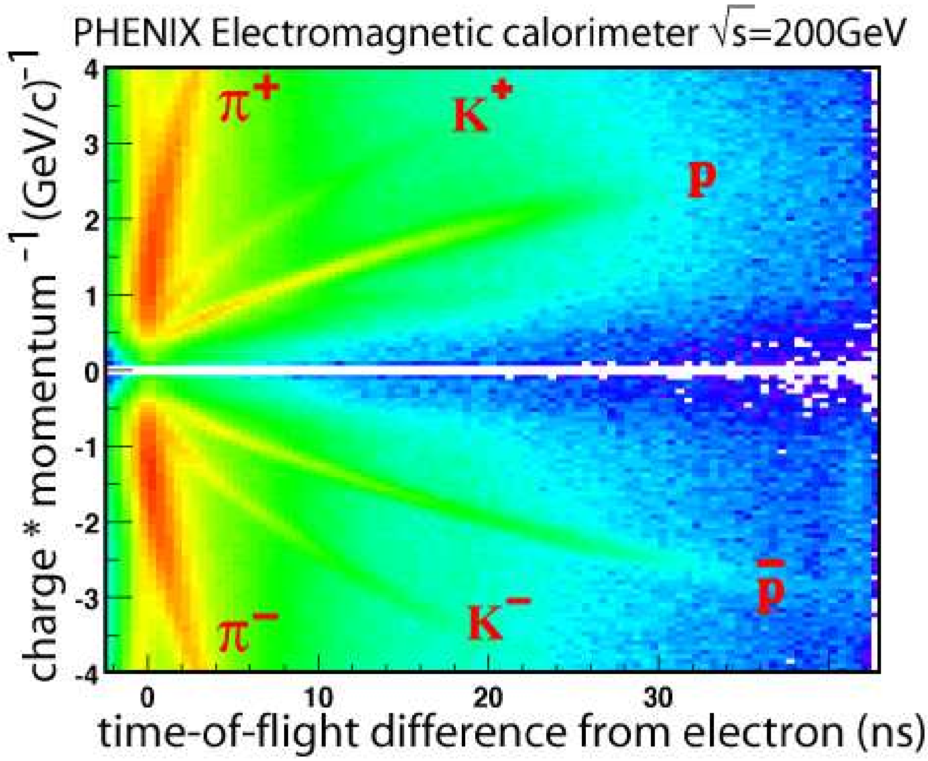

Figure 4.14: Particle Identification Through the Electromagnetic Calorimeter

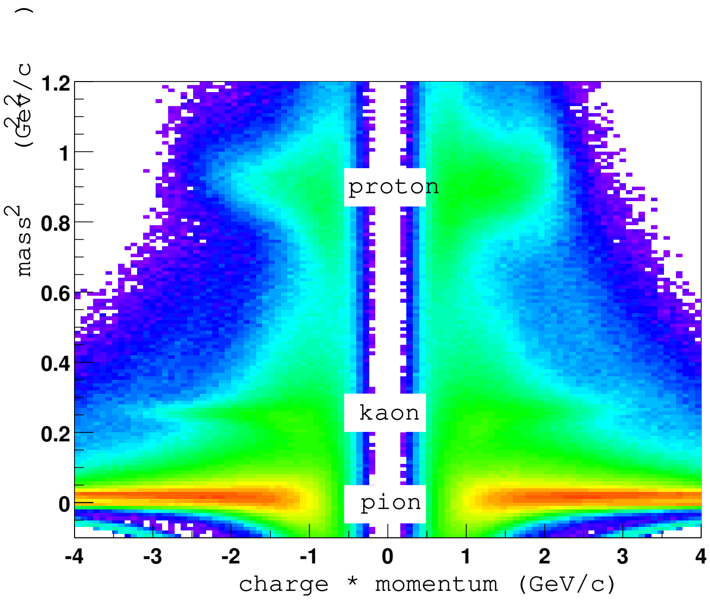

Figure 4.15: Mass Squared of Identified Particles in the Electromagnetic Calorimeter

equation

$$m^2 = \frac{p^2(1-\beta^2)}{\beta^2}$$

where $\beta \equiv v/c$ is determined from the time-of-flight and the path length. The variable p is the particle momentum. Experimental resolution uncertainties could lead to the deduced β being apparently greater than unity for some particle tracks, although this is not the case for kaons in PHENIX.

In Fig. 4.16 the mass-squared spectrum is plotted for six momentum bins ± 75 MeV centered at 325 to 1075 MeV. Except for the last bin which appears more as a shoulder on the background tail from the lower mass pions, there are distinctive peaks in the other five momentum bins. However, it can be seen that the centroids of these peaks vary significantly as a function of momentum. This occurs because the timing calibration of the EMCal was not perfected prior to the production of the nanoDSTs. Therefore, for this analysis, we introduced a momentum dependent mass rescaling to compensate for the slight timing mis-calibration. The results of the improved mass-squared spectrum are shown in Fig. 4.17. With this renormalization of the mass spectrum, it is then possible to set tighter momentum dependent mass windows in

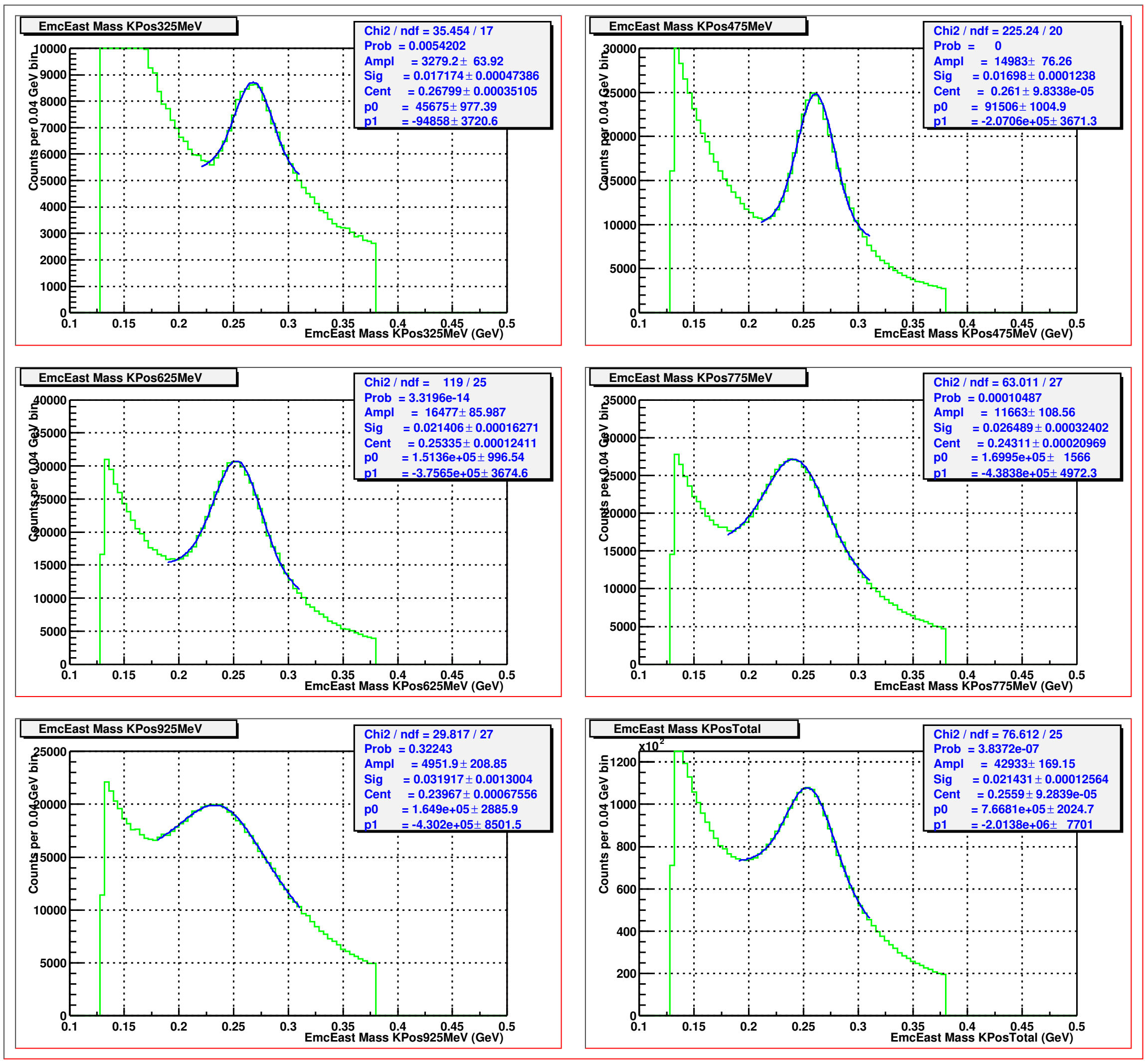

Figure 4.16: Partial mass-squared spectrum for positive particles deduced from the PHENIX East EMCal subsystem, before momentum–dependent corrections. The spectra are in bins of particle momentum from 325 to 1075 MeV, with bin widths of ± 75 MeV. There are Gaussian peaks fitted on top of a linear + quadratic background in each case.

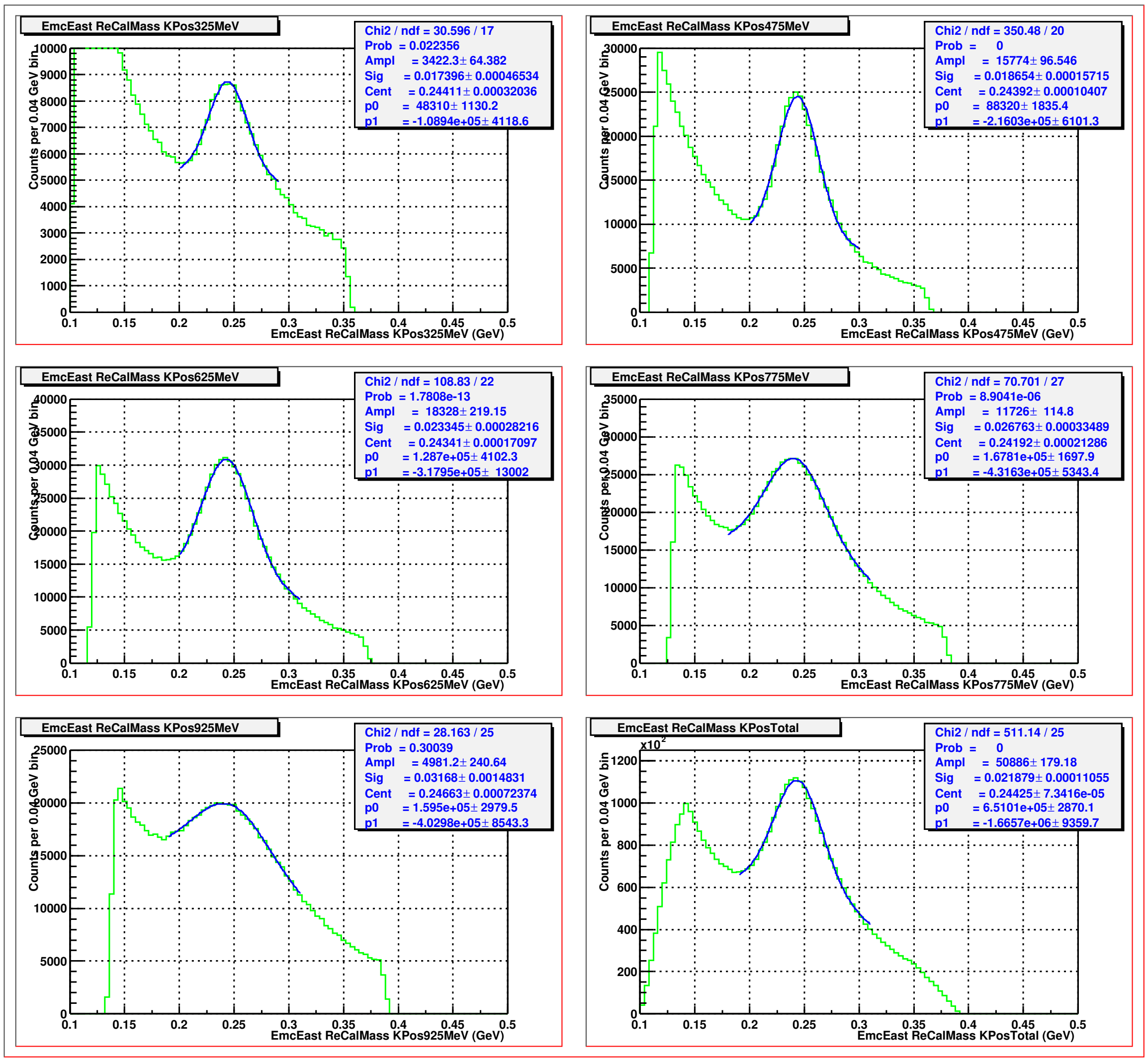

Figure 4.17: Partial mass-squared spectrum for positive particles deduced from the PHENIX East EMCal subsystem, after momentum–dependent corrections. The steep shoulder at low mass is from the pions.

p (GeV/C)	K^+	K^-	Ratio K^+/K^-
0.325 ± 0.075	0.2680 ± 0.0004	0.2538 ± 0.0001	1.0559 ± 0.0016
0.475	0.2610 ± 0.0001	0.2522 ± 0.0001	1.0349 ± 0.0006
0.625	0.2534 ± 0.0001	0.2478 ± 0.0001	1.0226 ± 0.0006
0.775	0.2431 ± 0.0002	0.2413 ± 0.0002	1.0075 ± 0.0012
0.925	0.2397 ± 0.0007	0.2387 ± 0.0004	1.0042 ± 0.0034

Table 4.5: Momentum Dependence of the Kaon Mass–Squared Centroids from the EMCal

order to tag the candidate kaon tracks with better signal-to-background probability. Based on the distinctive mass peaks shown in Fig. 4.17, particles with momentum between 300 and 1000 MeV/c are considered for particle identification in the EMCal in the $\phi \to K^+K^-$ analysis in this analysis.

The equivalent before–and–after mass spectra for the negative particles are shown in Fig. 4.18 and Fig. 4.19. The fitted centroids of the mass peaks are tabulated in Table 4.5. From these results one can observe an interesting systematic difference between the positive kaons and the negative kaons. The positive kaons have a greater centroid variation as compared to the negative kaons. Perhaps related to that, the negative kaon mass peaks in each momentum bin are slightly sharper than for the positive kaons. Such a systematic discrepancy cannot be explained by a simple time–zero offset which would apply equally to both charge signs. This effect is not fully understood yet.

4.6 Drift Chamber Ghost Track Rejection

When two or more tracks hit tracks hit the same wire planes in an event, they are also associated to the same PC1 hit clusters. This represents an ambiguity in the drift chamber momentum measurement algorithm. By geometry of the hit, they are of the same charge sign. They will exit the drift chamber in a very close proximity. So

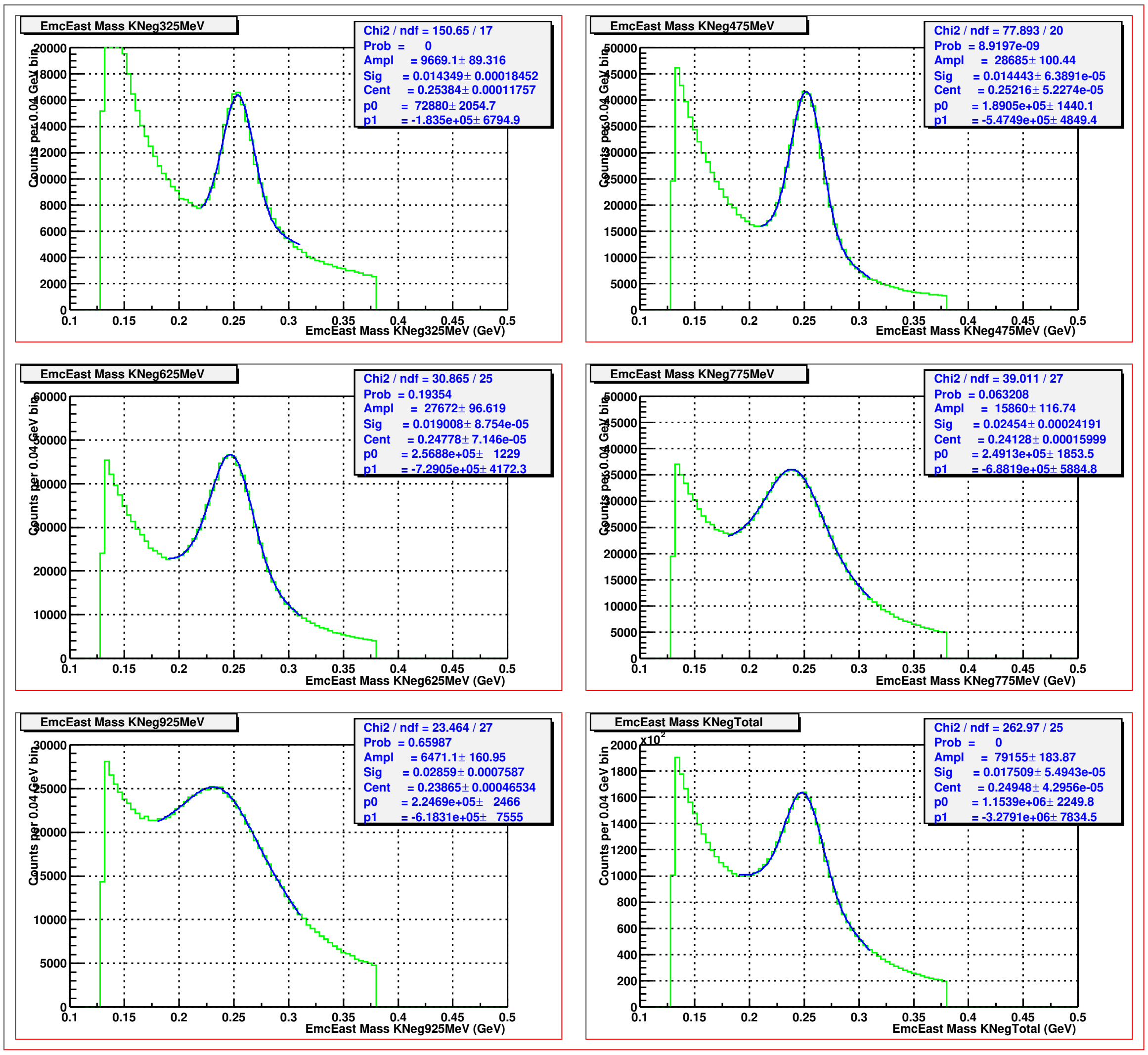

Figure 4.18: Partial mass-squared spectrum deduced for negative particles from the PHENIX East EMCal subsystem, before timing corrections. The spectra are in bins of particle momentum from 325 to 1075 MeV, with bin widths of ±75 MeV. There are Gaussian peaks fitted on top of a linear + quadratic background in each case.

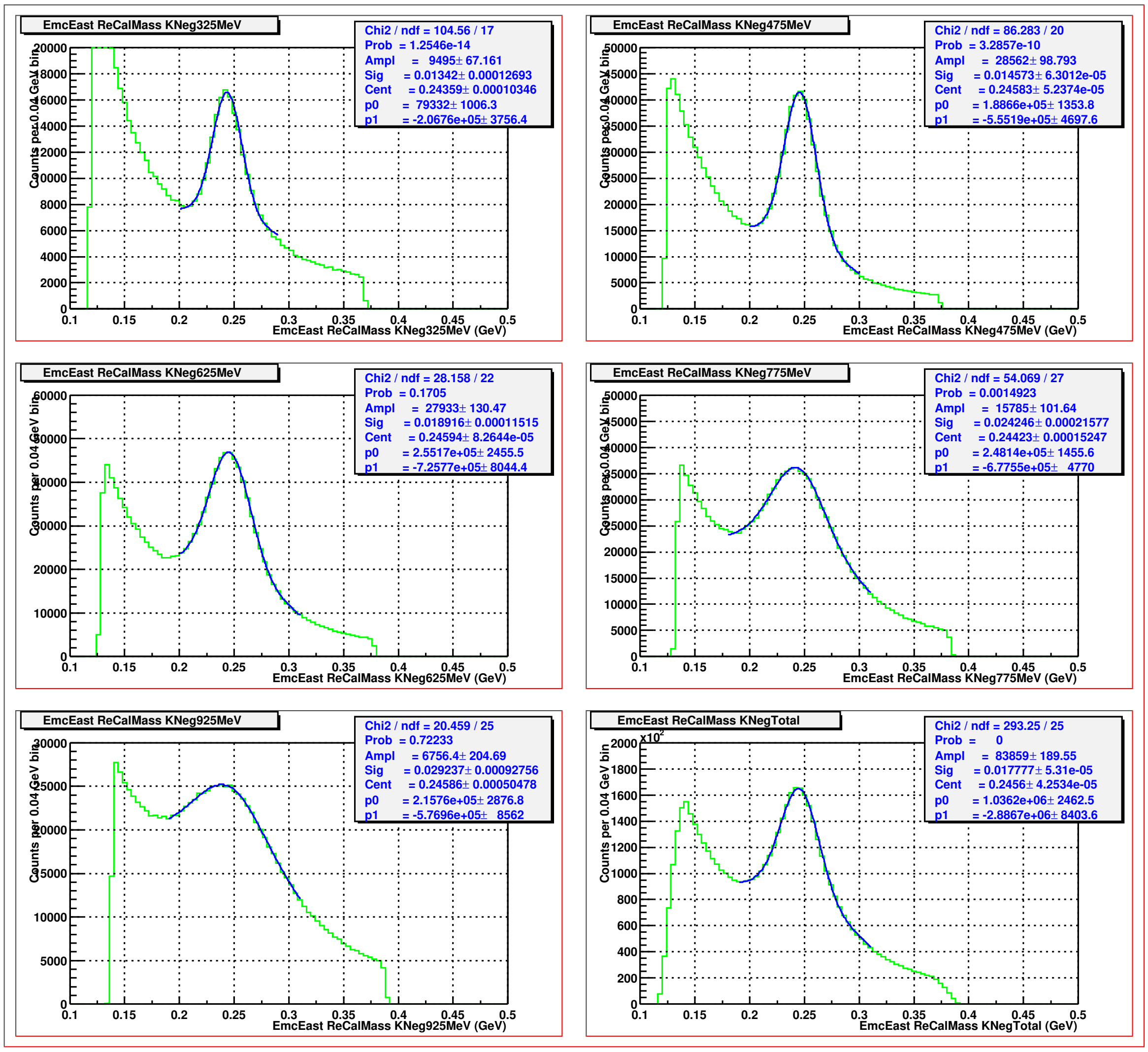

Figure 4.19: Partial mass-squared spectrum for negative particles deduced from the PHENIX East EMCal subsystem, after timing corrections. The spectra are in bins of particle momentum from 325 to 1075 MeV, with bin widths of ±75 MeV. There are Gaussian peaks fitted on top of a linear + quadratic background in each case.

when the difference of the drift chamber exit z-coordinate $\Delta zed = |zed_1 - zed_2|$ or the exit ϕ -coordinate $\Delta\phi = |\phi_1 - \phi_2|$ are measured, a spurious peak is observed. In Fig. (4.20) are plotted the Δzed and $\Delta\phi$ for positive kaon pairs and negative kaon pairs. Spikes are seen near Δzed close to zero and $\Delta\phi$ close to zero.

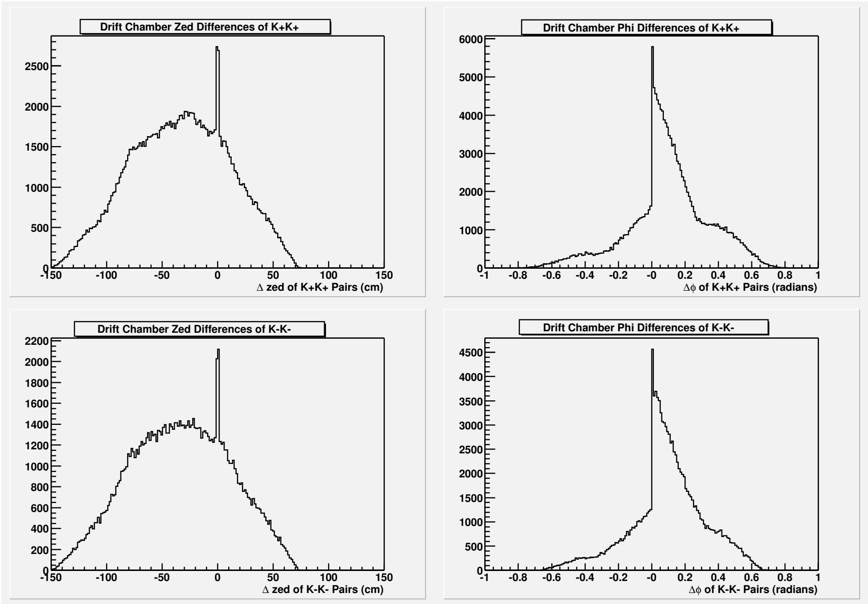

Figure 4.20: The $\Delta zed = |zed_1 - zed_2|$ and $\Delta\phi = |\phi_1 - \phi_2|$ Plots for K+K+ and K-K- Pairs.

We need to find conditions to eliminate these ghosts. The ghost pairs must have very small differences in zed and ϕ values. In Fig. (4.21) are plotted the Δzed and for like sign pairs with a condition that $\Delta\phi < 0.3$. The $\Delta\phi$ for like sign pairs are plotted with $\Delta zed < 1.0$.

After an extensive study, we determined the Drift Chamber Ghost pair criteria. The Drift Chamber Ghost criteria used in this analysis are:

- The *DchZed* values are within 2 mm
- The *DchPhi* values are within 0.03 radians

If there are two same sign Dch/PC1 tracklets which meet the above two criteria, then

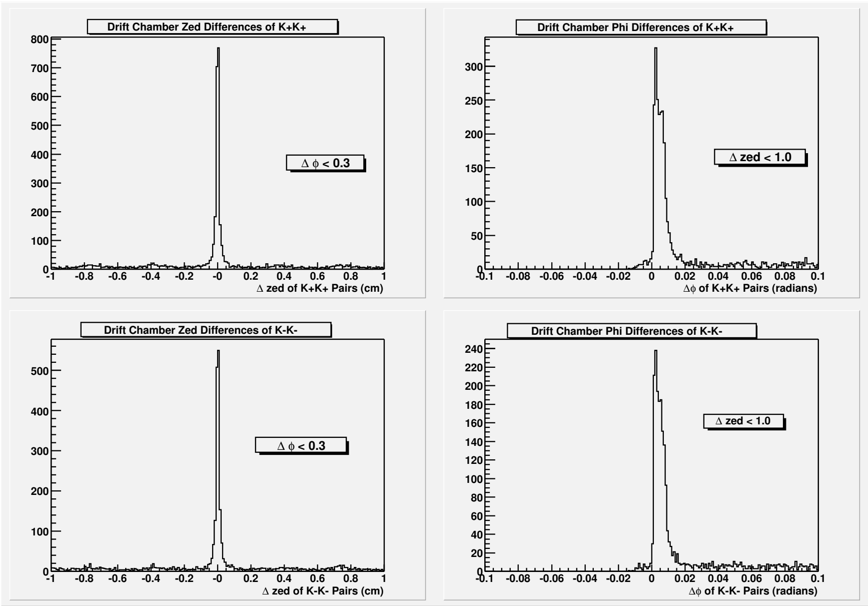

Figure 4.21: The Δzed and $\Delta\phi$ Plots for K+K+ and K-K- Pairs for tracks in close proximity.

a random choice is made to discard one of these and keep the other. The numerical *DchZed* and *DchPhi* limits are derived by looking at their respective spectra as shown in Fig. 4.21.

The ghost rejection condition is applied to data. In Fig. (4.22) are plotted the Δzed and $\Delta\phi$ for positive kaon pairs and negative kaon pairs after the ghost rejection condition. It is apparent from the plot that the ghosts are rejected from the sample.

4.7 Intruder Rejection

In the Time-of-Flight Detector the time measurements are done when tracks hit a slat of the TOF. The subsequent energy and mass measurements are derived from this information together with the pathlength. In the EMCal, the time and energy information are measured from the EMCal tower hit cluster. There are some instances where more than one track hit a TOF slat or an EMCal tower. The time and energy information for these tracks are corrupted.

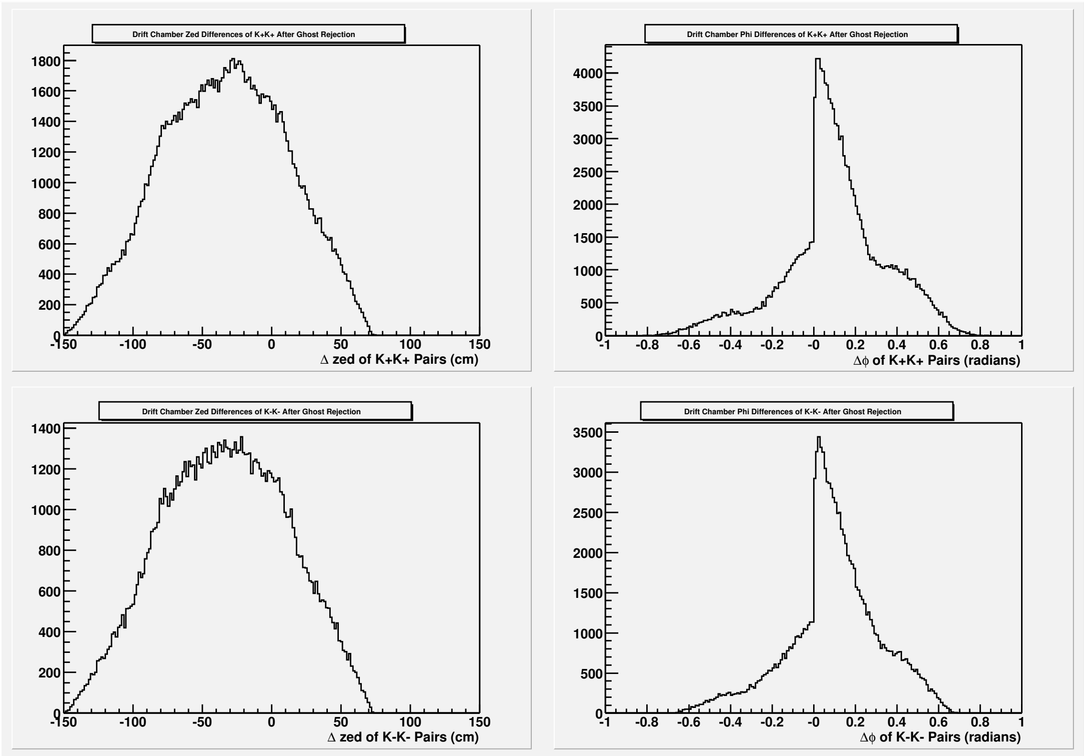

Figure 4.22: The $\Delta zed = |zed_1 - zed_2|$ and $\Delta\phi = |\phi_1 - \phi_2|$ Plots for K+K+ and K-K- Pairs after Ghost Rejection.

The simultaneous multiple hits in a TOF slat or an EMCal tower has very important consequence for the pair invariant reconstruction. For instance, it was seen that there is a structure above the ϕ mass at around 1.06 GeV (see Reference[44]). We call this peak as the *intruder peak*. Such a peak is shown in Fig. 4.23. The structure was initially thought as the K_S^0 peak, where pions coming from $K_S^0 \to \pi^+\pi^-$ decay were thought as identified as kaon in TOF. But the yield of the intruder is too large to be explained by the doubly misidentified pions.

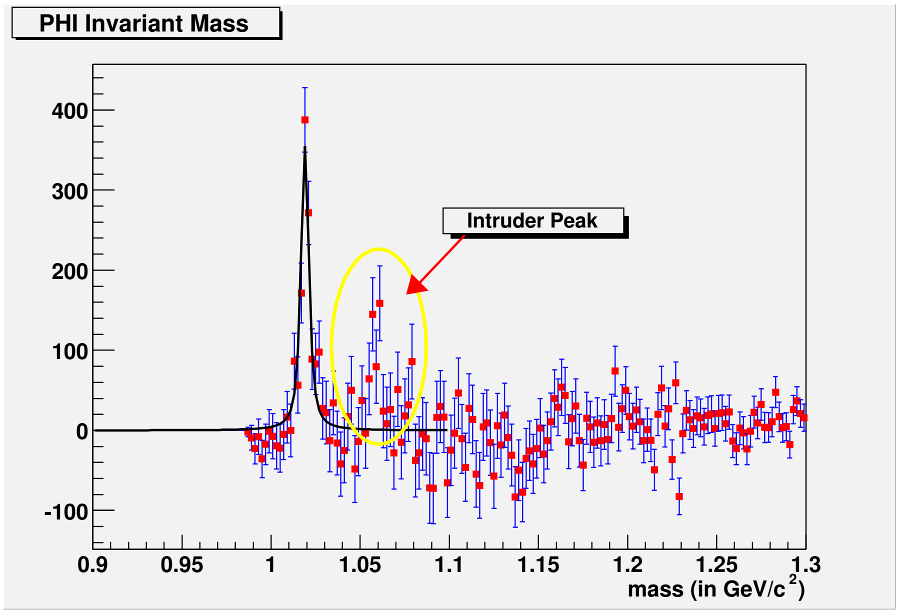

Figure 4.23: The Intruder peak in the appearing in the K+K- Invariant pair mass distribution

We can hypothesize for the intruders. The hypothesis is as follows.

1. In the intruder peak, let one of the two tracks be a real kaon. Let us call it $trk1$.

2. The other one ($trk2$) is a track of opposite charge that points to the same TOF hit or EMCAL cluster of $trk1$. Thus the timing information of $trk1$ and $trk2$ are the same.

3. Since $\text{TOF}_{trk1} = \text{TOF}_{trk2}$, mass_{trk1} is probably similar to mass_{trk2}. Thus if trk1 is a kaon, trk2 is also assigned as kaon.

4. The condition (2) means that, in the rest frame of the pair (trk1+trk2), the apparent decay momentum of trk1 and trk2 is similar and they should be about 200 MeV/c (the magnetic p_t kick of the Central Magnet). This kinematic condition can cause a peak in the effective mass of (trk1+trk2).

The hypothesis explains the following feature of the intruder

- The yield of intruder increases with centrality.

- There is little signal in TOF-EMC combination.

- The mass value is roughly correct. The expected mass peak position produced by this mechanism roughly is

$$M_{intruder} = 2\sqrt{M_k^2 + (p_t)_{kick}^2} \tag{4.32}$$

  For kaon using M_k = 493 MeV and $(p_t)_{kick}$ = 200 MeV, we have $M_{intruder}$ = 1.064 GeV. Similarly for proton, $M_{intruder}$ =1.918 GeV.

Following the hypothesis, we use the following steps to eliminate the intruders.

- Impose the global cuts
  - -30cm<bbcz<30cm
  - 0<isminbias<93

- Consider tracks which have best Dch quality (31 or 63)

- Eliminate the drift chambers ghost tracks. The Dch ghosts are of the same charge and they are within $|\Delta zed| < 0.2$ and $|\Delta\phi| < 0.03$. One of the tracks of the pair that satisfies condition to be ghost is rejected randomly.

- Tracks that survive the ghost rejection are subject to the intruder rejection. To reject intruders in TOF we do the following:

  – identify tracks in TOF. We use a 3σ radius matching at TOF (tofsdphi*tofsdphi + tofsdz*tofsdz < 9)

  – compare the slat of the tracks. If there are two hits on a slat in an event, the timing information of the tracks is bad, and they show up as intruders. So if the slat of two tracks is same (slat1==slat2), both of them are rejected.

  To reject intruders in EMCal we do the following:

  – identify tracks in EMCal. We use a 3σ radius matching at EMCal (emcsdphi*emcsdphi + emcsdz*emcsdz < 9)

  – compare the sectors, energies and time of flight of the tracks. If two tracks in the same EMC sector have same energy and same time (sect1==sect2 && ecorr1==ecorr2 && temc1==temc2), both of them are rejected.

The Drift Chamber ghost pair rejection cuts are made **before** the intruder pair cuts are considered. The Drift Chamber ghost pairs have a high probability of having the sharing the same time element, as can be expected for ghost tracks in the Dch/PC1 region being projected to the outer tracking subsystems.

4.8 Chronological Order of Cuts Applied to Data

Here we list the different cuts applied to the data. The order is very important and is strictly followed.

- BBC vertex cut: $|bbcz| < 30.0$cm.

- Minimum Bias Condition: $IsMinBias$.

- Centrality Condition: $0 < CentClock < 93$.

- Dch Ghost Rejection:
  - Same charge pairs: Charge1 == Charge2
  - Dch Quality == (31 || 63)
  - $\Delta Zed < 2$ mm
  - $\Delta\phi < 0.03$ radians

  One member of the pairs is randomly rejected.

- Intruder Rejection: Tracks that survive the Dch ghost rejection
  - Fiducial cut: -75.0 cm $< zed <$ 75.0 cm
  - Dch Quality == (31 || 63)
  - In TOF
    - Energy loss at TOF wall: $tofe < 2$ MeV.
    - Track Association: 3-σ track association at TOF
    - Momentum Range: 0.3 GeV/c $< p <$ 2.0 GeV/c
    - Same Slate: if Slat1 == Slat2, both of the tracks are rejected.
  - In EMCal
    - Hot Channel Rejection: $warnmap \& 0x00000400 == 0 \;\&\&\; warnmap \& 0x02000000 == 0$.
    - Track Association: 3-σ track association at EMCal
    - Momentum Range: 0.3 GeV/c $< p <$ 1.0 GeV/c
    - Same Energy and Time: if (Time1 == Time2 && Energy1==Energy2), both of the tracks are rejected.

- Fiducial cut: -75.0 cm $< zed <$ 75.0 cm

- Dch Quality == (31 || 63)
- In TOF
  - 0.3 GeV/c < p < 2.0 GeV/c
  - Energy loss at TOF wall: $tofe$ < 2 MeV
  - Track Association: 3-σ track association at TOF
  - PID cut: 2-σ calibrated mass squared of kaons $| isK | < 2.0$
- In EMCal
  - 0.3 GeV/c < p < 1.0 GeV/c
  - Hot Channel Rejection:
    $warnmap\&0x00000400 == 0 \;\&\&\; warnmap\&0x02000000 == 0$
  - Track Association: 3-σ track association at EMCal
  - Track Association: 3-σ track association at PC3
  - PID cut: 2-σ calibrated mass squared of kaons
    $| mass2kaon - 0.493677 * 0.493677 | < 2.0 * \sigma$.

Chapter 5

Single Kaon Analysis

Before presenting the results of the $\phi \to K^+K-$ analysis we show first the results of an inclusive kaon analysis. The inclusive kaon analysis is based on exactly the same single track and pair track cuts described previously in the Tracking Cuts subsection 4.8 for the pairs analysis. The $\frac{1}{2\pi\, m_T}\frac{d^2N}{dm_T\, dy}$ for this inclusive kaon yield will be compared with that obtained independently by the Hadron Physics Working Group (PWG) in its separate analysis. The Hadron PWG uses much tighter particle cuts with about a factor of 1.6–2.0 less acceptance than we can afford for the pairs analysis. A comparison of the MC correction factors for this analysis and those of the Hadron PWG are shown in Tables 5.1 and 5. In the comparison it is seen that for the K^+ yield, the acceptance factor for this analysis is approximately a factor of 2.0 larger than is the Hadron PWG acceptance factor, independent of momentum. Similarly, the K^- acceptance factor is approximately a factor of 1.7 larger. The different ratios as a function of charge sign is likely due to the different fiducial cuts made in the two acceptance calculations for the relatively narrow aperture TOF subsystem.

The transverse momentum spectra for K^+ and K^- are shown in Fig. 5.5 and 5.6

When these two sets of acceptance factors are used in the extractions of the yields for the inclusive kaons, one obtains the results shown in Figs. 5.1, 5.2, 5.3 and 5.4. A comparison of the extracted $dN/dy\, dm_T$ and inverse slopes is given in Table 5.

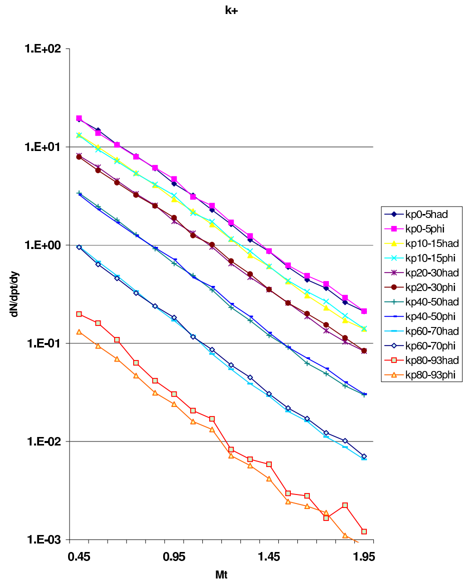

Figure 5.1: Comparison of the yields for K^+ as a function of centrality and transverse momentum, as determined by this analysis and the Hadron PWG. Odd bins in centrality. Points labeled as "had" come from the Hadron PWG. Points labeled "phi" is from this analysis.

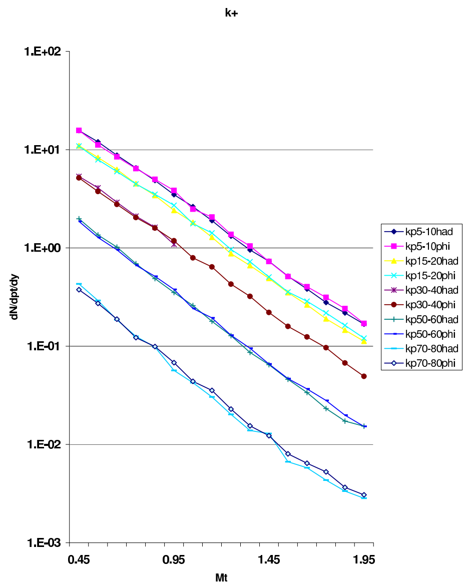

Figure 5.2: Same as Fig. 5.1 for even bins in centralality.

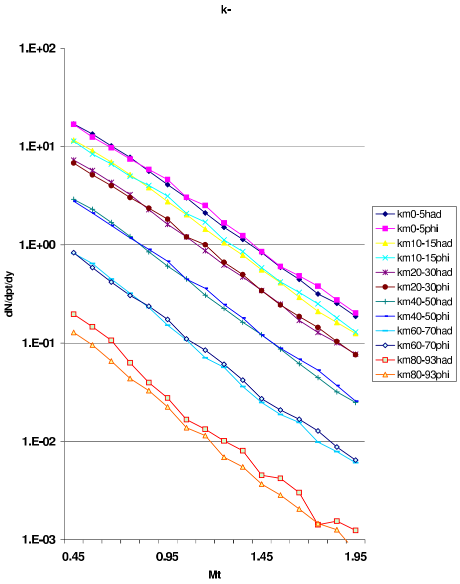

Figure 5.3: Comparison of the yields for K^- as a function of centrality and transverse momentum, as determined by this analysis and the Hadron PWG. Odd bins in centrality. Points labeled as “had” come from the Hadron PWG. Points labeled “phi” is from this analysis.

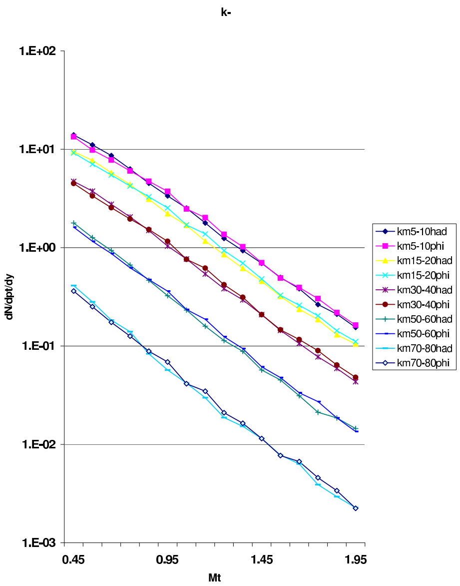

Figure 5.4: Same as Fig. 5.3 for even bins in centralality.

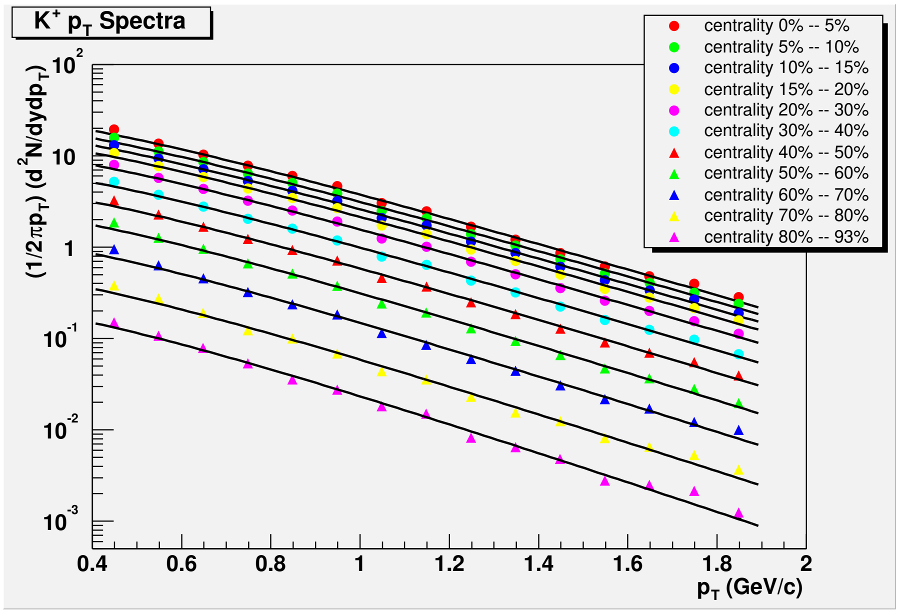

Figure 5.5: K^+ transverse mass spectra measured in the current analysis

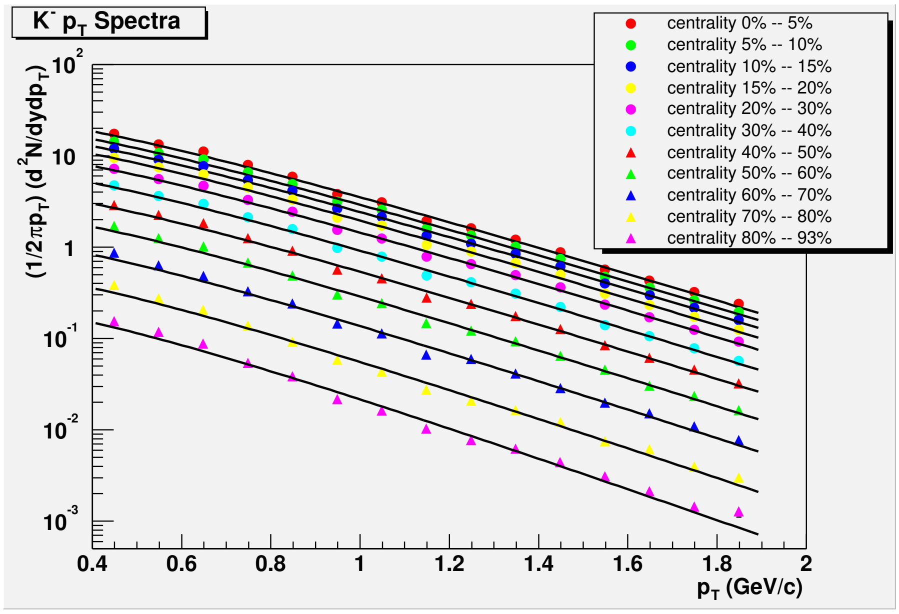

Figure 5.6: K^- transverse mass spectra measured in the current analysis

Table 5.1: Comparison Monte Carlo Correction Factors for Single K^+

p_T (GeV/C)	K^+ CF phi	K^+ CF Hadron PWG	Ratio (Hadron PWG/phi CF)
0.45	230 ± 19	461 ± 10	2.01 ± 0.17
0.55	145 ± 10	304 ± 6	2.09 ± 0.15
0.65	114 ± 7	234 ± 4	2.05 ± 0.14
0.75	97 ± 6	199 ± 3	2.04 ± 0.13
0.85	91 ± 6	183 ± 3	2.01 ± 0.13
0.95	88 ± 4	163 ± 3	1.86 ± 0.12
1.05	73 ± 4	156 ± 3	2.13 ± 0.13
1.15	76 ± 4	143 ± 3	1.87 ± 0.11
1.25	67 ± 4	131 ± 2	1.96 ± 0.12
1.35	65 ± 4	123 ± 2	1.88 ± 0.11
1.45	60 ± 3	122 ± 2	2.05 ± 0.11
1.55	56 ± 3	116 ± 2	2.08 ± 0.12
1.65	58 ± 3	112 ± 2	1.94 ± 0.11
1.75	59 ± 3	111 ± 2	1.89 ± 0.11
1.85	55 ± 3	105 ± 2	2.12 ± 0.11

As one can see there are agreement in all bins of centrality except the most peripheral bin. The inverse slopes found by this analysis are about 10-40 MeV larger. These differences are probably to be expected because we believe our looser cuts will allow in more background. This is being studied by using tighter cuts.

The agreement of our kaons spectra with that of the Hadron PWG gives us confidence that we are doing the following things correctly

a) acceptance of kaons (including pid/tracking etc)

b) single track embedding corrections. We note that the ghost pair and intruder pair rejections are being taken into consideration here.

p_T (GeV/C)	K^- CF		Ratio (Hadron PWG/phi CF)
	phi	Hadron PWG	
0.45	261 ± 21	408 ± 8	1.57 ± 0.13
0.55	170 ± 12	274 ± 5	1.62 ± 0.12
0.65	144 ± 10	210 ± 4	1.46 ± 0.11
0.75	114 ± 7	176 ± 3	1.53 ± 0.10
0.85	101 ± 6	153 ± 3	1.52 ± 0.10
0.95	80 ± 4	139 ± 3	1.81 ± 0.11
1.05	82 ± 5	132 ± 2	1.61 ± 0.10
1.15	65 ± 3	118 ± 2	1.82 ± 0.10
1.25	71 ± 4	113 ± 2	1.59 ± 0.10
1.35	70 ± 4	111 ± 2	1.59 ± 0.09
1.45	68 ± 4	109 ± 2	1.61 ± 0.09
1.55	58 ± 3	104 ± 2	1.79 ± 0.10
1.65	57 ± 3	101 ± 2	1.77 ± 0.10
1.75	55 ± 3	96 ± 2	1.75 ± 0.10
1.85	53 ± 3	95 ± 2	1.79 ± 0.10

Table 5.2: Comparison Monte Carlo Correction Factors for Single K^-

c) run-by-run corrections

d) general run numeric of finding the correct number of triggers etc, and application of the relevant factors (e.g. $1/2\pi$) in the invariant yields.

Centrality	K^+				K^-			
%	dN/dy[a]	dN/dy[b]	T[a]	T[b]	dN/dy[a]	dN/dy[b]	T[a]	T[b]
0–5	46.36	46.58	0.286	0.292	43.43	43.58	0.289	0.300
5–10	37.96	37.67	0.287	0.294	35.87	35.00	0.289	0.302
10–15	32.01	31.62	0.283	0.293	29.55	29.54	0.287	0.300
15–20	26.53	26.49	0.283	0.293	24.40	24.42	0.285	0.297
20–30	19.51	19.05	0.282	0.291	18.09	17.66	0.285	0.296
30–40	12.55	12.19	0.279	0.287	11.69	11.37	0.277	0.291
40–50	7.59	7.42	0.269	0.281	7.00	6.89	0.271	0.285
50–60	4.21	4.06	0.260	0.272	3.91	3.74	0.260	0.278
60–70	2.06	1.97	0.250	0.267	1.90	1.84	0.251	0.270
70–90	0.83	0.79	0.236	0.260	0.81	0.75	0.237	0.261
80–93	0.43	0.28	0.227	0.255	0.41	0.27	0.226	0.251

Table 5.3: Comparison of Inclusive Kaon dN/dy and T Extracted by Two Different PHENIX Analyses

[a] this analysis
[b] Hadron PWG analysis

Chapter 6

Pair Signal Generation

After applying all relevant cuts on the data described in Section 4.8, we end up with the kaon sample. Part of these kaons are identified in the Time-of-Flight detector and the rest are in The PbSc section of the east arm Electromagnetic Calorimeter. These kaons are now can be combined to extract the ϕ invariant mass. Since the sample contains kaons from TOF and kaons from EMCal, with different momentum range, combining all kaons to form invariant pairs are not wise idea. This due to the fact that the combinatoric background would assume different shapes depending on the p_T distribution of the single kaons. Therefore kaon pairs are combined in the following way:

- TOF-TOF Pairs: Both members of the K^+K^- pairs are identified in the Time-of-Flight Detector. We will call them as TOF-TOF Pairs.

- EMC-EMC Pairs: Both members of the K^+K^- pairs are identified in the Electromagnetic Calorimeter. We will call them as EMC-EMC Pairs.

- TOF-EMC Pairs: One of the members of the K^+K^- pairs are identified in the Time-of-Flight Detector and the other in the Electromagnetic Calorimeter. We will call them as TOF-EMC Pairs.

It is worth mentioning here that the signal from TOF-EMC Pairs are predominantly from K^+ in TOF and K^- in EMC. The opposite combination does not give any signal. This due to the PHENIX central magnetic field and the PHENIX detector acceptance. The magnetic field lines are along the beam direction, which is the z-axis. The detectors are x-distance away from the collision vertex forming a $y-z$ plane. So, when the tracks are produced at the vertex, they will experience a $\vec{B}$ field along z. Due to the velocity component along x, the tracks will experience a force $\vec{F} = e\,\vec{v} \times \vec{B}$ which will be in the $e\,\hat{x} \times \hat{z} = -e\,\hat{y}$ direction. So the positive and negative tracks will be bent in opposite direction in y . Therefore if a ϕ (or any other parent particle) decays into a pair of positive and negative daughters, the daughters will drift in the opposite direction in y. The positive component of the pair will be bent towards $-y$ direction, whereas the negative component will be bent in the $+y$ direction. Therefore, when a pair is reconstructed, the positive partner will be in the more $-y$ side compared to its negative partner. In PHENIX east arm, TOF is located between -300 cm and 100 cm, whereas the EMCal is located between 100 cm and 500 cm along the y. Therefore in the case of ϕ when we take one track from TOF and the other from EMCal, for the obvious reason just explained, the K^+ will be from TOF and K^- will be from EMCal.

The K^+ and K^- from the same event are paired together. This gives the actual pair distribution. These lead to a signal riding over a large combinatoric background. The background needs to be subtracted in order to extract signal. The combinatoric background is obtained by using event buffer method. The buffer size is the segment of a run. The kaons are stored into a set of vertex and centrality bins in order to approximate the statistical distribution of the background. The subtraction of the properly normalized background for the actual distribution yields ϕ signal. The outline to extract ϕ signal is as follows.

1. Three types of combinations: TOF-TOF, EMC-EMC and TOF-EMC.
2. K^+ and K^- from same event are paired together. This gives actual pair distribution.
3. For the mixing of the of the background pairs, it is important to mix tracks which are of similar detector geometry and interaction geometry. We take tracks that pass through the similar detector area. Thus we divide events in terms of small bins of the vertex. In order that the tracks have similar collision cross-section, we divide events in bins of centrality. K^+ and K^- in a Run segment are stored into 15 Z-vertex bin of 4 cm, between -30 cm and +30 cm, and 18 centrality bins from 0% in an increment of 5%, the last bin is 85% to 92%.
4. K^+ from one event is mixed with K^- from different event, but within the same centrality and vertex bin. This gives mixed pair distribution.
5. The mixed pair distribution is properly normalized (the normalization will be discussed in Section 6.1).
6. The normalized background is subtracted from the actual pair distribution to get the ϕ signal.

6.1 Normalization of Combinatoric Background

In this section we will develop the mathematical description of the normalization of combinatoric background. The important concept here are the Binomial Distribution, Poisson Distribution and the relation between the expected value $E[X]$ or the mean of and the variance $VAR[X]$ or the mean-squared deviation of a random variable X.

Relation Between $VAR[X]$ and $E[X]$

$$VAR[X] = E\left[(X - E[X])^2\right]$$

$$
\begin{aligned}
&= E\left[X^2 \;-\; 2E[X]X \;+\; E[X]^2\right] \\
&= E[X^2] \;-\; 2E[X]E[X] \;+\; E[X]^2 \\
&= E[X^2] \;-\; 2E[X]^2
\end{aligned} \tag{6.1}
$$

Therefore,

$$E[X^2] \;=\; VAR[X] \;+\; E[X]^2 \tag{6.2}$$

Binomial Distribution

Let us consider N uncorrelated tracks in a sample. The ϵ be the probability of measuring n tracks out of the sample. This is same as the n number of successes in N independent Bernoulli trials[1]. The probabilities of n is given by the Binomial Distribution

$$B(n) \;=\; \frac{N!}{n!\;(N-n)!}\;\epsilon^n\;(1-\epsilon)^{N-n} \tag{6.3}$$

The expected value and the variance of a binomial distribution is given by

$$E[X] \;=\; \epsilon N \tag{6.4}$$

$$VAR[X] \;=\; \epsilon N(1-\epsilon) \tag{6.5}$$

Since the expected value is the mean of the measurement, we can write

$$\overline{n} \;=\; \epsilon N \tag{6.6}$$

Using Eqs. (6.2),(6.4) and (6.5) we can write

$$\overline{n^2} \;=\; E[X^2] \;=\; \epsilon N(1-\epsilon) \;+\; \epsilon^2 N^2 \tag{6.7}$$

[1]A Bernoulli trial involves performing an experiment once and noting whether a particular event A occurs. The outcome of the Bernoulli trial is said to be a *success* if A occurs and a *failure* otherwise.

Poisson Distribution

A Poisson random variable arises in situations where the events occur completely at random in time or space. In a heavy ion collision the number N of tracks produced per event are assumed as a Poissonian distribution. The distribution is given by

$$P(N) \;=\; \frac{N^n}{n!}\, e^{-N} \tag{6.8}$$

The expected value and the variance of a Poisson distribution is given by

$$E[X] \;=\; N \tag{6.9}$$

$$VAR[X] \;=\; N \tag{6.10}$$

Since the expected value is the mean of the measurement, we can write

$$< N > \;=\; N \tag{6.11}$$

Using Eqs. (6.2),(6.9) and (6.10) we can write

$$< N^2 > \;=\; E[X^2] \;=\; < N >^2 \;+\; < N > \tag{6.12}$$

Now let us concentrate on deriving the normalization factor using the Poisson and Binomial relations. The number N of tracks have a Poisson distribution. There are n positive tracks and $(N-n)$ negative tracks. The positive and negative tracks follow the binomial distribution. So, there will be $n(n-1)/2$ positive pairs, $(N-n)(N-n-1)/2$ negative pairs and $n(N-n)$ unlike sign pairs. So in a single event, the number of ++ pairs will be given by

$$\begin{aligned} n_{++} &= \sum_n \frac{n(n-1)}{2} B(n) \\ &= \frac{1}{2} \sum_n n^2 B(n) - \sum_n n B(n) \\ &= \frac{1}{2} \left(\overline{n^2} \;-\; \overline{n}\right) \\ &= \frac{1}{2}\, \epsilon^2 N(N-1) \end{aligned} \tag{6.13}$$

The number of $--$ pairs will be given by

$$
\begin{aligned}
n_{--} &= \sum_n \frac{(N-n)(N-n-1)}{2} B(n) \\
&= \frac{1}{2}\left[N^2 \sum_n B(n) - 2N \sum_n nB(n) + \sum_n n^2 B(n) - N \sum_n B(n) + \sum_n nB(n)\right] \\
&= \frac{1}{2}\left[N^2 - 2N\overline{n} + \overline{n^2} - N + \overline{n}\right] \\
&= \frac{1}{2}(1-\epsilon)^2 N(N-1)
\end{aligned}
$$

The number of $+-$ pairs will be given by

$$
\begin{aligned}
n_{+-} &= \sum_n n(N-n)B(n) \\
&= \sum_n nB(n) - \sum_n n^2 B(n) \\
&= (N\overline{n} \; - \; \overline{n^2}) \\
&= \epsilon(1-\epsilon)N(N-1) \qquad (6.14)
\end{aligned}
$$

So at the end of the day when we accumulate all events, the we can find the mean of $< n_{++,--,+-} >$ averaged over all events weighted by the probability distribution of n which we assume a Poissonian. Therefore, from Eqs. (6.12),(6.13),(6.14) and (6.14) we find

$$
\begin{aligned}
< n_{++} > &= \frac{1}{2}\epsilon^2 \left[\sum_N N^2 P(N) - \sum_N NP(N)\right] \\
&= \frac{1}{2}\epsilon^2 \left[< N^2 > - < N >\right] \\
&= \frac{1}{2}\epsilon^2 < N >^2 \qquad (6.15)
\end{aligned}
$$

$$
\begin{aligned}
< n_{--} > &= \frac{1}{2}(1-\epsilon)^2 \left[\sum_N N^2 P(N) - \sum_N NP(N)\right] \\
&= \frac{1}{2}(1-\epsilon)^2 \left[< N^2 > - < N >\right] \\
&= \frac{1}{2}(1-\epsilon)^2 < N >^2 \qquad (6.16)
\end{aligned}
$$

$$
\begin{aligned}
< n_{+-} > &= \epsilon(1-\epsilon)\left[\sum_N N^2 P(N) - \sum_N N P(N)\right] \\
&= \epsilon(1-\epsilon)\left[< N^2 > - < N >\right] \\
&= \epsilon(1-\epsilon) < N >^2
\end{aligned}
\tag{6.17}
$$

From Eqs. (6.15),(6.16) and (6.17) we find

$$
< n_{+-} > \; = \; 2\sqrt{< n_{++} > \; . \; < n_{--} >} \tag{6.18}
$$

Eq. (6.18) states that the mean number of unlike sign pairs per event are related to the number of like sign pairs. So if we make a measurement over N_{evt} events, the total number of $++$ pairs ($N_{++} = N_{evt}. < n_{++} >$), $--$ pairs ($N_{--} = N_{evt}. < n_{--} >$) and the $+-$ pairs ($N_{+-} = N_{evt}. < n_{+-} >$) are identically related:

$$
N_{+-} \; = \; 2\sqrt{N_{++} \; . \; N_{--}} \tag{6.19}
$$

So we will be counting the number of like sign and unlike sign pairs while making actual pair distribution and normalize the mixed pair distribution as Eq. (6.19).

6.2 Cross Check of the Normalization Factor

When the kaon pairs are constructed, the same event like-sign and unlike-sign pairs as well as the mixed event like-sign and unlike-sign pairs are constructed. The experimental determination of the ++ and – pairs are very straightforward. The first step is to get the data sample and constitute the +- pairs. Then out of the +'s and -'s that constitute the +- pairs, find all possible combinations for ++ and –. This is true for both the same event pairs and mixed event pairs. Since we make three types of combinations, TOF-TOF, EMC-EMC and TOF-EMC, lets elaborate the idea of constructing ++ and – pairs in a little details.

TOF-TOF

Let T_+ and T_- be the number of positive and negative kaons in the sample from TOF. All T_+'s are combined with all T_-'s for unlike sign pairs generation. Therefore

- +- pairs are all possible combinations of T_+T_-
- ++ pairs are all possible combinations of T_+T_+
- – pairs are all possible combinations of T_-T_-

EMC-EMC

Let E_+ and E_- be the number of positive and negative kaons in the sample from EMC. All E_+'s are combined with all E_-'s for unlike sign pairs generation. Therefore

- +- pairs are all possible combinations of E_+E_-
- ++ pairs are all possible combinations of E_+E_+
- – pairs are all possible combinations of E_-E_-

TOF-EMC

For this combination we impose a condition that a K^+ in TOF be combined with a K^- in EMC or a K^- in TOF be combined with a K^+ in EMC. The total number of positive charges in the sample is T_+ and the total number of the negative charges is E_-. Therefore

- +- pairs are all possible combinations of T_+E_-
- ++ pairs are all possible combinations of T_+T_+
- – pairs are all possible combinations of E_-E_-

One of the cross check of the goodness of the normalization is looking at the ratio of the real like-sign pairs to the predicted like sign pairs. If $N_{+-}^{\rm same}$ is the number of same event unlike-sign pairs, $N_{++}^{\rm same}$ is the number of same event $++$ pairs, $N_{--}^{\rm same}$ is the number of same event $--$ pairs and $N_{+-}^{\rm mixed}$, $N_{++}^{\rm mixed}$, $N_{--}^{\rm mixed}$ are their mixed event counterparts, then the predicted mixed pair $+-$ pairs are scaled to the normalization factor Eq.(6.19):

$$N \;=\; 2\,\sqrt{N_{++}^{\rm same}\,.\,N_{--}^{\rm same}} \tag{6.20}$$

In other words,

$$N_{+-}^{\rm mixed} \;\longrightarrow\; 2\,\sqrt{N_{++}^{\rm same}\,.\,N_{--}^{\rm same}} \tag{6.21}$$

Therefore the predicted mixed event $++$ and $--$ pairs are given by

$$N_{++}^{\rm pred} \;=\; \frac{N_{++}^{\rm mixed}}{N_{+-}^{\rm mixed}}\,.\,N \;=\; \frac{N_{++}^{\rm mixed}}{N_{+-}^{\rm mixed}}\,.\,2\,\sqrt{N_{++}^{\rm same}\,.\,N_{--}^{\rm same}} \tag{6.22}$$

$$N_{--}^{\rm pred} \;=\; \frac{N_{--}^{\rm mixed}}{N_{+-}^{\rm mixed}}\,.\,2\,\sqrt{N_{++}^{\rm same}\,.\,N_{--}^{\rm same}} \tag{6.23}$$

We look at the ratio following three ratios for different centralities:

$$R_{++} \;=\; \frac{N_{++}^{\rm same}}{N_{++}^{\rm pred}} \tag{6.24}$$

$$R_{--} \;=\; \frac{N_{--}^{\rm same}}{N_{--}^{\rm pred}} \tag{6.25}$$

$$R \;=\; \sqrt{\frac{N_{++}^{\rm same}\;N_{--}^{\rm same}}{N_{++}^{\rm pred}\;N_{--}^{\rm pred}}} \tag{6.26}$$

It will be shown that the normalization has a precision of ~ 0.005 (Tables 6.1 through 6.3)

6.2.1 TOF-TOF

The integral predicted and measured like sign spectra for the TOF-TOF combination is given in Table 6.1.

Table 6.1: The integral predicted and measured like and unlike sign spectra for the TOF-TOF

cent	N^{same}_{+-}	N^{same}_{++}	N^{same}_{--}	N^{mix}_{+-}	N^{mix}_{++}	N^{mix}_{--}	$\frac{N^{\text{same}}_{+-}}{N^{\text{mix}}_{+-}}$	$\frac{N^{\text{same}}_{++}}{N^{\text{mix}}_{++}}$	$\frac{N^{\text{same}}_{--}}{N^{\text{mix}}_{--}}$	R
0 - 10	130310	73362	56968	129295.0	73304.4	57472.6	1.0079	1.0008	0.9912	0.9920
10 - 20	70311	39483	30642	69565.5	39465.6	30819.6	1.0107	1.0004	0.9942	0.9947
20 - 30	33193	18685	14403	32809.8	18779.8	14499.6	1.0117	0.9950	0.9933	0.9883
30 - 40	14817	8123	6238	14236.8	8122.1	6284.9	1.0408	1.0001	0.9925	0.9927
40 - 50	5513	2979	2306	5242.0	3002.6	2317.3	1.0517	0.9921	0.9951	0.9873
50 - 60	1743	880	715	1586.4	919.5	691.0	1.0987	0.9570	1.0348	0.9903
60 - 70	437	207	193	399.8	229.8	177.2	1.0932	0.9007	1.0893	0.9811
70 - 80	103	33	37	69.9	42.4	33.7	1.4738	0.7779	1.0994	0.8553
80 - 90	36	8	5	12.6	7.5	5.7	2.8	1.0722	0.8753	0.9385
mb	256463	143760	111507	253221	143868	112307	1.0128	0.9992	0.9929	0.9921
0 - 10	130310	73362	56968	129295	73304.4	57472.6	1.0079	1.0008	0.9912	0.9920
10 - 40	118321	66291	51283	116612	66364.6	51605.2	1.0147	0.9989	0.9938	0.9927
40 - 92	7832	4107	3256	7313.7	4202.71	3225.8	1.0709	0.9772	1.0094	0.9864

The minimum bias like sign invariant mass spectra and the ratio of actual pairs and predicted pairs are shown in Fig (6.1) through Fig (6.4). In Fig (6.1) and Fig (6.3), the same event like-sign pairs are represented in the red points. They are superimposed on the predicted mixed event like-sign pairs in yellow. Fig (6.2) and Fig (6.4) shows the ratio of like-sign invariant mass spectra and the predicted background pairs. As expected the ratio is very close to one.

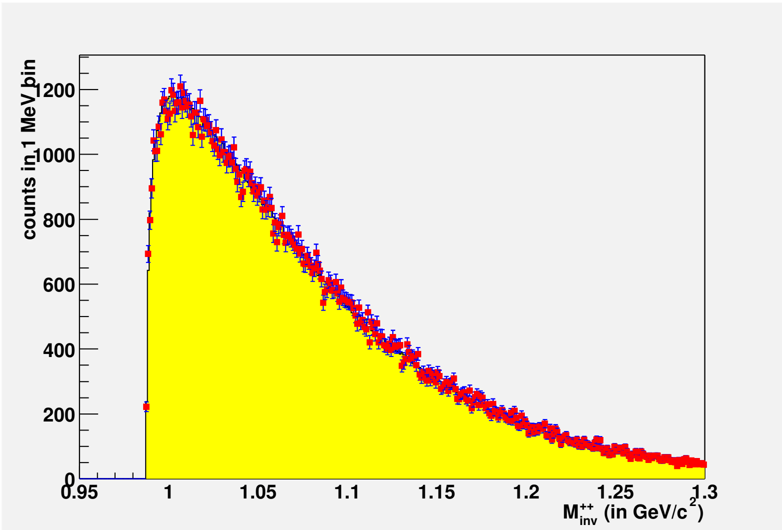

Figure 6.1: Measured and predicted ++ sign spectra in TOF-TOF for minimum bias events

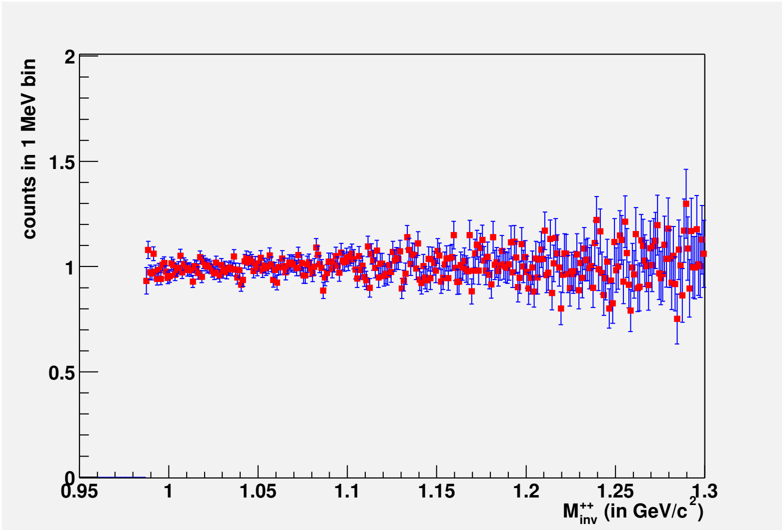

Figure 6.2: Ratio of measured and predicted ++ sign spectra in TOF-TOF for minimum bias events

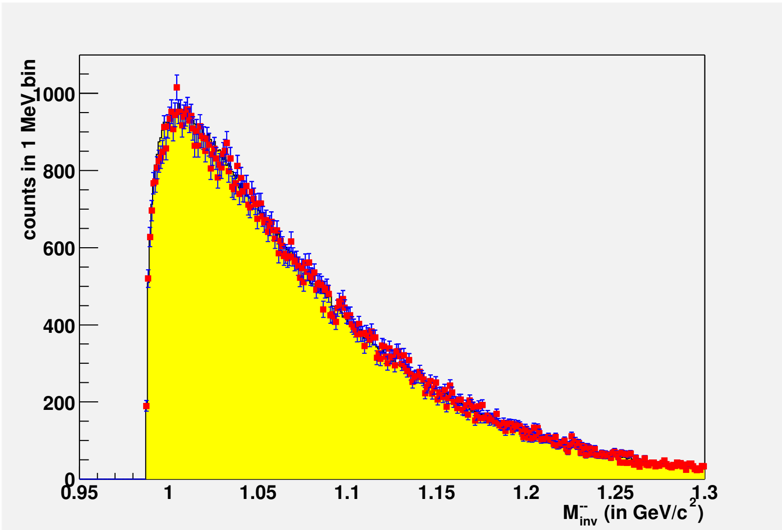

Figure 6.3: Measured and predicted – sign spectra in TOF-TOF for minimum bias events

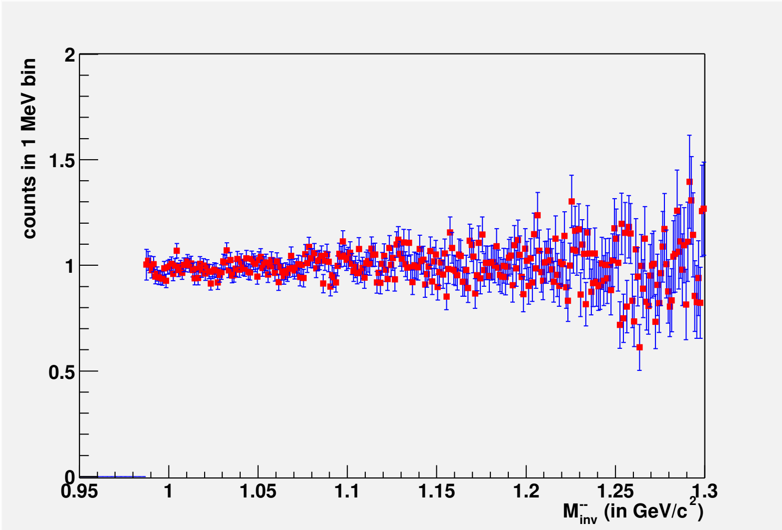

Figure 6.4: Ratio of measured and predicted – sign spectra in TOF-TOF for minimum bias events

6.2.2 EMC-EMC

The integral predicted and measured like sign spectra for the EMC-EMC combination is given in Table 6.2.

The minimum bias like and unlike sign invariant mass spectra and the ratio of actual pairs and predicted pairs are shown in Fig (6.5) through Fig (6.8). In Fig (6.5) and Fig (6.7), the same event like-sign pairs are represented in the red points. They

Table 6.2: The integral predicted and measured like and unlike sign spectra for the EMC-EMC

cent	N_{+-}^{same}	N_{++}^{same}	N_{--}^{same}	N_{+-}^{mix}	N_{++}^{mix}	N_{--}^{mix}	$\frac{N_{+-}^{\text{same}}}{N_{+-}^{\text{mix}}}$	$\frac{N_{++}^{\text{same}}}{N_{++}^{\text{mix}}}$	$\frac{N_{--}^{\text{same}}}{N_{--}^{\text{mix}}}$	R
0 - 10	111963	43802	70477	111122	43961.7	70296	1.0076	0.9964	1.0026	0.9989
10 - 20	61041	23633	38825	60582.2	23783.5	38649.9	1.0076	0.9937	1.0045	0.9982
20 - 30	30201	11492	18787	29387.1	11593.8	18697.8	1.0277	0.9912	1.0048	0.9959
30 - 40	13370	4963	8467	12964.8	5024.7	8320.5	1.0313	0.9877	1.0176	1.0051
40 - 50	5374	2014	3353	5197.3	2025.8	3358.5	1.0340	0.9942	0.9984	0.9926
50 - 60	1734	603	1088	1620.0	638.7	1028.2	1.0704	0.9441	1.0582	0.9990
60 - 70	475	191	275	458.4	179.5	299.9	1.0363	1.0643	0.9169	0.9758
70 - 80	101	33	52	82.8	33.2	53.0	1.2191	0.9946	0.9812	0.9759
80 - 90	37	10	19	27.6	9.5	18.4	1.3421	1.0577	1.0338	1.0935
mb	224296	86741	141343	221452	87258.8	140719	1.0128	0.9941	1.0044	0.9985
0 - 10	111963	43802	70477	111122	43961.7	70296	1.0076	0.9964	1.0026	0.9989
10 - 40	104612	40088	66079	102936	40402.2	65670.1	1.0163	0.9922	1.0062	0.9984

are superimposed on the predicted mixed event like-sign pairs in yellow. Fig (6.6) and Fig (6.8) shows the ratio of like-sign invariant mass spectra and the predicted background pairs. As expected the ratio is very close to one.

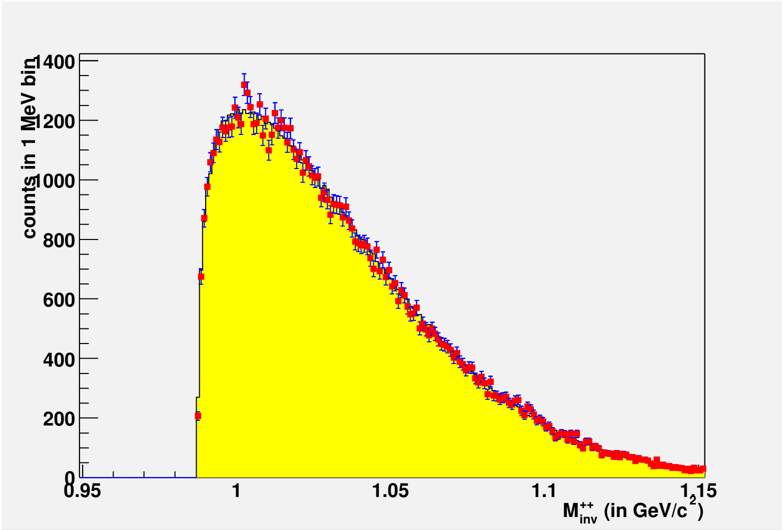

Figure 6.5: Measured and predicted ++ sign spectra in EMC-EMC for minimum bias events

6.2.3 TOF-EMC

The integral predicted and measured like sign spectra for the TOF-EMC combination is given in Table 6.3.

The minimum bias like and unlike sign invariant mass spectra and the ratio of actual pairs and predicted pairs are shown in Fig (6.9) through Fig (6.12). In Fig (6.9) and Fig (6.11), the same event like-sign pairs are represented in the red points. They are superimposed on the predicted mixed event like-sign pairs in yellow. Fig (6.10) and Fig (6.12) shows the ratio of like-sign invariant mass spectra and the predicted background pairs. As expected the ratio is very close to one.

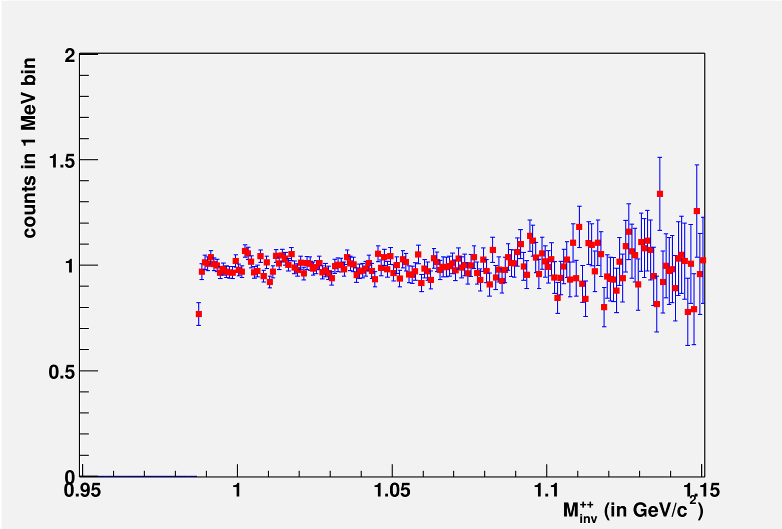

Figure 6.6: Ratio of measured and predicted ++ sign spectra in EMC-EMC for minimum bias events

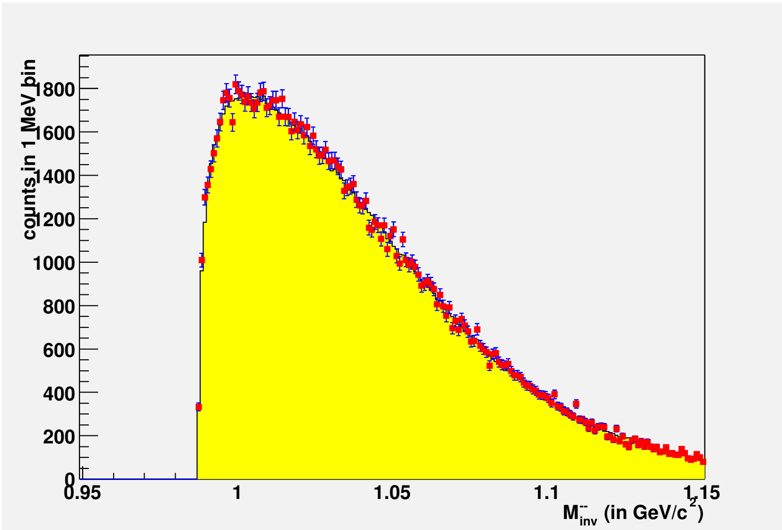

Figure 6.7: Measured and predicted – sign spectra in EMC-EMC for minimum bias events

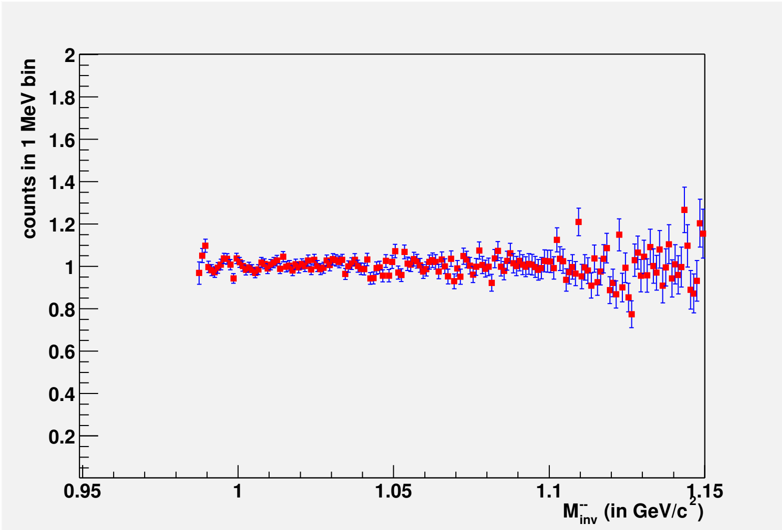

Figure 6.8: Ratio of measured and predicted – sign spectra in EMC-EMC for minimum bias events

Table 6.3: The integral predicted and measured like and unlike sign spectra for the TOF-EMC

cent	N_{+-}^{same}	N_{++}^{same}	N_{--}^{same}	N_{+-}^{mix}	N_{++}^{mix}	N_{--}^{mix}	$\frac{N_{+-}^{\text{same}}}{N_{+-}^{\text{mix}}}$	$\frac{N_{++}^{\text{same}}}{N_{++}^{\text{mix}}}$	$\frac{N_{--}^{\text{same}}}{N_{--}^{\text{mix}}}$	R
0 - 10	245241	117000	127291	244074	117585	128065	1.0048	0.9950	0.9940	0.9890
10 - 20	132590	63024	69386	132257	63481.5	69665.1	1.0025	0.9928	0.9960	0.9888
20 - 30	64365	30127	33128	63183.8	30283.7	33159.9	1.0187	0.9948	0.9990	0.9939
30 - 40	27842	13059	14693	27703.9	13124.5	14679.7	1.0050	0.9950	1.0009	0.9959
40 - 50	10854	4981	5651	10610.9	5048.2	5697.8	1.0229	0.9867	0.9918	0.9786
50 - 60	3483	1481	1800	3265.5	1556.1	1731.8	1.0666	0.9518	1.0394	0.9892
60 - 70	947	398	468	863.2	398.3	464.4	1.0971	0.9991	1.0077	1.0068
70 - 80	213	66	89	153.3	71.4	83.3	1.3896	0.9241	1.0681	0.9870
80 - 90	63	18	24	41.6	18.7	24.5	1.5155	0.9625	0.9796	0.9428
mb	485598	230154	252530	482165	231585	253565	1.0071	0.9938	0.9959	0.9898
0 - 10	245241	117000	127291	244074	117585	128065	1.0048	0.9950	0.9940	0.9890
10 - 40	224797	106210	117207	223146	106893	117505	1.0074	0.9936	0.9975	0.9911
40 - 92	15560	6944	8032	14936.4	7095.2	8002.0	1.0418	0.9787	1.0038	0.9824

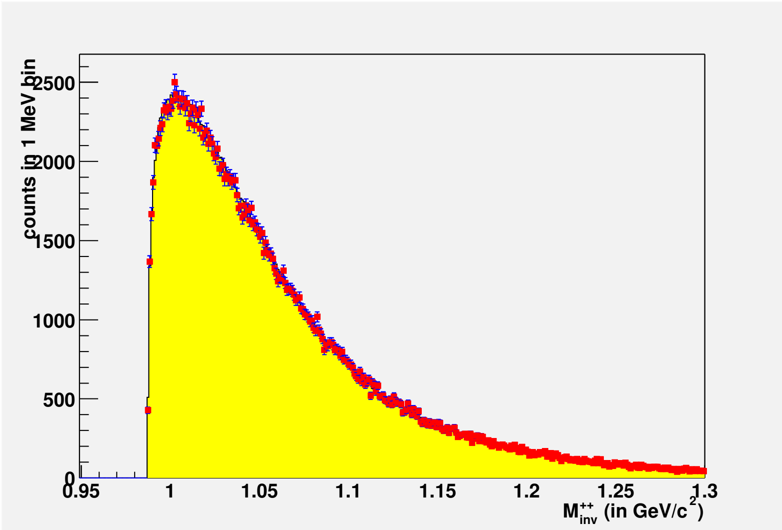

Figure 6.9: Measured and predicted ++ sign spectra in TOF-EMC for minimum bias events

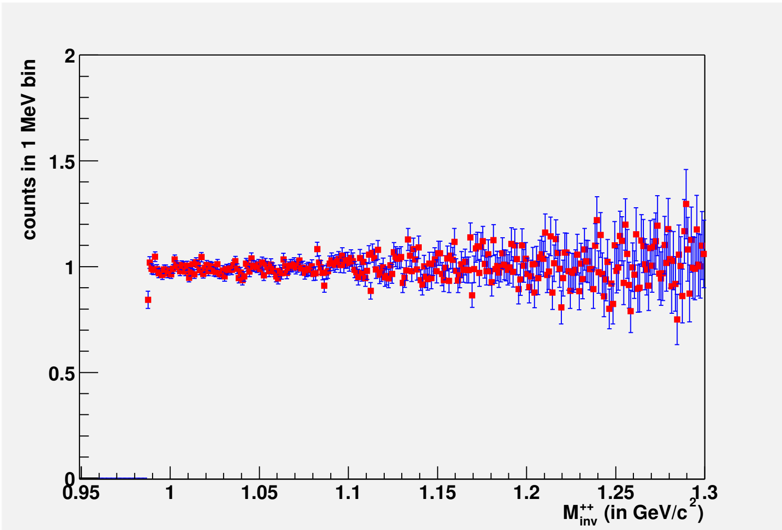

Figure 6.10: Ratio of measured and predicted ++ sign spectra in TOF-EMC for minimum bias events

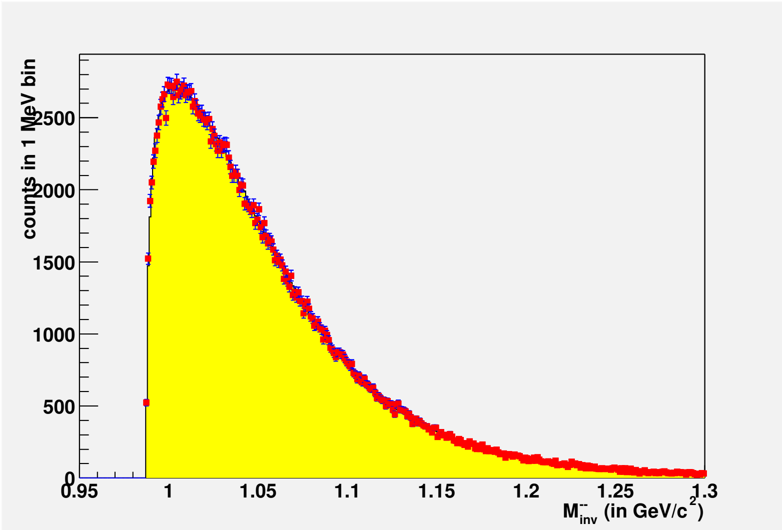

Figure 6.11: Measured and predicted – sign spectra in TOF-EMC for minimum bias events

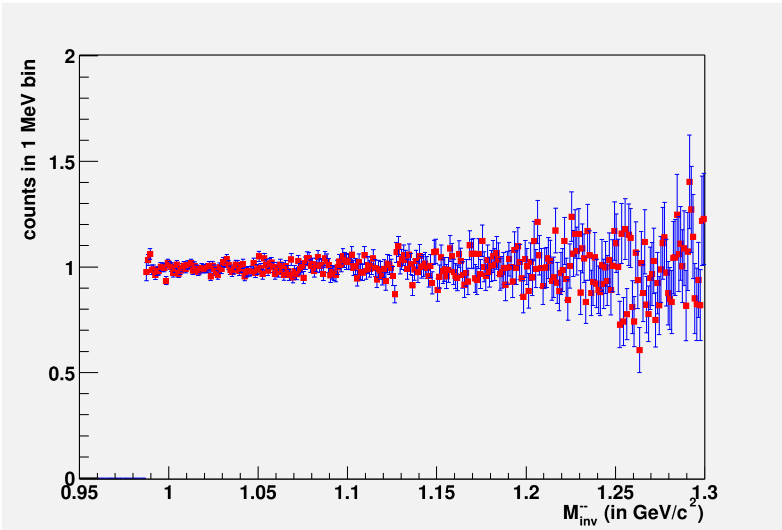

Figure 6.12: Ratio of measured and predicted – sign spectra in TOF-EMC for minimum bias events

6.3 Fitting of the ϕ Peak

The ϕ invariant mass spectra are extracted after subtracting the normalized mixed event unlike sign pairs invariant mass distribution from the same event unlike sign pairs invariant mass distribution. The spectra need to be fitted with a function that describes the width and the mass centroid of the reconstructed ϕ. The appropriate function for fitting the ϕ spectra is a relativistic Breit-Wigner function. But since the invariant mass distribution incorporates the detector mass resolution in it, the detector mass resolution needs to be taken out from the relativistic Breit-Wigner function in order to get the actual mass and width of ϕ. Thus we use a relativistic Breit-Wigner function convoluted with a Gaussian, with the Gaussian of width of the detector mass resolution. PHENIX has excellent momentum resolution, which translates to an equally excellent mass resolution. We can make 1-MeV bins for the invariant mass distribution and subtract the normalized background from the real pair distribution bin by bin to extract the ϕ spectra and fit with a relativistic Breit-Wigner convoluted with a Gaussian to extract the width and mass of ϕ.

6.3.1 Relativistic Breit-Wigner Function

$$RBW = \frac{A}{\pi} \frac{m\,(m_0\Gamma_m)^2}{(m^2 - m_0^2)^2 + (m_0\Gamma_m)^2} \tag{6.27}$$

$$\Gamma_m = \Gamma \sqrt{\frac{m^2/4 - m_K^2}{m_0^2/4 - m_K^2}}\, 2 \frac{m^2/4 - m_K^2}{(m^2 + m_0^2)/4 - m_K^2} \tag{6.28}$$

Convolution of a Relativistic Breit-Wigner Function with a Gaussian Function

For the relativistic Breit-Wigner function we use Eq. (6.27). For the Gaussian Function we use the following expression:

$$f(m) = \frac{1}{\sqrt{2\pi}\sigma} \exp\left[-\frac{1}{2}\left(\frac{m - m_0}{\sigma}\right)^2\right] \tag{6.29}$$

where σ is the detector mass resolution. The simple relation between direct integration and integration by summation can be written as:

$$\int_a^b f(x)dx \approx \lim_{n\to\infty} \sum_{i=1}^{n} f(c_i)\Delta x_i \tag{6.30}$$

where

$$\begin{aligned}\Delta x_i &= \frac{b-a}{n}\\ c_i &= a + \frac{b-a}{n} i, \quad i = 1, 2, ..., n\end{aligned}$$

Therefore for a relativistic Breit-Wigner function $R(m, m_0, \Gamma)$, of resonance m_0 and the full-width at half maxima Γ and a Gaussian function $G(m, m_0, \sigma)$, of mean m_0 and the RMS σ, the convolution integration is given by

$$\begin{aligned}R * G &= \int_a^b R(\tau, m_0, \Gamma)\ G(m-\tau, m_0, \sigma)\ d\tau\\ &= \int_a^b R(m-\tau, m_0, \Gamma)\ G(\tau, m_0, \sigma)\ d\tau \end{aligned}\tag{6.31}$$

which can be approximated as:

$$\begin{aligned}\int_a^b R(m-\tau, m_0, \Gamma)\ G(\tau, m_0, \sigma) dx &\approx \lim_{n\to\infty} \sum_{i=1}^{n} R(m-c_i, m_0, \Gamma)\ G(c_i, m_0, \sigma)\Delta\tau_i\\ \Delta\tau_i &= \frac{b-a}{n}\\ c_i &= a + \frac{b-a}{n} i, \quad i = 1, 2, ..., n\end{aligned}$$

The summation is performed using trapezoidal method.

6.3.2 Detector Mass Resolution

Phenix has excellent mass resolution. The mass resolution is the direct consequence of the excellent detector momentum resolution. The momentum resolution is given by

$$\left(\frac{\delta p}{p}\right)^2 = \left(\frac{\sigma_\alpha}{K_1}\right)^2 + \left(\frac{\sigma_{ms}}{K_1\beta}\right)^2 \tag{6.32}$$

Type	σ_α (mrad)	σ_{ms} (mrad GeV)	σ_{tof} (ps)
Positives	0.83 ± 0.09	0.92 ± 0.03	120 ± 2
Negatives	0.89 ± 0.07	0.75 ± 0.02	119 ± 2

Table 6.4: Momentum resolution parameters for Au+Au data (Run 2).

where σ_α is the Drift Chamber angular resolution and σ_{ms} is resolution if multiple scattering. The resolution parameter can be obtained from the width of the mass squared distribution of identified particles. The momentum dependence of the mass squared distribution is described in Section 4.5. From the fit the parameters can be derived. They are given by [46] The momentum resolution for pions, kaons and protons can be simulated using the experimental parameters from Table 6.4. The momentum resolution is shown in Fig. 6.13

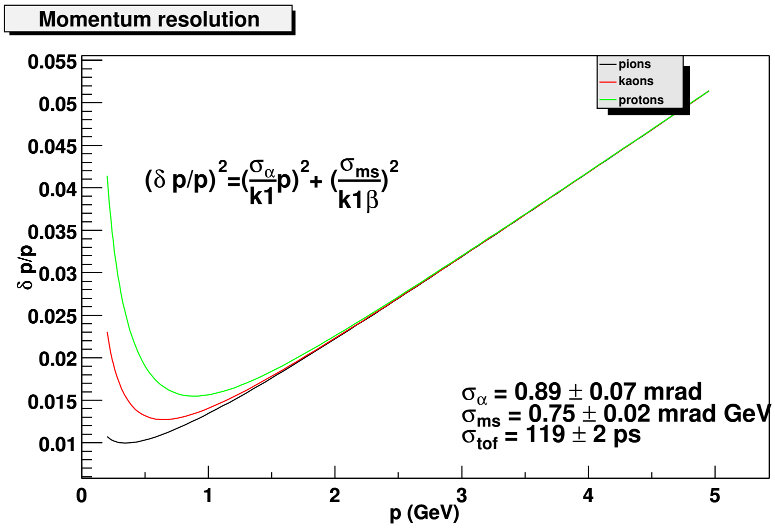

Figure 6.13: PHENIX momentum resolution for Year-2

The momentum resolution can be translated into the pair mass resolution for the K^+K^- pairs in the PHENIX central arm. The procedure is following [47]:

- We generate single ϕ meson events and throw into the complete PHENIX east arm acceptance.

- The ϕ's are decayed into K^+K^- pairs. The momenta of the daughters are randomized as per the momentum distribution of the real kaons.

- The detector momentum resolutions are taken from Table 6.4. They are randomized within their uncertainty.

- Pairs are reconstructed with the altered kaon momenta

- The mass resolution can be obtained from the distribution of the difference of the mass of the generated ϕ and the reconstructed.

Therefore, the momentum of the decay kaons is smeared. The mass of the reconstructed ϕ is computed as

$$M_2 = (E_1 + E_2)^2 - p_1^2 - p_2^2 - 2p_1p_2\cos\theta_{12} \tag{6.33}$$

where $E_{1,2}$ are the energy of the daughters, $p_{1,2}$ are their momenta and θ_{12} is the opening angle. We also study the effect of the uncertainty in the opening angle on the mass resolution. The pair opening angle error is taken from the simulation of single kaon momentum direction error. The simulation result is shown in Fig. 6.14. We plot the difference of the reconstructed mass and the mass of the generated ϕ. We look at some extreme cases. The top left of the plot is for no error in the opening angle. It results in a 1.20 MeV/c^2 mass resolution. An introduction of a 0.15 degree opening angle error adds 70 KeV to the resolution (top right). We also look at the resolution as a function of the pair transverse momentum. For low p_T pairs, the resolution is 1.14 MeV/c^2 as seen on the bottom left plot, whereas for the high p_T pairs the resolution is 1.40 MeV/c^2. So we can say that the overall detector pair mass resolution for the K^+K^- pairs are about 1.25 MeV/c^2. This detector mass resolution will be used in the convolution of the relativistic Breit-Wigner to extract the ϕ mass and width.

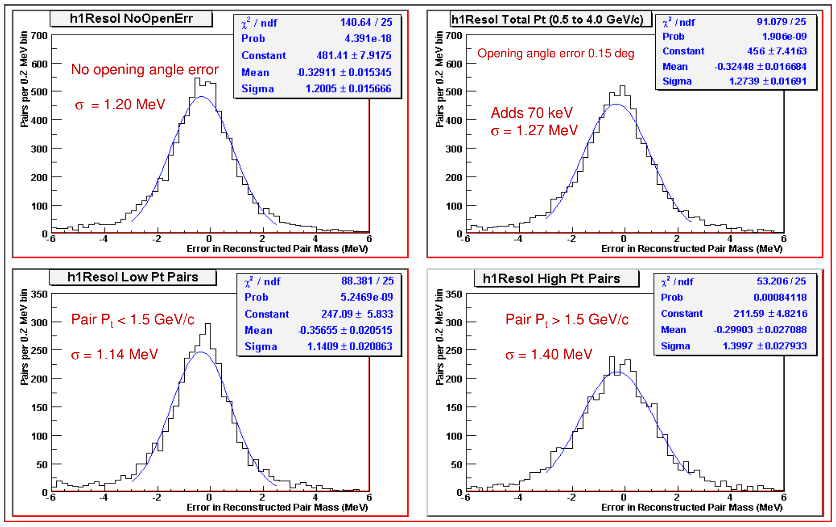

Figure 6.14: K^+K^- Pair Mass Resolution

6.4 ϕ Invariant Mass Distribution

We will show the ϕ same event and normalized mixed event pairs invariant mass distributions. The background subtracted ϕ peak will be fitted with a relativistic Breit-Wigner convoluted with a Gaussian of width of 1.25 MeV to take out the detector mass resolution effect. The ϕ mass centroid, full-width at half maxima $|Gamma$ and the number of ϕ signal and background within a mass window of $1.014\ GeV/c^2 < M_{inv} < 1.024\ GeV/c^2$ will be tabulated for the three combinations of pair mixing. We will divide our data into three centralities, most peripheral $0\% - 10\%$, mid-central $10\% - 40\%$, and peripheral $40\% - 92\%$. The spectra will be shown in for these centralities and for the minimum bias distribution.

6.4.1 TOF-TOF

The ϕ invariant mass distribution for the TOF-TOF pairs are shown Fig (6.15) through Fig (6.22). In Figs (6.15), (6.17), (6.19) and (6.21) the same event unlike-sign pair invariant mass are represented in the red points. They are superimposed on the predicted mixed event unlike-sign pairs invariant mass in yellow. Fig (6.16), (6.18), (6.20) and (6.22) shows the background subtracted invariant mass plots. Very distinct ϕ peaks are observed. They are fitted with a relativistic Breit-Wigner convoluted with a Gaussian. The ϕ signal, mass and width is tabulated in Table 6.5.

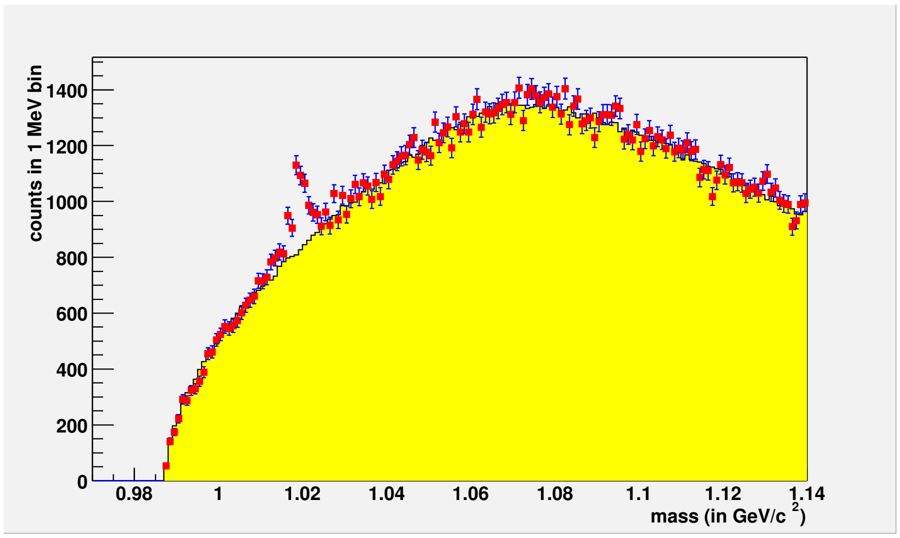

Figure 6.15: Unlike sign signal and combinatoric mass spectra in TOF-TOF for minimum bias events

Centrality	ϕ Signal	Bkg	S/B	Mass (GeV/c^2)	Γ (MeV/c^2)
Min Bias	1410 $\pm$ 131	8264	1/5.9	1.01926 $\pm$ 0.00017	2.54856 $\pm$ 0.574336
0% – 10%	398 $\pm$ 88	4191	1/10.5	1.01949 $\pm$ 0.00027	0.69829 $\pm$ 0.9 2962
10% – 40%	839 $\pm$ 89	3802	1/4.5	1.01915 $\pm$ 0.00025	3.41784 $\pm$ 0.744719
40% – 92%	205 $\pm$ 26	239	1/1.2	1.01881 $\pm$ 0.00031	3.68493 $\pm$ 1.01659

Table 6.5: ϕ Signal, background, Mass centroid and the full-width at half maxima for TOF-TOF Pairs The Signal and backgrounds are counted in the mass window of $1.014\ GeV/c^2 < M_{inv} < 1.024\ GeV/c^2$.

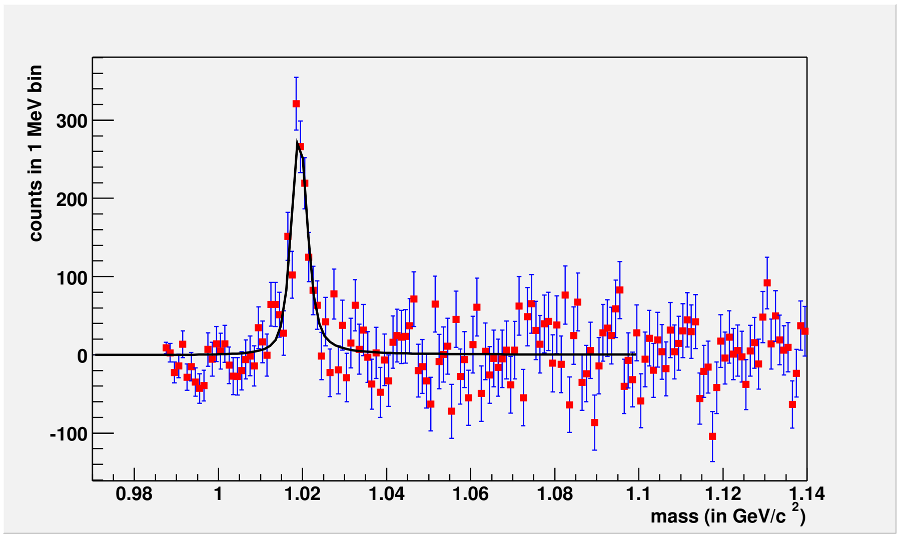

Figure 6.16: Invariant mass spectra in TOF-TOF for minimum bias events

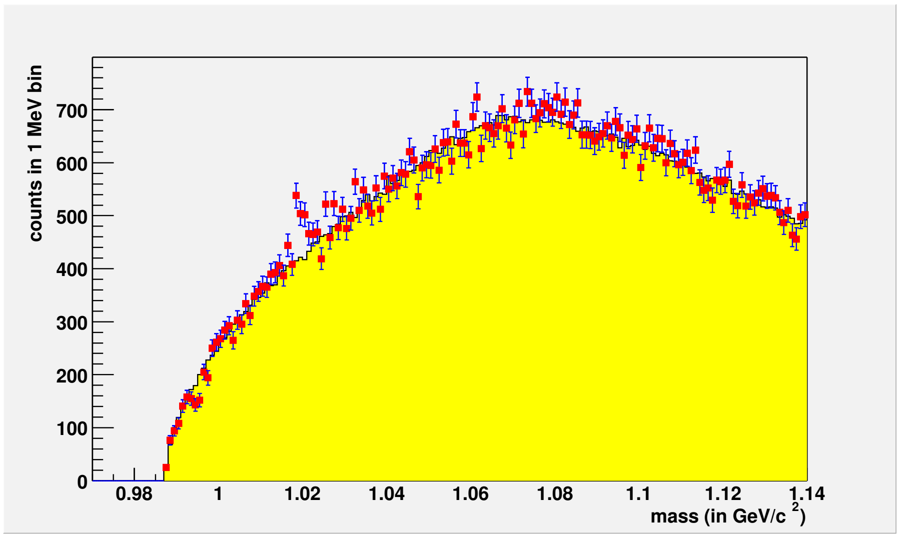

Figure 6.17: Unlike sign signal and combinatoric mass spectra in TOF-TOF for most central (0% $-$ 10%) events

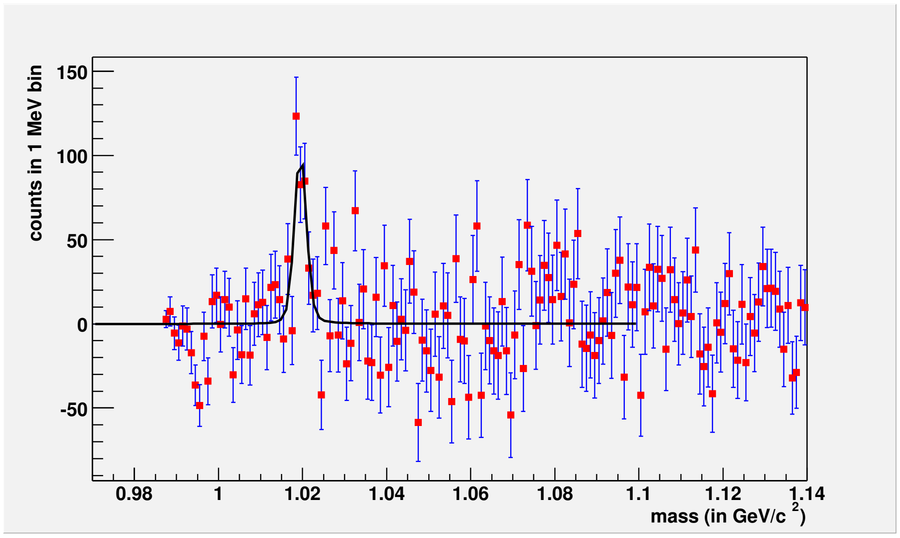

Figure 6.18: Invariant mass spectra in TOF-TOF for most central ($0\% - 10\%$) events

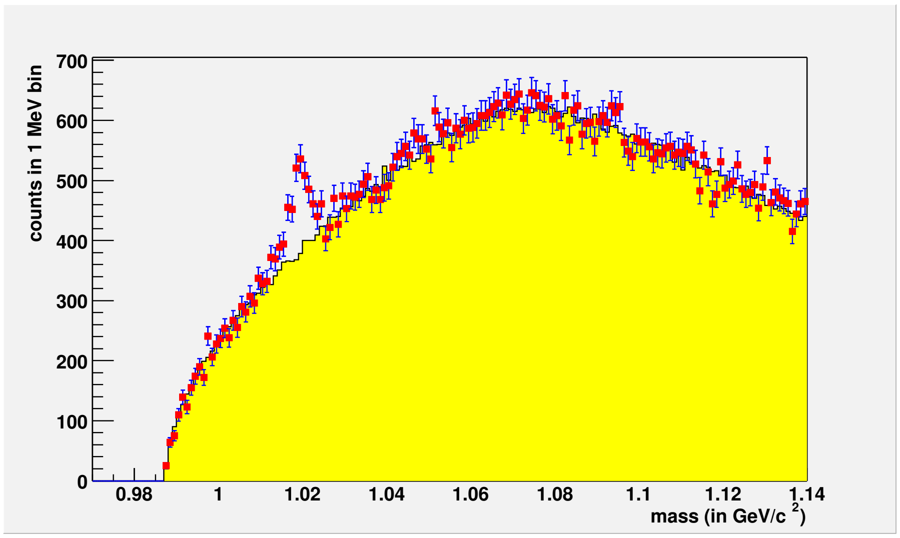

Figure 6.19: Unlike sign signal and combinatoric mass spectra in TOF-TOF for mid-central ($10\% - 40\%$) events

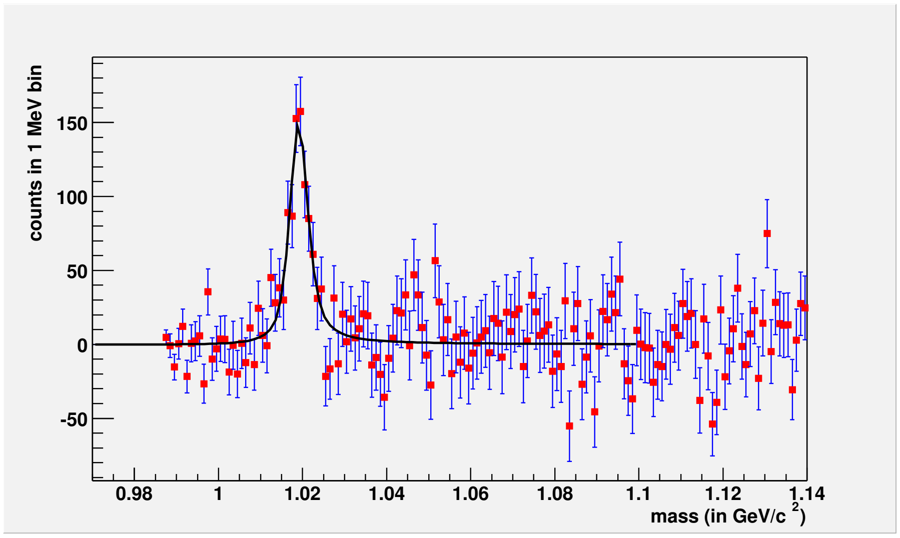

Figure 6.20: Invariant mass spectra in TOF-TOF for mid-central (10% − 40%) events

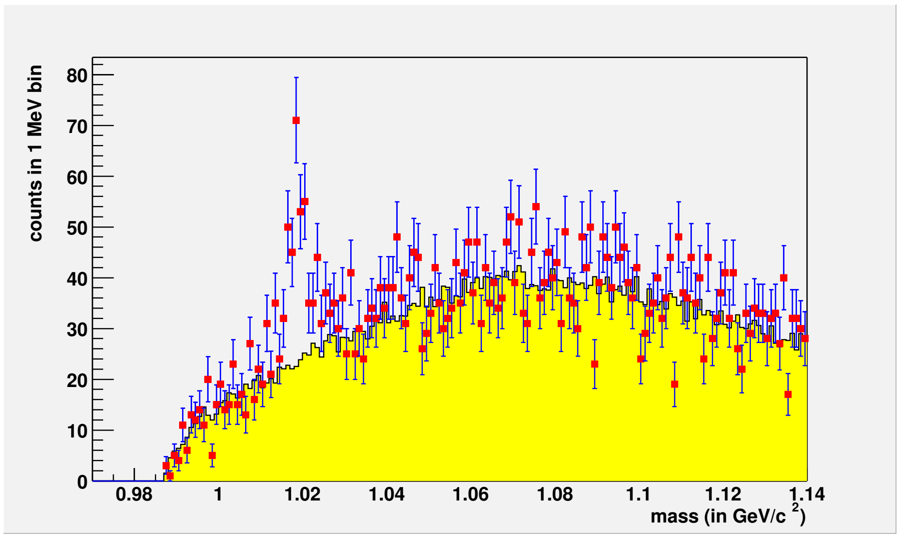

Figure 6.21: Unlike sign signal and combinatoric mass spectra in TOF-TOF for peripheral (40% − 92%) events

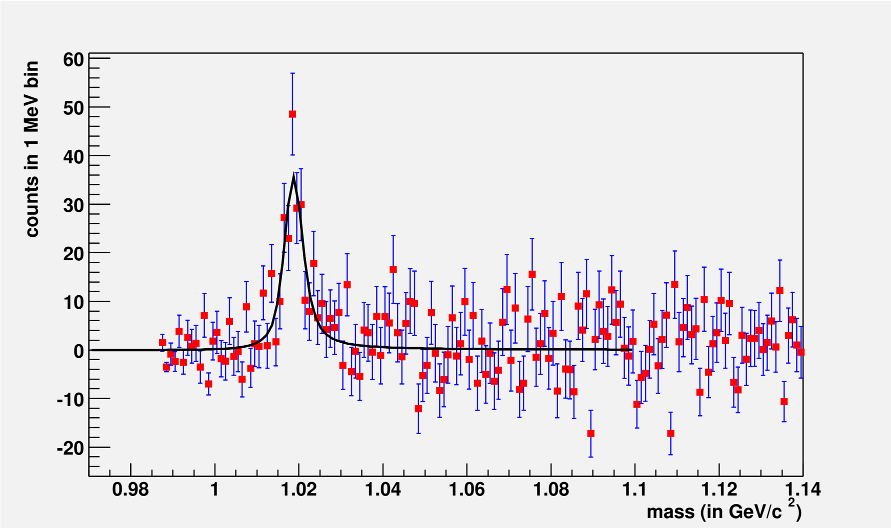

Figure 6.22: Invariant mass spectra in TOF-TOF for peripheral (40% − 92%) events

6.4.2 TOF-EMC

The ϕ invariant mass distribution for the TOF-EMC pairs are shown Fig (6.23) through Fig (6.30). In Figs (6.23), (6.25), (6.27) and (6.29) the same event unlike-sign pair invariant mass are represented in the red points. They are superimposed on the predicted mixed event unlike-sign pairs invariant mass in yellow. Fig (6.24), (6.26), (6.28) and (6.30) shows the background subtracted invariant mass plots. Very distinct ϕ peaks are observed. They are fitted with a relativistic Breit-Wigner convoluted with a Gaussian. The ϕ signal, mass and width is tabulated in Table 6.6.

6.4.3 EMC-EMC

The ϕ invariant mass distribution for the EMC-EMC pairs are shown Fig (6.31) through Fig (6.38). In Figs (6.31), (6.33), (6.35) and (6.37) the same event unlike-sign pair invariant mass are represented in the red points. They are superimposed on the predicted mixed event unlike-sign pairs invariant mass in yellow. Fig (6.32), (6.34), (6.36) and (6.38) shows the background subtracted invariant mass plots. Very distinct ϕ peaks are observed. They are fitted with a relativistic Breit-Wigner convoluted with

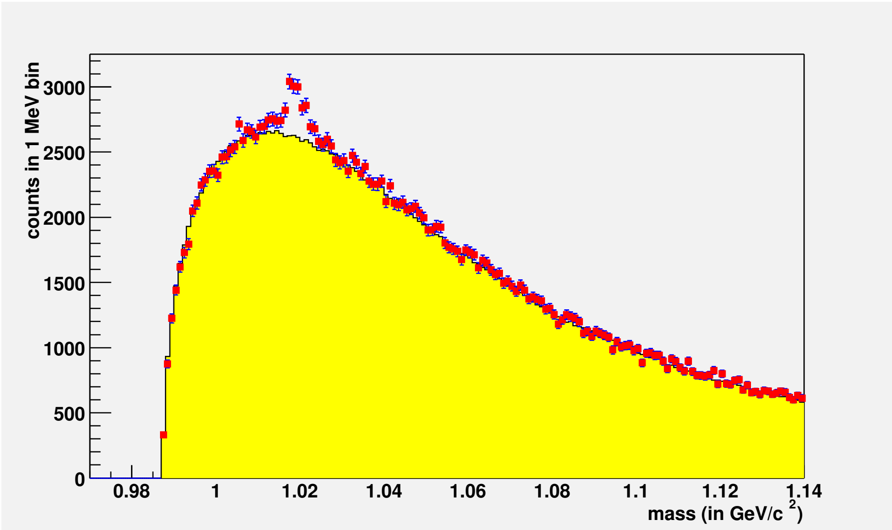

Figure 6.23: Unlike sign signal and combinatoric mass spectra in TOF-EMC for minimum bias events

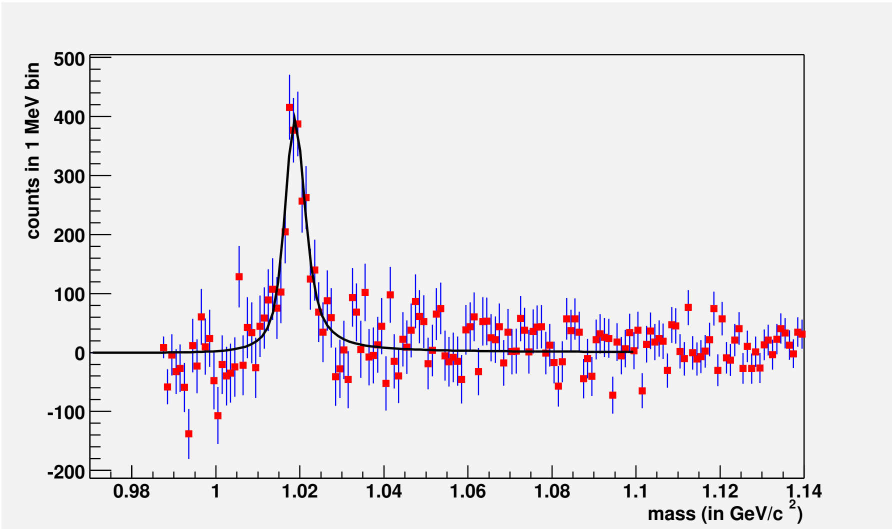

Figure 6.24: Invariant mass spectra in TOF-EMC for minimum bias events

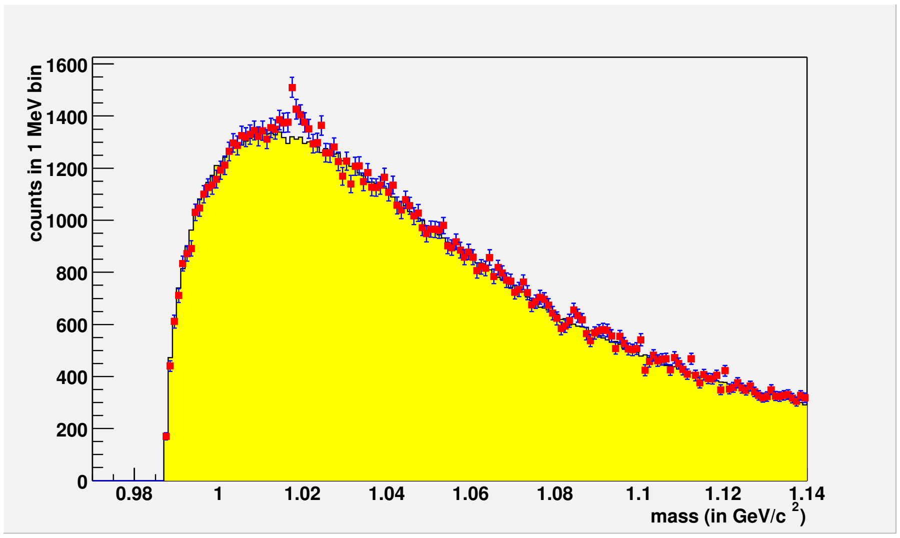

Figure 6.25: Unlike sign signal and combinatoric mass spectra in TOF-EMC for most central (0% − 10%) events

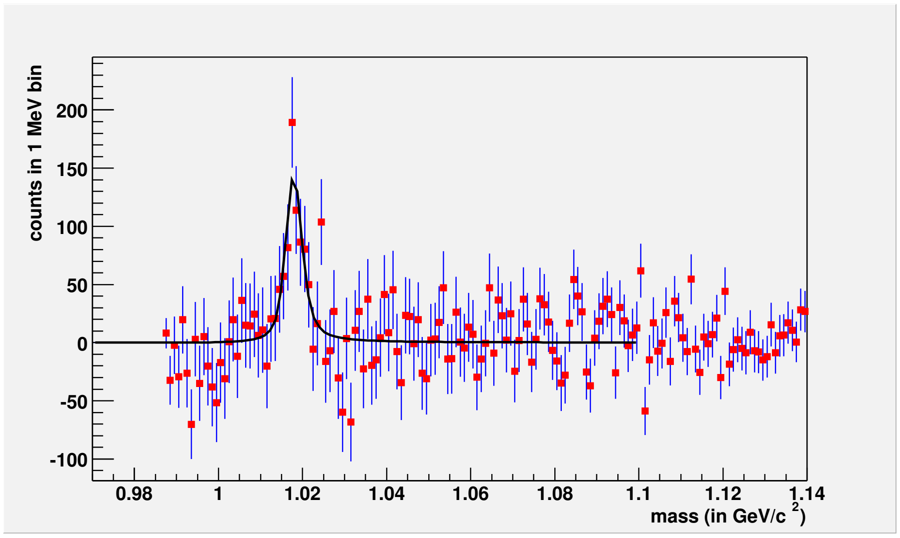

Figure 6.26: Invariant mass spectra in TOF-EMC for most central (0% − 10%) events

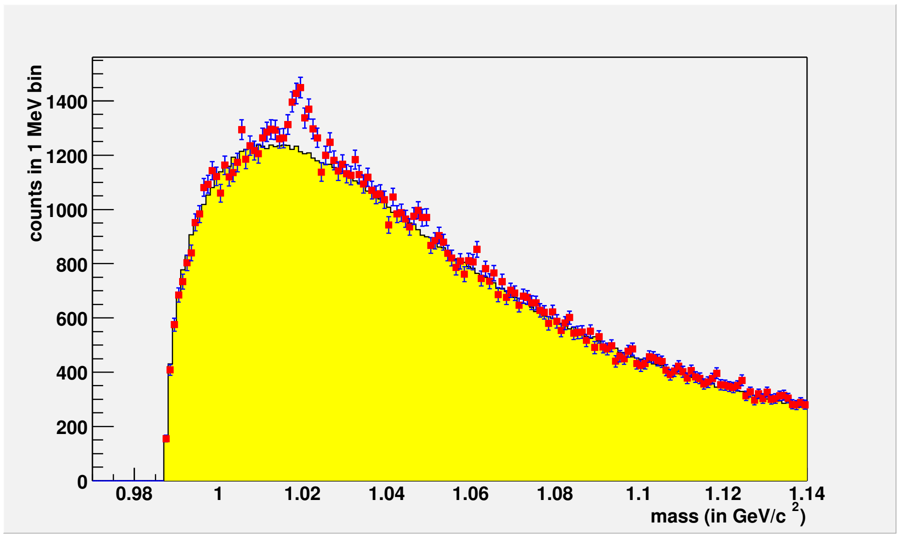

Figure 6.27: Unlike sign signal and combinatoric mass spectra in TOF-EMC for mid-central (10% – 40%) events

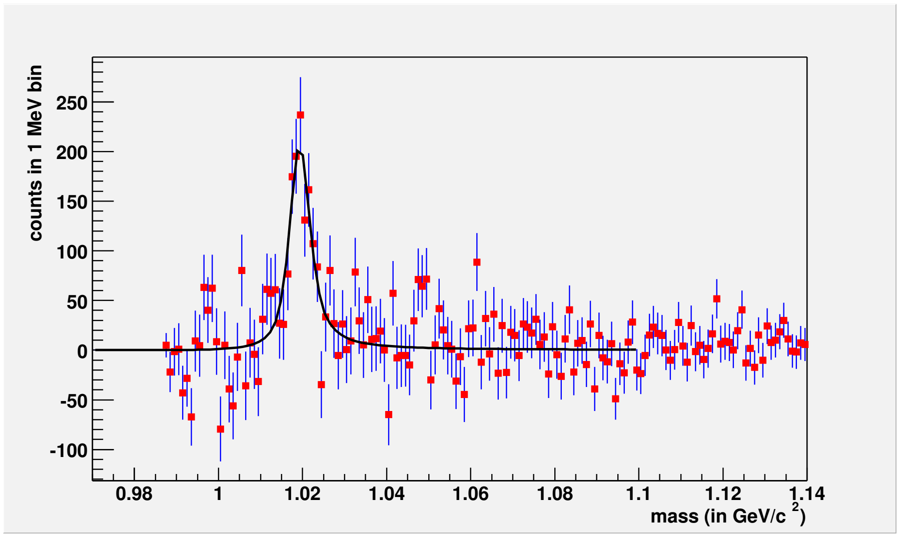

Figure 6.28: Invariant mass spectra in TOF-EMC for mid-central (10% – 40%) events

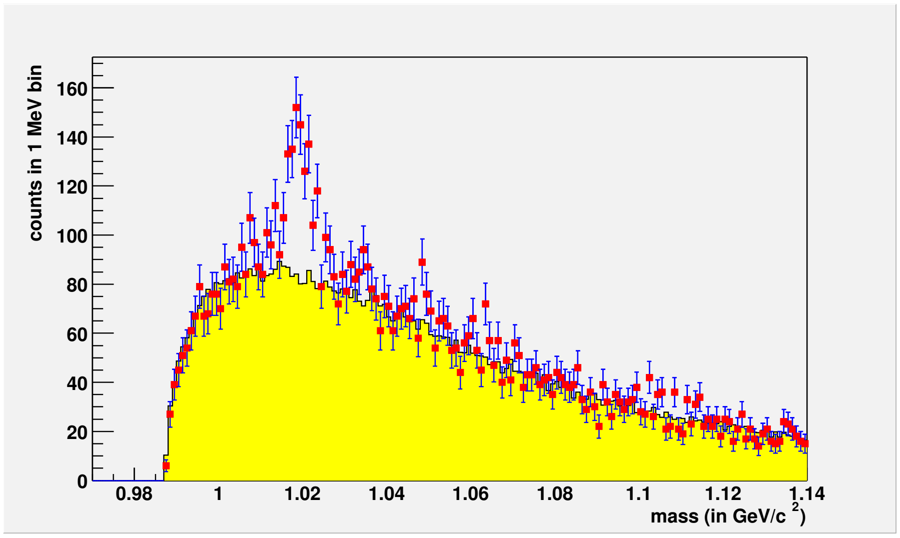

Figure 6.29: Unlike sign signal and combinatoric mass spectra in TOF-EMC for peripheral ($40\% - 92\%$) events

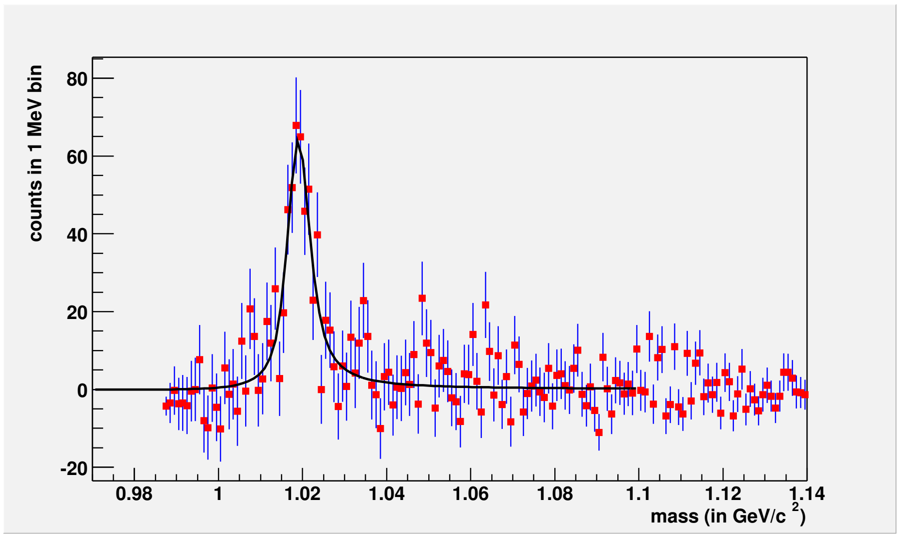

Figure 6.30: Invariant mass spectra in TOF-EMC for peripheral ($40\% - 92\%$) events

Centrality	ϕ Signal	Bkg	S/B	Mass (GeV/c^2)	Γ (MeV/c^2)
Min Bias	2345 $\pm$ 221	26078	1/11.1	1.01890 $\pm$ 0.00024	4.32445 $\pm$ 0.77512
0% – 10%	716 $\pm$ 151	13081	1/18.7	1.01796 $\pm$ 0.00041	2.65208 $\pm$ 1.30345
10% – 40%	1219 $\pm$ 153	12159	1/9.97	1.01942 $\pm$ 0.00031	4.27146 $\pm$ 1.03496
40% – 92%	413 $\pm$ 48	836	1/2.02	1.01915 $\pm$ 0.00033	5.13431 $\pm$ 0.99798

Table 6.6: ϕ Signal, background, Mass centroid and the full-width at half maxima for TOF-EMC Pairs The Signal and backgrounds are counted in the mass window of $1.014\ GeV/c^2 < M_{inv} < 1.024\ GeV/c^2$.

a Gaussian. The ϕ signal, mass and width is tabulated in Table 6.7.

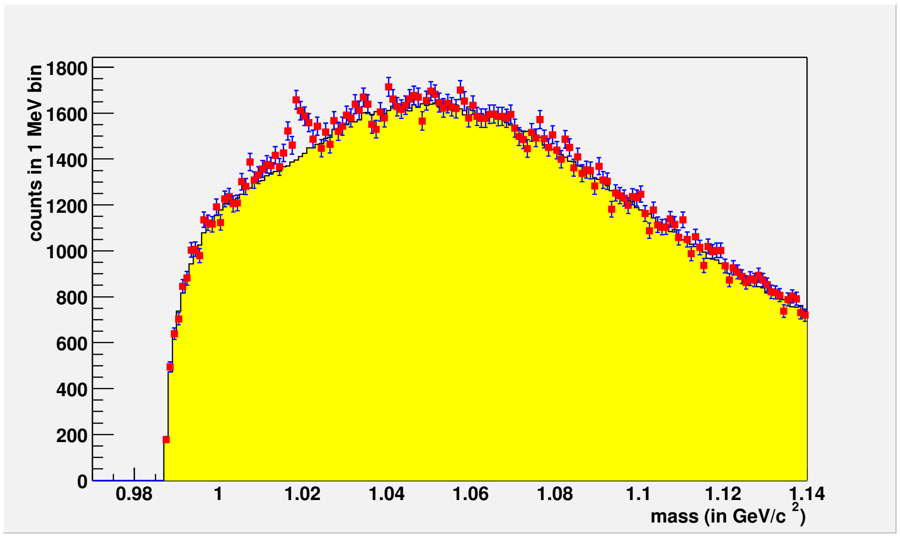

Figure 6.31: Unlike sign signal and combinatoric mass spectra in EMC-EMC for minimum bias events

6.5 Summary

In this chapter we concentrated on the techniques of the extraction of the ϕ invariant mass spectra. The mathematical description on the normalization of the combinatoric background was given. Also the fitting function for the ϕ invariant mass spectra were

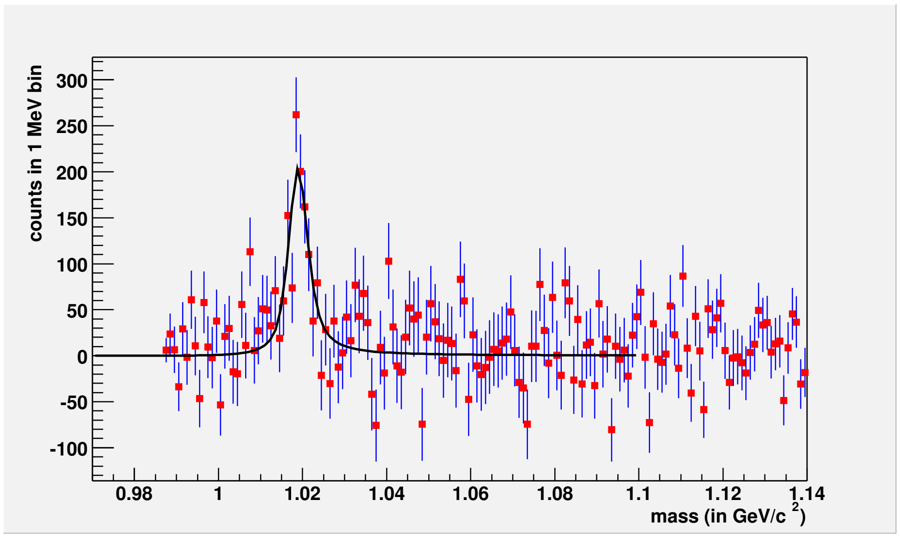

Figure 6.32: Invariant mass spectra in EMC-EMC for minimum bias events

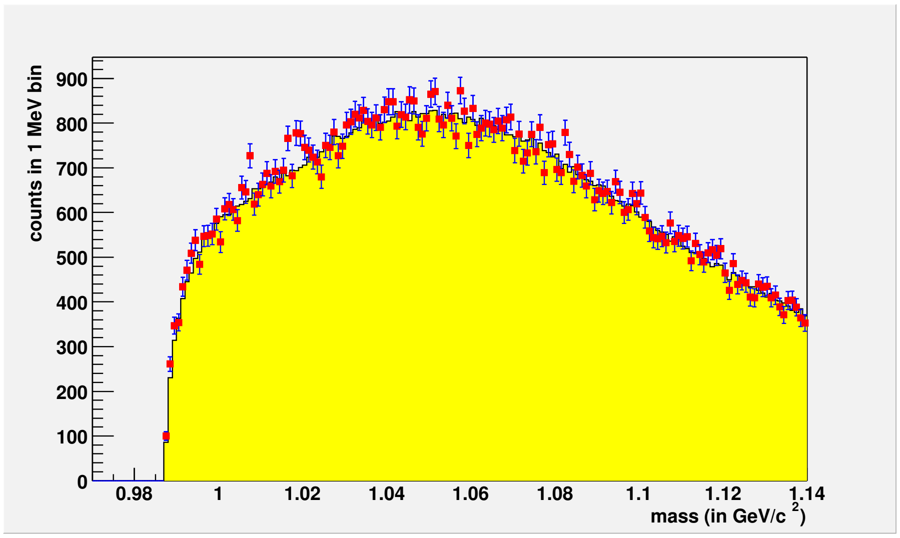

Figure 6.33: Unlike sign signal and combinatoric mass spectra in EMC-EMC for most central ($0\% - 10\%$) events

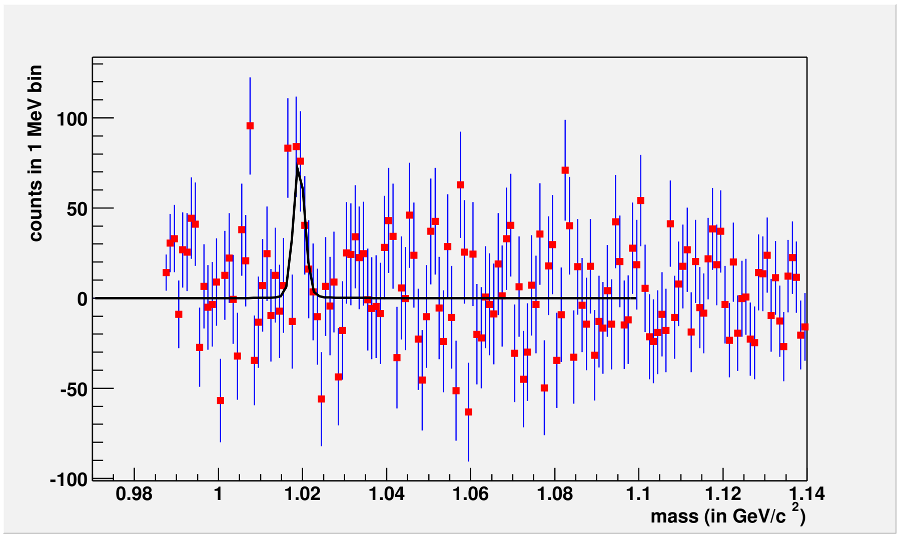

Figure 6.34: Invariant mass spectra in EMC-EMC for most central (0% – 10%) events

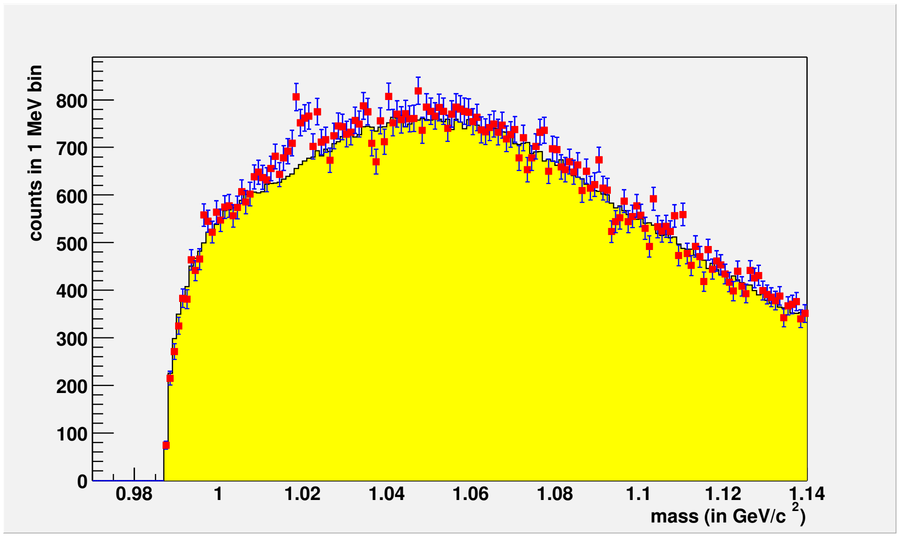

Figure 6.35: Unlike sign signal and combinatoric mass spectra in EMC-EMC for mid-central (10% – 40%) events

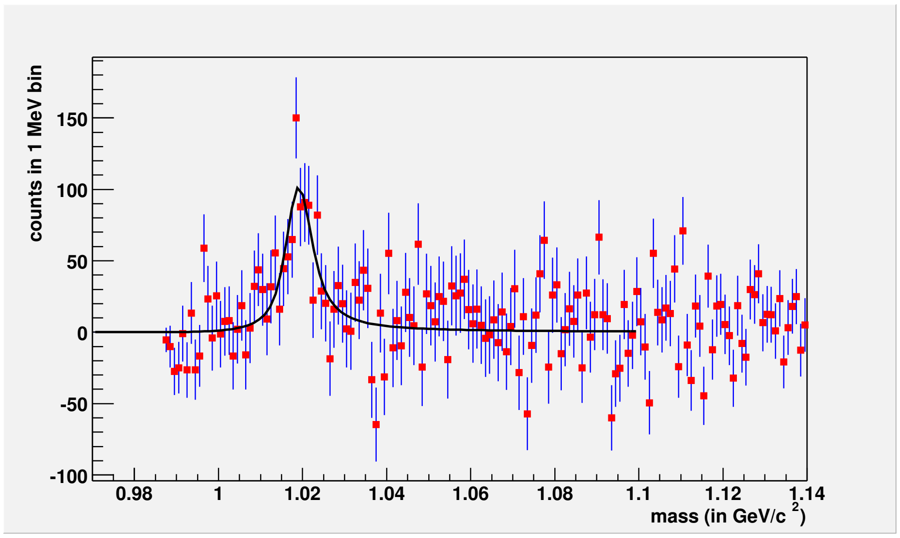

Figure 6.36: Invariant mass spectra in EMC-EMC for mid-central (10% – 40%) events

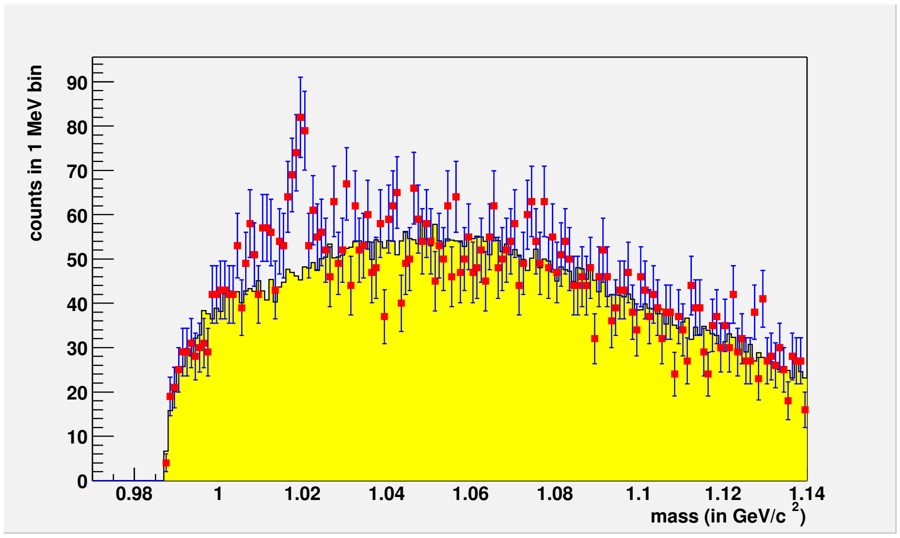

Figure 6.37: Unlike sign signal and combinatoric mass spectra in EMC-EMC for peripheral (40% – 92%) events

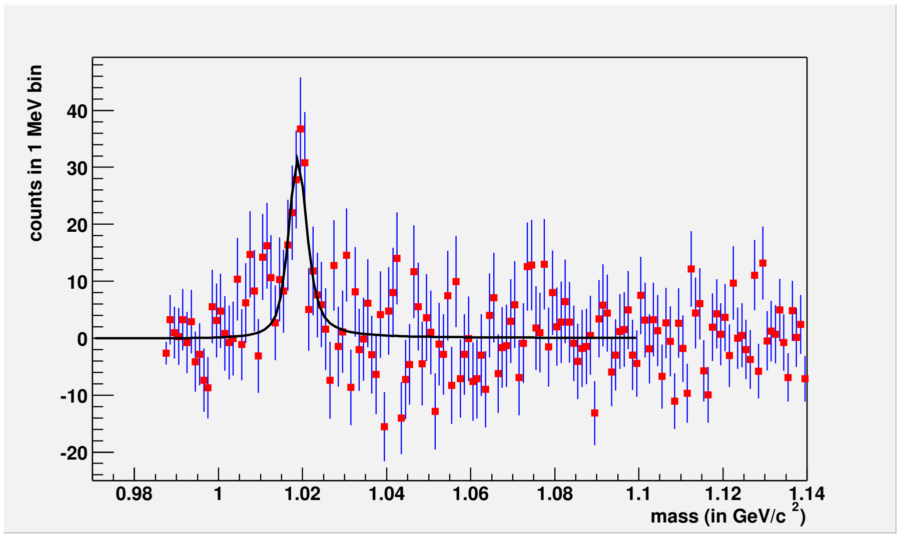

Figure 6.38: Invariant mass spectra in EMC-EMC for peripheral ($40\% - 92\%$) events

Centrality	ϕ Signal	Bkg	S/B	Mass (GeV/c^2)	Γ (MeV/c^2)
Min Bias	1156 ± 175	14063	1/12.2	1.0190 ± 0.0003	3.8520 ± 1.2246
$0\% - 10\%$	279 ± 116	7011	1/25.1	1.0192 ± 0.0005	3.2400 ± 1.6554
$10\% - 40\%$	700 ± 121	6585	1/9.4	1.0193 ± 0.0005	6.5327 ± 2.0384
$40\% - 92\%$	177 ± 34	467	1/2.6	1.0189 ± 0.0004	3.4694 ± 1.4975

Table 6.7: ϕ Signal, background, Mass centroid and the full-width at half maxima for EMC-EMC Pairs The Signal and backgrounds are counted in the mass window of $1.014\ GeV/c^2 < M_{inv} < 1.024\ GeV/c^2$.

discussed. There we introduced the detector mass resolution which needs to be taken into account for the ϕ mass centroid and width measurement.

We have extracted the ϕ invariant mass spectra for TOF-TOF, TOF-EMC and EMC-EMC pairs. Each of the combinations were studied for three centralities together with their minimum bias distribution. The spectra were fitted with a relativistic Breit-Wigner convoluted with a Gaussian of width of 1.25 MeV. We tabulated the ϕ signal, combinatoric background in the mass window of between 1.014 GeV/c^2 and 1.024 GeV/c^2. The ϕ mass centroid and the full-width at half-maxima were extracted from the fitting. From Tables 6.5 through 6.7, it is seen that the mass centroids are consistent with the PDG value of 1.019567 GeV/c^2, but the widths are showing a trend of varying with the centrality. Since the statistics is low, we will combine the TOF-TOF, TOF-EMC and EMC-EMC pairs together and study the centrality dependence of the ϕ mass and Γ in Chapter8.

Chapter 7

Corrections

The analysis on $\phi \rightarrow K^+K^-$ uses the two sectors of the Time of Flight detector and two sectors of the Electromagnetic calorimeter in the PHENIX east arm. The rapidity coverage is ± 0.35 units. The TOF azimuthal coverage is about 30^o and the EMCal coverage is about 45^o. The particles that are produced in the collisions are not fully detected in the PHENIX spectrometer. Also during the reconstruction of the tracks, some tracks are lost due to detector inefficiency. This is specially true for more central collisions where particle multiplicities are higher. The analysis uses combinations of DC+PC1+TOF/PbSc for tracking and particle identification. During the run any detector or a part of the detector may have dead areas due to high or low power supply outages. This also might effect the ϕ yield. All of these effects need to be corrected in order to determine the yield of ϕ production. In this chapter we will discuss about the various corrections we will apply to our raw yields to extract the yield of ϕ production.

We will be basically making three types of correction:

- Detector Geometrical acceptance correction.
- Correction for the efficiency loss due to high occupancy (Embedding correction)
- Correction for the run by run variation of the detector efficiency.

7.1 Acceptance Correction

In order to correct for the geometrical acceptance of the detector, we need to throw a number of tracks in the detector, reconstruct them using the same conditions as the real data and find out how many of them we can reconstruct and accept within our spectrometer at the end. The ratio of the accepted tracks and the generated tracks will give the acceptance correction of the detector. The steps for the acceptance corrections are:

- Generate random particles
- pass the tracks through the detector simulation software
- reconstruct the tracks with the same conditions as in real data
- find the ratio of the accepted tracks and the generated tracks, preferably bin by bin.

7.1.1 Single Particle Monte Carlo

The first step for the acceptance correction is the production of Monte-Carlo particles. Single ϕ events were generated using the EXODUS [48] event generator. EXODUS is a phenomenological event generator. It allows to simulate the phase-space distributions of primary mesons such as π^0, η, η', ρ, ω, and ϕ. In addition, acceptance filtering and detector resolution are available. The phase-space distributions, i.e. the p_t and rapidity distributions, of these primary particles are sampled according to standard parameterizations which are provided by the means of ROOT histograms and, therefore, can be adjusted by the user at will. The masses of the short-lived resonance ρ, ω, and ϕ are sampled according to the standard parameterization from [49]. The input parameters of the single ϕ events are :

- flat in rapidity within $|y| \leq 0.6$ units

- uniform in azimuth $0 < \phi < 2\pi$

- flat in z within $|z| < 30.0$ cm

- exponential in transverse mass

$$\frac{dN}{dp_T} = p_T \exp\left(-\frac{m_T}{T}\right) \tag{7.1}$$

  with T, the inverse slope, being taken as 320 MeV.

The input rapidity distribution is shown in Fig. 7.1. The rapidity is flat in $|y|\, leq\, 0.6$. The transverse mass distribution and the transverse momentum distributions are shown in Figs. 7.2 and Fig. 7.3 demonstrating the exponential of the distributions. The mass of the input particles, which are ϕ's, are shown in Fig. 7.4. The input mass distribution has a Breit-Wigner shape. The fit to a Breit-Wigner shows a Γ of 4.43765 MeV/c^2 of the input ϕ's. The transverse mass spectra of the input is shown in Fig. 7.5. These single ϕ are decayed into K^+K^- pairs. The information of the

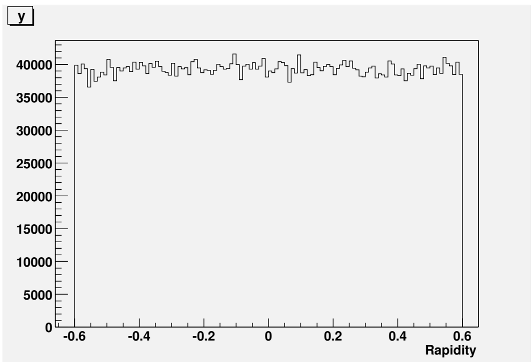

Figure 7.1: The flat rapidity distribution of generated single ϕ's with EXODUS

decayed ϕ within the EXODUS are stored in ASCII OSCAR files. The events are then passed through the PHENIX detector simulation software, known as PISA [1] The

[1]PISA stands for **P**HENIX **I**ntegrated **S**imulation **A**pplication . It is the GEANT3 based simulation package for PHENIX.

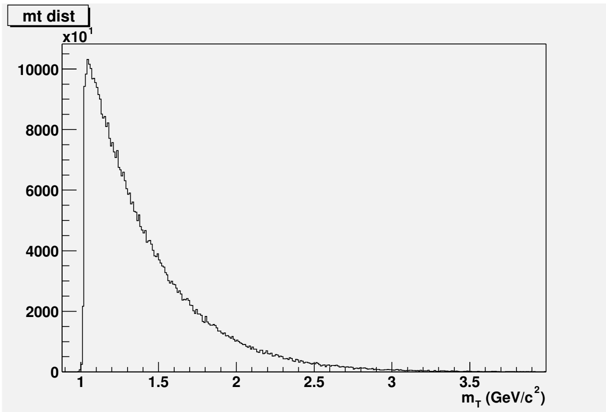

Figure 7.2: The exponential transverse mass distribution of generated single ϕ's with EXODUS

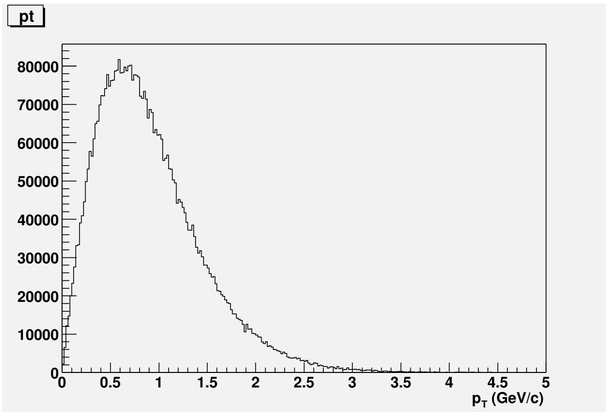

Figure 7.3: The exponential transverse momentum distribution of generated single ϕ's with EXODUS

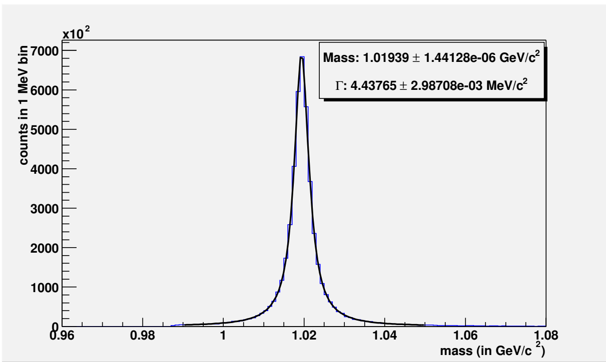

Figure 7.4: The Breit-Wigner mass distribution of generated single ϕ's with EXODUS

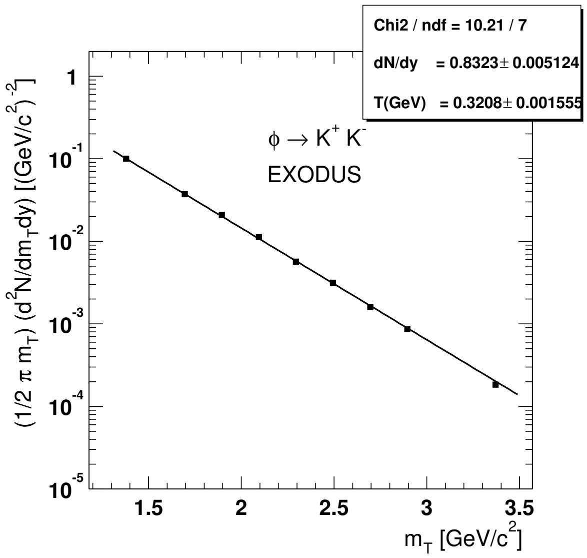

Figure 7.5: The transverse mass spectra of generated single ϕ's with EXODUS

simulated detector response is tuned to match the real response. This is achieved by using a wire-efficiency map, known as dead-channel maps and wire positions in the data. We used the dead channel map corresponding to the run number 31464, which was deemed as one of the good runs as far as the detector efficiency is concerned. The simulated event reconstruction is time consuming and in order to speed up the process some conditions such as, at least three DC wire plane hits ($dchReqFlag = 3$), at least one hit on PC1 ($dchReqFlag = 1$) and at least one hit at the EMCal ($forcedEMCalAccept = 1$), were applied.

7.1.2 Acceptance Correction Factor

The ϕ 's were reconstructed with the detected K^+K^- pairs using the same chain of software as in real data. We make three types of combinations, TOF-TOF, TOF-EMC and EMC-EMC. We use different m_T bins for the study of the transverse mass distribution. The complete sets of the m_T bins are given in Section 9.1. We will evaluate the correction factors for each of these bins. There are number of conditions and cuts applied in various stages in the analysis (see Section 4.8 for the list of cuts). All of these cuts are tuned with the real data and will be discussed in Section 7.4.

EMCal Mass Squared Renormalization in Monte Carlo

It was observed that the mass squared distribution for the kaons identified in the EMCal in the real data were not properly normalized (see Section 4.5.2). A similar effect were seen in the Monte Carlo kaons in the EMCal. Therefore we need to renormalize the mass squared in EMCal and get a momentum dependent description of the mass squared width for particle identification cut. We can not use the same parameters as in real data, since the behavior of the mass squared distribution do not follow the same pattern in the two cases. So the normalization of the Monte Carlo kaons should be done independently from the real data, but we must same number of sigmas for PID cuts both in real data and simulation.

In order to make the correction for the normalization of the mass squared, we divide the data into 28 momentum bins form 300 MeV/c^2 to 1 GeV/c^2 in a bin width of 25 MeV/c^2. For each bin we plot the mass squared of kaons and fit with Gaussian. The fit gives the mass squared centroid and the width for that momentum bin. This is done separately for K^+ and K^-. The mass squared centroids for the kaons as function of the momentum are shown in Figs. 7.6 and 7.7. We see that the mass squared show dependence on the momentum and in most cases the mass squared value is away from the expected mass squared of kaon mass squared which is $\sim$ 0.2437 $[rmGeV/c^2]^2$. This needs to be corrected so that there is no momentum dependence of the mass squared and the mass squared is close to the kaon mass squared value. The following corrections were applied to the mass squared:

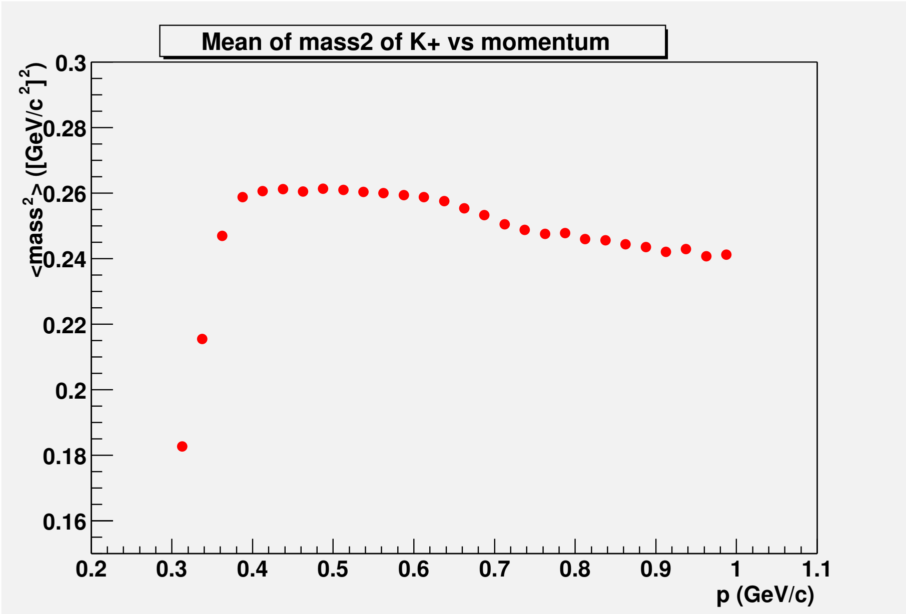

Figure 7.6: The mass squared vs the momentum for the simulated K^+'s in EMCal

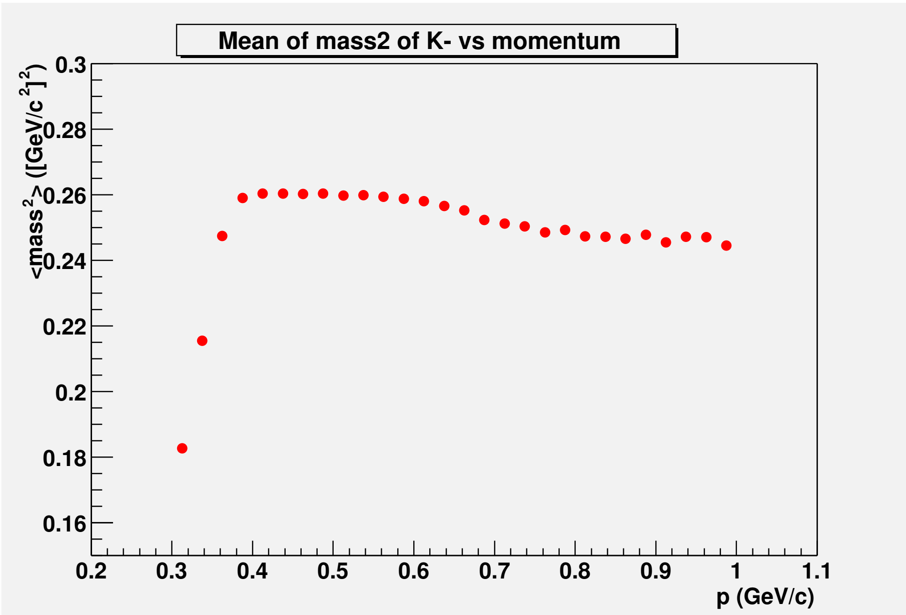

Figure 7.7: The mass squared vs the momentum for the simulated K^-'s in EMCal

Correction for K^+ mass squared

$$
\begin{aligned}
if(p < 0.3874)\ \mathrm{mass}^2 &= \mathrm{mass}^2 - (-0.462327 + 1.28471 * p); \\
if(p \geq 0.3874\&\&p < 0.6124)\ \mathrm{mass}^2 &= \mathrm{mass}^2 - (0.0163468 - 0.000991655 * p); \\
if(p \geq 0.6124)\ \mathrm{mass}^2 &= \mathrm{mass}^2 - (0.0473041 - 0.0543629 * p);
\end{aligned}
$$

Correction for K^- mass squared

$$
\begin{aligned}
if(p < 0.3874)\ \mathrm{mass}^2 &= \mathrm{mass}^2 - (-0.464717 + 1.29249 * p); \\
if(p \geq 0.3874\&\&p < 0.6124)\ \mathrm{mass}^2 &= \mathrm{mass}^2 - (0.0175443 - 0.00292094 * p); \\
if(p \geq 0.6124)\ \mathrm{mass}^2 &= \mathrm{mass}^2 - (0.0372939 - 0.0396876 * p);
\end{aligned}
$$

Figs. 7.8 and 7.9 show the mass squared spectra after the corrections had been applied. The momentum dependence mass squared distribution is greatly reduced. Also from the linear fit parameter we see that the mass squared are aligned very close to the square of the kaon mass. We also need a momentum dependence description for the width of the kaon mass squared. The momentum dependence of the widths for the K^+'s and K^-'s are shown in Figs. 7.10 and 7.11. The momentum dependence can be described by a function like

$$f(p) = A + Bp + \frac{C}{p} \tag{7.2}$$

where for K^+

$$
\begin{aligned}
A &= -0.0607796\ [\mathrm{GeV/c^2}]^2 \\
B &= 0.102420\ \mathrm{GeV/c^3} \\
C &= 0.0147638\ [\mathrm{GeV/c^2}]^2.[\mathrm{GeV/c}]
\end{aligned}
$$

And for K^-

$$A = -0.0646239\ [\mathrm{GeV/c^2}]^2$$

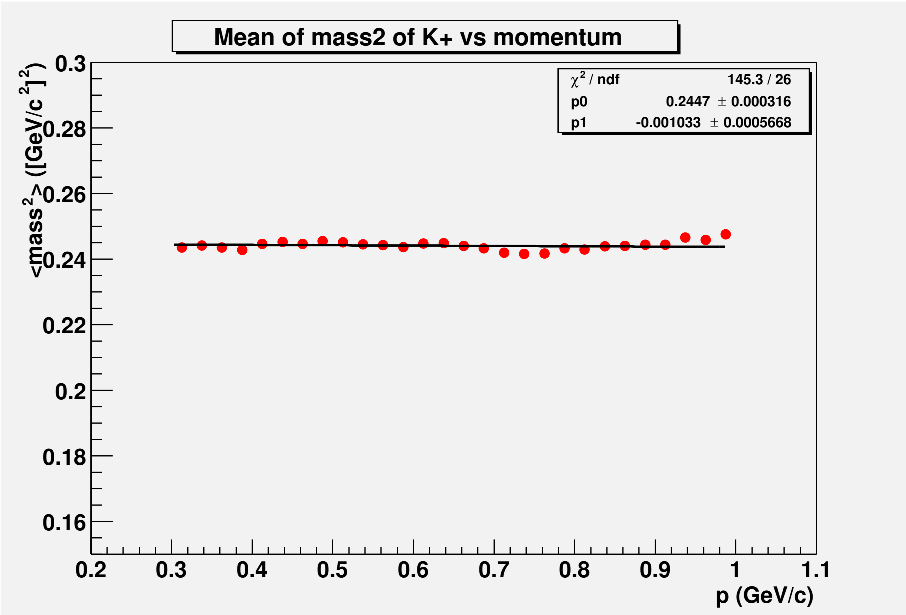

Figure 7.8: The mass squared vs the momentum for the simulated K^+'s in EMCal after correction

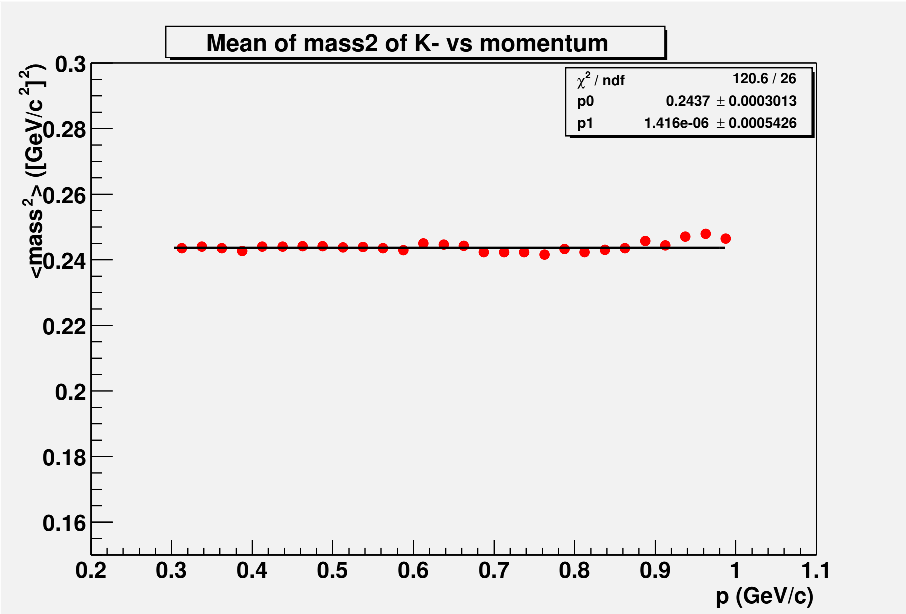

Figure 7.9: The mass squared vs the momentum for the simulated K^-'s in EMCal after correction

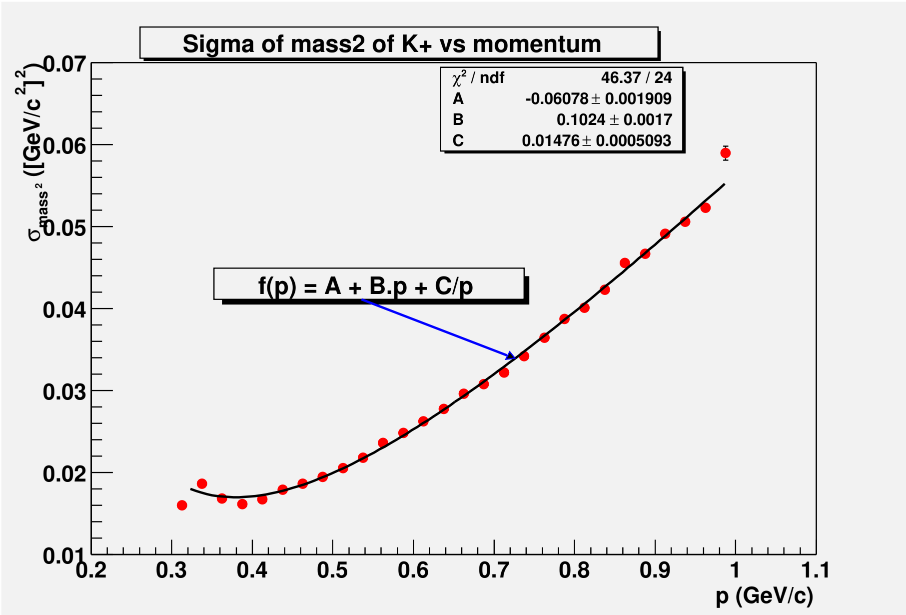

Figure 7.10: The width of the mass squared vs the momentum for the simulated K^+'s in EMCal

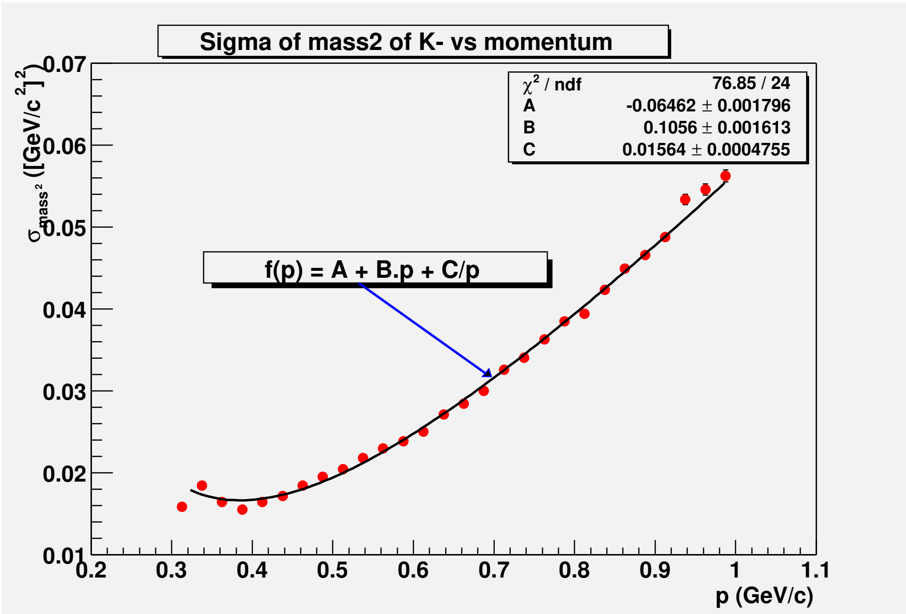

Figure 7.11: The width of the mass squared vs the momentum for the simulated K^-'s in EMCal

$$B = 0.105569 \ \mathrm{GeV/c^3}$$
$$C = 0.0156431 \ [\mathrm{GeV/c^2}]^2.[\mathrm{GeV/c}]$$

For the particle identification purposes in the east arm EMCal for the simulated tracks, we applied the corrections and selected a 2-σ band of kaons using the momentum dependence description of the width.

The geometrical acceptance correction factor is given by

$$CF = \frac{N_\phi^{\mathrm{Generated}}\,(|y| < 0.5)}{N_\phi^{\mathrm{Reconstructed}}} \tag{7.3}$$

We tabulate the correction factors for the m_T bins used for TOF-TOF, TOF-EMC and EMC-EMC combinations in Tables 7.1, 7.2 and 7.3. The acceptance correction

m_T (GeV/c^2)	$N_\phi^{\mathrm{Generated}}\,(\lvert y\rvert < 0.5)$	$N_\phi^{\mathrm{Reconstructed}}$	CF
1.2 – 1.6	1.11681e+07	310	36026.3 ± 2046.15
1.6 – 1.8	2.55608e+06	419	6100.44 ± 298.026
1.8 – 2.0	1.54946e+06	555	2791.82 ± 118.506
2.0 – 2.2	912296	580	1572.92 ± 65.3122
2.2 – 2.4	550120	435	1264.64 ± 60.635
2.4 – 2.8	499565	515	970.029 ± 42.7446
2.8 – 3.0	101686	145	701.286 ± 58.2386
3.0 – 4.0	127101	213	596.718 ± 40.8864

Table 7.1: Acceptance correction factors as a function of m_T for TOF-TOF pairs

factors for ϕ from in the transverse mass bins for TOF-TOF pairs are shown in Fig. 7.12, for TOF-EMC pairs are shown in Fig. 7.13 and for EMC-EMC pairs are shown in Fig. 7.14.

7.2 Embedding Correction

Usually the detector track reconstruction efficiency decreases with the event multiplicity. Also the particle identification efficiency also decreases for more central

m_T (GeV/c^2)	$N_\phi^{\text{Generated}}$ ($\lvert y\rvert < 0.5$)	$N_\phi^{\text{Reconstructed}}$	CF
1.2 – 1.6	1.11681e+07	1601	6975.73 ± 174.339
1.6 – 1.8	2.55608e+06	1723	1483.51 ± 35.7394
1.8 – 2.0	1.54946e+06	1242	1247.55 ± 35.3996
2.0 – 2.2	912296	606	1505.44 ± 61.1543
2.2 – 2.4	550120	226	2434.16 ± 161.918
2.4 – 2.8	499565	119	4198.03 ± 384.832

Table 7.2: Acceptance correction factors as a function of m_T for TOF-EMC pairs

m_T (GeV/c^2)	$N_\phi^{\text{Generated}}$ ($\lvert y\rvert < 0.5$)	$N_\phi^{\text{Reconstructed}}$	CF
1.2 – 1.6	1.11681e+07	1194	9353.55 ± 270.691
1.6 – 1.8	2.55608e+06	1440	1775.06 ± 46.7769
1.8 – 2.0	1.54946e+06	1240	1249.57 ± 35.4853
2.0 – 2.2	912296	348	2621.54 ± 140.529

Table 7.3: Acceptance correction factors as a function of m_T for EMC-EMC pairs

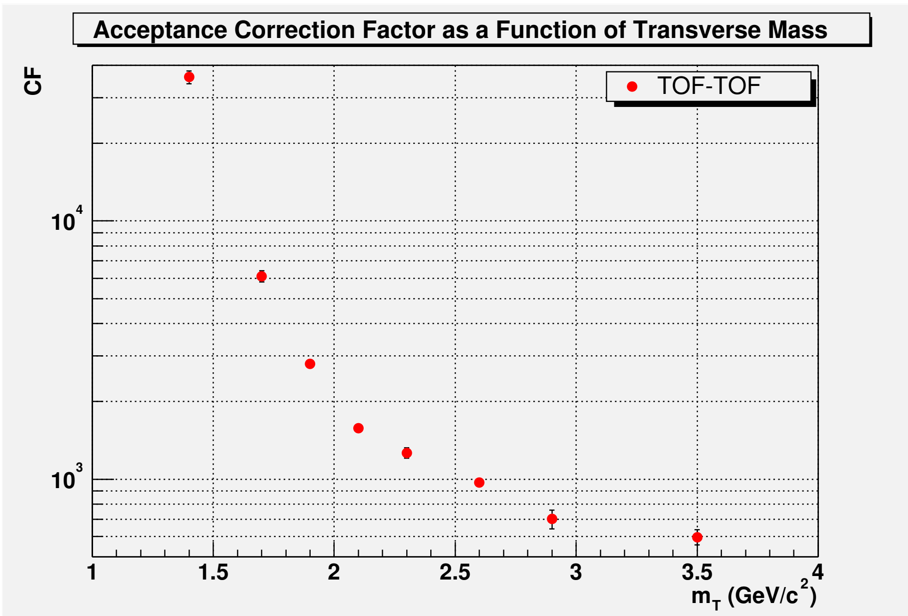

Figure 7.12: Acceptance Correction factor as a function of m_T for TOF-TOF

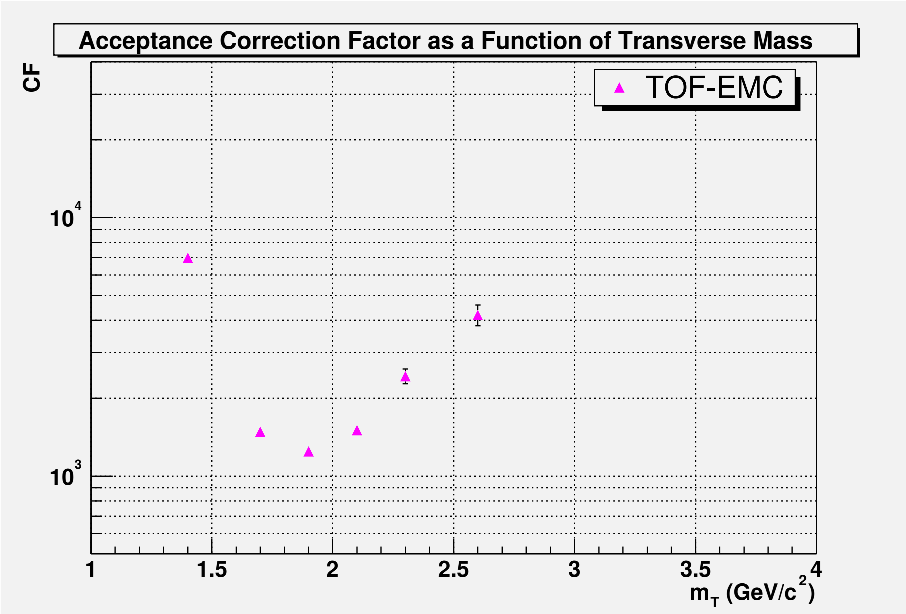

Figure 7.13: Acceptance Correction factor as a function of m_T for TOF-EMC

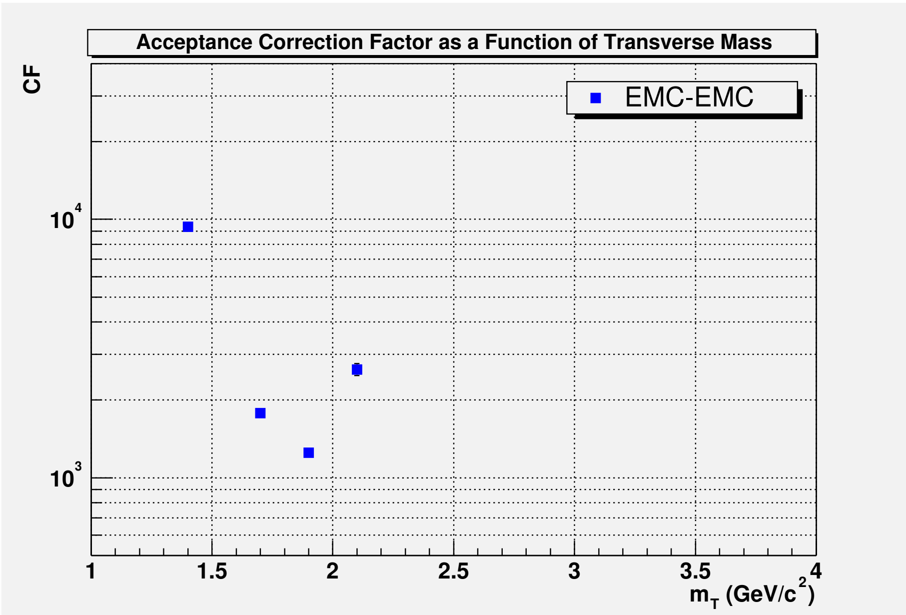

Figure 7.14: Acceptance Correction factor as a function of m_T for EMC-EMC

events. In the drift chamber for the high track density events tracks may be misreconstructed. In the Time-of-flight, more than one track may hit the same TOF slat at the same time and thereby corrupting the timing information. This leads to a wrong mass squared and the PID will be wrong in those situations. Also in EMCal, more than one track can hit the same EMCal tower resulting in same time and energy information. All these inefficiencies need to be corrected.

For the corrections of such inefficiencies, we need to find how many tracks are lost in track matching and PID cuts in each types of centralities. For this purpose we embed single particles from Monte Carlo onto real data. They are then reconstructed and at the end we find what fraction of the simulated tracks we get back. This is done for all centralities. In this way we determine the correction for the detector inefficiency. The results for single kaon and $\phi \to K^+K^-$ pairs at the TOF wall are presented in the Table 7.4. The embedding results for PbSc (east) are shown in Table 7.5. The embedding results for PbSc (east)(K^-) - TOF (K^+) are shown in Table 7.6.

Centrality (%)	$\epsilon^{emb}_{K^+}$	$\epsilon^{emb}_{K^-}$	$\epsilon^{emb}_{K^+} \times \epsilon^{emb}_{K^-}$	$\epsilon_{K^+K^-}$
0 - 92 (MB)	0.9379 ± 0.0016	0.9393 ± 0.0016	0.8810 ± 0.0022	0.9037 ± 0.008
0 - 10	0.8424 ± 0.003	0.8465 ± 0.003	0.7131 ± 0.0037	0.7549 ± 0.015
10 - 20	0.9015 ± 0.004	0.9014 ± 0.004	0.8126 ± 0.0056	0.8541 ± 0.022
20 - 30	0.9387 ± 0.005	0.9401 ± 0.005	0.8825 ± 0.007	0.8869 ± 0.028
30 - 40	0.9633 ± 0.006	0.9603 ± 0.006	0.9250 ± 0.008	0.9246 ± 0.032
40 - 50	0.9787 ± 0.005	0.9789 ± 0.005	0.9580 ± 0.007	0.9753 ± 0.026
50 - 60	0.9859 ± 0.005	0.9878 ± 0.005	0.9739 ± 0.007	0.9742 ± 0.025
60 - 70	0.9936 ± 0.005	0.9942 ± 0.006	0.9878 ± 0.008	0.9850 ± 0.029
70 - 80	0.9978 ± 0.006	0.9985 ± 0.006	0.9963 ± 0.009	1.000 ± 0.033
80 - 92	0.9976 ± 0.006	0.9989 ± 0.006	0.9965 ± 0.009	0.9955 ± 0.033

Table 7.4: Embedding efficiencies for single kaons and kaon pairs from the ϕ mesons at TOF

Centrality (%)	$\epsilon_{K^+}^{emb}$	$\epsilon_{K^-}^{emb}$	$\epsilon_{K^+}^{emb} \times \epsilon_{K^-}^{emb}$	$\epsilon_{K^+K^-}$
0 - 92 (MB)	0.9239 ± 0.004	0.9312 ± 0.004	0.8603 ± 0.005	0.8619 ± 0.018
0 - 10	0.8067 ± 0.007	0.8205 ± 0.007	0.6619 ± 0.008	0.6590 ± 0.030
10 - 20	0.8817 ± 0.010	0.8945 ± 0.010	0.7887 ± 0.012	0.8022 ± 0.055
20 - 30	0.9214 ± 0.013	0.9303 ± 0.013	0.8572 ± 0.017	0.8497 ± 0.061
30 - 40	0.9423 ± 0.013	0.9558 ± 0.015	0.9007 ± 0.019	0.8616 ± 0.068
40 - 50	0.9717 ± 0.011	0.9765 ± 0.012	0.9569 ± 0.016	0.9231 ± 0.057
50 - 60	0.9825 ± 0.011	0.9855 ± 0.011	0.9683 ± 0.015	0.9667 ± 0.059
60 - 70	0.9914 ± 0.013	0.9948 ± 0.014	0.9863 ± 0.019	0.9804 ± 0.068
70 - 80	0.9964 ± 0.015	0.9934 ± 0.015	0.9898 ± 0.021	0.9825 ± 0.075
80 - 92	0.9998 ± 0.014	0.9962 ± 0.015	0.9960 ± 0.021	1.0000 ± 0.07551

Table 7.5: Embedding efficiencies for single kaons and kaon pairs from the ϕ mesons at PbSc (east)

Centrality (%)	$\epsilon_{K^+}^{emb}$	$\epsilon_{K^-}^{emb}$	$\epsilon_{K^+}^{emb} \times \epsilon_{K^-}^{emb}$	$\epsilon_{K^+K^-}$
MB (0 - 92)	0.9306 ± 0.004	0.9227 ± 0.004	0.8620 ± 0.005	0.8746 ± 0.018
0 - 10	0.8471 ± 0.008	0.8143 ± 0.007	0.6898 ± 0.009	0.7116 ± 0.029
10 - 20	0.8956 ± 0.012	0.8794 ± 0.011	0.7876 ± 0.014	0.8252 ± 0.047
20 - 30	0.9393 ± 0.015	0.9259 ± 0.014	0.8698 ± 0.019	0.8725 ± 0.061
30 - 40	0.9567 ± 0.017	0.9557 ± 0.016	0.9143 ± 0.022	0.9103 ± 0.073
40 - 50	0.9728 ± 0.013	0.9677 ± 0.012	0.9414 ± 0.017	0.9422 ± 0.057
50 - 60	0.9805 ± 0.013	0.9794 ± 0.012	0.9603 ± 0.017	0.9628 ± 0.056
60 - 70	0.9879 ± 0.016	0.9958 ± 0.015	0.9838 ± 0.022	0.9695 ± 0.069
70 - 80	0.9911 ± 0.018	0.9951 ± 0.017	0.9862 ± 0.025	1.0000 ± 0.080
80 - 92	0.9906 ± 0.017	0.9945 ± 0.016	0.9851 ± 0.023	0.9834 ± 0.070

Table 7.6: Embedding efficiencies for single kaons and kaon pairs from the ϕ mesons with TOF (K^+) - East (K^-) combination.

7.3 Run-by-run Efficiency Correction

The complete analysis chain for the $\phi \rightarrow K^+K^-$ uses the following detectors:

$$\text{DC} \rightarrow \text{PC1} \rightarrow \text{TOF}$$

$$\text{DC} \rightarrow \text{PC1} \rightarrow \text{PC3} \rightarrow \text{EMCal}$$

At any instance during the run a part of a detector or a combinations of the detectors can become inefficient for reasons such as power outage, electronics circuitry failure among others. For example, the number of K^+'s and K^-'s per minimum bias trigger in the east arm EMCal over the runs used in this analysis looks like in Figs. 7.15 and 7.16. We need to amend for these types of inefficiencies.

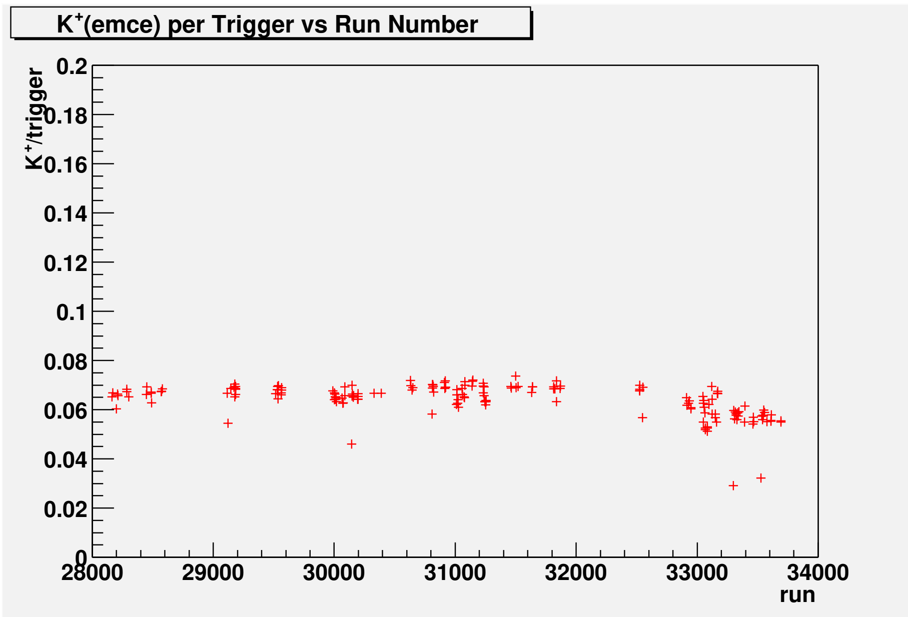

Figure 7.15: Acceptance K^+'s per trigger in the east arm EMCal over the runs

For that purpose we take one of the runs as the reference and normalize the K^+ and K^+ raw yields per event of all other runs with respect to the reference. The run number 31464 was one of the good runs. We calculated the numbers $A_{K^+} = N_{K^+}/$

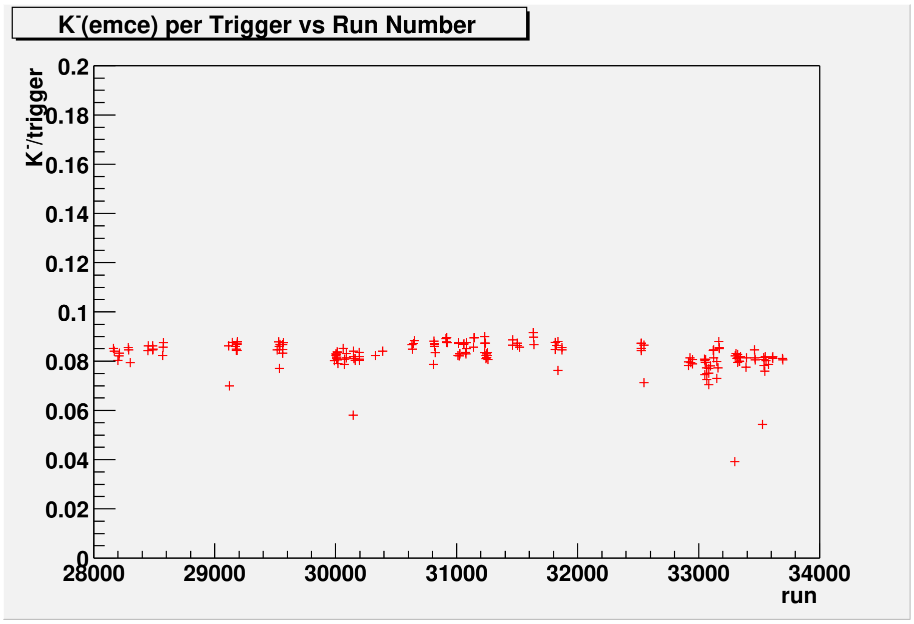

Figure 7.16: Acceptance K^{+}'s per trigger in the east arm EMCal over the runs

event and $A_{K^-} = N_{K^-}/$ event for each run for different centrality and momentum bins.

Using the above numbers, we calculated the K_+ and K^- efficiencies of each run with respect to the run 31464 as:

$$\epsilon_{K^+} = \frac{A^{31464}_{K^+}}{A_{K^+}} \tag{7.4}$$

$$\epsilon_{K^-} = \frac{A^{31464}_{K^-}}{A_{K^-}} \tag{7.5}$$

Finally, we computed an average of $\epsilon_{K^{+/-}}$ weighted over the number of events (in each run) as:

$$< \epsilon_{K^+} >= \frac{\Sigma \epsilon^{run}_{K^+} \times N^{run}_{event}}{\Sigma N^{i}_{event}} \tag{7.6}$$

$$< \epsilon_{K^-} >= \frac{\Sigma \epsilon^{run}_{K^-} \times N^{run}_{event}}{\Sigma N^{i}_{event}} \tag{7.7}$$

The summation was carried out over all runs.

We call it as the average run-by-run efficiency for the single kaons. The pair efficiency is calculated by simply taking the product of the single efficiencies as:

$$< \epsilon_{K^+K^-} >=< \epsilon_{K^+} > \times < \epsilon_{K^-} > \tag{7.8}$$

7.3.1 Results for TOF

The run-by-run efficiency for positive and negative kaons as a function of the number of participant (centrality) are shown in the Fig. 7.17. The minimum bias efficiencies are also indicated by dotted lines. In either case, we did not observe any centrality dependence of run-by-run kaon efficiency.

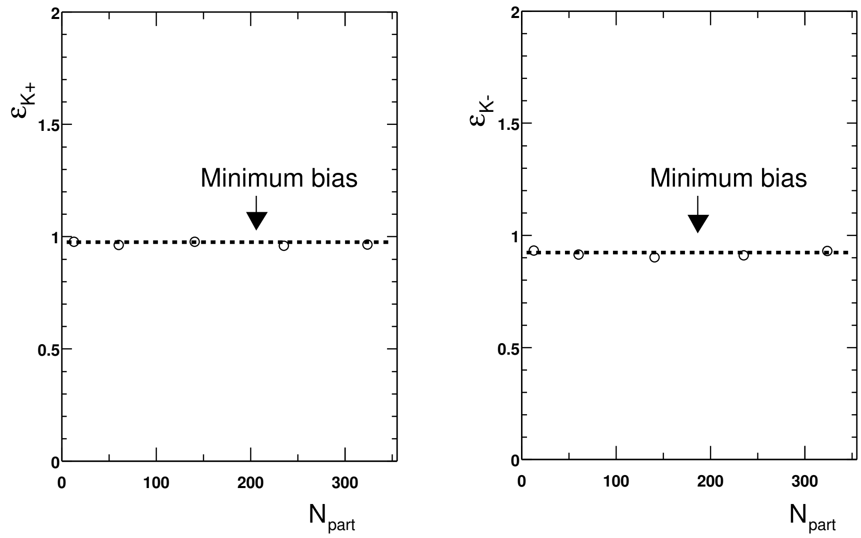

Figure 7.17: Run-by-run efficiency for K^+ (left) and K^- (right) as a function of the number of participants (centrality). The dotted line in each plot indicates the minimum bias efficiency

The above study is done for the kaons integrated over all momentum bins.

In order to investigate the momentum dependence of run-by-run variation, we plotted run-by-run efficiency as a function of the kaon momenta in Fig. 7.18. The figure shows that the run-by-run efficiency of the kaons is constant within $\pm$ 3%.

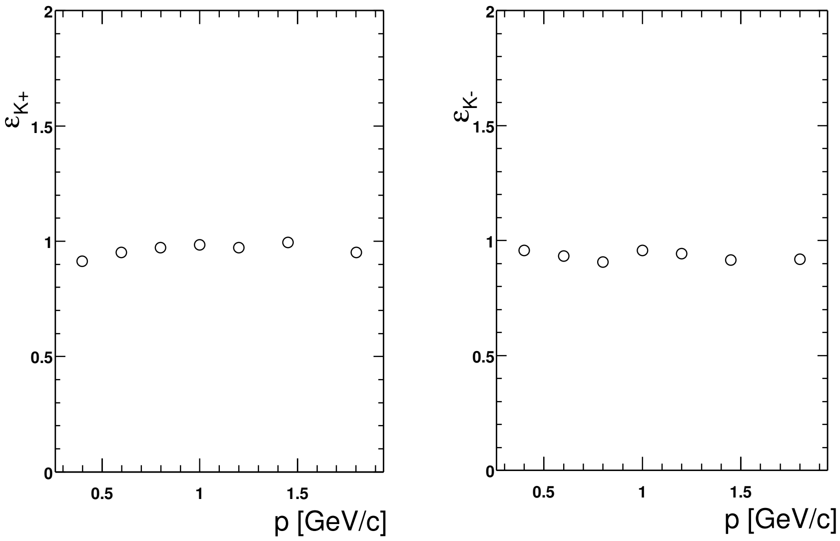

Figure 7.18: Run-by-run efficiency for K^+ (left) and K^- (right) as a function of the kaon momenta.

Since there is no centrality and/or momentum dependence, we use the minimum bias run-by-run efficiencies for K^+ and K^- which are $0.976255 \pm 8.12052e-05$ and $0.924427 \pm 7.38575e-05$ respectively. Accordingly, the run-by-run pair efficiency is the product of the singles, i.e., $0.9024 \pm 1.097e-04$.

7.3.2 Results for EMCal

The run-by-run efficiency for the east - east combinations has been studied as a function of the kaon momenta. The results are shown in Figure 7.19. We find that the run-by-run efficiencies is independent of kaon momenta and are consistent with the minimum bias run-by-run efficiency factors which are:

$\epsilon_{K^+} = 0.9418 \pm 7 \times 10^{-5}$ and

$\epsilon_{K^-} = 0.9435 \pm 8 \times 10^{-5}$.

The net run-by-run efficiency for the kaon pairs for PbSc east is, therefore,

$\epsilon_{K^+.K^-} = \epsilon_{K^+} \times \epsilon_{K^-} = 0.8886 \pm 0.0001$.

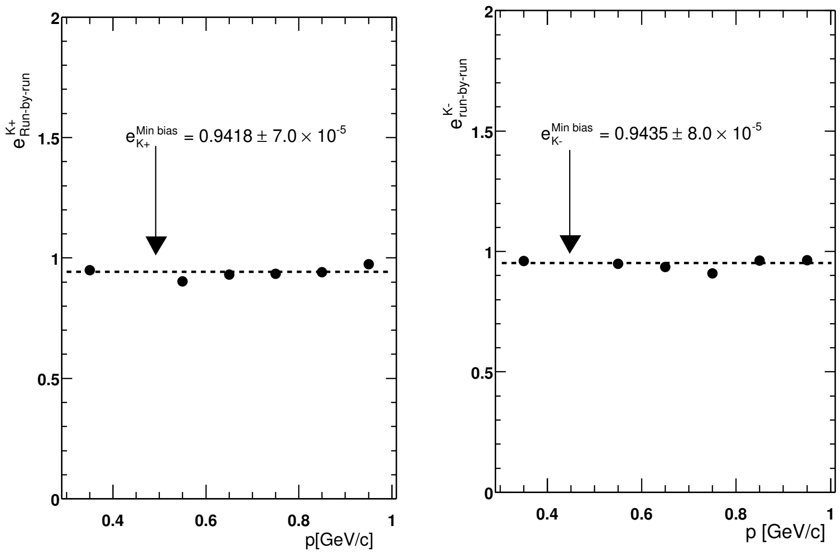

Figure 7.19: Run-by-run efficiency for K^+ (left) and K^- (right) as a function of the kaon momenta for east-east combination.

7.3.3 Results for TOF-EMCal

Computation of the run-by-run efficiency for TOF-East combination is a bit tricky for the K^+K^- pair acceptance.

When we do the pair analysis for TOF– East combination, there are two possibilities, K^+ from TOF and K^- from PbSc east and K^- from TOF and K^+ from PbSc east. The measured invariant mass spectra for the two cases are shown in the Fig. 7.20. This shows that there is no pair acceptance for TOF (K^-) - East (K^+) case for $M_{inv} < 1.06$ GeV/c^2 which includes the ϕ mass region. So, any run-by-run fluctuation within this combination should not have any effect on the ϕ yields extracted for TOF-East combination. This suggests that the run-by-run efficiency factor for the TOF-East combination is:

$\epsilon_{K^+.K^-} = \epsilon^{TOF}_{K^+} \times \epsilon^{East}_{K^-} = 0.9210 \pm 0.00005.$

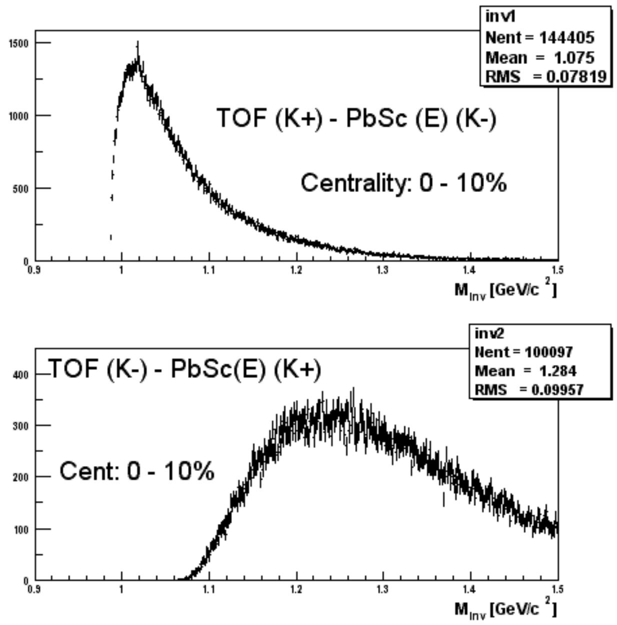

Figure 7.20: Invariant mass spectra for TOF – East combination for TOF (+) – East (-) (up) and TOF (-) – East (+) (down) pairs

7.3.4 Summary

The run-by-run efficiencies for all combinations are shown in Table 7.3.4.

Combination	$\epsilon_{K^+.K^-}$
TOF – TOF	0.9762 ± 0.000081
TOF – East	0.9210 ± 0.00005
East – East	0.8886 ± 0.0001

Table 7.7: Run-by-run correction factors

7.4 Tuning of Monte Carlo with Data

We have applied various matching and particle identification cut on the data and the Monte Carlo as well. We need to correct for the any residual in the matching of the data and the Monte Carlo. Thus we need to tune the mean values of the matching and cut parameters in the Monte Carlo with those in real data. Once the centroids are tuned, the sigmas of the parameters can be tuned.

The matching and particle identifications we use are dz_{TOF}, $d\phi_{\mathrm{TOF}}$, isK, dz_{pc3}, $d\phi_{\mathrm{pc3}}$, dz_{EMC}, $d\phi_{\mathrm{EMC}}$. Since these parameters are Gaussian in shape, let any of these measurements in real data is represented

$$y_{data} \;=\; A_{data}.\exp\left(-\frac{(x_d \;-\; x_{d0})^2}{2\,\sigma_d^2}\right) \tag{7.9}$$

Similarly for the Monte Carlo

$$y_{mc} \;=\; A_{mc}.\exp\left(-\frac{(x_m \;-\; x_{m0})^2}{2\,\sigma_m^2}\right) \tag{7.10}$$

In condition for the matching of Monte Carlo to data can be written as

$$\frac{y_{mc}}{y_{data}} \;=\; \frac{A_{mc}}{A_{data}} \tag{7.11}$$

which requires

$$\frac{(x_d \;-\; x_{d0})^2}{2\,\sigma_d^2} \;=\; \frac{(x_m \;-\; x_{m0})^2}{2\,\sigma_m^2} \tag{7.12}$$

So to tune the centroids in the Monte Carlo with the centroid in data we need to add an offset to the Monte Carlo mean:

$$x_{offset} \;=\; x_{d0} \;-\; x_{m0} \tag{7.13}$$

The sigmas are matched by multiplying the matching variables by σ_d/σ_m. The mean and sigmas of the parameters are shown in Figs. 7.21 through 7.34.

The effect of the Monte Carlo tuning is very small. In the TOF-TOF case there is a 3% decrease in the reconstructed ϕ's after the tuning, whereas for EMC-EMC it is abut out 3%. For TOF-EMC, we can approximate the correction as $\sqrt{1.03}\,.\,\sqrt{1.01} \sim 1.02$.

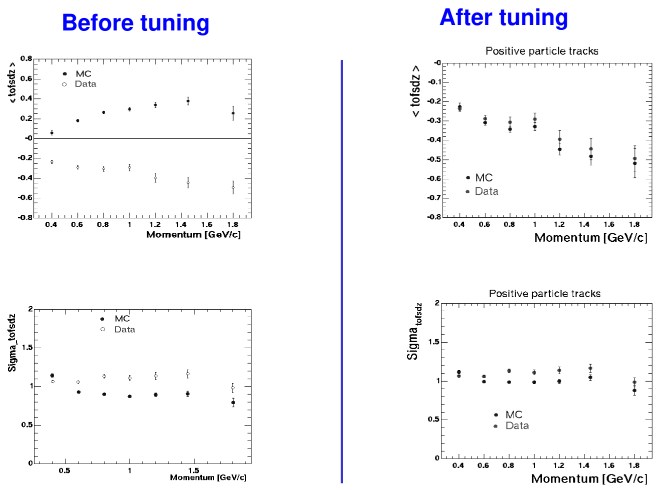

Figure 7.21: Centroid and sigma of dz_{TOF} for positive tracks before and after matching

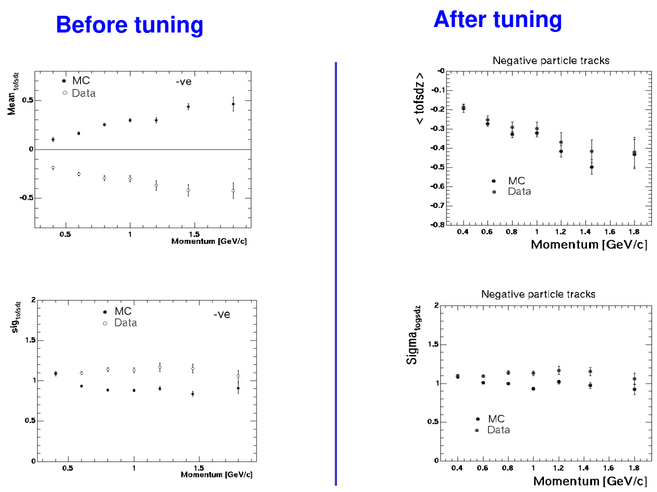

Figure 7.22: Centroid and sigma of dz_{TOF} for negative tracks before and after matching

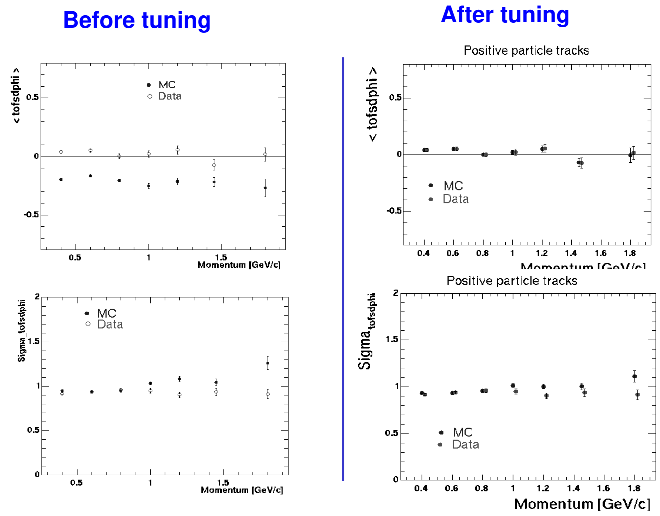

Figure 7.23: Centroid and sigma of $d\phi_{\mathrm{TOF}}$ for positive tracks before and after matching

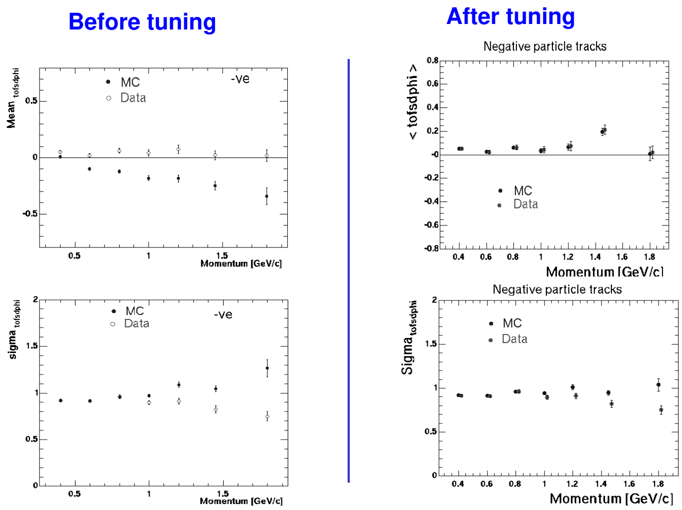

Figure 7.24: Centroid and sigma of $d\phi_{\mathrm{TOF}}$ for negative tracks before and after matching

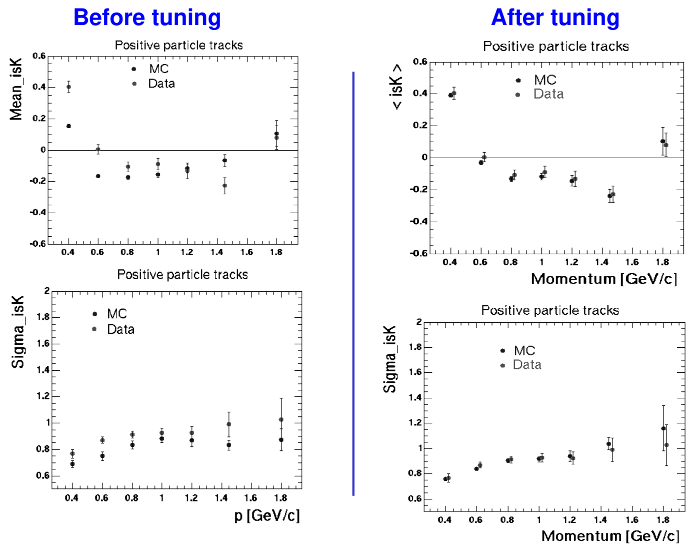

Figure 7.25: Centroid and sigma of isK for positive tracks before and after matching

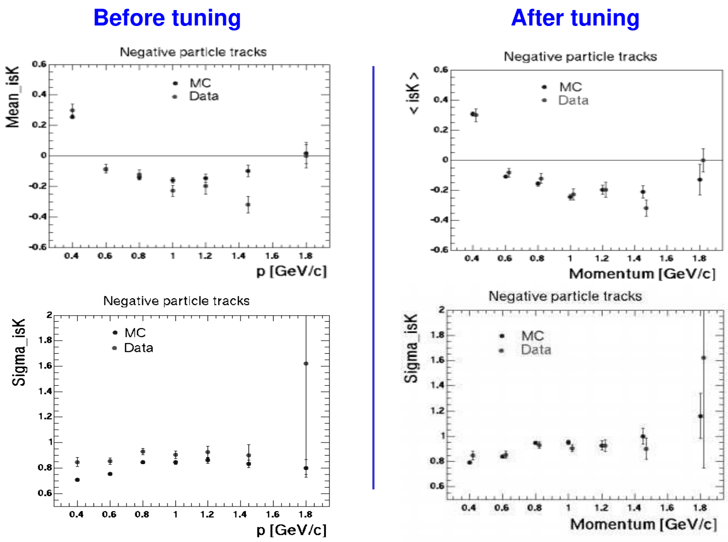

Figure 7.26: Centroid and sigma of isK for negative tracks before and after matching

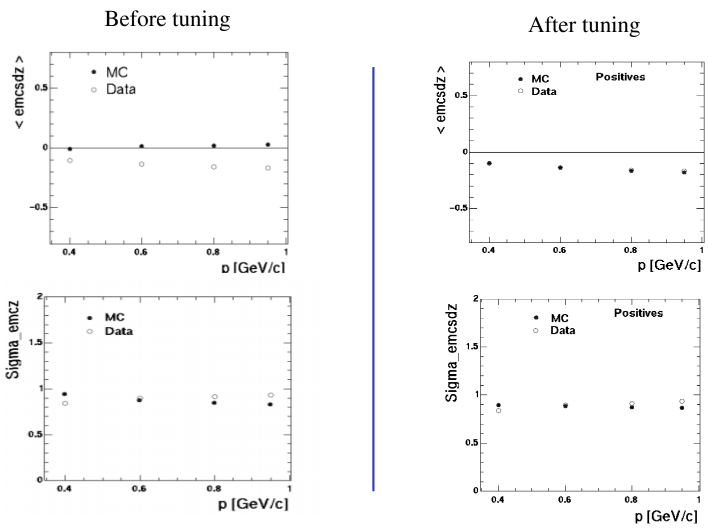

Figure 7.27: Centroid and sigma of dz_{EMC} for positive tracks before and after matching

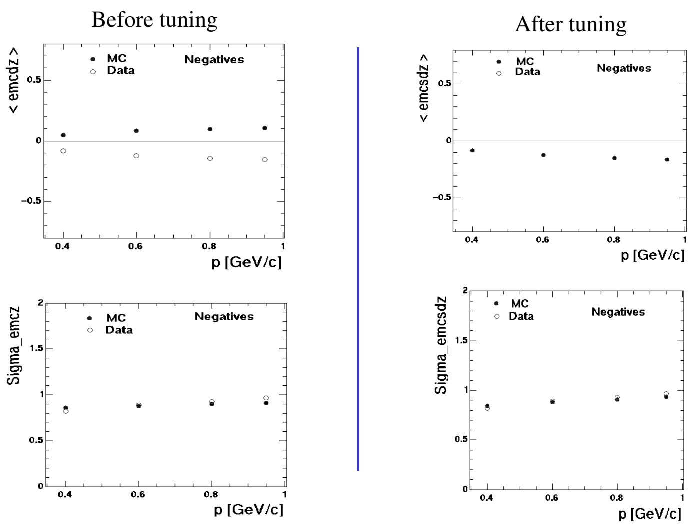

Figure 7.28: Centroid and sigma of dz_{EMC} for negative tracks before and after matching

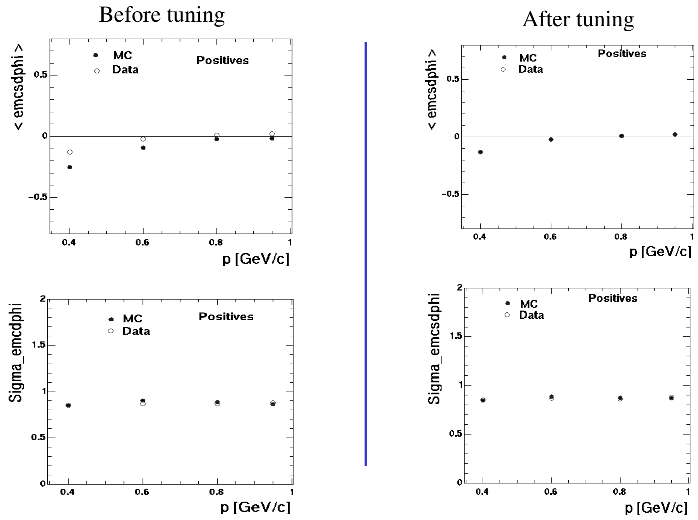

Figure 7.29: Centroid and sigma of $d\phi_{\mathrm{EMC}}$ for positive tracks before and after matching

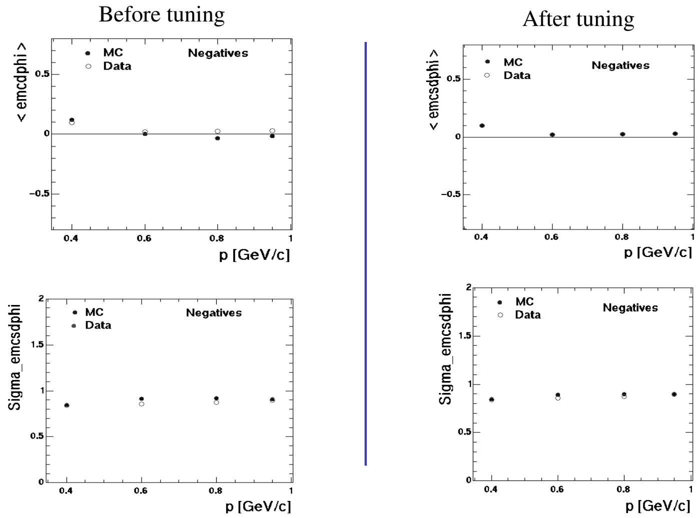

Figure 7.30: Centroid and sigma of $d\phi_{\mathrm{EMC}}$ for negative tracks before and after matching

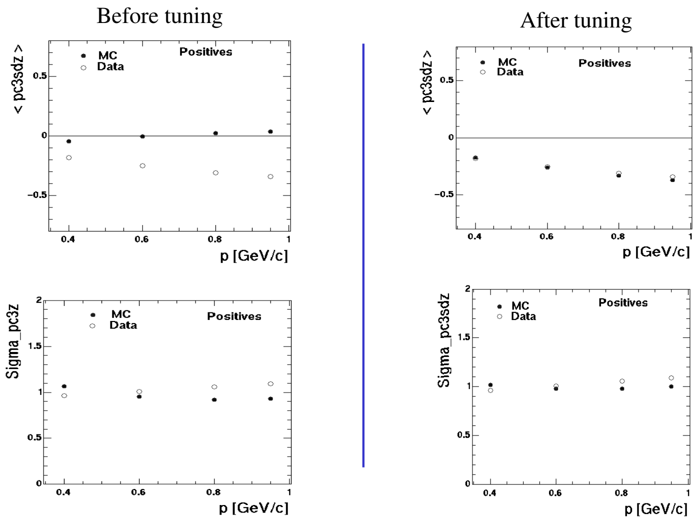

Figure 7.31: Centroid and sigma of dz_{PC3} for positive tracks before and after matching

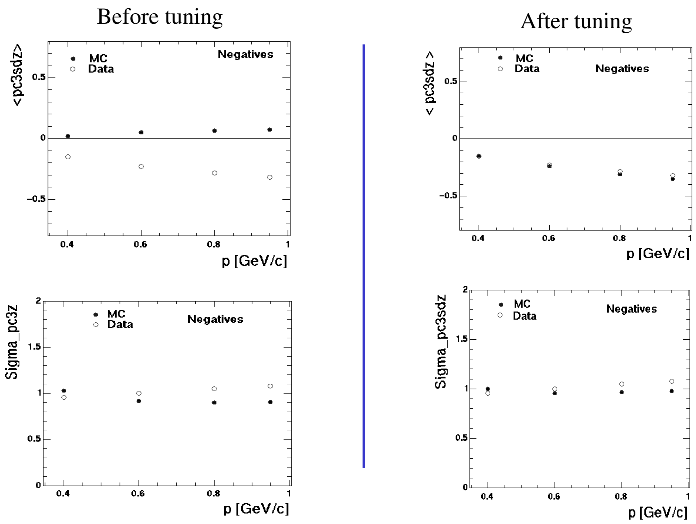

Figure 7.32: Centroid and sigma of dz_{PC3} for negative tracks before and after matching

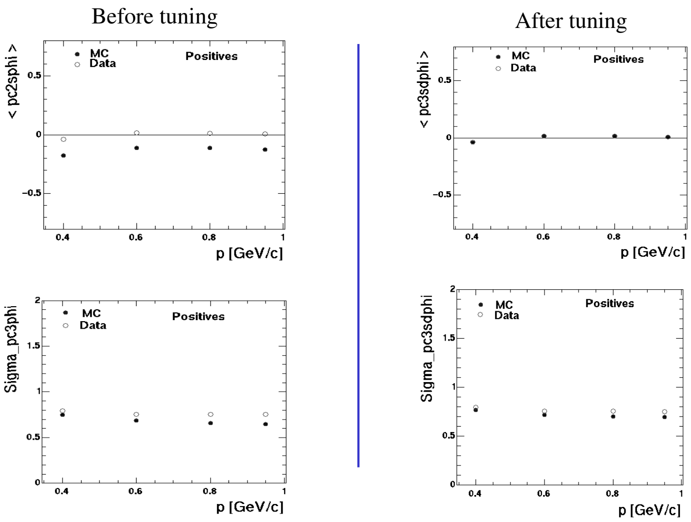

Figure 7.33: Centroid and sigma of $d\phi_{\mathrm{PC3}}$ for positive tracks before and after matching

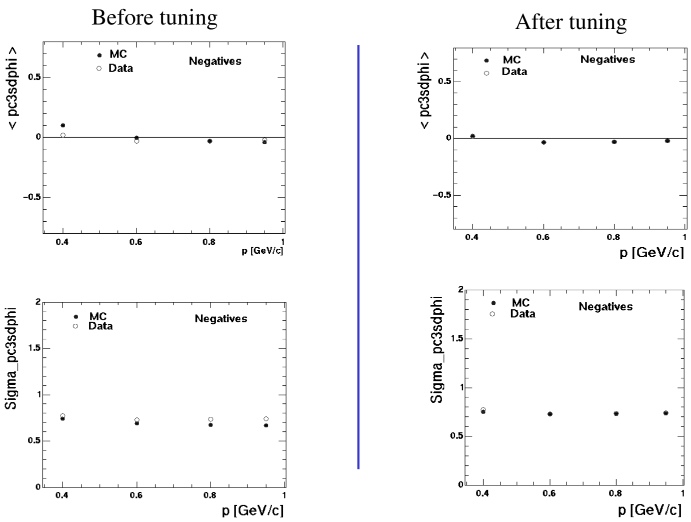

Figure 7.34: Centroid and sigma of $d\phi_{\mathrm{PC3}}$ for negative tracks before and after matching

7.5 Correction for the Relativistic Breit-Wigner Shape of the Data

The Monte Carlo is done for non-relativistic Breit-Wigner, but the real data follows relativistic Breit-Wigner. So a correction has to be made to account for this effect. The correction also depends on the mass window for signal extraction. Γ_{tune} is the correction for the mass window originating from the Monte Carlo. We give this correction for different mass windows in Table 7.8.

Mass Window (GeV/c^2)	Yield fraction in Breit-Wigner	Yield fraction in Rel Breit-Wigner	Γ_{tune}
1.014 - 1.024	0.726	0.690	1.06
1.009 - 1.029	0.862	0.821	1.05
1.004 - 1.034	0.908	0.869	1.04

Table 7.8: Correction for Breit-Wigner to Relativistic Breit-Wigner of the Monte Carlo for Different Mass Windows

Chapter 8

Result-I: ϕ Lineshape

In this section we will present results on the ϕ lineshape. It was observed in Section 6.4 that the ϕ mass centroids are consistent with the PDG value of 1.019567 GeV/c^2, but the widths are showing a trend of varying with the centrality. Due to the limited statistics for combinations such as TOF-TOF, TOF-EMC and EMC-EMC, a definite conclusion could not be drawn for the centrality variation of the width and mass. But we can add the contribution from the three combinations together and study the centrality dependence of ϕ mass and width. Also we will study the mass and width of $\overline{\Lambda}$ as a possible cross check of the centrality dependence of the ϕ mass and width, since $\overline{\Lambda}$ has zero natural width and the width is due to its decay in flight. The study of the variation of $\overline{\Lambda}$ mass and width as a function of centrality will not contain any medium effect and if there is any detector effect present it will manifest in the $\overline{\Lambda}$ analysis.

8.1 ϕ Invariant Mass Distribution from All East

We have reconstructed ϕ 's from TOF-TOF, TOF-EMC and EMC-EMC combinations. We can combine the contributions from the three combinations, which is the contribution from all of the East arm, and be denoted by AllEast. This will increase statistics significantly as compared to contribution from any individual combination.

It will also enable to reconstruct ϕ in many centrality bins. The statistics enables us to study ϕ mass and width in five centrality bins, $0\% - 10\%$, $10\% - 20\%$, $20\% - 40\%$, $40\% - 60\%$ and $60\% - 92\%$.

Since we have three components to add, we need to be careful to add them. The normalization should be proportional to the normalization of the individual components. Let us consider that there are N_{++i}, N_{--i}, N_{+-i} numbers of like and unlike sign pairs in the component i and B_{+-i} is the number if mixed event unlike sign pairs. Then B_{+-i} is normalized to $2\sqrt{N_{++i} \,.\, N_{--i}}$ as given in Eq. (6.19). Thus we can write the normalization constant for component i as:

$$N_i = \frac{2\sqrt{N_{++i} \,.\, N_{--i}}}{B_{+-i}} \tag{8.1}$$

The AllEast combination will contain $N_{+-} = \sum_i N_{+-i}$ same event unlike sign pairs and $B_{+-} = \sum_i B_{+-i}$ mixed event unlike sign pairs. The normalization factor is then simply given by

$$N = \frac{\sum_i N_{+-i}\ N_i}{\sum_i N_{+-i}} \tag{8.2}$$

The ϕ invariant mass distribution for the AllEast combination are shown Fig (8.1) through Fig (8.12). In Figs (8.1), (8.3), (8.5), (8.7)(8.9) and (8.11) the same event unlike-sign pair invariant mass are represented in the red points. They are superimposed on the predicted mixed event unlike-sign pairs invariant mass in yellow. Fig (8.2), (8.4), (8.6), (8.8), (8.10) and (8.12) shows the background subtracted invariant mass plots. Very distinct ϕ peaks are observed. They are fitted with a relativistic Breit-Wigner convoluted with a Gaussian. The ϕ signal, mass and width is tabulated in Table 8.1.

8.2 Centrality Dependence of Mass and Width

The ϕ mass centroid obtained from the fitting are plotted vs centrality in Fig 8.13. The red points correspond to the data points corresponding to the centrality bin and

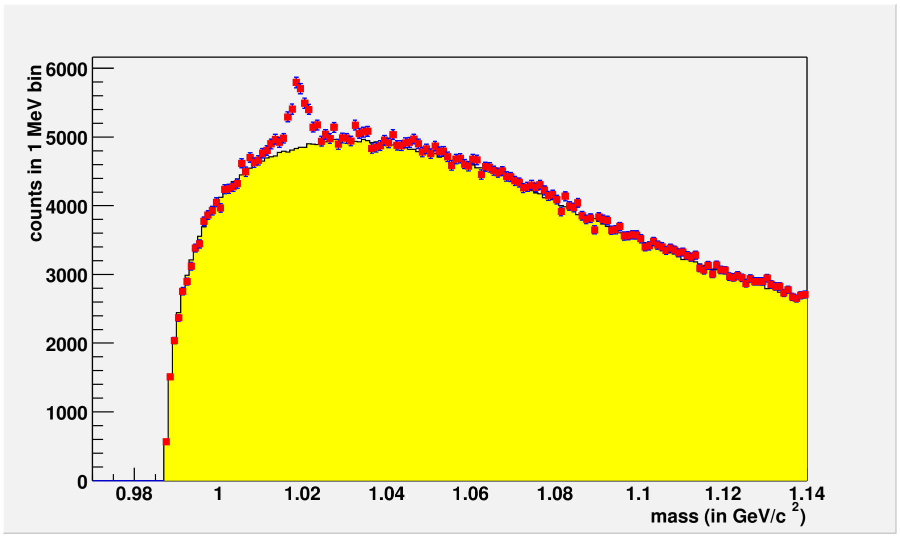

Figure 8.1: Unlike sign signal and combinatoric mass spectra in AllEast for minimum bias events

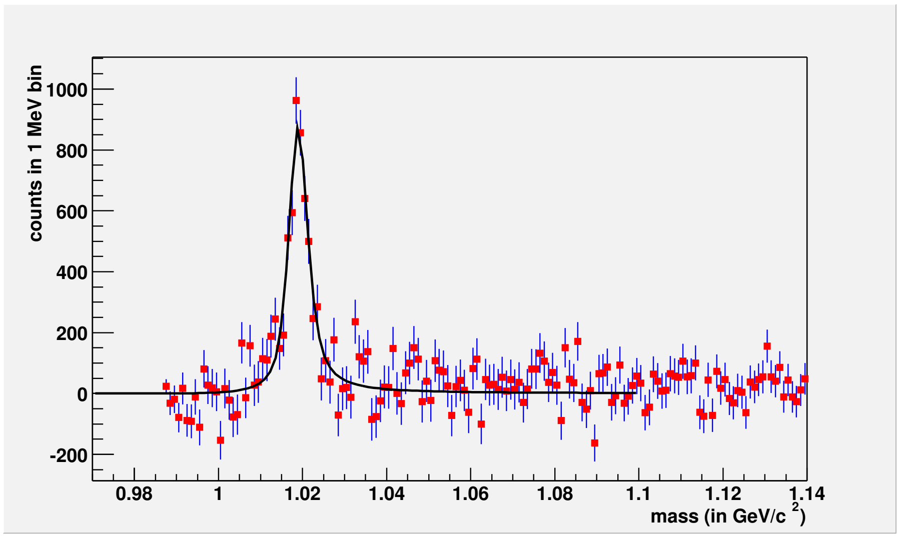

Figure 8.2: Invariant mass spectra in AllEast for minimum bias events

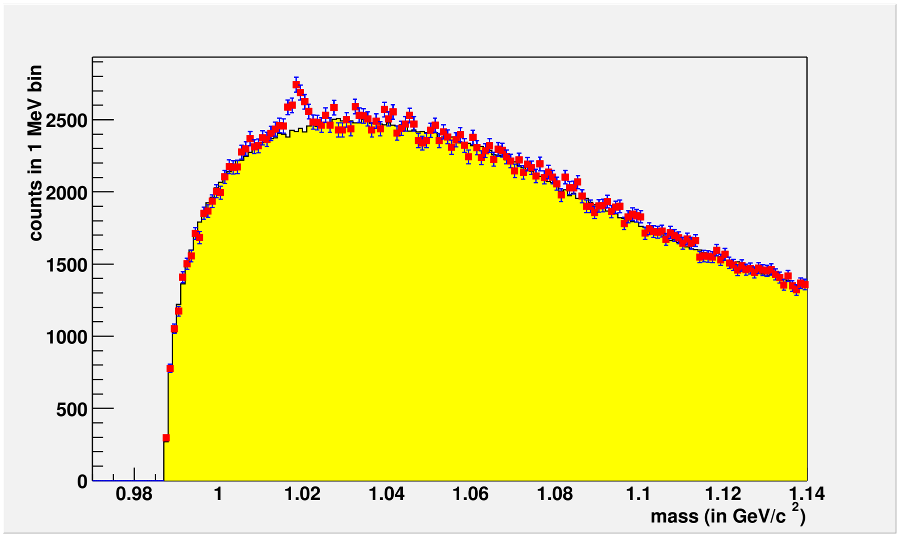

Figure 8.3: Unlike sign signal and combinatoric mass spectra in AllEast for most central (0% $-$ 10%) events

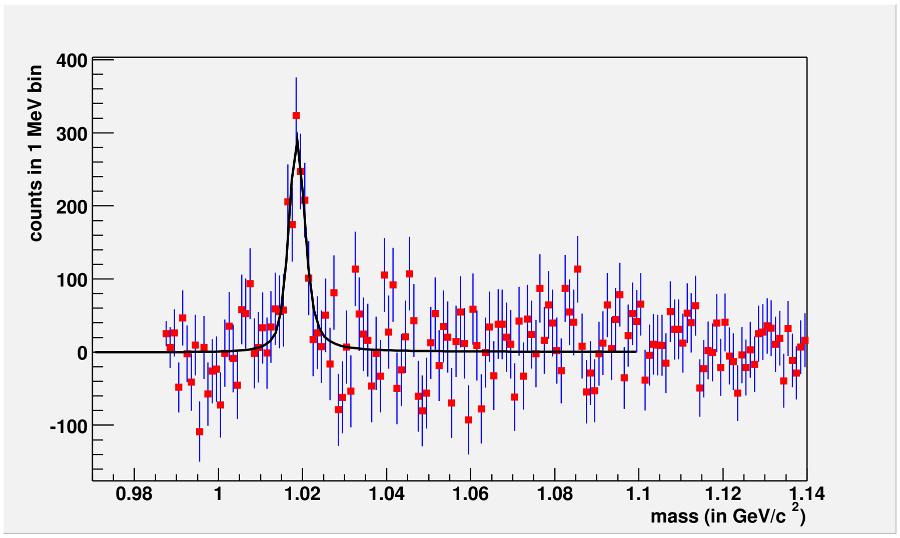

Figure 8.4: Invariant mass spectra in AllEast for most central (0% $-$ 10%) events

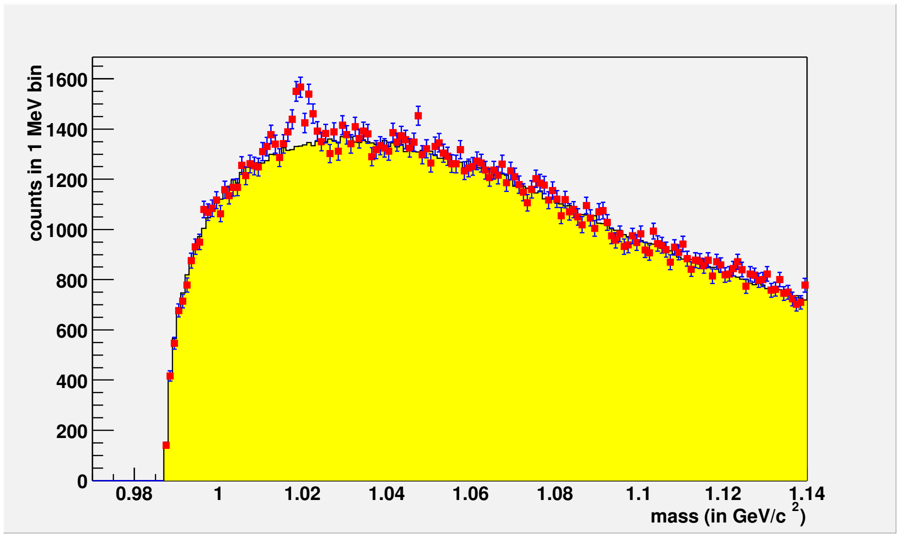

Figure 8.5: Unlike sign signal and combinatoric mass spectra in AllEast for mid-central (10% $-$ 20%) events

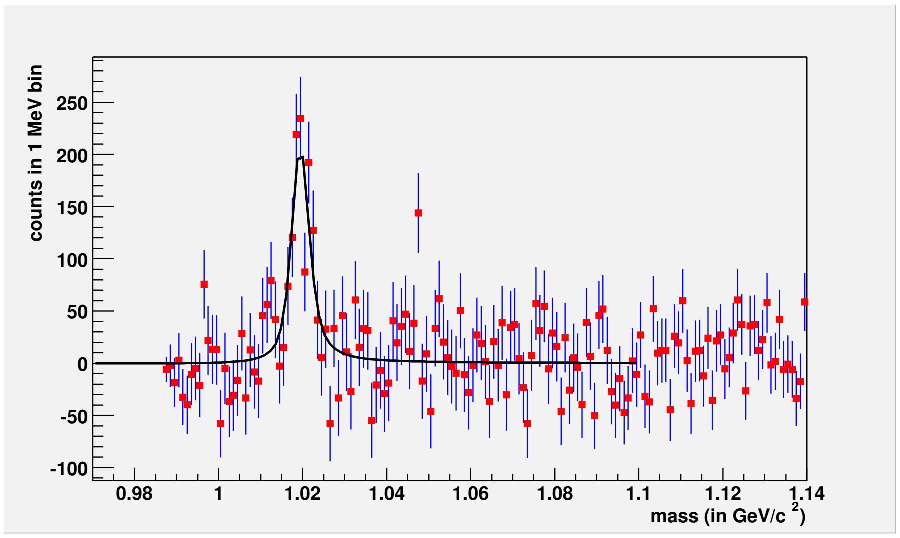

Figure 8.6: Invariant mass spectra in AllEast for mid-central (10% $-$ 20%) events

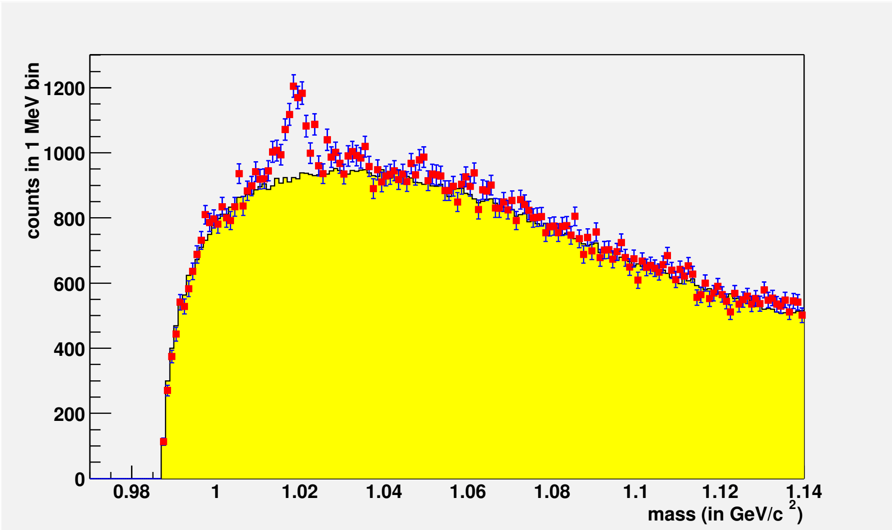

Figure 8.7: Unlike sign signal and combinatoric mass spectra in AllEast for mid-central (20% − 40%) events

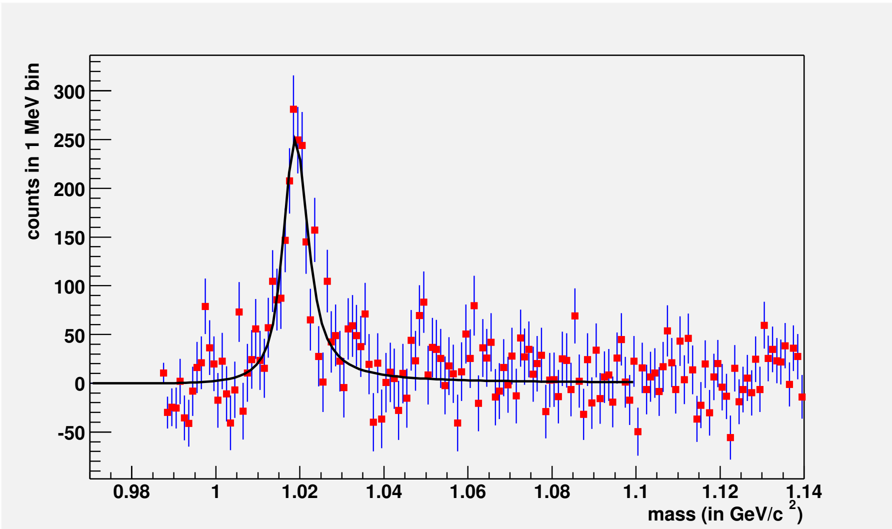

Figure 8.8: Invariant mass spectra in AllEast for mid-central (20% − 40%) events

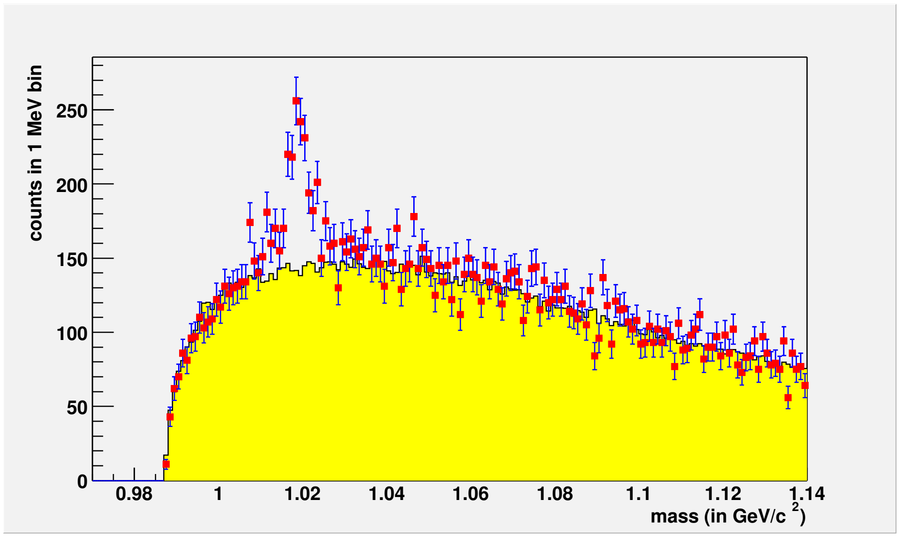

Figure 8.9: Unlike sign signal and combinatoric mass spectra in AllEast for peripheral ($40\% \ - \ 60\%$) events

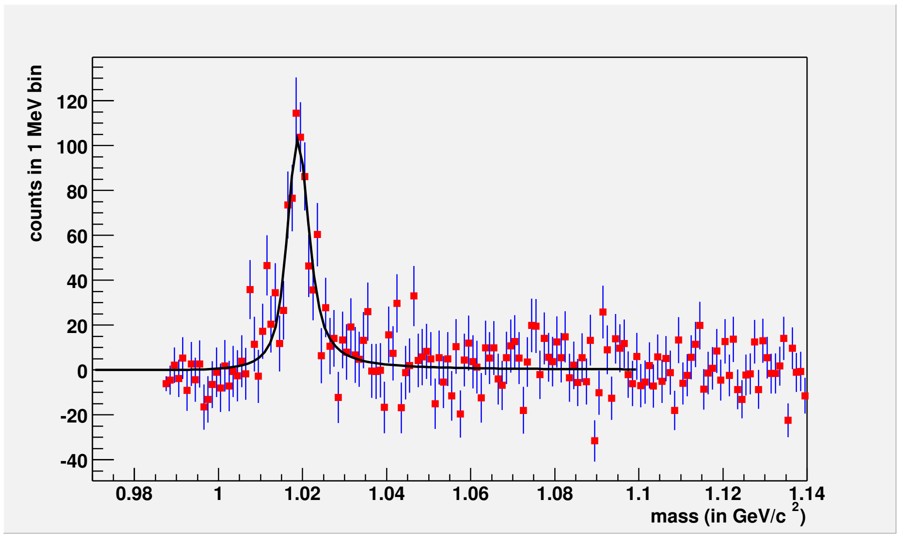

Figure 8.10: Invariant mass spectra in AllEast for peripheral ($40\% \ - \ 60\%$) events

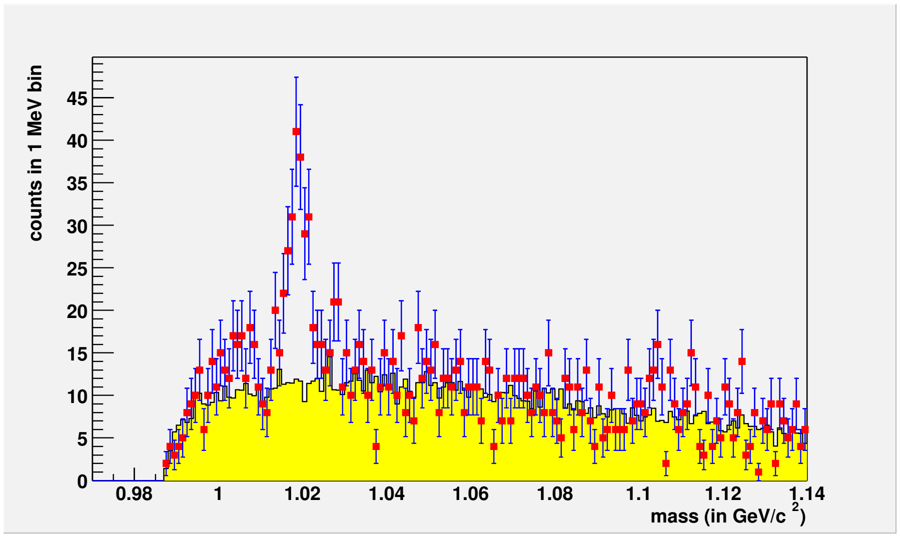

Figure 8.11: Unlike sign signal and combinatoric mass spectra in AllEast for peripheral (60% − 92%) events

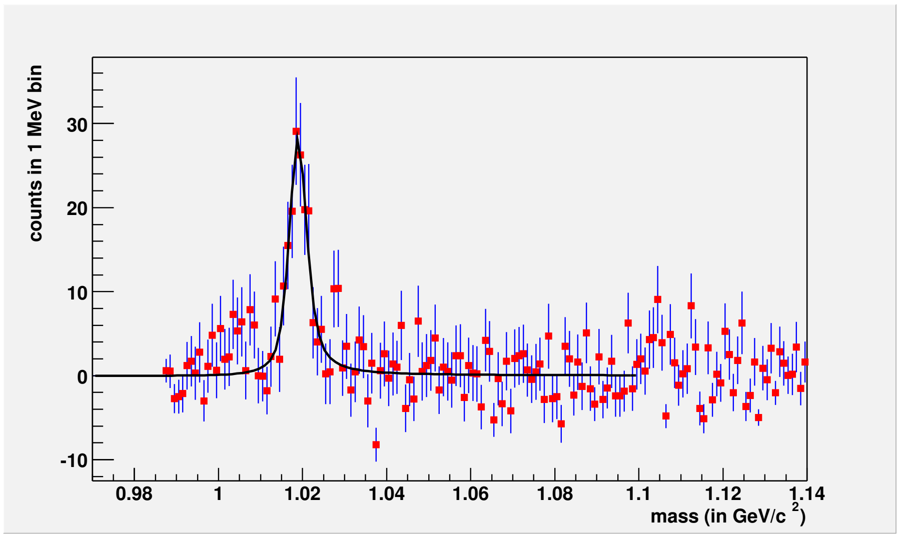

Figure 8.12: Invariant mass spectra in AllEast for peripheral (60% − 92%) events

Centrality	ϕ Signal	Bkg	S/B	Mass (GeV/c^2)	Γ (MeV/c^2)
Min Bias	4936±307	48380	1/9.8	1.01903±0.00014	3.77502±0.475022
0% – 10%	1415±202	24260	1/17.1	1.01868±0.00028	2.55023±0.858423
10% – 20%	1108±151	13280	1/12.0	1.01950±0.00032	3.25329±0.903986
20% – 40%	1669±144	9247	1/5.5	1.01908±0.00025	5.82092±0.925963
40% – 60%	636±58	1433	1/2.3	1.01900±0.00025	4.73418±0.841538
40% – 92%	153±19	115	1/0.8	1.01897±0.00031	3.20214±0.80 7876

Table 8.1: ϕ Signal, background, Mass centroid and the full-width at half maxima for AllEast Pairs The Signal and backgrounds are counted in the mass window of 1.014 $GeV/c^2 < M_{inv} < 1.024$ GeV/c^2.

the blue line is the value of the minimum bias spectra. It is evident that the data points agree very well with each other within the statistical limits and are very close to the PDG value. There is no centrality dependence in the ϕ mass centroid.

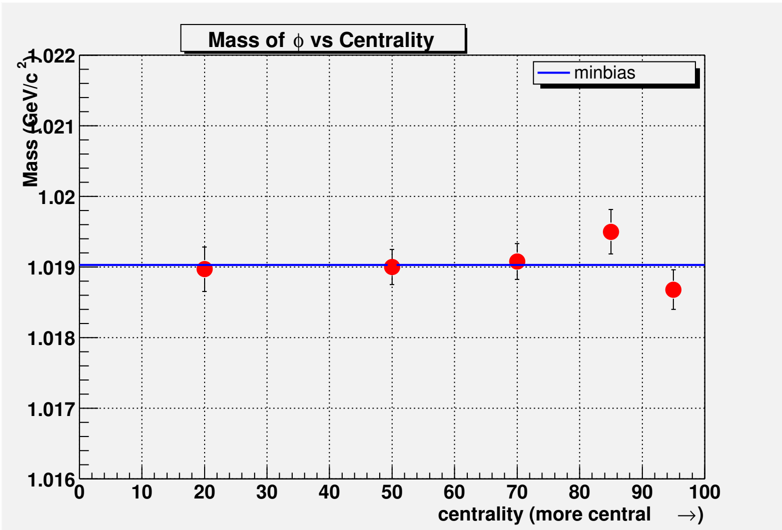

Figure 8.13: The ϕ mass centroid from the AllEast combinations as a function of the centrality

But there is a big surprise in the centrality dependence of the ϕ width. The ϕ width obtained from the fitting are plotted vs centrality in Fig 8.14. The red points correspond to the data points corresponding to the centrality bin and the blue line is the value of the minimum bias spectra. The centrality dependence of the ϕ width is a

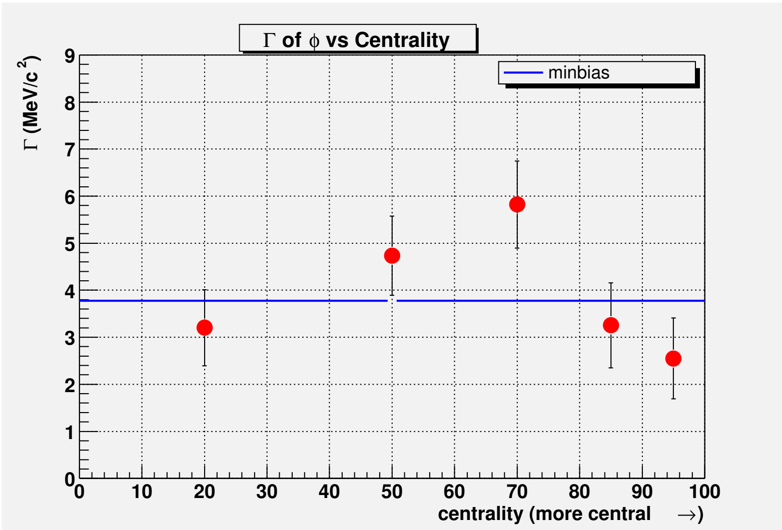

Figure 8.14: The ϕ width from the AllEast combinations as a function of the centrality

new phenomena observed. The dependence is strikingly strong. In fact the difference in the lowest and highest points are more than 2-σ of the statistical uncertainty. We need to exclude any possibility of detector effect or statistical fluctuation to prove that what we see here in Fig. 8.14 is real. The detector effect, if there is any, can be tested with from the study of Λ or $\overline{\Lambda}$ width.

8.3 Analysis on $\overline{\Lambda}$

The Λ or $\overline{\Lambda}$ can be reconstructed in the PHENIX central arm. We will reconstruct the $\overline{\Lambda}$ in their weak decay channel $\overline{\Lambda} \rightarrow \overline{p}\pi^+$. The mass of $\overline{\Lambda}$ is 1.115683 GeV/c^2 and zero natural width. The width of $\overline{\Lambda}$ is due to its decay in flight.

The run conditions and data sample selection is similar to those for ϕ analysis as described in Section 4.8, except for the following. In the TOF, the momentum range of $\overline{p}$ are between 500 MeV/c and 3.0 GeV/c, and for π^+ s between 250 MeV/c and 1.8 GeV/c. Also a 2.5-σ PID cut on the calibrated mass squared of $\overline{p}$ and π^+ ($|\ isP\ | < 2.0$ and $|\ isPi\ | < 2.0$). For tracks identified in the EMCal $isPi$ and isK are calculated using EMCal resolution of 480 ps and a 2-σ PID cut applied to both protons and pions. We follow exactly the same procedure for invariant mass reconstruction as for ϕ. For the normalization of the background the like-sign normalization fails. Therefore we use normalize the unlike sign spectrum in the mass range 1.13 GeV/c^2 $<\ M_{inv}\ <$ 2.5 GeV/c^2. Since the width of the $\overline{\Lambda}$ comes from its decay in flight, the shape of the invariant mass spectra is expected to be a Gaussian. We need to incorporate the detector mass resolution of ~1.24 MeV.c^2 while fitting. To fit the peak we fit a Gaussian with a second Gaussian of width as the detector mass resolution. We make use of the fact that the convolution of a Gaussian of width σ_1 with another Gaussian of width σ_2 is again a Gaussian of width $\sqrt{\sigma_1^2\ +\ \sigma_2^2}$.

8.3.1 $\overline{\Lambda}$ Invariant Mass Distribution from All East

The $\overline{\Lambda}$ invariant mass distribution for the AllEast combination are shown Fig (8.15) through Fig (8.24). In Figs (8.15), (8.17), (8.19)(8.21) and (8.23) the same event unlike-sign pair invariant mass are represented in the red points. They are superimposed on the predicted mixed event unlike-sign pairs invariant mass in yellow. Fig (8.16), (8.18), (8.20), (8.22) and (8.24) shows the background subtracted invariant mass plots. Very distinct $\overline{\Lambda}$ peaks are observed. They are fitted with a Gaussian convoluted with another Gaussian. The $\overline{\Lambda}$ signal, mass and width is tabulated in Table 8.2.

8.3.2 Centrality Dependence of $\overline{\Lambda}$ Mass and Width

The $\overline{\Lambda}$ mass centroid obtained from the fitting are plotted vs centrality in Fig 8.25. The data points agree very well with each other within the statistical limits. There is no apparent centrality dependence in the $\overline{\Lambda}$ mass centroid.

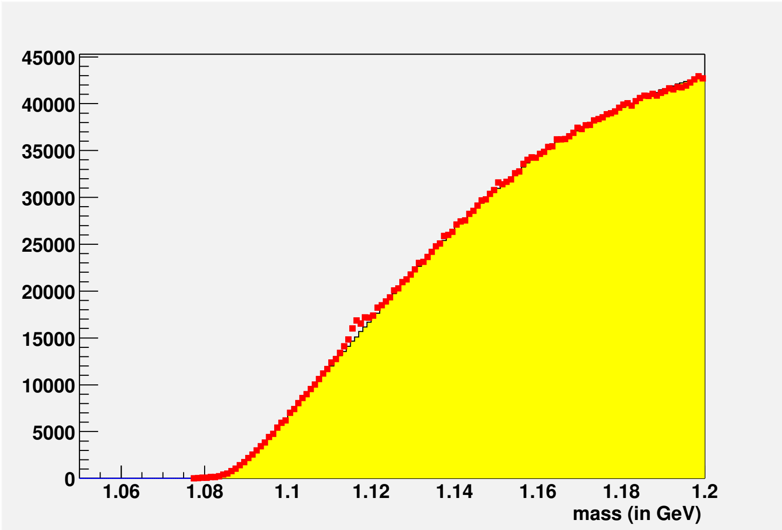

Figure 8.15: Unlike sign signal and combinatoric mass spectra in AllEast for most central (0% − 10%) events

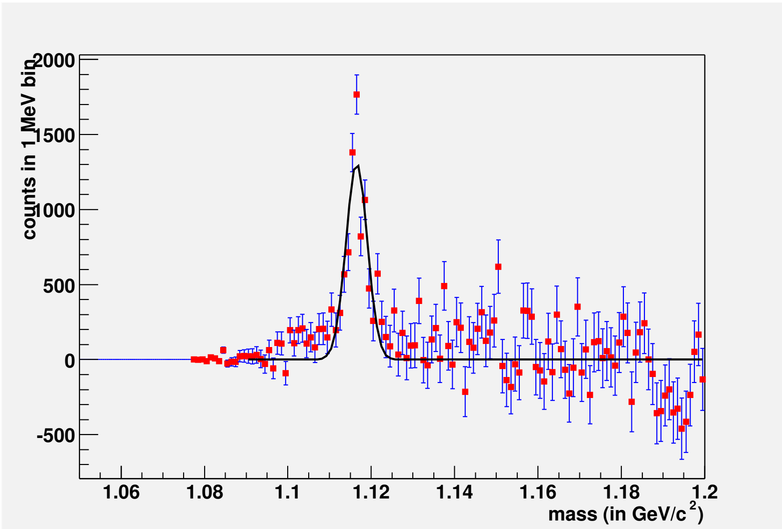

Figure 8.16: Invariant mass spectra in AllEast for most central (0% − 10%) events

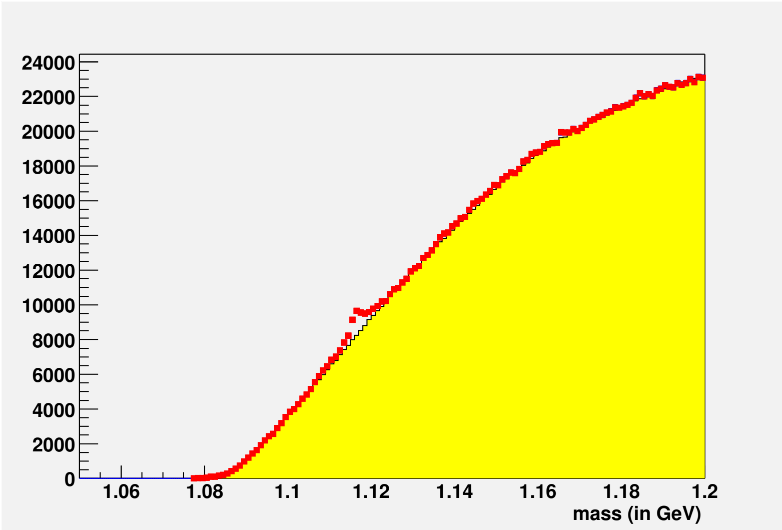

Figure 8.17: Unlike sign signal and combinatoric mass spectra in AllEast for mid-central (10% − 20%) events

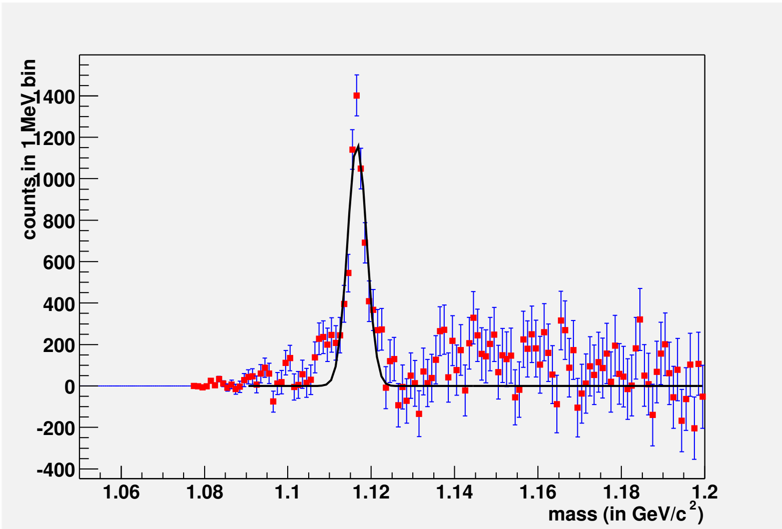

Figure 8.18: Invariant mass spectra in AllEast for mid-central (10% − 20%) events

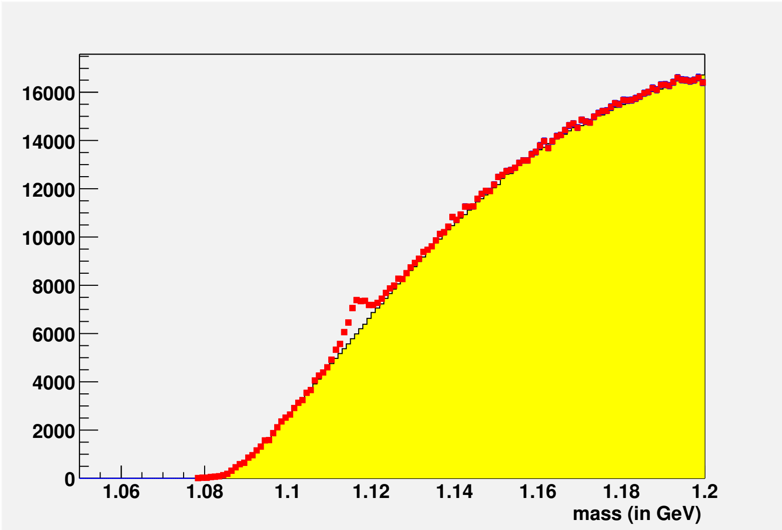

Figure 8.19: Unlike sign signal and combinatoric mass spectra in AllEast for mid-central (20% − 40%) events

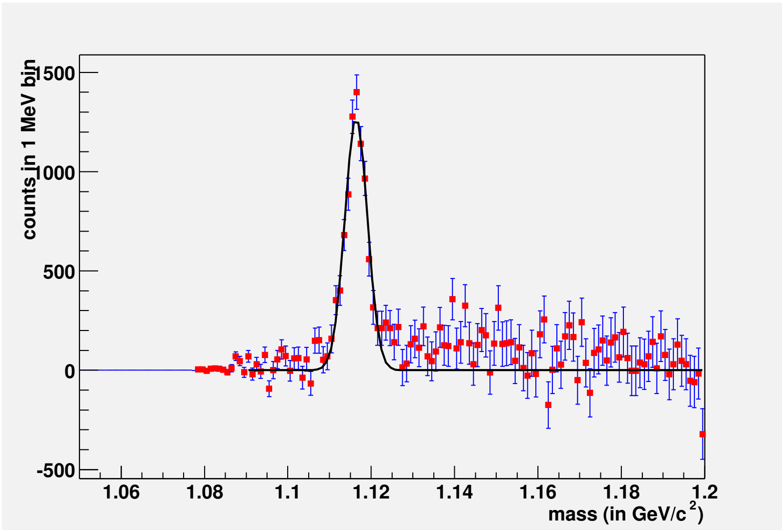

Figure 8.20: Invariant mass spectra in AllEast for mid-central (20% − 40%) events

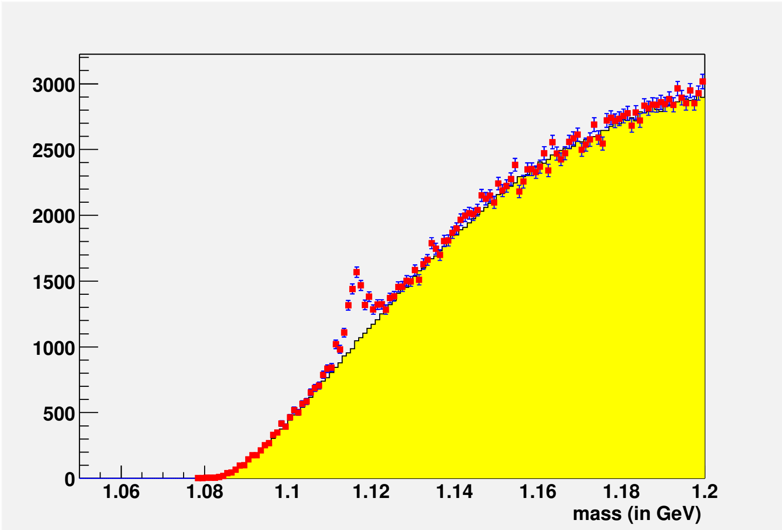

Figure 8.21: Unlike sign signal and combinatoric mass spectra in AllEast for peripheral (40% − 60%) events

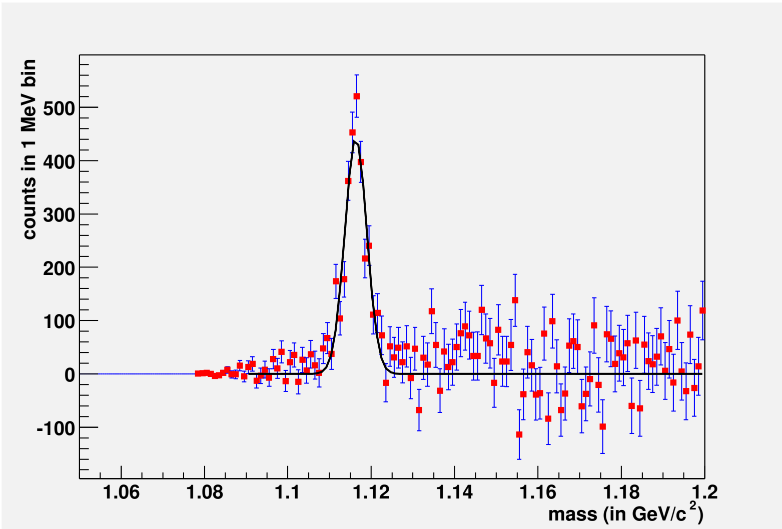

Figure 8.22: Invariant mass spectra in AllEast for peripheral (40% − 60%) events

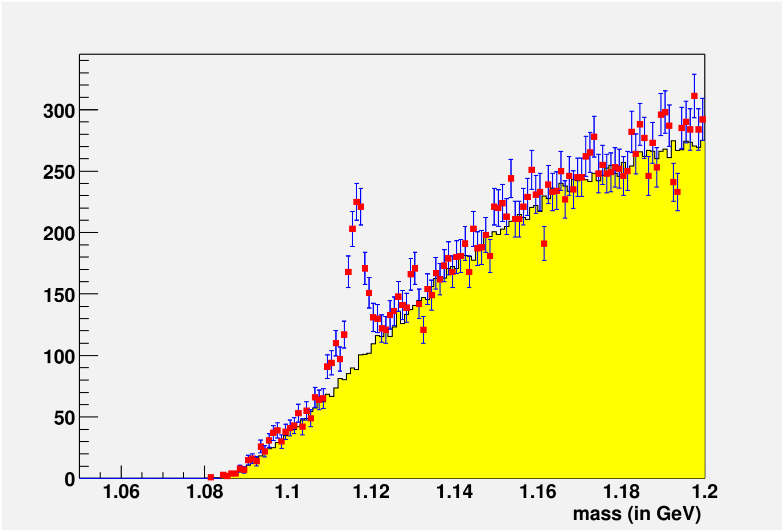

Figure 8.23: Unlike sign signal and combinatoric mass spectra in AllEast for peripheral (60% − 92%) events

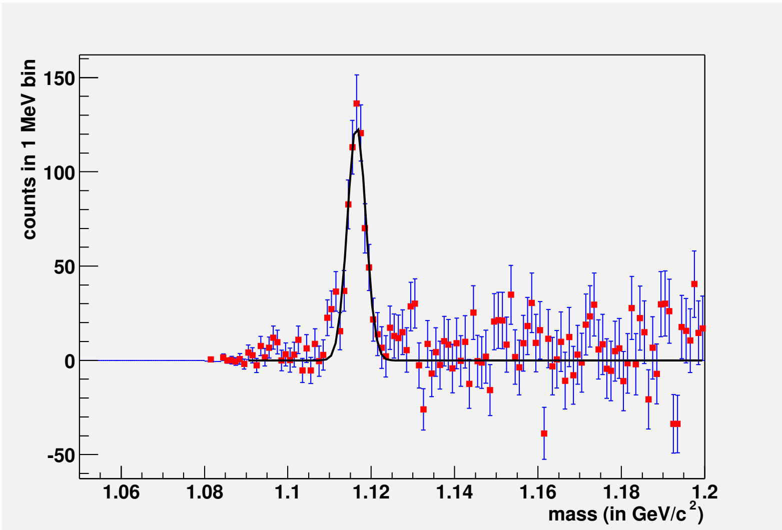

Figure 8.24: Invariant mass spectra in AllEast for peripheral (60% − 92%) events

Centrality	$\overline{\Lambda}$ Signal	Bkg	S/B	Mass (GeV/c^2)	Width (MeV/c^2)
0% – 10%	7359±501	136132	1/18.5	1.11651±0.00017	2.23480±0.287191
10% – 20%	6245±385	74354	1/11.9	1.11661±0.00013	1.93197±0.241372
20% – 40%	7627±301	54008	1/7.1	1.11638±0.00011	2.41237±0.148170
40% – 60%	2582±138	9282	1/3.6	1.11631±0.00014	2.33445±0.195168
60% – 92%	645±51	838	1/1.3	1.11649±0.00015	1.81984±0.236996

Table 8.2: $\overline{\Lambda}$ Signal, background, Mass centroid and the width for AllEast Pairs The Signal and backgrounds are counted in the mass window between 1.112 GeV/c^2 and 1.122 GeV/c^2.

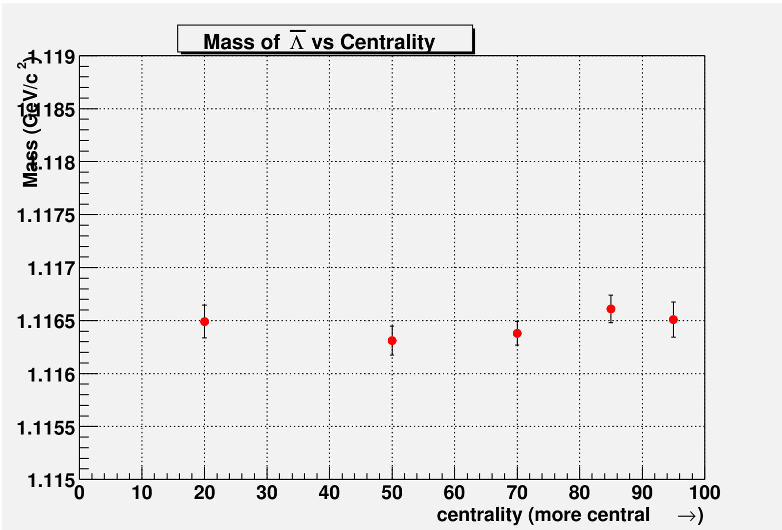

Figure 8.25: The $\overline{\Lambda}$ mass centroid from the AllEast combinations as a function of the centrality

The $\overline{\Lambda}$ width obtained from the fitting are plotted vs centrality in Fig. 8.26. We do not see any centrality dependence of the $\overline{\Lambda}$ width. We also investigate if there is any

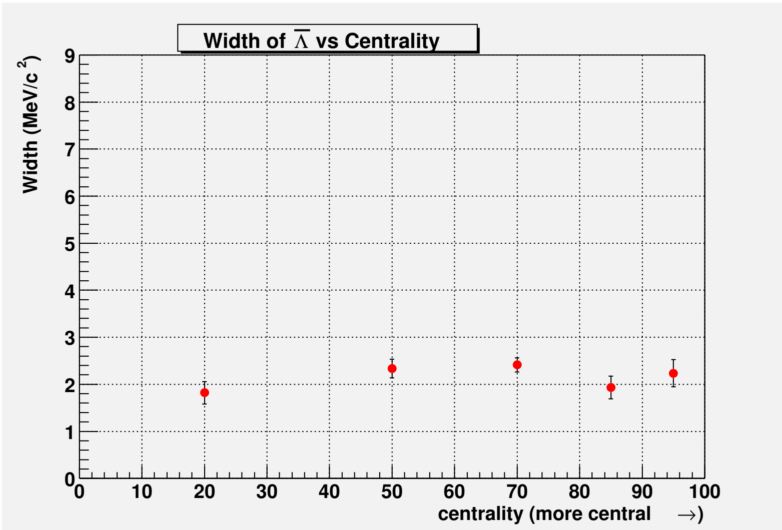

Figure 8.26: The $\overline{\Lambda}$ width from the AllEast combinations as a function of the centrality

effect $\overline{\Lambda}$ decay vertex on the $\overline{\Lambda}$ width. low-p_T $\overline{\Lambda}$ will decay close to the collision vertex, whereas high-p_T $\overline{\Lambda}$ will decay away from vertex. We plot the $\overline{\Lambda}$ width vs centrality for two transverse mass range of $\overline{\Lambda}$, low-p_T $\overline{\Lambda}$ for 0.5 GeV/c $< p_T <$ 1.3 GeV/c and high-p_T $\overline{\Lambda}$ for 1.3 GeV/c $< p_T <$ 3.0 GeV/c in Figs. 8.27 and 8.28 to see if there is any effect of where the decay occurs in the flight path on the width. There is no dependence of the p_T on the width of $\overline{\Lambda}$.

Thus there is no centrality dependence of the $\overline{\Lambda}$ width. This confirms that there is no detector effect on the observed centrality dependence of ϕ width. To demonstrate how large the effect is we plot both the ϕ width and $\overline{\Lambda}$ width in Fig. 8.29

8.4 Is it a Statistical Fluctuation

Another check we need to make on the centrality dependence of the ϕ width is whether it is a statistical fluctuation. To test that we simulate ϕ s in the PHENIX central

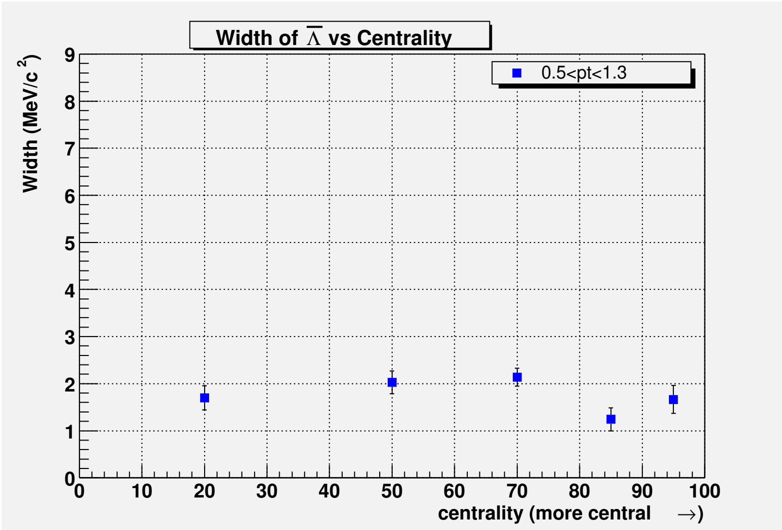

Figure 8.27: The $\overline{\Lambda}$ width from the AllEast combinations as a function of the centrality for low-p_T $\overline{\Lambda}$

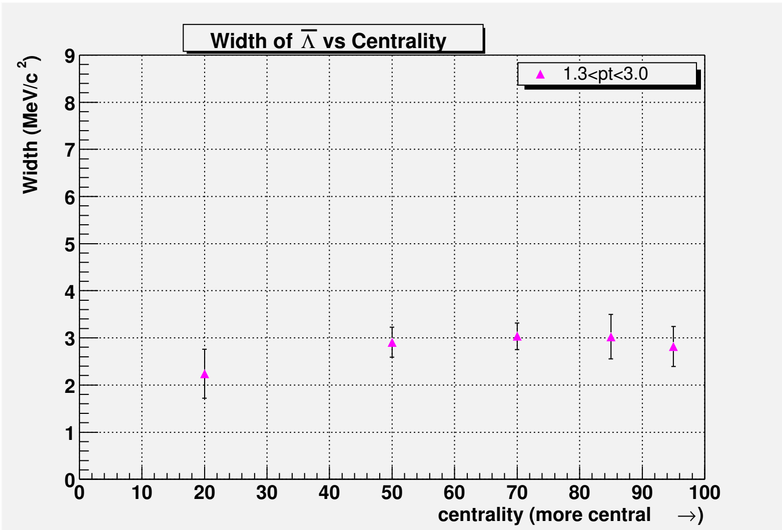

Figure 8.28: The $\overline{\Lambda}$ width from the AllEast combinations as a function of the centrality for high-p_T $\overline{\Lambda}$

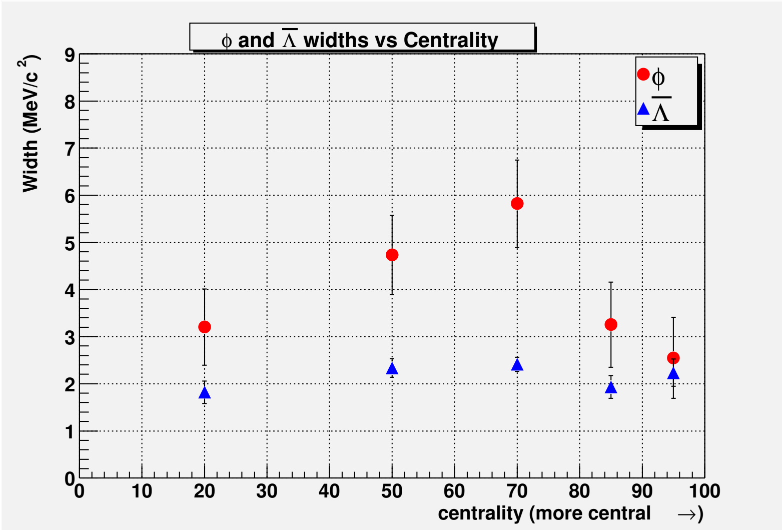

Figure 8.29: The Γ of ϕ and $\overline{\Lambda}$ width from the AllEast combinations as a function of the centrality.

arm with the same conditions as seen in the year-2 real data. That is we generate ϕ's of same signal to background ratio as in the real data. The generated ϕ's have 4.2 MeV/c^2 Breit-Wigner width. We generate 1000 such events and for each event we measure the width and mass centroid of reconstructed ϕ's. Fig. 8.30 shows such a plot. We have generated events for central collisions as well as for minimum bias condition. The left half of the plot are for central collision S/B conditions, and the right half is for minimum bias S/B condition. The top two plots are the distribution for the simulated phi signal. It mimics the real data signal to background ratio. These ϕ's are then processed through the PHENIX central arm simulation detector and the mass centroid and the width are measured after the reconstruction. We produce 100 events. The mass centroid of the reconstructed ϕ's are shown in the middle two plots for the 1000 events and the width of them are shown in the bottom two plots. Since in real data we see ϕ width going below 3 MeV/c^2 we ask what is the statistical probability of such an event. From the study we can say that such a probability is about 11% or less. The statistical probability of finding a width of 2.5 MeV/c^2 , which

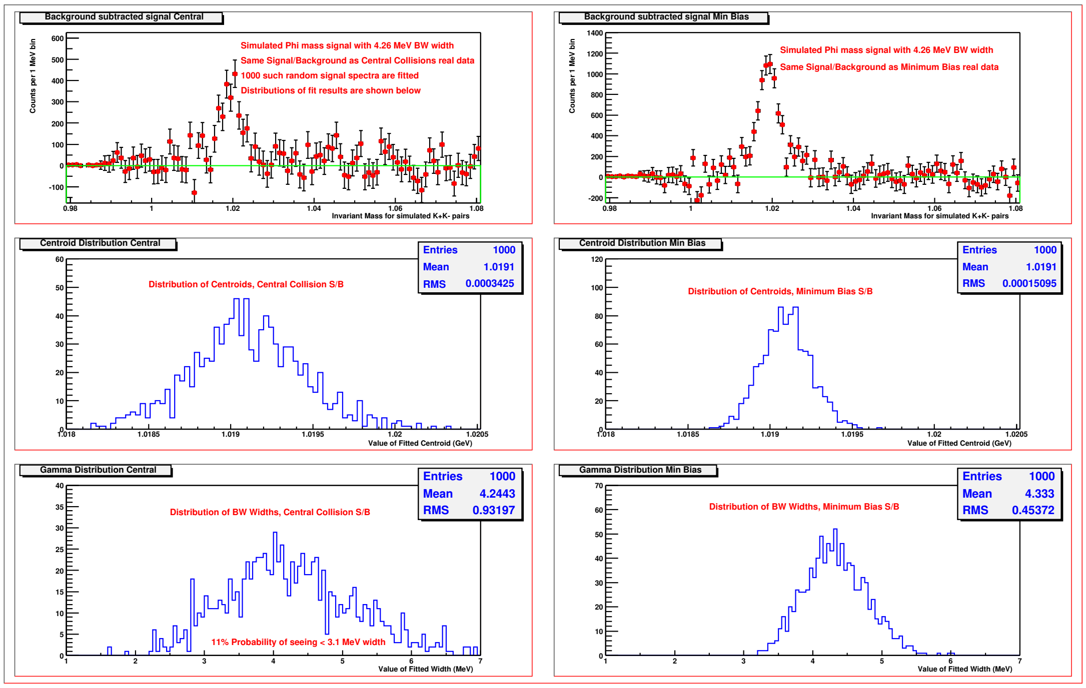

Figure 8.30: Study on the statistical fluctuation of ϕ for year-2 run condition

is seen in the most central collisions, are even lower and less than 5%. Therefore the centrality dependence of the ϕ width can not be attributed as a statistical fluctuation.

Chapter 9

Analysis of the ϕ Yields

One of the two very important studies we aim to perform is the ϕ transverse mass distribution and extraction of ϕ yield and inverse slope parameters, the other being the mass centroid and width of ϕ. In this chapter we present the measurements on the ϕ yield. We will make the measurement for minimum bias data and also look for the centrality dependence of the yield. The temperature of ϕ will also be presented.

9.1 Strategy

The differential yield is give by Eq. (2.32). So me make a number of (m_T, y) bins. Since the rapidity coverage of PHENIX is only ± 0.35 units, we in fact make only one bin in rapidity and a number of bins in the transverse mass, depending on the transverse mass distribution of the reconstructed ϕ's. For the TOF-TOF combination the range of the transverse mass is 1.2 GeV/c^2 to 4.0 GeV/c^2. For TOF-EMC combination 1.2 GeV/c^2 $< m_T <$ 2.8 GeV/c^2 and for EMC-EMC combination it is 1.2 GeV/c^2 $< m_T <$ 2.2 GeV/c^2. The analysis is done in the following way:

1. Make a number of m_T bins. The bins we make are:

   (a) TOF-TOF combination: $8 m_T$ bins; 1.2 - 1.6, 1.6 - 1.8, 1.8 - 2.0, 2.0 - 2.2, 2.2 - 2.4, 2.4 - 2.8, 2.8 - 3.0.

(b) TOF-EMC combination: $6 m_T$ bins; 1.2 - 1.6, 1.6 - 1.8, 1.8 - 2.0, 2.0 - 2.2, 2.2 - 2.4, 2.4 - 2.8.

(c) TOF-TOF combination: $4 m_T$ bins; 1.2 - 1.6, 1.6 - 1.8, 1.8 - 2.0, 2.0 - 2.2.

2. Divide the data into different centrality classes.

   (a) Most central: $0\% - 10\%$

   (b) Mid central: $10\% - 40\%$

   (c) Peripheral: $40\% - 92\%$

   (d) Minimum Bias: $0\% - 92\%$

3. For each m_T and centrality bin find the number of raw ϕ yield. This is done by counting the number of signals over the number of normalized background within the mass window of $1.014\text{GeV/c}^2 < M_{inv} < 1.024\ \text{GeV/c}^2$.

4. The raw yield is then corrected for the detector acceptance, run-by-run detector efficiency, and correction for the efficiency loss due to high occupancy (embedding correction), tuning correction of the simulated data and the correction applied to the simulated data for the Breit-Wigner nature of the distribution. Also the branching ratio of $\phi \rightarrow K^+K^-$ is taken into account.

5. The differential yield is computed with all the correction applied to it.

6. The differential yields are then plotted versus the transverse mass and fitted with an exponential. The fit parameters give the ϕ yield dN/dy and the inverse slope parameter or the temperature.

9.2 Differential Yield

The ϕ differential yield is calculated as in the Eq.(9.1).

$$\frac{1}{2\pi m_T}\frac{d^2N}{dm_T dy} = \frac{1}{2\pi m_T}\frac{N_\phi}{N_{evt}}\mathrm{CF}\frac{1}{\epsilon_{\mathrm{embed}}}\frac{1}{\mathrm{BR}}\frac{1}{\Delta \mathrm{m_T}}.\mathrm{Corrections} \tag{9.1}$$

where,

$$\begin{aligned}
\mathrm{CF} &= \frac{MC_{thrown}}{MC_{accepted}} \\
\mathrm{Corrections} &= \epsilon_{run-by-run}.MC_{tune}.\Gamma_{tune} \\
MC_{tune} &= 1.03 \\
\Gamma_{tune} &= 1.06
\end{aligned}$$

MC_{thrown} and $MC_{accepted}$ are the number of Monte-Carlo particle thrown in each m_T bin and the number accepted in that bin. ϵ_{embed} is the embedding efficiency. $\epsilon_{run-by-run}$ is the run by run correction . BR is branching ratio of ϕ decaying into K^+K^- channel and is given by 0.49. Δm_T is the spread of the m_T bin. $\mathrm{MC_{tune}}$ is the correction between the various cuts made in the MC vs the data. Γ_{tune} is correction for the mass window originating from the Monte Carlo. The Monte Carlo is done for non-relativistic Breit-Wigner, but the real data follows relativistic Breit-Wigner. So a correction has to be made to account for this effect.

The raw yields were obtained using counts over background in the range [1.014,1.024]

$$S = \mathrm{T} - \mathrm{B}, \tag{9.2}$$

where T is the number of counts from the real pairs, which contains signal and background, and B is the number of counts from the background pairs, normalized to $2\sqrt{N^{Real}_{++}.N^{Real}_{--}}$, in a given m_T window.

9.2.1 Estimation of Statistical Error

The sources of the statistical errors for the differential yield are;

1. statistical error from data

2. statistical error from the embedding correction

3. statistical error from the correction factor

The statistical errors from them can be propagated to the differential yield in quadrature. If S is the measurement in the data, C is the correction factor, E is the embedding correction and ΔS , ΔC and ΔE are their statistical errors, the statistical error of the differential yield can be written as,

$$\frac{\Delta A}{A} = \sqrt{\left(\frac{\Delta S}{S}\right)^2 + \left(\frac{\Delta C}{C}\right)^2 + \left(\frac{\Delta E}{E}\right)^2} \tag{9.3}$$

The error on the data consists of two parts: one coming from the actual pair distribution, and the other from the normalized background that is subtracted to get the signal. If we consider that T as the measurement of the actual pair distribution which consists of the signal S and background B, then we extract the signal by subtracting the normalized mixed event distribution B'. Thus we can write We extract

$$T = S + B \tag{9.4}$$

$$S = T - B' \tag{9.5}$$

Therefore

$$(\Delta S)^2 = (\Delta T)^2 + (\Delta B')^2 \tag{9.6}$$

Now if B_{tot} is the measured mixed event background then

$$B' = f \cdot B_{tot} \tag{9.7}$$

where

$$f = \frac{2\sqrt{N_{++}N_{--}}}{B_{tot}} \tag{9.8}$$

Therefore,

$$(\Delta B')^2 = (\Delta f)^2 + (\Delta B_{tot})^2 \tag{9.9}$$

Now,

$$\left(\frac{\Delta f}{f}\right)^2 = 2\left[\left(\frac{1}{2}\frac{\Delta N_{++}}{N_{++}}\right)^2 + \left(\frac{1}{2}\frac{\Delta N_{--}}{N_{--}}\right)^2 + \left(\frac{\Delta B_{tot}}{B_{tot}}\right)^2\right] \tag{9.10}$$

Using Eqs. (9.6), (9.9), and (9.10) in (9.3) we find the statistical error of the differential yield.

9.2.2 Correction for the m_T-Centroid

The fact that the transverse mass distribution is not flat and the nature of the transverse mass spectra make it imperative to adjust the centroid value of m_T to be used in Eq. (9.1). The Monte Carlo correction factor applied to the differential yield calculation has two components: the generated Monte Carlo and the reconstructed Monte Carlo. Therefore, when the correction factor is applied, as far as the shape of the transverse mass distribution is concerned, it does the following:

$$\begin{aligned} \text{Data} \times \text{CF} &\equiv \text{Data} \times \frac{\text{Generated Monte Carlo}}{\text{Reconstructed Monte Carlo}} \\ &\equiv m_T \text{ shape of data} \times \frac{m_T \text{ shape of Generated Monte Carlo}}{m_T \text{ shape of Reconstructed Monte Carlo}} \end{aligned}$$

The m_T centroids for the Generated and Reconstructed Monte Carlo and the Data for different bins are given in Tables 9.1 through 9.3. Presumably the m_T shape of the data is taken care by the m_T shape of the Reconstructed Monte Carlo, since both of them are reconstructed following the exact same procedure and software. We could use the center of the bin if the generated Monte Carlo were flat. But it is not. It has an exponential shape and it is generated at a temperature of 320 MeV. Therefore the center of the bin cannot be used for the calculation of the differential yield and the data points cannot be put in the bin center. A correction has to be done to take the effect in account. The corrections for the centroid value of m_T are twofold. First, the correction for the exponential nature of the spectra. Although this should in principle should be enough, but an additional correction has be made for wider bins. This is especially true for the bins at the edge of the distribution. Thus, the second is the correction for the edge effect of the distribution. We discuss about the correction here.

m_T (GeV/c^2)	Bin Center (GeV/c^2)	Bin Centroid (GeV/c^2)		
		Data	MC$_{acc}$	MC$_{thrown}$
1.2 - 1.6	1.4	1.477	1.474	1.368
1.6 - 1.8	1.7	1.705	1.705	1.691
1.8 - 2.0	1.9	1.901	1.904	1.891
2.0 - 2.2	2.1	2.098	2.101	2.091
2.2 - 2.4	2.3	2.297	2.294	2.291
2.4 - 2.8	2.6	2.581	2.581	2.565
2.8 - 3.0	2.9	2.891	2.892	2.888
3.0 - 4.0	3.5	3.245	3.238	3.289

Table 9.1: The centroids of m_T distribution in bins used for the differential yield calculations for TOF-TOF pairs.

m_T (GeV/c^2)	Bin Center (GeV/c^2)	Bin Centroid (GeV/c^2)		
		Data	MC$_{acc}$	MC$_{thrown}$
1.2 - 1.6	1.4	1.478	1.479	1.368
1.6 - 1.8	1.7	1.704	1.700	1.691
1.8 - 2.0	1.9	1.896	1.891	1.891
2.0 - 2.2	2.1	2.094	2.090	2.091
2.2 - 2.4	2.3	2.293	2.286	2.291
2.4 - 2.8	2.6	2.568	2.523	2.565

Table 9.2: The centroids of m_T distribution in bins used for the differential yield calculations for TOF-EMC pairs.

Correction1: Correction for a Steeply Falling Spectrum

When a steeply falling spectra such as an exponential distribution is plotted, the bin center is shifted due to the nature of the spectrum. The shift of the bin should be taken into account for such a spectrum. The calculation for this correction follows

m_T (GeV/c^2)	Bin Center (GeV/c^2)	Bin Centroid (GeV/c^2)		
		Data	MC$_{acc}$	MC$_{thrown}$
1.2 - 1.6	1.4	1.480	1.474	1.368
1.6 - 1.8	1.7	1.701	1.702	1.691
1.8 - 2.0	1.9	1.888	1.890	1.891
2.0 - 2.2	2.1	2.066	2.067	2.091

Table 9.3: The centroids of m_T distribution in bins used for the differential yield calculations for EMC-EMC pairs.

from the Reference [50]. Let us consider a steeply falling spectrum in a quantity x_o

$$d\mathcal{P}(x_o) = f(x_o)dx_o$$

The integral of the distribution in a bin of width Δ and the bin center x_o is

$$F(x_o,\ \Delta) \ = \ \frac{1}{\Delta}\int_{x_o-\frac{\Delta}{2}}^{x_o+\frac{\Delta}{2}} f(x)dx$$

The differential distribution in the bin is estimated as,

$$\overline{f(x_o)} \equiv \frac{F(x_o,\ \Delta)}{\Delta}$$

The plotting point x_o is chosen so that it lies on the true curve:

$$\overline{f(x_o)} \ = \ \frac{1}{\Delta}\int_{x_o-\frac{\Delta}{2}}^{x_o+\frac{\Delta}{2}} f(x)dx \ \equiv f(\overline{x_o})$$

If the distribution is an exponential of the form;

$$f(x) \ = \ A\exp\left(-bx\right)$$

then

$$\overline{f(x_o)} \ = \ \frac{A\,f(x_o)}{b\,\Delta}\left[\exp\left(b\Delta/2\right) \ - \ \exp\left(-b\Delta/2\right)\right]$$

Since

$$e^{z} \ - \ e^{-z} \ = \ 2(\Big[z \ + \ z^3/3!\Big] \simeq 2\,z\,e^{z^2/3!} \tag{9.11}$$

Therefore,

$$\overline{f(x_o)} \;=\; A\exp\left(-bx_o\right)\,\exp\left(b^2\Delta^2/24\right) \;=\; f(\overline{x_o})$$

Therefore the place to plot the point is slightly shifted from the center of the bin

$$x_o = x_o \;-\; \frac{b\Delta^2}{24} \tag{9.12}$$

Correction2: Correction for the Edge Effect

The Correction1, correction for the Steeply Falling Spectrum, neglects the higher order terms. It is evident from Eq. (9.11). Thus they can account for the correction for small bins. We can see this from Tables 9.5, 9.6 and 9.7 if we compare columns 12 and 3. The additional correction is needed for wider bins. Of course we could use the centroid of the Generated Monte Carlo for this purpose, provided they were generated at the *same* temperature as the real data. That is, we need an information about the inverse slope parameter of the ϕ from real data and then generate the Monte carlo accordingly. But there is very simple solution for this. We can do the following:

- Follow the procedure for the Correction1. Make the transverse mass distribution and extract the inverse slope parameters. This inverse slope parameter will be very close to the actual inverse slope parameter.

- Use this inverse slope parameter to estimate mathematically the centroid of the bin.

- Use the m_T centroid value from the preceding step and redo the transverse mass distribution. Extract the inverse slope parameter from the fit.

- Make one or more iteration until the values do not change significantly.

The mathematical estimation of the centroid of an exponential distribution $f(m_T) = m_T\, e^{-m_T/T}$ in range $[a\, b]$ can be written as

$$< m_T > \;=\; \frac{\int_a^b dm_T\, m_T f m_T}{\int_a^b dm_T\, f m_T} \tag{9.13}$$

After some algebra we find that the centroid of the distribution in the bin can be written as:

$$< m_T > \;=\; T\left[\frac{e^{-a/T}\left(a^2/T^2+2a/T+2\right)-e^{-b/T}\left(b^2/T^2+2b/T+2\right)}{e^{-a/T}\left(1+a/T\right)-e^{-b/T}\left(1+b/T\right)}\right] \tag{9.14}$$

Using the approximate temperature after Correction1 in Eq. (9.14 we can find the centroid of the bin for the temperature of the actual distribution. The inverse slope parameters after Correction1 are given in Table 9.4. These temperatures were used in Eqn. 9.14. The m_T centroids for the bins after the corrections are shown in Tables 9.5 through 9.7. The numbers at the last column, which are obtained after iterative processes outlined before, will be used to get the final m_T spectra.

Centrality	T (MeV)		
	TOF-TOF	TOF-EMC	EMC-EMC
0%–10%	451 ± 80	411 ± 125	269 ± 277
10%–40%	415 ± 32	423 ± 106	330 ± 100
40%–92%	410 ± 42	347 ± 59	310 ± 103
minbias	424 ± 29	401 ± 59	336 ± 74

Table 9.4: Inverse slope parameters extracted after Correction1

9.3 Yield and Spectra

With the yield and the error of the yield calculated, we can plot the transverse mass distribution of ϕ. The transverse mass distribution follows an exponential distribution

$$\frac{1}{2\pi m_T}\frac{d^2N}{dm_T dy} = \frac{1}{2\pi}\,A\,\mathrm{e}^{-(m_T\,m_0)/T} \tag{9.15}$$

To find the shift $\overline{x}_0$ due to the exponential distribution, we need the parameter b to be used in Eq.(9.12). We can readily see from Eq.(9.17) that $b = 1/T$. So we first fit the m_T distribution with no shift in the bin center. The fits gives us the value of T. We use this value in Eq.(9.12) to find the approximate shift. We then

m_T (GeV/c^2)	MC$_{thrown}$ (GeV/c^2)	Correction1 (GeV/c^2)	Correction2 (GeV/c^2)
$0\% - 10\%$ events			
1.2 - 1.6	1.368	1.38522	1.37903
1.6 - 1.8	1.691	1.69631	1.69429
1.8 - 2.0	1.891	1.89631	1.89409
2.0 - 2.2	2.091	2.09631	2.09392
2.2 - 2.4	2.291	2.29631	2.29378
2.4 - 2.8	2.565	2.58522	2.57467
2.8 - 3.0	2.888	2.89631	2.89349
3.0 - 4.0	3.289	3.40763	3.34264
$10\% - 40\%$ events			
1.2 - 1.6	1.368	1.38392	1.37662
1.6 - 1.8	1.691	1.69598	1.69368
1.8 - 2.0	1.891	1.89598	1.89347
2.0 - 2.2	2.091	2.09598	2.09331
2.2 - 2.4	2.291	2.29598	2.29317
2.4 - 2.8	2.565	2.58392	2.57228
2.8 - 3.0	2.888	2.89598	2.89287
3.0 - 4.0	3.289	3.39952	3.33013
$40\% - 92\%$ events			
1.2 - 1.6	1.368	1.38376	1.37642
1.6 - 1.8	1.691	1.69594	1.69363
1.8 - 2.0	1.891	1.89594	1.89342
2.0 - 2.2	2.091	2.09594	2.09326
2.2 - 2.4	2.291	2.29594	2.29312
2.4 - 2.8	2.565	2.58376	2.57208
2.8 - 3.0	2.888	2.89594	2.89282
3.0 - 4.0	3.289	3.39848	3.32912
minbias events			
1.2 - 1.6	1.368	1.38426	1.37724
1.6 - 1.8	1.691	1.69606	1.69384
1.8 - 2.0	1.891	1.89606	1.89363
2.0 - 2.2	2.091	2.09606	2.09347
2.2 - 2.4	2.291	2.29606	2.29333
2.4 - 2.8	2.565	2.58426	2.57289
2.8 - 3.0	2.888	2.89606	2.89303
3.0 - 4.0	3.289	3.40161	3.33330

Table 9.5: The corrected m_T centroids in bins used for the differential yield calculations for TOF-TOF pairs

m_T (GeV/c^2)	MC$_{thrown}$ (GeV/c^2)	Correction1 (GeV/c^2)	Correction2 (GeV/c^2)
$0\% - 10\%$ events			
1.2 - 1.6	1.368	1.38376	1.37725
1.6 - 1.8	1.691	1.69594	1.69384
1.8 - 2.0	1.891	1.89594	1.89364
2.0 - 2.2	2.091	2.09594	2.09347
2.2 - 2.4	2.291	2.29594	2.29333
2.4 - 2.8	2.565	2.58376	2.57291
$10\% - 40\%$ events			
1.2 - 1.6	1.368	1.38424	1.37808
1.6 - 1.8	1.691	1.69606	1.69405
1.8 - 2.0	1.891	1.89606	1.89385
2.0 - 2.2	2.091	2.09606	2.09368
2.2 - 2.4	2.291	2.29606	2.29354
2.4 - 2.8	2.565	2.58424	2.57373
$40\% - 92\%$ events			
1.2 - 1.6	1.368	1.38077	1.37158
1.6 - 1.8	1.691	1.69519	1.69239
1.8 - 2.0	1.891	1.89519	1.89218
2.0 - 2.2	2.091	2.09519	2.09202
2.2 - 2.4	2.291	2.29519	2.29188
2.4 - 2.8	2.565	2.58077	2.56729
minbias events			
1.2 - 1.6	1.368	1.38339	1.37651
1.6 - 1.8	1.691	1.69585	1.69365
1.8 - 2.0	1.891	1.89585	1.89345
2.0 - 2.2	2.091	2.09585	2.09328
2.2 - 2.4	2.291	2.29585	2.29314
2.4 - 2.8	2.565	2.58339	2.57217

Table 9.6: The corrected m_T centroids in bins used for the differential yield calculations for TOF-EMC pairs

m_T (GeV/c^2)	MC$_{thrown}$ (GeV/c^2)	Correction1 (GeV/c^2)	Correction2 (GeV/c^2)
$0\% - 10\%$ events			
1.2 - 1.6	1.368	1.38648	1.37649
1.6 - 1.8	1.691	1.69662	1.69365
1.8 - 2.0	1.891	1.89662	1.89344
2.0 - 2.2	2.091		
$10\% - 40\%$ events			
1.2 - 1.6	1.368	1.37981	1.36992
1.6 - 1.8	1.691	1.69495	1.69196
1.8 - 2.0	1.891	1.89495	1.89176
2.0 - 2.2	2.091	2.09495	2.09159
$40\% - 92\%$ events			
1.2 - 1.6	1.368	1.37848	1.36751
1.6 - 1.8	1.691	1.69462	1.69134
1.8 - 2.0	1.891	1.89462	1.89113
2.0 - 2.2	2.091	2.09462	2.09097
minbias events			
1.2 - 1.6	1.368	1.38017	1.37064
1.6 - 1.8	1.691	1.69504	1.69215
1.8 - 2.0	1.891	1.89504	1.89194
2.0 - 2.2	2.091	2.09504	2.09178

Table 9.7: The corrected m_T centroids in bins used for the differential yield calculations for EMC-EMC

re-plot taking the bin shift into account and fit to get the value if T. The do a second iteration to calculate $\overline{x}_0$ using the latest value of T. We then re-plot and refit. We make this iteration over many times until the temperature shows no change.

From the fitting of the transverse mass distribution to the exponential given in Eq.(9.15), we can extract the inverse slope parameter. Also the yield can be extracted by integrating over the complete range of the measured transverse mass. Multiplying both sides of Eq. (9.15) by $dm_T\, m_T$ we see that left side gives

$$\frac{1}{2\pi}\frac{dN}{dy}$$

The right side, after some algebra, gives

$$\frac{A\,T}{2\pi}\,(m_0\,+\,T)$$

Thus we find that the constant A can be written as

$$A \;=\; \frac{\frac{dN}{dy}}{T\;(m_0\,+\,T)} \tag{9.16}$$

Putting the expression for A from Eq. (9.16) in Eq. (9.15) and taking $m_0\;=\;m_\phi$, the rest mass of ϕ we get

$$\frac{1}{2\pi m_T}\frac{d^2N}{dm_T dy} = \frac{dN/dy}{2\pi T(m_\phi + T)}\mathrm{e}^{-(m_T - m_\phi)/T} \tag{9.17}$$

While fitting, the parameter m_ϕ was kept fixed and the inverse slope parameter T and the yield dN/dy were free parameters. The transverse mass spectra for the different combinations are shown in Figs. 9.1 through 9.12. All the relevant numbers used for the plots are given in Appendix B.

TOF-TOF

The transverse mass distribution for the TOF-TOF combinations are shown in Figs. 9.1 through 9.4. The transverse mass for the reconstructed up to 4 GeV/c^2. The yields and the inverse slope parameters are shown in Table 9.8.

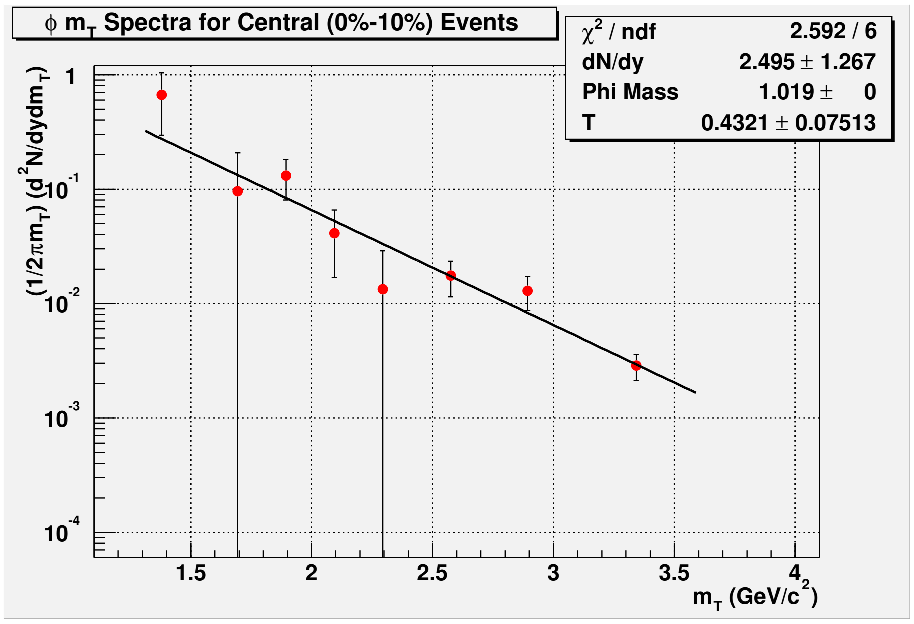

Figure 9.1: Transverse mass distribution of the ϕ's reconstructed from the TOF-TOF pairs for 0%-10% events. The yield and inverse slope parameter are extracted from the fit.

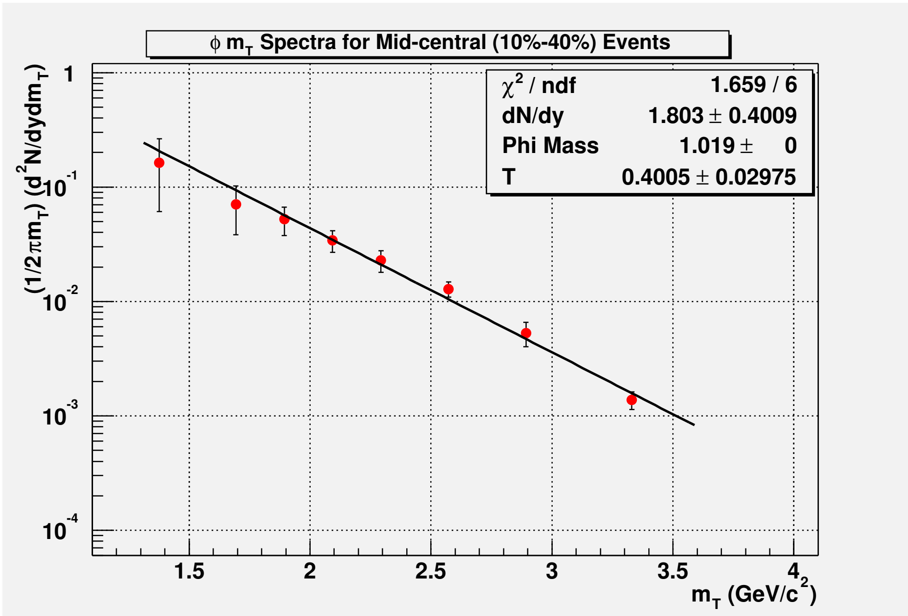

Figure 9.2: Transverse mass distribution of the ϕ's reconstructed from the TOF-TOF pairs for 10%-40% events. The yield and inverse slope parameter are extracted from the fit.

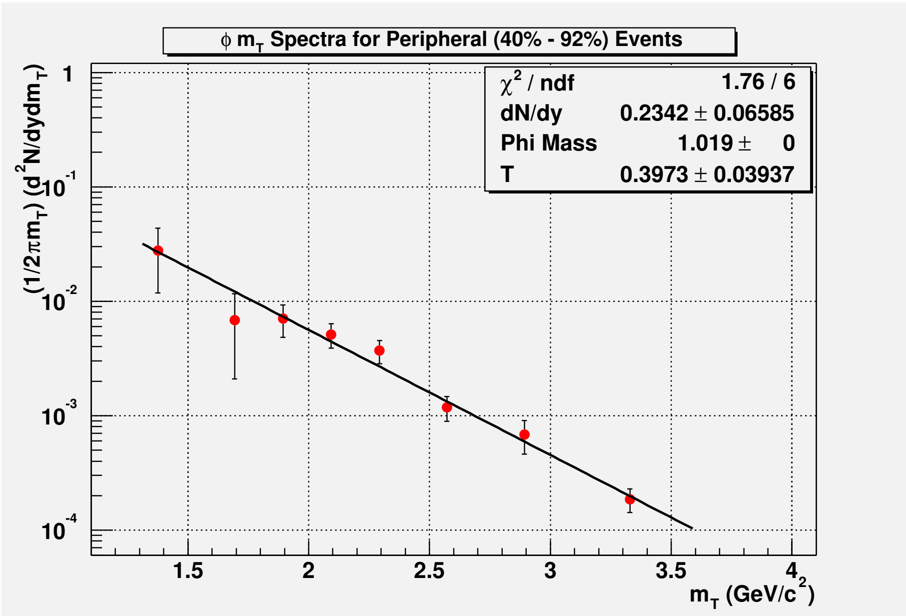

Figure 9.3: Transverse mass distribution of the ϕ's reconstructed from the TOF-TOF pairs for 40%-92% events. The yield and inverse slope parameter are extracted from the fit.

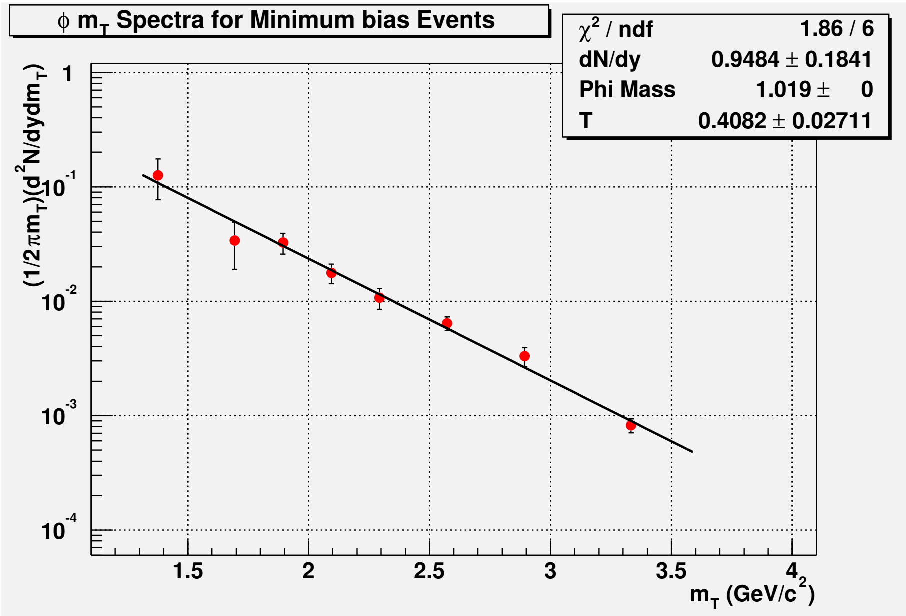

Figure 9.4: Transverse mass distribution of the ϕ's reconstructed from the TOF-TOF pairs for minimum bias events. The yield and inverse slope parameter are extracted from the fit.

Centrality	dN/dy	T (MeV)
0%–10%	2.5 $\pm$ 1.27	432 $\pm$ 75
10%–40%	1.8 $\pm$ 0.40	401 ± 30
40%–92%	0.23 $\pm$ 0.06	397 $\pm$ 39
minbias	0.95 $\pm$ 0.18	408 $\pm$ 27

Table 9.8: dN/dy and Temperatures for $\phi \to K^+K^-$ TOF–TOF Pairs

TOF-EMC

The transverse mass distribution for the TOF-EMC combinations are shown in Figs. 9.5 through 9.8. The yields and the inverse slope parameters are shown in Table 9.9.

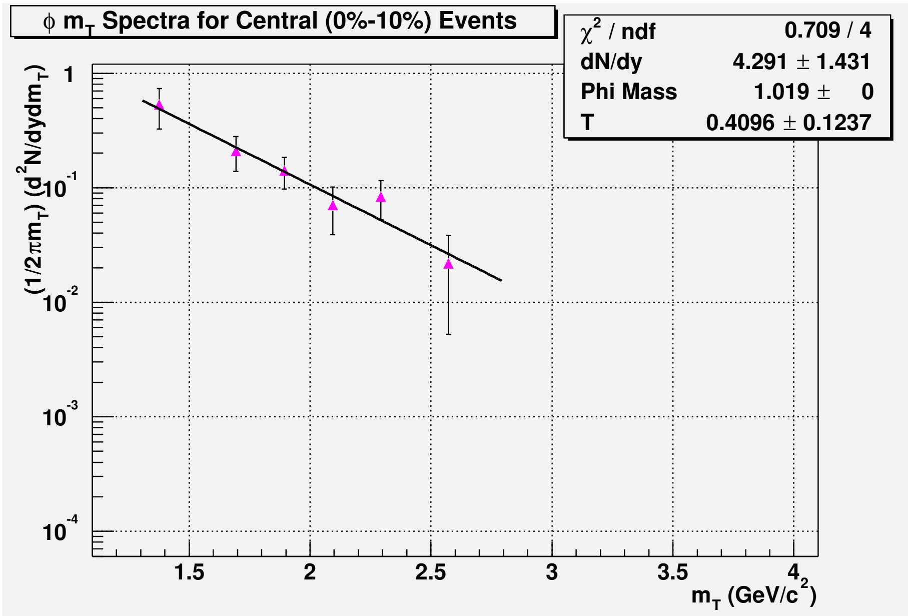

Figure 9.5: Transverse mass distribution of the ϕ's reconstructed from the TOF-EMC pairs for 0%-10% events. The yield and inverse slope parameter are extracted from the fit.

EMC-EMC

The transverse mass distribution for the EMC-EMC combinations are shown in Figs. 9.9 through 9.12. The yields and the inverse slope parameters are shown in

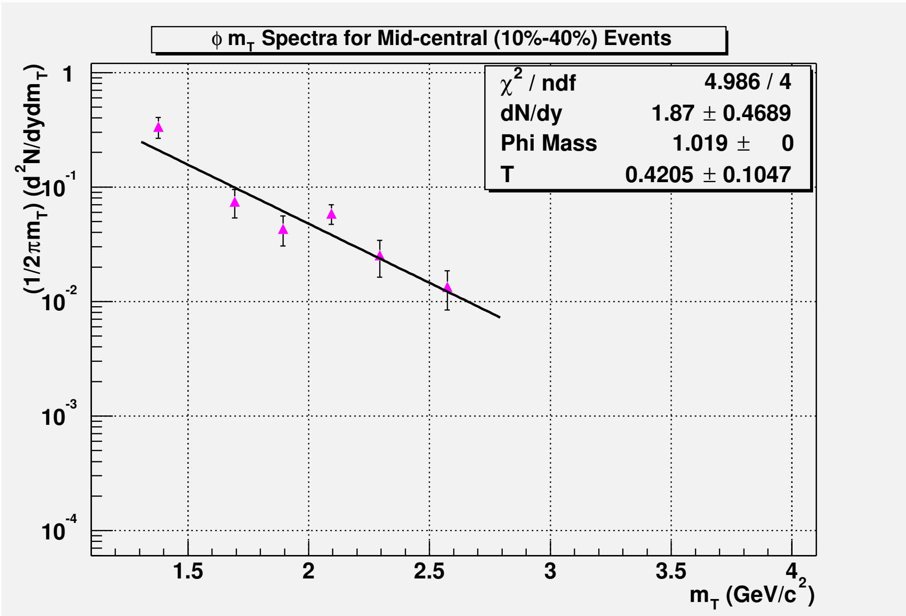

Figure 9.6: Transverse mass distribution of the ϕ's reconstructed from the TOF-EMC pairs for 10%-40% events. The yield and inverse slope parameter are extracted from the fit.

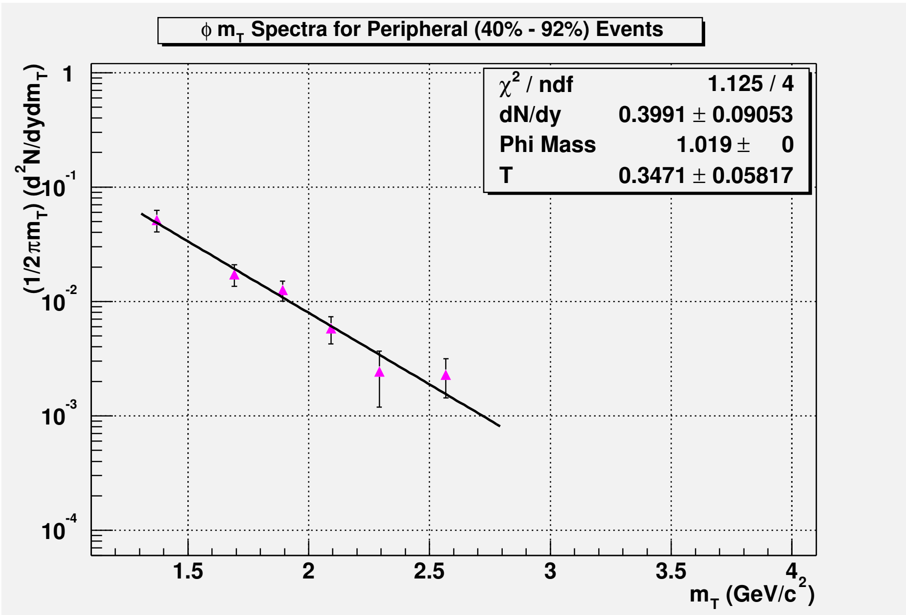

Figure 9.7: Transverse mass distribution of the ϕ's reconstructed from the TOF-EMC pairs for 40%-92% events. The yield and inverse slope parameter are extracted from the fit.

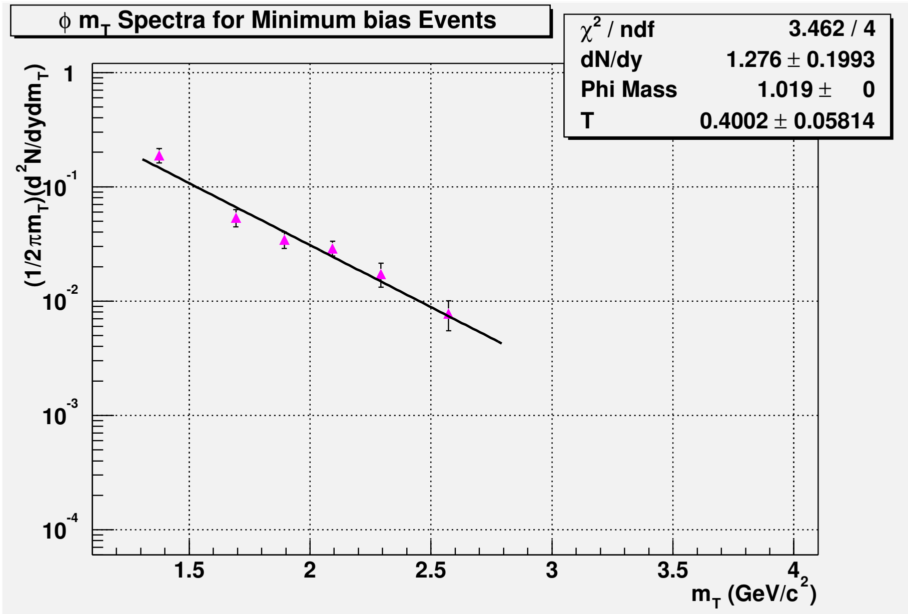

Figure 9.8: Transverse mass distribution of the ϕ's reconstructed from the TOF-EMC pairs for minimum bias events. The yield and inverse slope parameter are extracted from the fit.

Centrality	dN/dy	T (MeV)
0%–10%	4.29 ± 1.43	410 ± 124
10%–40%	1.87 ± 0.47	421 ± 105
40%–92%	0.40 ± 0.09	347 ± 58
minbias	1.28 ± 0.20	400 ± 58

Table 9.9: dN/dy and Temperatures for $\phi \to K^+K^-$ TOF–EMC Pairs

Table 9.10.

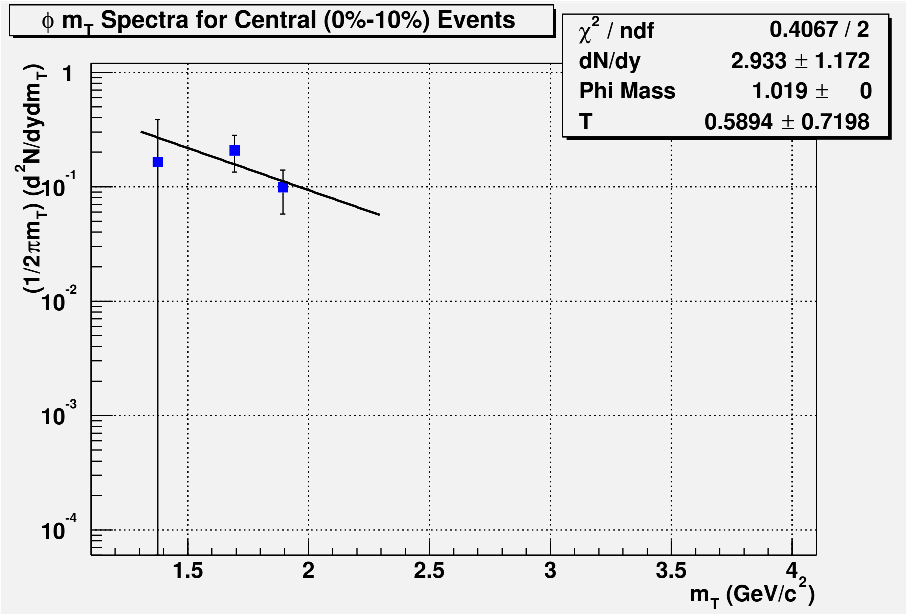

Figure 9.9: Transverse mass distribution of the ϕ's reconstructed from the EMC-EMC pairs for 0%-10% events. The yield and inverse slope parameter are extracted from the fit.

Centrality	dN/dy	T (MeV)
0%–10%	2.93 ± 1.72	589 ± 720
10%–40%	1.93 ± 0.63	332 ± 99
40%–92%	0.26 ± 0.10	312 ± 103
minbias	1.03 ± 0.24	338 ± 74

Table 9.10: dN/dy and Temperatures for $\phi \to K^+K^-$ EMC–EMC Pairs

Average Yield

From Tables 9.8 through 9.10 we can see that the central values of the dN/dy agree with each other within their statistical uncertainty. Thus we can make the average of the three measurements. This is one of the very important aspect of this analysis. We can make three independent analysis for the yield through two completely independent

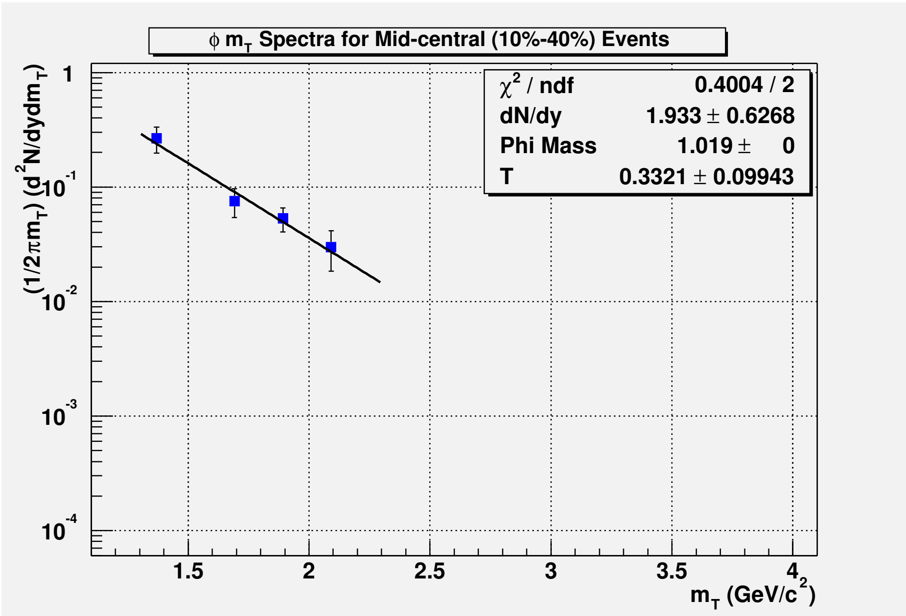

Figure 9.10: Transverse mass distribution of the ϕ's reconstructed from the EMC-EMC pairs for 10%-40% events. The yield and inverse slope parameter are extracted from the fit.

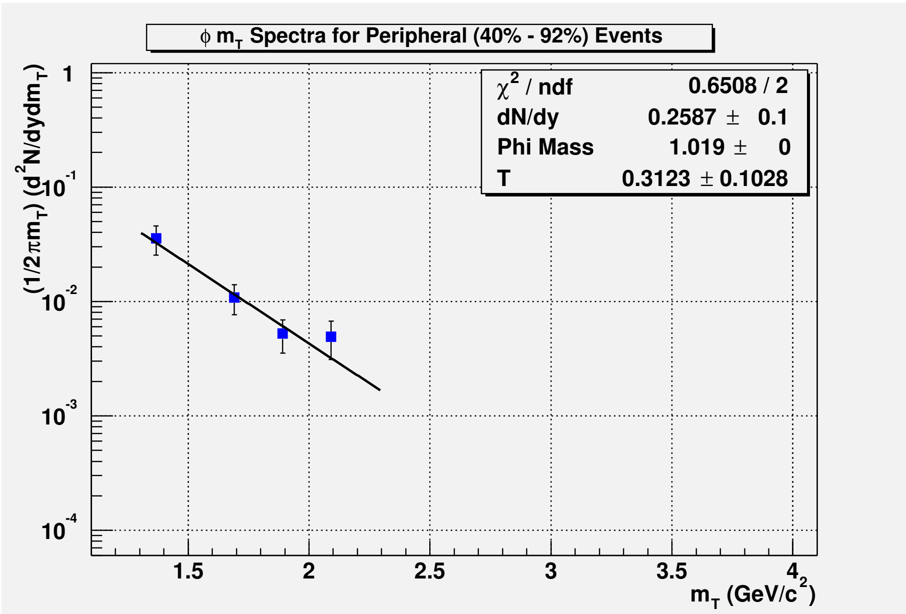

Figure 9.11: Transverse mass distribution of the ϕ's reconstructed from the EMC-EMC pairs for 40%-92% events. The yield and inverse slope parameter are extracted from the fit.

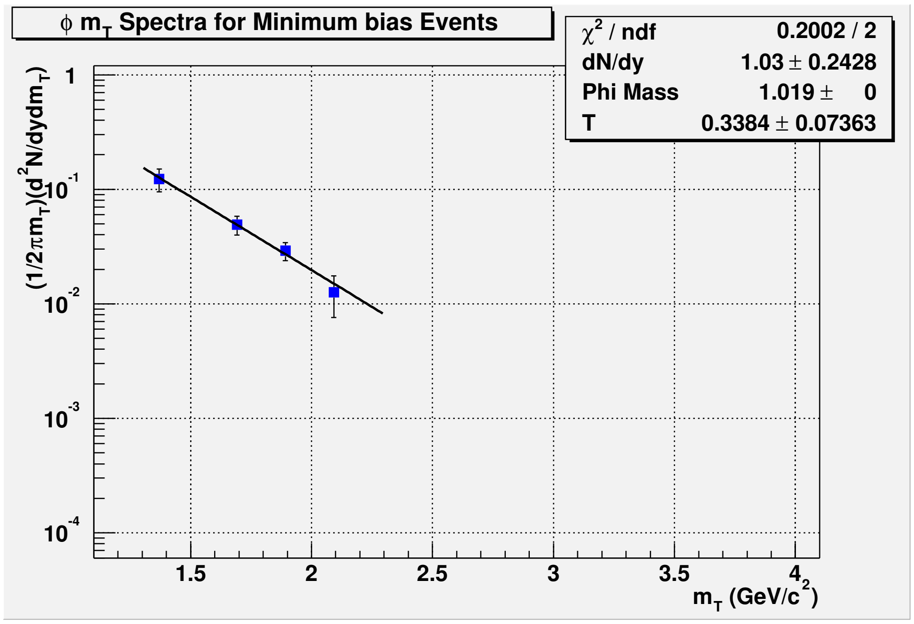

Figure 9.12: Transverse mass distribution of the ϕ's reconstructed from the EMC-EMC pairs for minimum bias events. The yield and inverse slope parameter are extracted from the fit.

detectors. For the average of the measurements, we will show that the values in each individual bins are within their error bars. We will take the average of the values in each bin. The average values will then be fitted with the exponential to extract the average of the yields and the inverse slope parameters.

In Figs. 9.13 through 9.16 is shown the differential yields vs the transverse mass for the different centralities we chose for the TOF-TOF, TOF-EMC and EMC-EMC combinations. We can see that the data points are quite consistent with each other within the statistical fluctuations. Therefore we take the average of the measurements data points in each bin. The errors of the data points are propagated as a quadrature for the average. The average of the data points are shown in Figs. 9.17 through 9.20. They are fitted and the average yield and the temperatures are extracted. They are tabulated in Table 9.11.

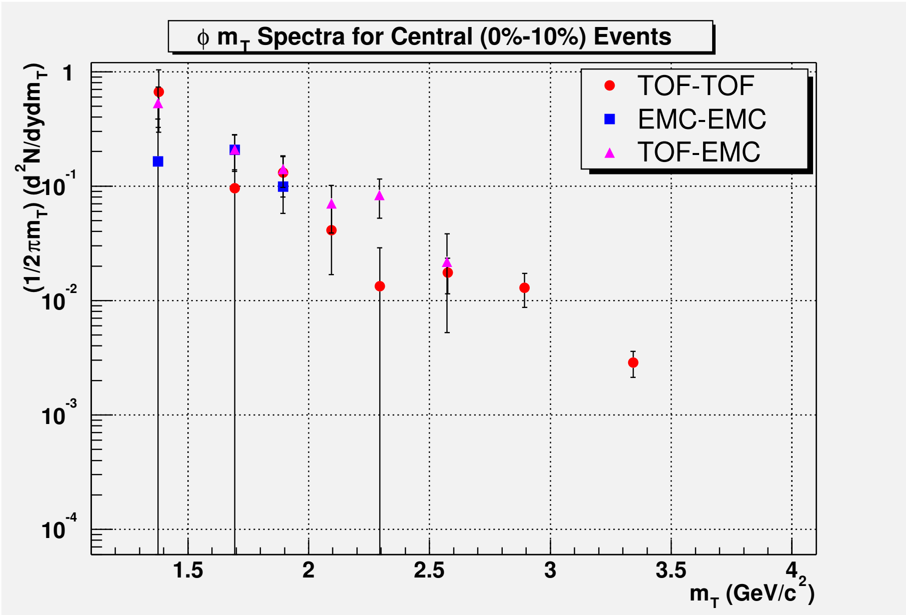

Figure 9.13: Transverse mass distribution of the ϕ's reconstructed from the three combinations for 0%-10% events.

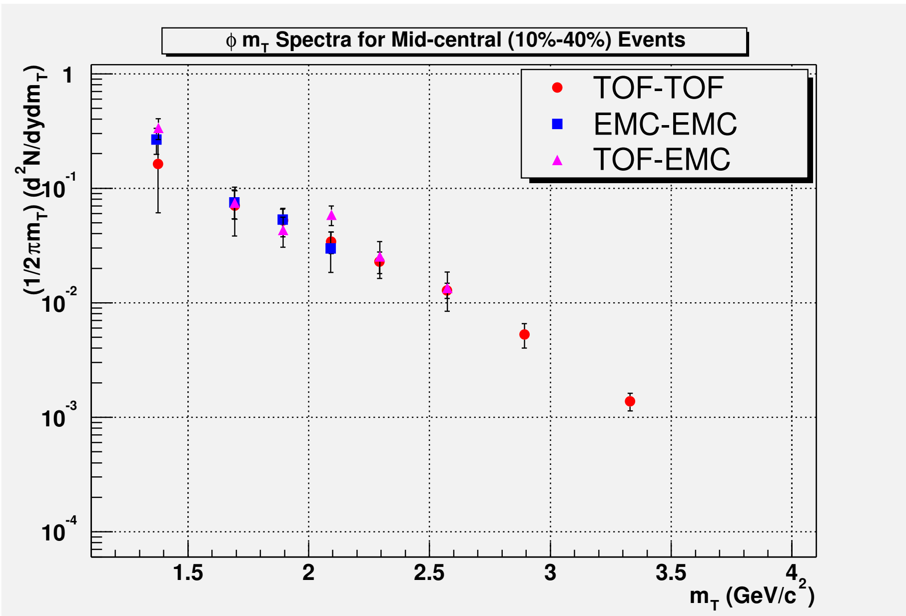

Figure 9.14: Transverse mass distribution of the ϕ's reconstructed from the three combinations for 10%-40% events.

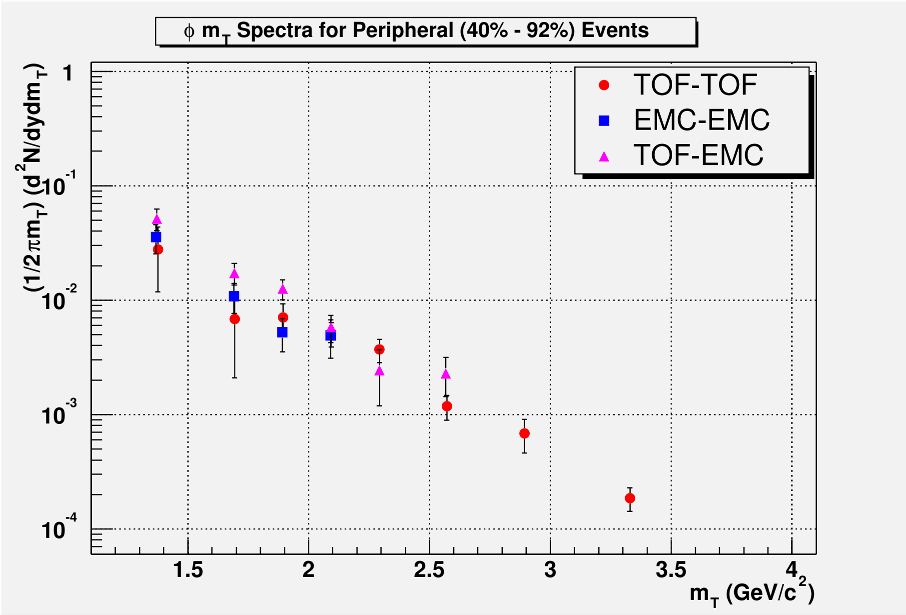

Figure 9.15: Transverse mass distribution of the ϕ's reconstructed from the three combinations for 40%-92% events.

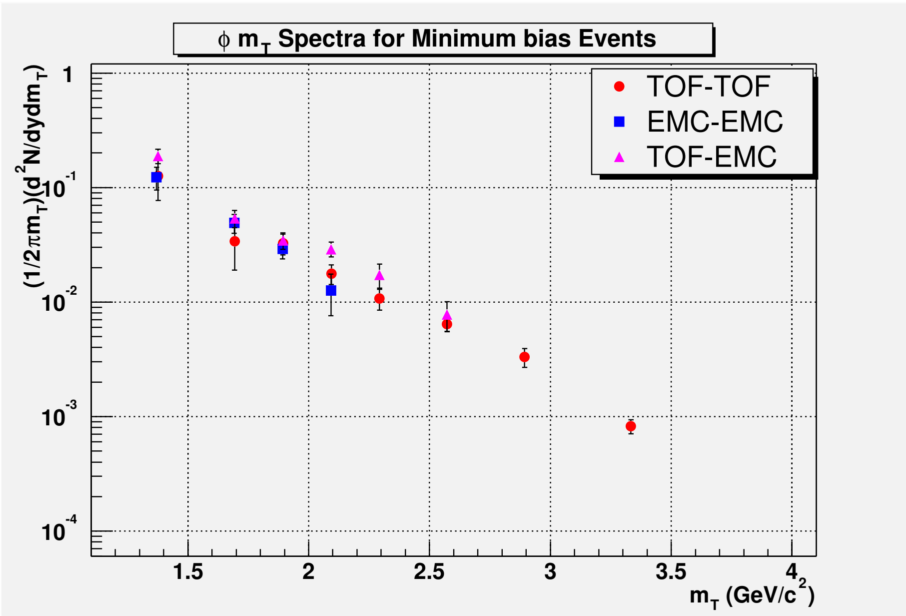

Figure 9.16: Transverse mass distribution of the ϕ's reconstructed from the three combinations for minimum bias events.

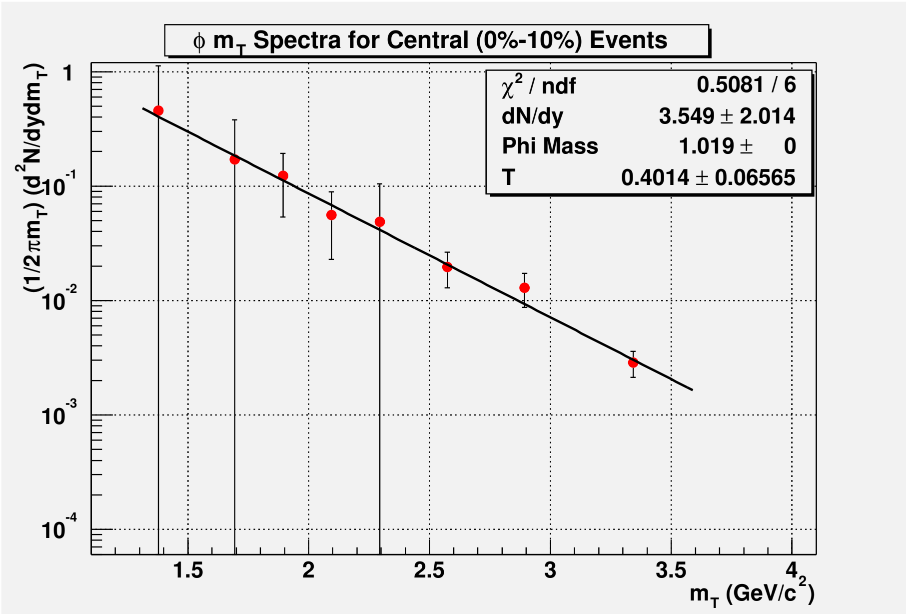

Figure 9.17: Transverse mass distribution of the ϕ's from the average of the three combinations for 0%-10% events.

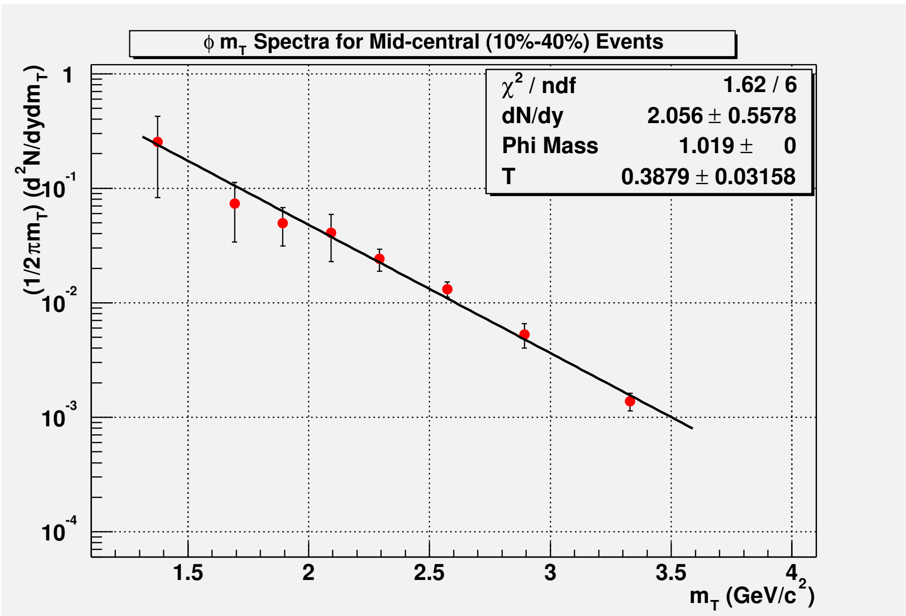

Figure 9.18: Transverse mass distribution of the ϕ's from the average of the three combinations for 10%-40% events.

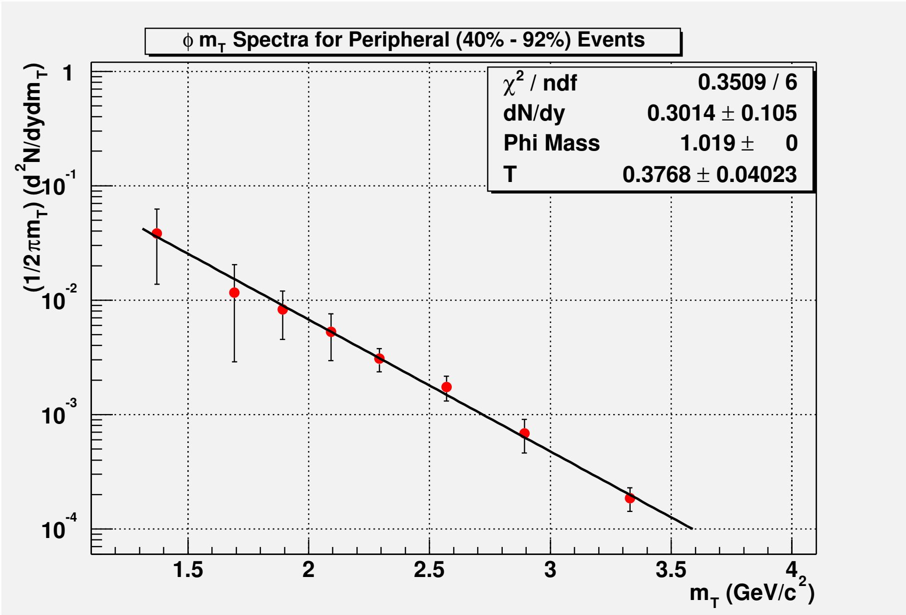

Figure 9.19: Transverse mass distribution of the ϕ's from the average of the three combinations for 40%-92% events.

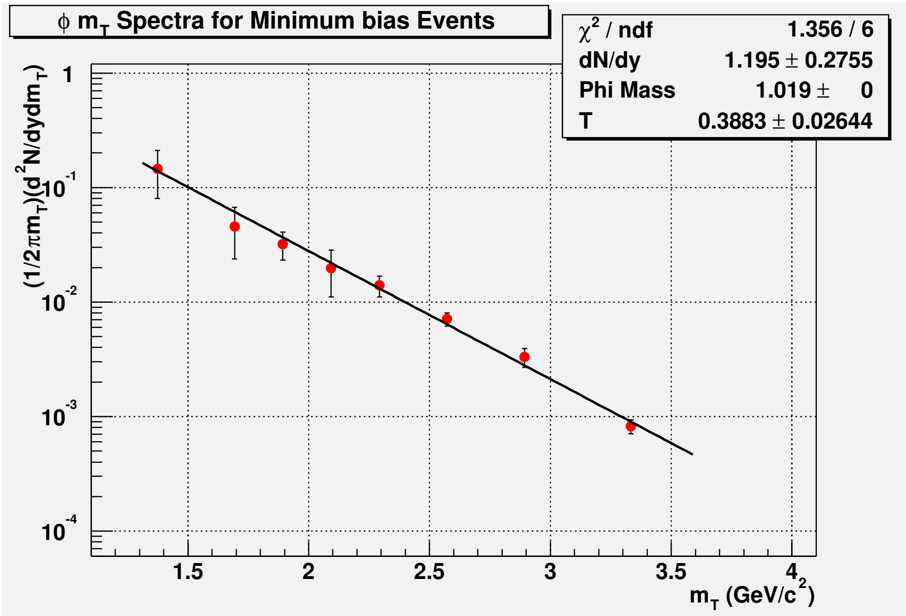

Figure 9.20: Transverse mass distribution of the ϕ's from the average of the three combinations for minimum bias events.

Centrality	dN/dy	T (MeV)
0%–10%	3.55 ± 2.01	401 ± 56
10%–40%	2.06 ± 0.56	388 ± 32
40%–92%	0.30 ± 0.11	377 ± 40
minbias	1.20 ± 0.28	388 ± 26

Table 9.11: dN/dy and Temperatures for $\phi \to K^+K^-$ from the average of the three measurements

9.4 Systematic Errors

In this chapter we present the estimation for the systematic errors. While extracting results for the yield or the lineshape analysis we used a number of conditions both on the real data and the single particle Monte carlo. Here we list the most important contributors to the systematic errors:

1. Fitting function
2. ϕ signal extraction window
3. Temperature dependence of the single particle Monte carlo generator.
4. Run by run efficiency
5. Bin crossing effect

9.4.1 Effect of Fitting Function on the Yield

One component of the systematic error of dN/dy comes from the choice of the fitting function of the transverse mass spectra. To see the effect of the fitting function on the yield, we fit with a Boltzmann function. The yield for different centralities extracted from an exponential fit and the Boltzmann fit is shown in Table 9.12 through 9.15.

The systematic errors fitting functions are within 12% for TOF-TOF, within 18% for TOF-EMC, within 23 % for EMC-EMC and within 15% for the average distribu-

Centrality	dN/dy from Exponential	dN/dy from Boltzmann	Difference %
0%-10%	2.495 ± 1.267	2.700 ± 1.535	8.2
10%-40%	1.803 ± 0.401	2.009 ± 0.498	11.4
40%-92%	0.234 ± 0.066	0.262 ± 0.083	12.0
minbias	0.948 ± 0.184	1.049 ± 0.228	10.7

Table 9.12: ϕ yield extracted with an exponential and a Boltzmann function for different centralities for TOF-TOF combination.

Centrality	dN/dy from Exponential	dN/dy from Boltzmann	Difference %
0%-10%	4.291 ± 1.431	4.747 ± 2.026	10.6
10%-40%	1.870 ± 0.469	2.044 ± 0.677	9.3
40%-92%	0.399 ± 0.091	0.471 ± 0.132	18.0
minbias	1.276 ± 0.199	1.423 ± 0.288	11.5

Table 9.13: ϕ yield extracted with an exponential and a Boltzmann function for different centralities for TOF-EMC combination.

Centrality	dN/dy from Exponential	dN/dy from Boltzmann	Difference %
0%-10%	2.933 ± 1.172	2.864 ± 1.225	2.4
10%-40%	1.933 ± 0.627	2.319 ± 0.981	20.0
40%-92%	0.259 ± 0.100	0.318 ± 0.158	22.8
minbias	1.030 ± 0.243	1.227 ± 0.375	19.1

Table 9.14: ϕ yield extracted with an exponential and a Boltzmann function for different centralities for EMC-EMC combination.

Centrality	dN/dy from Exponential	dN/dy from Boltzmann	Difference %
0%-10%	3.549 ± 2.014	3.951 ± 2.477	11.3
10%-40%	2.056 ± 0.558	2.320 ± 0.697	12.8
40%-92%	0.301 ± 0.105	0.344 ± 0.133	14.3
minbias	1.195 ± 0.276	1.348 ± 0.344	12.8

Table 9.15: ϕ yield extracted with an exponential and a Boltzmann function for different centralities for the Average of the three distributions.

tion. We should point out here that the EMC-EMC has the lowest number of data points. So the fittings are not expected to be very reliable. The most data points are in the TOF-TOF and average distributions. Also in TOF-EMC, which has 25% less data points than the TOF-TOF, show systematics ~10% except for the peripheral bin, where the uncertainty is 18%. With the most conservative approach, we assign a systematic error of 18% from the fitting uncertainty.

9.4.2 Effect of the Signal Extraction Window on Yield and the Inverse Slope Parameter

We have extracted ϕ signal and background within the mass window of $1.014 < M_{k^+K^-} < 1.024$ GeV/c^2, where $M_{k^+K^-}$ is the pair invariant mass. Let us look at different signal extraction window and find how it affects the dN/dy and T. We use $1.004 < M_{k^+K^-} < 1.034$ GeV/c^2 and $1.009 < M_{k^+K^-} < 1.029$ GeV/c^2 in addition to our selected window $1.014 < M_{k^+K^-} < 1.024$ GeV/c^2. We tabulate the ϕ signal, background and the simulated ϕ within the specified windows for three different centralities in Tables 9.16-9.18:

We also summarize the dN/dy and T extracted for different mass windows and centralities in Table 9.19. From Table 9.19 we see that the dN/dy and T are consistent with each other for different mass windows. Although we have shown yields from ±5MeV,±10MeV and ±15MeV windows, ±15MeV is too wide for any practi-

m_T GeV/c^2	±5 MeV Window $1.014 < M < 1.024$			±10 MeV Window $1.009 < M < 1.029$			±15 MeV Window $1.004 < M < 1.034$		
	Sig	Bkg	MC	Sig	Bkg	MC	Sig	Bkg	MC
1.2 - 1.6	43.25	531.75	310	55.50	1111.50	366	50.21	1665.8	384
1.6 - 1.8	22.46	668.55	419	21.60	1389.40	498	14.14	2053.86	519
1.8 - 2.0	74.90	747.10	555	76.25	1572.75	666	87.58	2306.42	697
2.0 - 2.2	46.43	703.57	580	66.92	1446.08	693	63.055	2104.95	727
2.2 - 2.4	20.43	537.57	435	64.53	1114.47	513	85.21	1625.79	537
2.4 - 2.6	37.38	379.62	298	23.56	780.45	342	10.57	1141.43	359
2.6 - 2.8	40.97	249.03	217	55.81	516.19	246	55.45	755.55	258
2.8 - 3.0	45.11	157.89	145	71.29	328.71	181	79.97	477.03	190
3.0 - 4.0	67.56	212.44	213	74.95	433.05	246	54.30	635.70	258

Table 9.16: ϕ signal, background and simulated ϕ in ±5MeV,±10MeV and ±15MeV pair invariant mass window for 0%-10% events

m_T GeV/c^2	±5 MeV Window $1.014 < M < 1.024$			±10 MeV Window $1.009 < M < 1.029$			±15 MeV Window $1.004 < M < 1.034$		
	Sig	Bkg	MC	Sig	Bkg	MC	Sig	Bkg	MC
1.2 - 1.6	36.71	478.29	310	54.25	997.75	366	61.52	1502.48	384
1.6 - 1.8	57.82	617.18	419	50.84	1278.16	498	62.89	1876.11	519
1.8 - 2.0	104.82	691.18	555	124.60	1441.40	666	110.48	2113.52	697
2.0 - 2.2	134.68	630.32	580	138.46	1318.54	693	128.67	1921.33	727
2.2 - 2.4	122.70	498.31	435	118.57	1029.43	513	115.89	1496.11	537
2.4 - 2.6	124.96	341.04	298	132.81	706.20	342	118.33	1039.67	359
2.6 - 2.8	76.59	218.41	217	97.51	458.49	246	120.38	669.62	258
2.8 - 3.0	64.57	140.43	145	89.50	296.50	181	106.98	438.07	190
3.0 - 4.0	113.98	185.02	213	137.07	381.94	246	152.99	567.02	258

Table 9.17: ϕ signal, background and simulated ϕ in ±5MeV,±10MeV and ±15MeV pair invariant mass window for 10%-40% events

m_T GeV/c^2	±5 MeV Window $1.014 < M < 1.024$			±10 MeV Window $1.009 < M < 1.029$			±15 MeV Window $1.004 < M < 1.034$		
	Sig	Bkg	MC	Sig	Bkg	MC	Sig	Bkg	MC
1.2 - 1.6	11.85	33.15	310	14.66	71.34	366	7.65	108.35	384
1.6 - 1.8	10.66	43.34	419	11.79	88.21	498	9.02	126.98	519
1.8 - 2.0	26.89	42.11	555	28.80	89.20	666	34.28	131.72	697
2.0 - 2.2	38.29	38.71	580	55.81	79.19	693	61.16	117.84	727
2.2 - 2.4	37.60	29.40	435	42.08	58.92	513	36.02	86.98	537
2.4 - 2.6	21.44	20.56	298	32.41	40.59	342	40.13	57.87	359
2.6 - 2.8	13.70	12.30	217	16.28	24.72	246	18.87	37.13	258
2.8 - 3.0	15.80	8.20	145	17.19	16.81	181	24.99	24.01	190
3.0 - 4.0	28.99	11.01	213	44.21	21.79	246	51.55	31.45	258

Table 9.18: ϕ signal, background and simulated ϕ in ±5MeV,±10MeV and ±15MeV pair invariant mass window for 40%-92% events

cal purpose of signal extraction when we consider the fact that width of ϕ is about 4.3 MeV. Thus we use results from ±5MeV,±10MeV to see the systematic effect. The maximum systematic effect on yield is 12% and on the inverse slope parameter is 7% when we compare the results in ±5MeV,±10MeV window.

cent	dN/dy			T (MeV)		
	W_1	W_2	W_3	W_1	W_2	W_3
0%-10%	2.5±1.27	2.8±1.41	3.1±1.8	432±75	437±75	404±77
10%-40%	1.8±0.40	1.6±0.40	1.4±0.42	401±30	428±37	446±45
40%-92%	0.23±0.07	0.22±0.06	0.21±0.06	408±27	430±45	456±50

Table 9.19: ϕ yield and inverse slope parameter for ±5MeV,±10MeV and ±15MeV pair invariant mass window for different centralities. W_1 on the table represents ±5MeV window, W_2 represents ±10MeV window and W_3 represents ±15MeV window,

Combination	N_ϕ^{gen} ($\lvert y\rvert < 0.6$)	N_ϕ^{gen} ($\lvert y\rvert < 0.5$)	N_ϕ^{rec}	CF at $T \sim 320$ MeV	CF at $T \sim 440 MeV$
TOF – TOF	32.3 M	26.92 M	3172	8451	4422
TOF – East	32.3 M	26.92 M	4494	5810	4563
East – east	32.3 M	26.92 M	3056	8808	7301

Table 9.20: Net CF for $\phi \to K^+K^-$ reconstruction for different subsystem combinations

9.4.3 Temperature dependence of the single particle Monte carlo generator

The single particle Monte carlo were generated following the function is Eq. 7.1:

$$\frac{dN}{dp_T} = p_T \exp\left(-\frac{m_T}{T}\right) \tag{9.18}$$

with T, the inverse slope, being taken as 320 MeV. We now determine how much the yield will be affected if we generate the Monte Carlo at a different temperature. For this purpose we chose a temperature of 440 MeV. We can scale the correction factor measured at 320 MeV to 440 MeV by using proper weights to account for the relative yield of the new vs. the original p_T distributions:

$$CF = \frac{N^{gen}}{N^{rec}} = \frac{N^{gen}}{\Sigma N_i^{rec}} = \frac{N^{gen}}{\Sigma \frac{N_i^{gen}}{F_i}} \tag{9.19}$$

where the sum runs over p_T bins and the F_i values (which represent the inverse of the reconstruction probability for a given p_T bin) are derived from the single pair MC simulation with the original parent distribution:

$$F_i = \frac{N_i^{gen-orig}}{N_i^{rec-orig}} \tag{9.20}$$

The overall correction factor at 320 MeV and its scaled value at 440 MeV is shown in Table 9.20. The overall correction factor for Monte Carlo generated at 400 MeV is 4357. Thus there is change of 2% in the correction factors. This will show up in the yield.

9.4.4 Run-by-run Efficiency

The run-by-run efficiency was calculated with respect to the run number 31464. In order to determine the systematic error arising from run by run efficiency correction, we recalculate the run by run efficiency with another run. But we should be careful for the choice of the run number. We should not choose a run which gives raw K^+ or K^- yields per trigger that deviates far from those of run 31464 sine we are correcting for those type of fluctuation in raw yields. The run to choose should have comparable K^+ or K^- yields per trigger to run 31464. For that purpose we choose run number 32523. The run-by-run efficiency using run 32523 and run 31464 is shown in Table 9.21. The systematic error coming from the run-by-run correction is small.

Combination	Run 31464			Run 32523			Difference
	ϵ_{K+}	ϵ_{K-}	ϵ_{K+K-}	ϵ_{K+}	ϵ_{K-}	ϵ_{K+K-}	$\left\lvert\frac{\epsilon^{31464}_{K+K-} - \epsilon^{32523}_{K+K-}}{\epsilon^{31464}_{K+K-}}\right\rvert$
TOF-TOF	0.9763	0.9244	0.9025	0.9812	0.9371	0.9195	1.9%
EMC-EMC	0.9418	0.9435	0.8886	0.9453	0.9591	0.9066	2.0%
TOF-EMC	0.9763	0.9435	0.9211	0.9812	0.9591	0.9411	2.2%

Table 9.21: Run by run efficiencies for run 31464 and run 32523

9.4.5 Bin Crossing Effect

In our analysis we make bins in the transverse mass and count the ϕ signal in each bin. If a ϕ has a true transverse mass m_T, then the probability that the reconstructed ϕ will have the same m_T depends on the momentum resolution of the detector. We have demonstrated that PHENIX has excellent detector momentum resolution. Therefore ϕ's in true transverse range are most likely to be reconstructed in the same transverse mass range. There is nevertheless a probability that a ϕ might be reconstructed in other m_T-bin. This may be plausible for the ϕ's at the bin boundary. We here intend to find the probability of such.

In our Monte Carlo we produce a number of ϕ's. In the usual way, we decay them and pass through the PHENIX detector simulation. We reconstruct the ϕ's and find the number of ϕ's in each m_T-bin. From the ratio of the reconstructed and generated ϕ's we calculate the correction factor CF. Next we do the same, but this time we miscalibrate the momentum by 1%. We calculate the CF in this case. From the two measurements we can find the effect of bin crossing. The results are shown in Table 9.22. The result is derived for the TOF and EMCal combination. 2nd to 4th columns are for the Monte Carlo with PHENIX momentum resolution. They are labeled with "Original". The "$< m_T >$ True" column represents the bin centroid of the generated ϕ's and the "$< m_T >$ Reco" column represents the bin centroid of the reconstructed ϕ's. In the next three columns represents the Monte Carlo with a 1% miscalibration of the momentum resolution. They are labeled by "Recalibrated". In the last column we calculate the ratio of the two correction factors. We can readily see that the bin sharing effect is very small. The correction factors agree very well to each other within their statistical fluctuation. The overall effect is less than 4%.

9.5 Centrality Dependence

We divided our data into three centrality classes, central (0%-10%), mid-central (10%-40%) and peripheral (40%-92%) in order to study the centrality dependence of the yield and the inverse slope parameters. In Fig. 9.21 we plot the yield dN/dy vs the centrality. The centrality is represented here by the number of participants. We plot the measurements from TOF-TOF in red points, the EMC-EMC with blue squared, the TOF-EMC in magenta triangles and the averages in red circles. The four adjacent points correspond to the same centrality. They are plotted apart in order for better viewing. It is seen that dN/dy increases with the centrality. We also plot the yield per participant ($dN/dy/N_p$) vs centrality in Fig. 9.22. There is no apparent centrality dependence observed. When we look at the yield per binary collision vs the centrality

m_T-bin (GeV/c^2)	Original			Recalibrated			CF Ratio
	$< m_T >$ True	$< m_T >$ Reco	CF	$< m_T >$ True	$< m_T >$ Reco	CF	
1.2–1.4	1.354	1.336	20883 $\pm$ 1752	1.343	1.346	25345 $\pm$ 2343	1.21 $\pm$ 0.15
1.4–1.6	1.516	1.507	3247 $\pm$ 125	1.513	1.517	3487 $\pm$ 140	1.07 $\pm$ 0.06
1.6–1.8	1.698	1.702	1405 $\pm$ 44	1.698	1.702	1434 $\pm$ 45	0.97 $\pm$ 0.04
1.8–2.0	1.889	1.892	1176 $\pm$ 42	1.907	1.891	1122 $\pm$ 39	0.95 $\pm$ 0.05
2.0–2.2	2.109	2.089	1420 $\pm$ 71	2.109	2.089	1318 $\pm$ 63	0.93 $\pm$ 0.06
2.2–2.4	2.307	2.287	1481 $\pm$ 99	2.289	2.293	1431 $\pm$ 99	0.97 $\pm$ 0.09
2.4–2.8	2.545	2.521	2775 $\pm$ 258	2.482	2.486	3251 $\pm$ 254	1.17 $\pm$ 0.16

Table 9.22: The bin crossing for momentum miscalibration.

in Fig. 9.23, within the statistical ans systematic uncertainties, there is no centrality dependence. The inverse slope parameters are plotted vs centrality in Fig. 9.24. The inverse slope parameters do not show any centrality dependence.

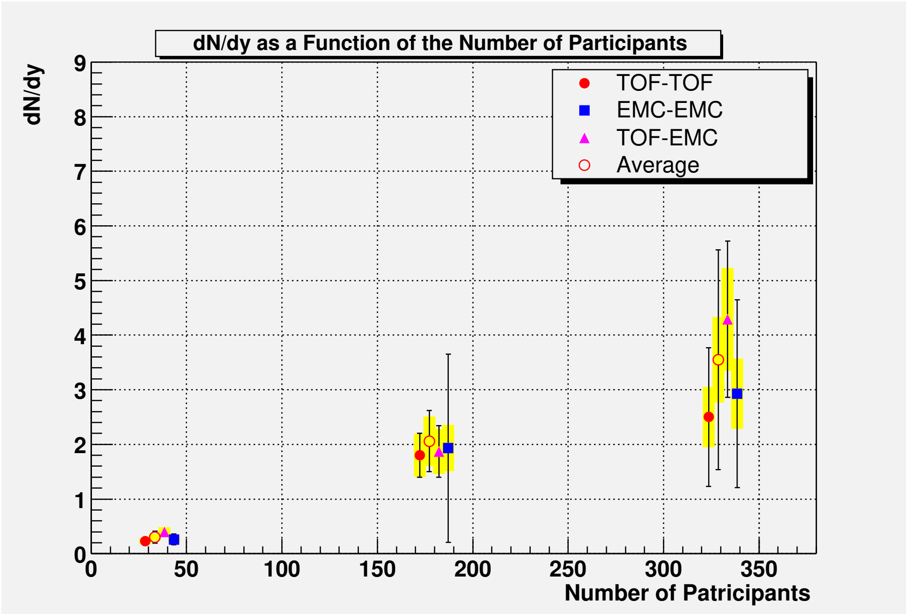

Figure 9.21: The ϕ yield as a function of the number of participants

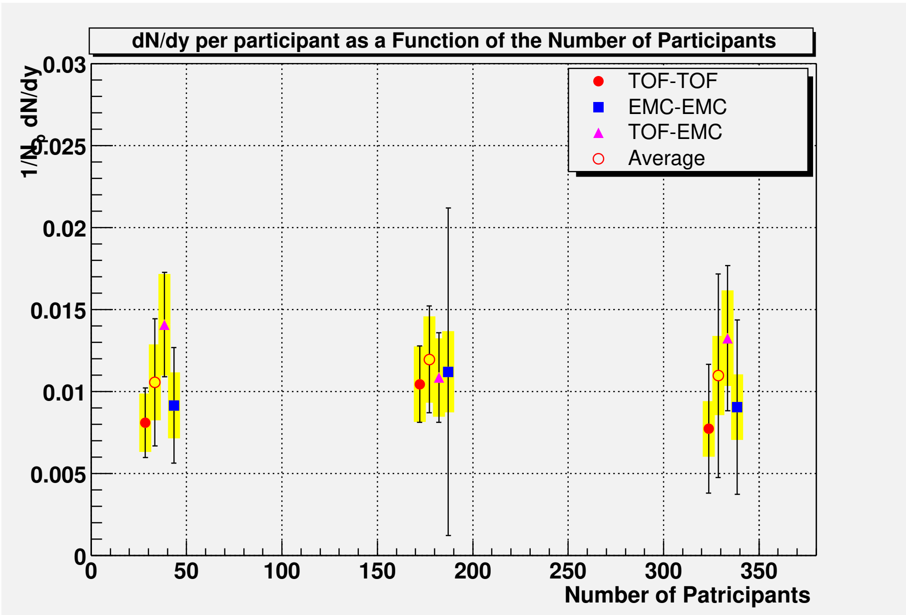

Figure 9.22: The ϕ yield per participant as a function of the number of participants

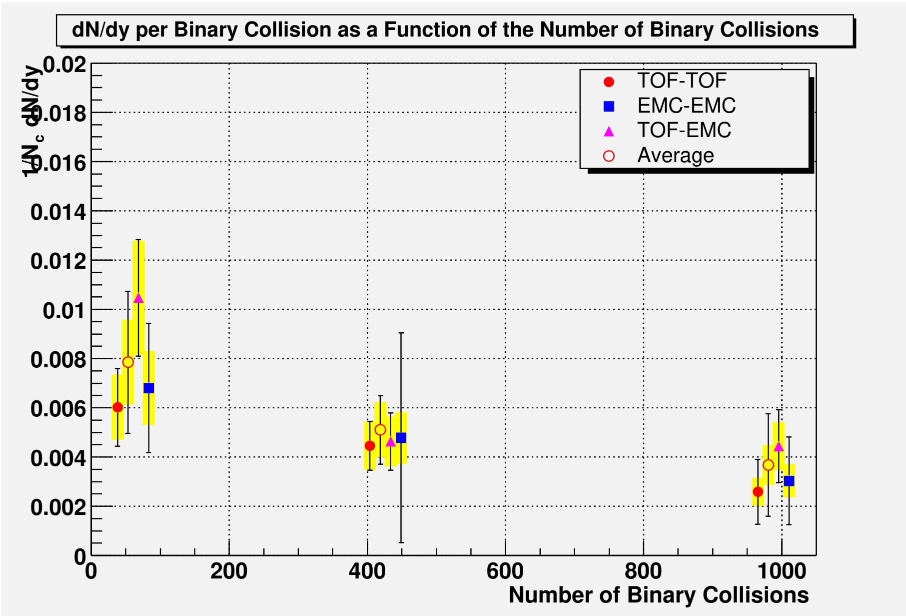

Figure 9.23: The ϕ yield per binary collisions as a function of the number of binary collisions

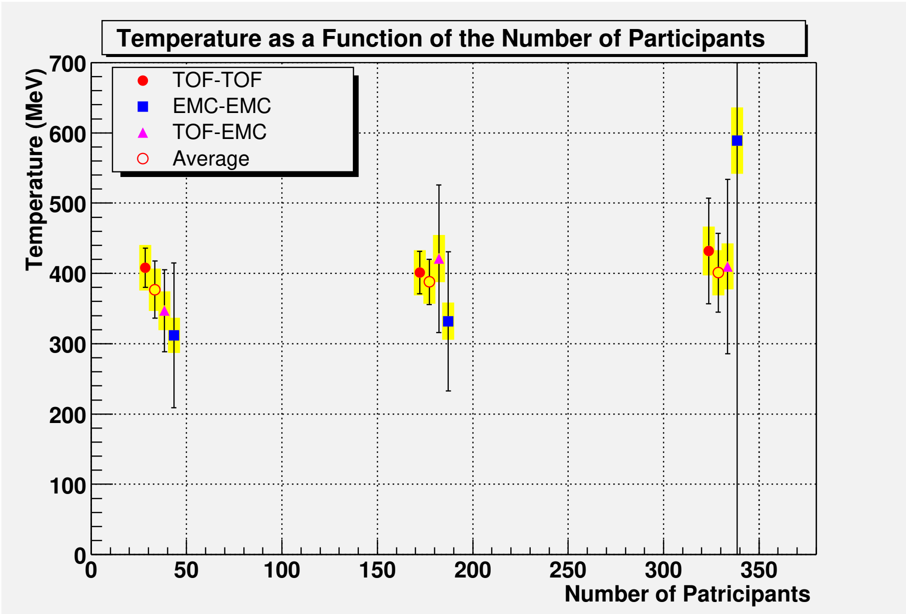

Figure 9.24: The ϕ inverse slope parameter as a function of the number of participants

Chapter 10

Summary and Conclusion

We have reconstructed the ϕ meson the K^+K^- decay channel at $\sqrt{s_{NN}} = 200$ GeV by the PHENIX experiment. The measurements were done with two independent detectors, the high resolution Time-of-Flight detector and the high statistics Electromagnetic Calorimeter. Three separate measurements were performed. All the measurements are consistent with each other showing the accuracy of the measurements.

10.1 Mass and Width of ϕ

The measures ϕ mass centroid is consistent with the PDB value [3] at all centralities. But a strong centrality dependence is observed in the ϕ width. The mass and width at different centralities is given in Table 10.1 The centrality dependence were tested versus the theory of statistical fluctuation and $\overline{\Lambda}$. There is no known theoretical explanation for this type of centrality dependence of the width.

10.2 ϕ Yield and Inverse Slope Parameter

The ϕ yield and the inverse slope parameter were extracted from an exponential fitting to the transverse mass distribution of the differential yields. The yields show a centrality dependence as the yield increases for more central events. The inverse

Centrality	Mass (GeV/c^2)	Γ (MeV/c^2)
Minimum Bias	1.01903 $\pm$ 0.00014	3.77502 $\pm$ 0.475022
0% – 10%	1.01868 $\pm$ 0.00028	2.55023 $\pm$ 0.858423
10% – 20%	1.01950 $\pm$ 0.00032	3.25329 $\pm$ 0.903986
20% – 40%	1.01908 $\pm$ 0.00025	5.82092 $\pm$ 0.925963
40% – 60%	1.01900 $\pm$ 0.00025	4.73418 $\pm$ 0.841538
40% – 92%	1.01897 $\pm$ 0.00031	3.20214 $\pm$ 0.80 7876

Table 10.1: ϕ Mass centroid and the full-width at half maxima for AllEast Pairs

slope parameters do not show any centrality dependence. The yield per participant do not show any centrality dependence.

One important aspect seen in the heavy ion Au-Au collisions at RHIC is the suppression of central π^0 yields at high transverse momenta ($p_T > 2$ GeV/c) with respect to the binary collision scaled p-p and peripheral Au-Au yields. We try to see whether we see such effect in ϕ. To do so, we look at the m_T-spectra for the ratio of the differential yields scaled by the number of binary collisions:

$$R_{CP} = \frac{yield^{0-10\%}/ < N_{coll}^{0-10\%} >}{yield^{60-92\%}/ < N_{coll}^{60-92\%} >} \tag{10.1}$$

In Fig. 10.1 we show the central to peripheral ratios of the binary collision scaled transverse mass spectra. Although there is large statistical fluctuation, the yield shows a binary collision scaling. Now we calculate the binary collision scaled integrated yield dN/dy ratios for different centralities and the peripheral. We also do the same, but with scaled to the number of collisions.

$$R_{CP}^{Ncoll} = \frac{yield^{cent}/ < N_{coll}^{cent} >}{yield^{60-92\%}/ < N_{coll}^{60-92\%} >} \tag{10.2}$$

$$R_{CP}^{Npart} = \frac{yield^{cent}/ < N_{part}^{cent} >}{yield^{60-92\%}/ < N_{part}^{60-92\%} >} \tag{10.3}$$

In Fig. 10.2 we show the ratios vs the centrality for the binary collision scaled integrated yield. It is not conclusive if there is a binary scaling or the ratio decreases

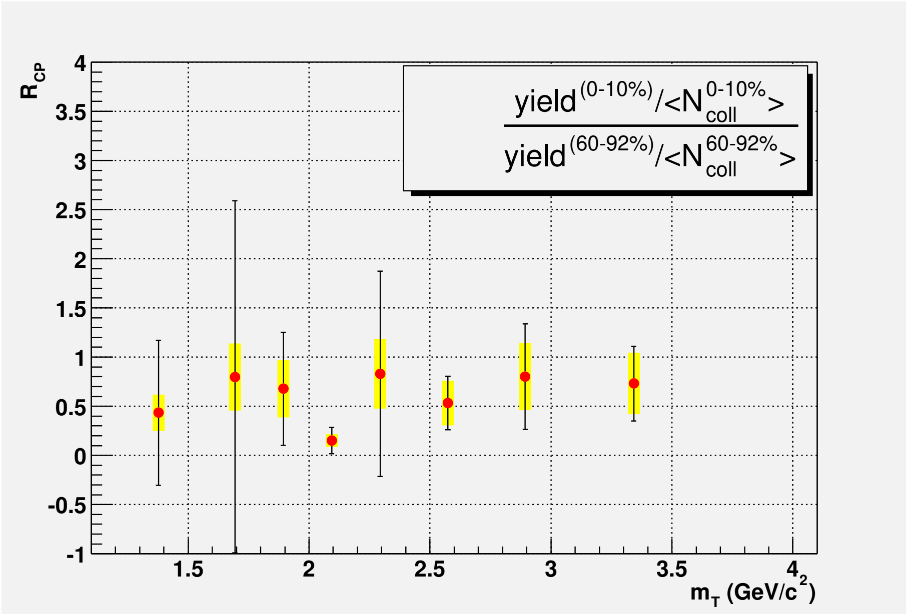

Figure 10.1: Central to peripheral ratio of the differential yields scaled by the binary collisions.

with the current statistics. More statistics is needed to comment definitively on this aspect. In Fig. 10.3 we show the ratios vs the centrality for the number of participant scaled integrated yield. Comparing Fig. 10.2 and Fig. 10.3 it is more likely that yield scales with the number of participants. But the current statistics does not permit to comment conclusively.

10.3 ϕ/K^- Ratio

In Fig. 10.4 we show the ϕ/K^- ratio as a function of the centrality. There is no centrality dependence of the ϕ/K^- ratio in the Au-Au collision at 200 GeV. This implies that the ϕ meson production at RHIC energies follow the strangeness production. We also show the ϕ/K^- ratio at different beam energies in Fig. 10.5. It appears that the ratio is almost constant over the beam energies.

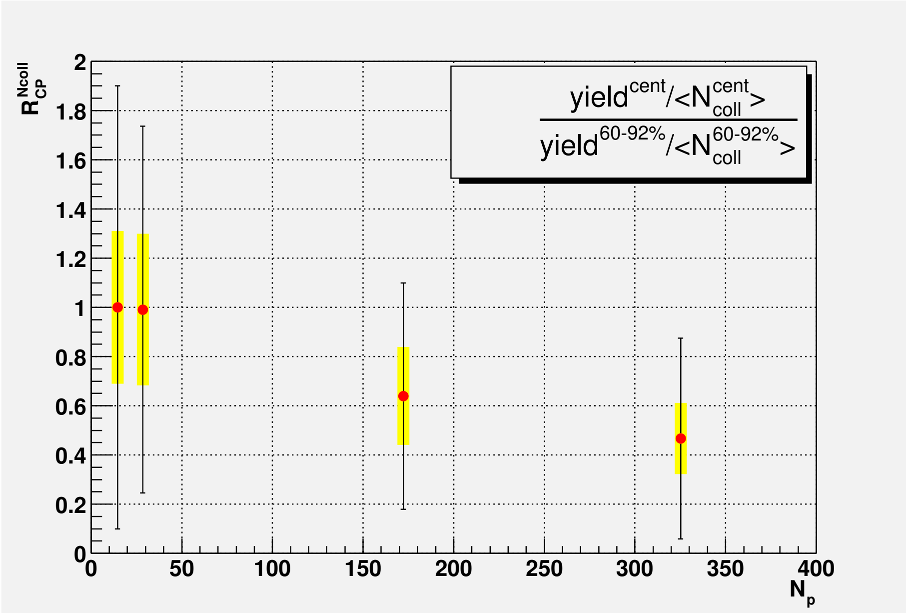

Figure 10.2: Central to peripheral ratio of the integrated yields scaled by the binary collisions vs the centrality.

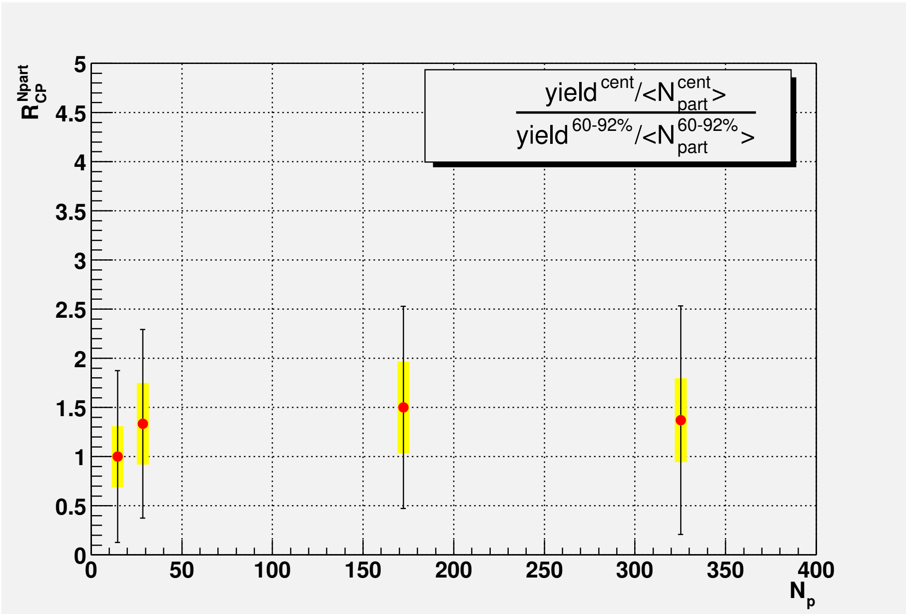

Figure 10.3: Central to peripheral ratio of the integrated yields scaled by the number of participants vs the centrality.

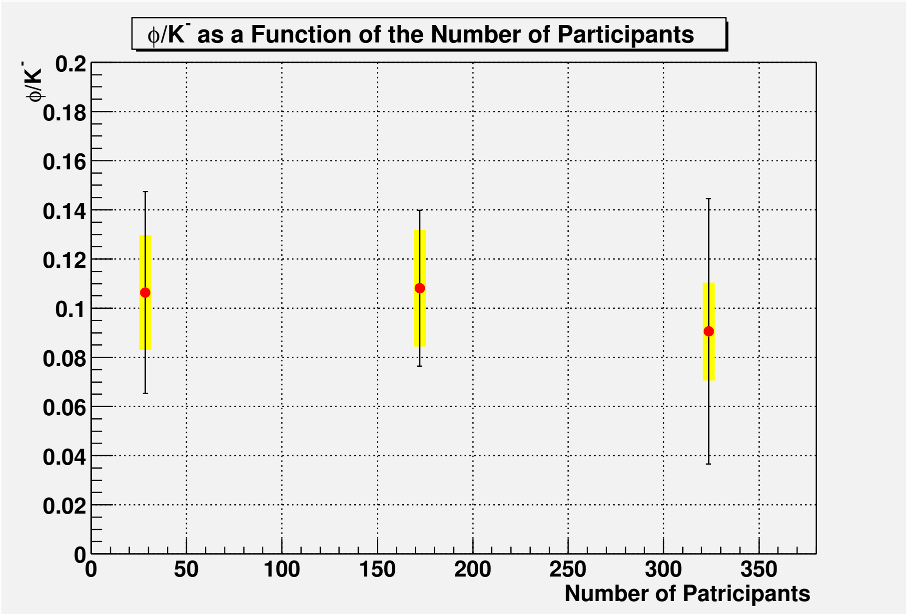

Figure 10.4: ϕ/K^- ratio at 200GeV RHIC Au-Au collisions vs the centrality

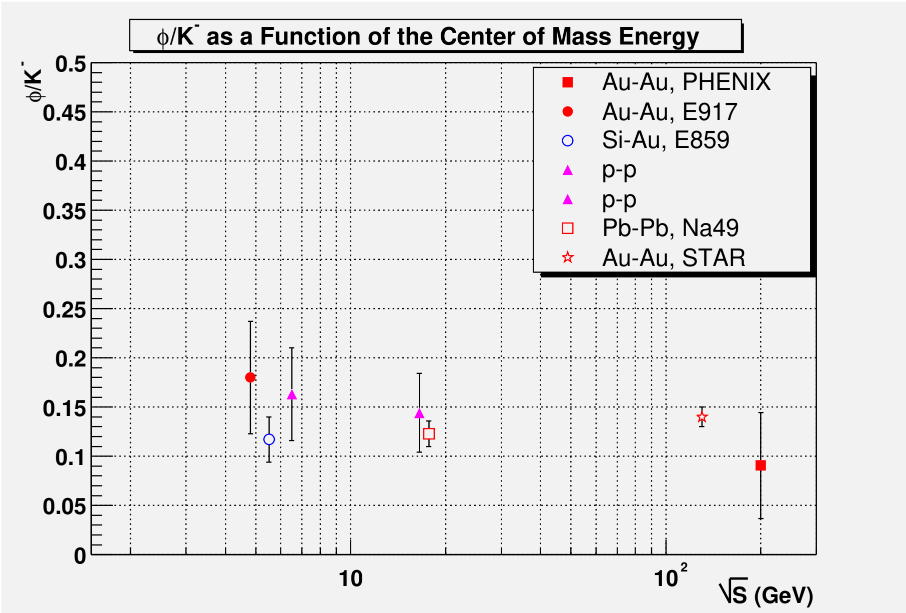

Figure 10.5: ϕ/K^- ratio From different experiments at different beam energies

10.4 Future Analysis

The first measurement of the ϕ mesons with the PHENIX experiment is performed. There are many important aspects we encountered in our results. The more important of them are that the ϕ yield do not show any centrality dependence. Another important result is the ratio of ϕ/K^- yield. It is independent of the collision geometry, implying that the ϕ follow the strangeness production. Another important observation is the universality of the ϕ/K^- ratio even the beam energies have been increased from a few GeV to 200 GeV at RHIC. One of the most intriguing observation was the centrality dependence of the ϕ width. Thanks to the excellent detector resolution in PHENIX we could study the ϕ lineshape over a number of centrality bins. This was indeed as important observation.

The future research endeavors in the ϕ analysis will be based on the above observations. In the RHIC Au-Au run in the coming year will deliver a large amount of data. With the improve statistics it will be possible to definitively comment on the binary collision scaling or the number of participant scaling of the yield. Also more statistics will confirm the centrality dependence of the ϕ width, although the simulation using the next Au-Au run environment precisely predicts the similar behavior of the ϕ width. Another important analysis that can be done is the reconstruction in the leptonic channel. The ratio of the leptonic and hadronic decay will point to any possible medium modification.

Bibliography

[1] D. Gross and F. Wilczek, Phys. Rev. Lett. **30** (1973).

[2] H. Politzer, Phys. Rev. Lett. **30** (1973).

[3] K. Hagiwara et al., Phys. Rev. D **66** (2002).

[4] S. Okubu, Phys. Lett. **5**, (1963).

[5] J. Iizuka, Prog. Theo. Phys. Suppl. **37-38** (1966).

[6] W.S. Chung, G.Q. Li, and C.M. Ko, Physics Letters **B401** (1997).

[7] E917 Collaboration

[8] H.J. Lipkin, Physics Letters **B60** (1976).

[9] A.J. Baltz and C. Dover. Phys. Rev. **C53** (1996).

[10] J. Rafelski, Phys. Rep. **88** (1982).

[11] J. Rafelski, Nucl. Phys. **A544** (1992).

[12] H. Eggers and J. Rafelski, Intl. J. Mod. Phys. **A6** (1991).

[13] P. Koch, B. Müller and J. Rafelski, Phys. Rep. **142** (1986).

[14] T. Matsui, B. Svetitsky and L. McLerran, Phys. Rev, **D34** (1986).

[15] C. Greiner, P. Koch, and H. Stöker, Phys. Rev. Lett. **58** (1987).

[16] T. Biro, P. Lévai and B. Müller, Phys. Rev, **D42** (1990).

[17] C. Ko and L. Xia, Nucl. Phys. **A498** (1989).

[18] C. Ko, Z. Wu and L. Xia, Phys. Rev. **C43** (1991).

[19] S. Nagamiya, Nucl. Phys. **A544** (1992).

[20] WA97 Collaboration, Phys. Lett. **433** (1998).

[21] NA49 Collaboration, Nucl. Phys. **A661** (1999).

[22] F. Karsch. *Proceedings of the Conference on Strong and Electroweak Matter*, World Scientific (1999).

[23] G. Brown and M. Rho, Phys. Rev. Lett. **66** (1991).

[24] T. Hatsuda and S. Lee, Phys. Rev. **C46** (1992).

[25] X. Jin and D. Leinweber, Phys. Rev. **C52** (1995).

[26] M. Asakawa and C. Ko, Nucl. Phys. **A560** (1993).

[27] F. Klingl, N. Kaiser and W. Weise, Nucl. Phys. **A624** (1997).

[28] S. Leupold, W. Peters and U. Mosel, Nucl. Phys. **A628** (1998).

[29] K. Saito, S. Tsushima and A.W. Thomas, Phys. Rev. **C55** (1997).

[30] H. Jean, J. Pickarewicz and A. Williams, Phys. Rev. **C49** (1994).

[31] H. Shiomo and T. Hatsuda, Phys. Lett. **B334** (1994).

[32] C. Song, P. Xia and C. Ko, Phys. Rev. **C52** (1995).

[33] R. Rapp, nucl-th/0204003 (2002).

[34] PHENIX Collaboration, PHENIX Conceptual Design Report, BNL-48922 (1993).

[35] PHENIX Collaboration, PHENIX Detector overview, PHENIX-NIM **A499** (2003).

[36] J. Burward-Hoy, S. Butsyk, T. Chujo, Axel Drees, T. K. Hemmick, B. Jacak, J. Jia, A. K.Purwar, J. Velkovska, PHENIX Analysis Note AN172 (2003).

[37] A.Lebedev, S. Bhagavatula, and M. Rosati, PHENIX Analysis Note AN (2000).

[38] PHENIX Collaboration, PHENIX on-line systems, PHENIX-NIM **A409** (2003).

[39] PHENIX, Physics Q/A for PHENIX Run2 data, *https://www.phenix.bnl.gov/phenix/WWW/p/draft/jacak/qa/* .

[40] J.L. Nagle, M. Chiu, J. Frantz and K. Reygers, PHENIX Analysis Note AN113 (2002).

[41] S.Kelly, S. Mioduszewski, D. Morrison, J. Nagle and K. Reygers, PHENIX Analysis Note AN033 (2001).

[42] K. Reygers, PHENIX Analysis Note AN78 (2001).

[43] Mickey Chiu, S. Mioduszewski, D. Morrison, J. Nagle and K. Reygers, PHENIX Analysis Note AN18 (2000).

[44] M. Muniruzzaman and R. Seto, PHENIX Analysis Note AN153 (2002).

[45] Y. Akiba and C. Maguire, Collaboration wide Communication, 12 September 2002.

[46] J. Burward-Hoy *et.al.*, PHENIX Analysis Note AN172 (2002).

[47] C. Maguire, Talk Presented at the APS Sprint Meeting, Philadelphia, April 5 - 8, 2003.

[48] Averbeck, R., Presentation at the *PHENIX Upgrade Workshop, Montauk 2001* see http://www.phenix.bnl.gov/WWW/p/draft/ralf/montauk.

[49] Gounaris, G.J., Sakurai, J.J., *Phys. Rev. Lett.* **21**(1968)244.

[50] M.J.Tannenbaum, PHENIX Analysis Note AN062 (2001).

Appendix A

Run Numbers used for This Analysis

Run	Number of Segments	Run	Number of Segments
28163	44	29179	11
28170	29	29183	54
28199	16	29184	36
28209	22	29185	25
28212	7	29186	22
28284	35	29515	18
28286	23	29529	20
28302	23	29531	51
28447	26	29534	11
28450	28	29536	63
28485	41	29537	48
28488	8	29561	16
28490	5	29562	10
28570	35	29563	40
28573	13	29566	10
28577	35	29987	58
29116	4	30000	42
29122	14	30001	42
29146	22	30003	18
29171	28	30007	69
29178	25	30009	34

Run	Number of Segments	Run	Number of Segments
30010	55	31024	9
30014	56	31025	32
30015	48	31058	45
30019	8	31060	17
30062	9	31072	55
30069	12	31075	25
30074	26	31079	38
30087	5	31080	13
30088	36	31140	6
30143	6	31143	10
30146	6	31145	18
30148	46	31230	39
30149	36	31232	31
30158	25	31233	6
30159	32	31239	36
30193	40	31240	28
30195	28	31243	41
30196	44	31244	49
30197	6	31249	17
30329	6	31252	47
30388	13	31254	22
30631	8	31256	31
30633	69	31460	8
30642	34	31464	48
30650	42	31500	9
30807	30	31503	25
30812	5	31520	22
30813	8	31631	10
30814	22	31637	8
30816	56	31639	41
30820	6	31814	38
30911	49	31815	9
30913	53	31824	22
30916	67	31836	11
30917	21	31837	25
30920	42	31868	49
31009	21	31870	36

Run	Number of Segments	Run	Number of Segments
31013	32	32523	43
31014	27	32524	25
31021	34	32525	42
32526	47	33169	9
32548	37	33299	30
32549	17	33303	72
32913	5	33309	40
32914	7	33314	25
32929	21	33321	6
32934	23	33323	18
32948	56	33327	6
32949	44	33336	52
33049	5	33337	26
33050	25	33345	40
33051	13	33392	6
33055	5	33393	5
33056	14	33460	10
33064	6	33463	20
33067	30	33468	13
33068	6	33526	8
33082	16	33535	25
33083	14	33541	40
33085	5	33542	62
33098	15	33547	27
33119	33	33550	21
33123	31	33557	35
33124	15	33577	14
33149	25	33610	9
33150	33	33611	16
33161	25	33612	32
33166	22	33693	20
33168	17	33694	40

Appendix B

Tables for Diffetential Cross Section and m_T Spectra

m_T GeV/c^2	Signal	Background	$\frac{1}{2\pi m_T}\frac{d^2N}{dydm_T}$	Error
1.37649	35.1503	2210.85	0.163987	0.221275
1.69365	144.015	2395.99	0.207255	0.0733441
1.89344	108.796	1874.2	0.0985889	0.0406982

Table B.1: Differential yield from EMC-EMC pairs for 0%–10% events

m_T GeV/c^2	Signal	Background	$\frac{1}{2\pi m_T}\frac{d^2N}{dydm_T}$	Error
1.36992	214.151	2029.85	0.265283	0.0680758
1.69196	197.562	2279.44	0.0752079	0.021304
1.89176	221.541	1776.46	0.0530988	0.0127436
2.09159	65.7408	487.259	0.0298987	0.0114599

Table B.2: Differential yield from EMC-EMC pairs for 10%–40% events

m_T GeV/c^2	Signal	Background	$\frac{1}{2\pi m_T}\frac{d^2N}{dydm_T}$	Error
1.36751	56.2693	150.731	0.0354761	0.0100865
1.69134	55.7669	163.233	0.0107896	0.00315927
1.89113	42.8312	121.169	0.0052173	0.00168919
2.09097	21.2765	31.7235	0.00491765	0.001804

Table B.3: Differential yield from EMC-EMC pairs for 40%–92% events

m_T GeV/c^2	Signal	Background	$\frac{1}{2\pi m_T}\frac{d^2N}{dydm_T}$	Error
1.37064	305.511	4391.49	0.12258	0.0278482
1.69215	397.634	4838.37	0.0490485	0.00907893
1.89194	373.151	3771.85	0.0289804	0.00510477
2.09178	85.1538	1032.85	0.0125491	0.00498041

Table B.4: Differential yield from EMC-EMC pairs for minimum bias events

m_T GeV/c^2	Signal	Background	$\frac{1}{2\pi m_T}\frac{d^2N}{dydm_T}$	Error
1.37903	43.2526	531.747	0.668635	0.372877
1.69429	22.4552	668.545	0.0956867	0.112129
1.89409	74.9016	747.098	0.130659	0.0503896
2.09392	46.4306	703.569	0.0412775	0.0244213
2.29378	20.4338	537.566	0.013333	0.0154289
2.57467	78.3474	628.653	0.017467	0.00598821
2.89349	45.1095	157.89	0.0129391	0.00423384
3.34264	67.5584	212.442	0.00285463	0.000735889

Table B.5: Differential yield from TOF-TOF pairs for 0%–10% events

m_T GeV/c^2	Signal	Background	$\frac{1}{2\pi m_T}\frac{d^2N}{dydm_T}$	Error
1.37662	36.7145	478.286	0.162351	0.101149
1.69368	57.8188	617.181	0.0703788	0.0320341
1.89347	104.821	691.179	0.0522301	0.014505
2.09331	134.68	630.32	0.0341996	0.0073966
2.29317	122.693	498.307	0.0228663	0.00492704
2.57228	201.55	559.45	0.0128429	0.00197096
2.89287	64.5687	140.431	0.00528971	0.00128426
3.33013	113.976	185.024	0.00138037	0.00024142

Table B.6: Differential yield from TOF-TOF pairs for 10%–40% events

m_T GeV/c^2	Signal	Background	$\frac{1}{2\pi m_T}\frac{d^2N}{dydm_T}$	Error
1.37642	11.8498	33.1502	0.02762	0.0157808
1.69363	10.6588	43.3412	0.00683793	0.00473965
1.89342	26.8887	42.1113	0.0070613	0.0022328
2.09326	38.2857	38.7143	0.00512384	0.00122333
2.29312	37.5982	29.4018	0.00369303	0.00084571
2.57208	35.1427	32.8573	0.00118027	0.0002885
2.89282	15.8003	8.19969	0.000682202	0.000221877
3.32912	28.989	11.011	0.000185087	4.34228e-05

Table B.7: Differential yield from TOF-TOF pairs for 40%–92% events

m_T GeV/c^2	Signal	Background	$\frac{1}{2\pi m_T}\frac{d^2N}{dydm_T}$	Error
1.37724	87.7138	1047.29	0.12596	0.0489201
1.69384	85.8847	1334.12	0.0339617	0.0149966
1.89363	200.771	1486.23	0.0324996	0.00679717
2.09347	213.792	1378.21	0.0176367	0.00337609
2.29333	176.497	1069.5	0.0106862	0.00220006
2.57289	309.963	1226.04	0.00641546	0.000861143
2.89303	124.201	307.799	0.00330561	0.000618335
3.3333	208.791	410.209	0.000820769	0.000113084

Table B.8: Differential yield from TOF-TOF pairs for minimum bias events

m_T GeV/c^2	Signal	Background	$\frac{1}{2\pi m_T}\frac{d^2N}{dydm_T}$	Error
1.37725	173.479	4237.52	0.531128	0.204928
1.69384	197.973	4144.03	0.209618	0.0704767
1.89364	176.33	2731.67	0.140441	0.043516
2.09347	80.8031	1195.2	0.0702474	0.0313179
2.29333	65.3004	502.7	0.0837923	0.0312742
2.57291	22.0489	252.951	0.0217462	0.0165005

Table B.9: Differential yield from TOF-EMC pairs for 0%–10% events

m_T GeV/c^2	Signal	Background	$\frac{1}{2\pi m_T}\frac{d^2N}{dydm_T}$	Error
1.37808	398.456	3890.54	0.335696	0.0689754
1.69405	255.212	3895.79	0.0743953	0.0208957
1.89385	197.387	2532.61	0.0432826	0.0126525
2.09368	244.458	1105.54	0.0585111	0.0115282
2.29354	71.6639	476.336	0.0253177	0.00897644
2.57373	49.6476	244.352	0.0134782	0.00508357

Table B.10: Differential yield from TOF-EMC pairs for 10%–40% events

m_T GeV/c^2	Signal	Background	$\frac{1}{2\pi m_T}\frac{d^2N}{dydm_T}$	Error
1.37158	115.82	283.18	0.0514227	0.0109534
1.69239	112.733	268.267	0.0172534	0.0036828
1.89218	109.117	168.883	0.0125609	0.00248556
2.09202	46.1126	71.8874	0.00579363	0.00155618
2.29188	13.1635	28.8365	0.00244097	0.00124899
2.56729	16.0187	13.9813	0.00228666	0.000856566

Table B.11: Differential yield from TOF-EMC pairs for 40%–92% events

m_T GeV/c^2	Signal	Background	$\frac{1}{2\pi m_T}\frac{d^2N}{dydm_T}$	Error
1.37651	686.95	8412.05	0.188982	0.0269525
1.69365	565.474	8308.53	0.0537767	0.00912088
1.89345	482.093	5433.91	0.0344867	0.00563451
2.09328	370.977	2373.02	0.0289666	0.00429865
2.29314	149.995	1008.01	0.0172866	0.00410277
2.57217	87.6634	511.337	0.00776692	0.00228805

Table B.12: Differential yield from TOF-EMC pairs for minimum bias events

m_T GeV/c^2	$\frac{1}{2\pi m_T}\frac{d^2N}{dydm_T}$	Error
1.37759	0.454583	0.665554
1.69393	0.170853	0.209157
1.89372	0.12323	0.0696197
2.0937	0.0557625	0.0329914
2.29356	0.0485626	0.0561967
2.57379	0.0196066	0.00672172
2.89349	0.0129391	0.00423384
3.34264	0.00285463	0.000735889

Table B.13: Differential yield from the average of the data points for 0%–10% events

m_T GeV/c^2	$\frac{1}{2\pi m_T}\frac{d^2N}{dydm_T}$	Error
1.37487	0.254443	0.171547
1.69323	0.0733274	0.0393119
1.89303	0.0495372	0.0181825
2.09286	0.0408698	0.0179868
2.29335	0.024092	0.00519115
2.573	0.0131605	0.0020197
2.89287	0.00528971	0.00128426
3.33013	0.00138037	0.00024142

Table B.14: Differential yield from the average of the data points for 10%–40% events

m_T GeV/c^2	$\frac{1}{2\pi m_T}\frac{d^2N}{dydm_T}$	Error
1.37184	0.0381729	0.0243615
1.69245	0.011627	0.0087487
1.89224	0.00827985	0.00374712
2.09208	0.00527837	0.00231031
2.2925	0.003067	0.000702348
2.56968	0.00173346	0.000423721
2.89282	0.000682202	0.000221877
3.32912	0.000185087	4.34228e-05

Table B.15: Differential yield from the average of the data points for 40%–90% events

m_T GeV/c^2	$\frac{1}{2\pi m_T}\frac{d^2N}{dydm_T}$	Error
1.3748	0.14584	0.0656245
1.69321	0.0455956	0.0218312
1.89301	0.0319889	0.00874704
2.09284	0.0197175	0.00868805
2.29323	0.0139864	0.0028795
2.57253	0.00709119	0.000951845
2.89303	0.00330561	0.000618335
3.3333	0.000820769	0.000113084

Table B.16: Differential yield from the average of the data points for minimum bias events